

https://dspace.org/

A Multi-Component, Dual-Release Topical Platform for Skin Cancer

Abobaker, Magdi Elzubir Ali

2025
University of the Witwatersrand, Johannesburg
https://hdl.handle.net/10539/48449
Abobaker, Magdi Elzubir Ali. (2025). A Multi-Component, Dual-Release Topical Platform for Skin Cancer [PhD thesis, University of the Witwatersrand, Johannesburg]. WIReDSpace. https://hdl.handle.net/10539/48449

Downloaded from a DSpace repository. https://dspace.org/

A MULTI-COMPONENT, DUAL-RELEASE TOPICAL PLATFORM FOR SKIN CANCER

MAGDI ELZUBIR ALI ABOBAKER

A thesis submitted to the Faculty of Health Sciences, University of the Witwatersrand, in fulfillment of the requirements for the degree of
Doctor of Philosophy



Supervisor:

Professor Yahya E. Choonara

Department of Pharmacy and Pharmacology, Faculty of Health Sciences, University of the Witwatersrand, Johannesburg, South Africa

Co-Supervisor:

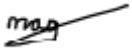
Doctor Mershen Govender

Department of Pharmacy and Pharmacology, Faculty of Health Sciences, University of the Witwatersrand, Johannesburg, South Africa

Johannesburg
2025

DECLARATION

I, Magdi Elzubir Ali Abobaker, hereby declare that this thesis is my own work. It is being submitted for the degree of Doctor of Philosophy in the Faculty of Health Sciences, University of the Witwatersrand, Johannesburg. It has not been submitted before for any degree or examination at this or any other University.

Signature  this …15th…. day of ……April….. 2025

DEDICATION

This thesis is lovingly dedicated to the cherished memory of my late father, whose guiding spirit remains a constant source of inspiration. To my beloved mother and wife, whose unwavering prayers, encouragement, and unconditional love have been pillars of strength throughout this journey, your resilience and care have made this achievement possible.

To my family, the spirits of my dear uncle Mustafa and Abdallah, as well as my friends and mentors, whose support, belief, and guidance have carried me through every step of this endeavor - this work is dedicated to you as well.

ANIMAL ETHICS DECLARATION

I, Magdi Elzubir Ali Abobaker, hereby confirm that the study titled “A Multi-Component, Dual-Release Topical Platform for Skin Cancer” has received approval from the Animal Ethics Screening Committee (AESC) of the University of the Witwatersrand for the use of porcine skin sourced from the Wits Research Animal Facility (WRAF, Johannesburg, South Africa) under the approved ethics waiver number 07-11-2024-O (A copy of the approval certificate has been included in Appendix A1).

RESEARCH OUTPUTS, GRANTS AND FUNDING

A. Publications

1. Magdi Abobaker, Mershen Govender, and Yahya E. Choonara (2024). Non-surgical Synergistic Interventions for the Treatment of Skin Cancer, *Current Pharmaceutical Design*, DOI: 10.2174/0113816128298264240530061039 (Appendix A2).

2. Magdi Abobaker, Mershen Govender, and Yahya E. Choonara (2025). Co-Formulation of Iron Oxide and PLGA Nanoparticles to Deliver Curcumin and IFNα for Synergistic Anti-Cancer Activity in A375 Melanoma Skin Cancer Cells, *Pharmaceutics*, submitted (Appendix A3).

3. Magdi Abobaker, Mershen Govender, and Yahya E. Choonara. Synergistic Surgical and Nano-Based Oncology Treatments for Skin Cancer. To be submitted to *Pharmaceutical Development and Technology*.

4. Magdi Abobaker, Mershen Govender, and Yahya E. Choonara. A Controlled-release Nanoparticulate System for the Delivery of IFN-Alpha'. To be submitted to *AAPS PharmSciTech.*

5. Magdi Abobaker, Mershen Govender, and Yahya E. Choonara. A Dual-controlled Release Nanoparticle-loaded Hydrogel Platform for the treatment of Melanoma Skin Cancer. To be submitted to *International Journal of Pharmaceutics*.

B. GRANTS AND FUNDING

1. Postgraduate Merit Award (PMA), University of the Witwatersrand, South Africa, 2021-2024.
2. Clinical Training Grant (CTG), Faculty of Health Sciences, University of the Witwatersrand, South Africa, 2022-2024.
3. Faculty Research Committee (FRC) Individual Research Grants, Faculty of Health Sciences, University of the Witwatersrand, South Africa, 2022-2024.

RESEARCH PRESENTATIONS

1. Magdi Abobaker, Mershen Govender, and Yahya E. Choonara. A Multi-Phasic Controlled Release System for the Treatment of Skin Cancer. Poster presented at the Faculty of Health Sciences Research Day and Postgraduate Expo, 5 September 2024, University of the Witwatersrand, Johannesburg, South Africa (Poster in Appendix A4).

2. Magdi Abobaker, COIL (Collaborative Online International Learning) Presentation: "Awareness of Public Health Challenges in South Africa and Spain.", Under the supervision of Paola Otero Gómez, Isabel Adoración Martín Antoniano, Sara Ruiz Gómez, Cristina Rodríguez Luque, and Yahya Choonara, 2024. Hosted by University San Pablo CEU and the University of the Witwatersrand (Appendix A5).

3. Magdi Abobaker, Mershen Govender, and Yahya E. Choonara. A Multi-Component, Dual Release Platform for the Treatment of Skin Cancer. Poster presented at the Faculty of Health Sciences Molecular Bioscience Research Thrust Postgraduate Research Day, 6 December 2024, University of the Witwatersrand, Johannesburg, South Africa. (Poster in Appendix A6)

SUMMARY

The central focus of this research was the design, development, and evaluation of a novel synergistic therapeutic approach for the treatment of skin cancer. Both non-melanoma skin cancer (NMSC) and malignant melanoma (MM) are highly prevalent, with MM causing significant mortality due to its metastatic nature and aggressive progression. NMSC is, however, more frequently diagnosed globally, accounting for a substantial portion of skin cancer cases, especially among Caucasians, with incidence rates steadily increasing over the last decade. Current treatments, although effective in early-stage skin cancers, are limited by numerous drawbacks, including drug resistance, off-target toxicity, high treatment costs, and undesirable side effects, especially in advanced cases. This thesis addresses these limitations by exploring a hydrogel-based nanotechnology-driven drug delivery system that combines chemotherapeutic and immunotherapeutic agents for enhanced efficacy, specificity, and patient compliance.

Initially, this work reviews the current therapeutic options for skin cancers, from simple surgical excision in early cases to complex combination treatments like chemotherapy, radiotherapy, immunotherapy, and phototherapy in more advanced stages. These treatments, while achieving significant improvements in patient outcomes, often lead to multiple adverse effects and complications. For instance, chemotherapy can result in systemic toxicity, while immunotherapy, using agents such as interferon-alpha (IFNα), requires high doses that lead to side effects like myalgia and leukopenia. By examining these issues, this thesis underscores the need for a more targeted, controlled drug delivery approach that can minimize side effects, prevent relapses, and improve patient quality of life.

To address these gaps, this research has investigated the potential of a non-surgical synergistic intervention combining iron oxide nanoparticles (FeONPs) functionalized with curcumin (Cur), a natural polyphenol with established anticancer properties, with IFNα, an immunotherapeutic agent for skin cancer, encapsulated within poly(lactic-co-glycolic acid) nanoparticles (IFNα-PLGANPs). Cur has shown the ability to disrupt cancer cell proliferation and invasion by affecting multiple signaling pathways, making it a promising candidate for melanoma treatment. It is, however, limited by a low bioavailability despite its known therapeutic potential. The FeONPs synthesized in this study therefore act as a carrier, enhancing curcumin's bioavailability, allowing for bioaccumulation at the skin cancer site after topical administration. This functionalization was achieved using a one-step coprecipitation technique, producing nanoparticles (NPs) with an average size of 95.37 nm,

preferred for effective topical drug delivery. The synthesis and characterization of the curcumin-functionalized (Cur-FeONPs) further demonstrated a stable structure, high biocompatibility, and enhanced therapeutic efficacy. Morphological analysis additionally confirmed a NP size below 100 nm, suitable for cellular uptake and improved bioavailability, with *in vitro* studies revealing selective cytotoxicity toward melanoma (A375) cells, with limited impact on NIH-3T3 fibroblast cells. A dual-release nanosystem was thereafter designed by combining the Cur-FeONPs with statistically optimized IFNα-PLGANPs (average size = 90.73 nm) developed for the controlled release of IFNα (≈88% after 5 days). This controlled release mechanism achieved multiple goals including protecting the drug from degradation, lowering the dose required at administration, therefore potentially decreasing treatment costs, but also for the separation of IFNα from Cur, which by its broad mechanisms of action has the potential to decrease treatment efficacy when combined with other anticancer interventions.

The final therapeutic drug delivery platform developed in this research is a multi-component, dual-release platform for skin cancer incorporating both the Cur-FeONPs and optimized IFNα-PLGANPs within a hydrogel matrix for topical administration. Hydrogels are advantageous for skin cancer treatment due to their flexibility, moisture retention, and ability to provide sustained drug release. Alginate (Alg)-based hydrogels, in particular are useful for topical applications, allowing for direct and localized drug delivery to skin lesions, while minimizing systemic toxicity. In this work, Alg has been used to develop a hydrogel matrix that can support the co-delivery of the combinative agents, mimicking the tumor's extracellular environment to improve cellular uptake and efficacy. Additionally, the inclusion of lecithin as a structural modifier enhances drug permeability, supporting optimal therapeutic agent release. Rheological studies on the combined NP-loaded platform revealed the hydrogel's temperature responsiveness, mechanical stability, and bioadhesion properties, making it suitable for sustained and localized drug delivery. The hydrogel platform also displayed dual-controlled permeation and release, ensuring prolonged therapeutic action in line with the aim of this study. *In vitro* antiproliferation and cytotoxicity studies further confirmed synergistic cytotoxic effects against melanoma cells while maintaining biocompatibility with fibroblast cells, highlighting their safety and efficacy. The research performed therefore validated the developed system's potential to achieve controlled drug delivery, minimize systemic toxicity, and enhance treatment outcomes using a synergistic nano-driven approach.

Overall, this study advances the field of skin cancer treatment by demonstrating the potential of a hydrogel-based NP-loaded topical drug delivery system for the treatment of skin cancer.

The combination of Cur-FeONPs and IFNα-PLGANPs researched presents a powerful therapeutic strategy, leveraging both non-surgical synergistic intervention effects to maximize efficacy, while minimizing adverse effects.

The findings from this research underscore the promise of this multi-faceted approach in enhancing treatment outcomes, with the developed hydrogel delivery system potentially a valuable tool for developing more effective, patient-specific treatment strategies, opening new avenues for future research in the field of skin cancer therapeutics. Ultimately, this thesis contributes to a growing body of knowledge on the use of nanotechnology and synergistic treatments in oncology, presenting a pathway towards more personalized, efficient, and patient-friendly cancer treatments.

ACKNOWLEDGEMENTS

First and foremost, I extend my heartfelt gratitude to Allah, whose boundless grace and mercy have guided me through every step of this journey. It is only through His blessings that I have been granted strength, resilience, and perseverance to complete this PhD. Truly, it is His wisdom that has illuminated my path, allowing me to turn challenges into learning experiences and to bring this endeavor to fruition.

I am deeply indebted to all who have supported me throughout my PhD journey at the University of the Witwatersrand. This thesis would not have been possible without the invaluable insights, guidance, and encouragement of so many individuals.

Firstly, I extend my deepest and most heartfelt gratitude to my supervisor, Dr. Mershen Govender. His exceptional technical expertise, insightful guidance, and unwavering encouragement have profoundly shaped and enriched this work. Dr. Govender's ability to seamlessly blend rigorous academic standards with a supportive and inspiring mentoring approach has been nothing short of transformation. His relentless dedication to fostering my growth, both as a researcher and as an individual, has left an indelible mark on my journey. I am immensely thankful for his thoughtful feedback, tireless support, and for instilling in me a commitment to excellence and innovation. This work stands as a testament to his remarkable mentorship and the profound impact he has had on my academic and professional development.

I am equally grateful to my primary supervisor, Professor Yahya E. Choonara, whose expertise, unwavering support, and mentorship have been central to the shaping of this research. His trust in my potential and insightful guidance helped me navigate every challenge, making this journey profoundly impactful.

I extend my sincere thanks to the Wits Advanced Drug Delivery Platform (WADDP) Research Unit for providing the resources, infrastructure, and inspiring environment that made this research possible. The platform's commitment to pioneering advancements in pharmaceutical sciences has motivated me deeply and has been essential to my research endeavors.

My appreciation also goes out to the technical staff of the Department of Pharmacy and Pharmacology and my colleagues and friends at WADDP, whose camaraderie, insights, and inspiration have made this journey both fulfilling and enjoyable. Collaborating with such a devoted group of professionals has enriched my research experience immeasurably.

I would like to express my heartfelt gratitude to the National Research Foundation (NRF), University of the Witwatersrand, South Africa, for their invaluable support. Their contribution has played a pivotal role in advancing this research. I am equally thankful to the Faculty Research Committee, Faculty of Health Sciences, University of the Witwatersrand, South Africa for their research support, which significantly facilitated various aspects of this project. Collectively, these contributions have been fundamental in enabling the successful progression and completion of this research journey.

Above all, I owe my deepest thanks to my beloved wife and mother, whose unwavering prayers and support have been my strength, even as they endure the hardships of war and conflict in our home country. Their resilience and love have sustained me, inspiring me to persevere with purpose and hope. To my children, whose patience and unspoken encouragement have been my driving force, and to my siblings for their unyielding support, I am forever grateful.

To all who have shared this journey, offering support, guidance, and encouragement: I thank you from the depths of my heart. This achievement is as much yours, as it is mine.

Thank you, everyone.

Magdi

TABLE OF CONTENTS

DECLARATION	i
DEDICATION	ii
ANIMAL ETHICS DECLARATION	iii
RESEARCH OUTPUTS, GRANTS AND FUNDING	iv
RESEARCH PRESENTATIONS	v
SUMMARY OF THE THESIS	vi
ACKNOWLEDGEMENTS	ix
TABLE OF CONTENTS	xi
LIST OF FIGURES	xix
LIST OF TABLES	xxxii
LIST OF ABBREVIATIONS	xxxiii
LIST OF EQUATIONS	xixv

TABLE OF CONTENTS

CHAPTER 1

INTRODUCTION

1 Introduction 1

1.1 Background to this study 1

1.1.1 The Physiology of Skin Cancer 1

1.2 Rationale and Motivation for this study 3

1.3. Novelty of This Research 7

1.4. Aim and Objectives 8

1.5 Overview of this Thesis 8

CHAPTER 2

SYNERGISTIC SURGICAL AND NANO-BASED ONCOLOGY TREATMENTS FOR SKIN CANCER

2.1 Introduction 11

2.2 Treatment of Skin Cancers 13

2.2.1 Surgical Resection 13

2.2.2. Combination Surgical Resection-Nanomaterial Interventions for MM 16

2.2.2.1 Chemotherapy-Loaded Nanomaterials 16

2.2.2.2 Nanosystems for Phototherapy 18

2.2.2.3 Nanosystems incorporating Radiotherapy 20

2.2.2.4 Immunomodulating Nanosystems 22

2.2.2.5 Nanomaterial-induced Hyperthermia 26

2.2.2.6 Nanomaterial-regulated Extracorporeal photopheresis. 27

2.2.3 Multicomponent combinations 28

2.3 Conclusion 30

CHAPTER 3

NON-SURGICAL SYNERGISTIC INTERVENTIONS FOR THE TREATMENT OF SKIN CANCER

3.1 Introduction 32

3.2 Non-surgical Combination Treatments for Skin Cancer 32

3.2.1 Synergistic Radiotherapy Interventions 33

3.2.1.1 Chemotherapy 33

3.2.1.2 Immunotherapy 34

3.2.1.3 Photothermal therapy 35

3.2.1.4 Hyperthermia Therapy 36

3.2.2 Chemotherapeutic Combinations 37

3.2.2.1 Phototherapy 37

3.2.2.2 Immunotherapy 40

3.2.2.3 Hyperthermia Therapy 41

3.2.2.4 Extracorporeal photopheresis (ECP) 43

3.2.3 Synergistic Phototherapy 43

3.2.3.1 Immunotherapy 44

3.2.3.2 Nanomaterials Therapy 45

3.2.4 Hyperthermic Interventions 46

3.2.4.1 Immunotherapy 48

3.2.5 Immunotherapy Interventions 50

3.2.5.1 Extracorporeal photopheresis 51

3.2.6 Multicomponent Non-Surgical Combination Therapies 51

3.3 Conclusion 52

CHAPTER 4

SYNTHESIS OF CURCUMIN-FUNCTIONALIZED IRON OXIDE NANOCOMPLEX SYSTEM FOR THE TREATMENT OF SKIN CANCER

4.1 Introduction 54

4.2 Materials and Methods 56

4.2.1 Materials 56

4.2.2 Synthesis of the Cur-FeONPs 56

4.2.3 Chemical Structure Validation 56

4.2.4 Determination of Particle Size, Zeta Potential, and Morphology 57

4.2.5 Differential Scanning Calorimetry 57

4.2.6 Crystallographic Structure- Analysis 57

4.2.7 Drug Loading and *In vitro* Drug release analysis 58

4.2.8 Cytocompatibility and Antiproliferation Activity Analyses 59

4.2.9 Statistical analysis 60

4.3 Results and Discussion 60

4.3.1 Evaluation of the Chemical Stability and Functional Transformation of the Cur-FeONPs 61

4.3.2 Particle Sizing and Morphological analysis of the Cur-FeONPs 62

4.3.2.1 Particle analyses 62

4.3.2.2 Scanning electron micrographs (SEM) and TEM Analysis 64

4.3.3 Thermal Analysis 66

4.3.4 Crystallinity studies 67

4.3.5 Determination of Cur-Loading of the Cur-FeONPs 69

4.3.6 In vitro Cur release Analysis 69

4.3.7 Cell culture and Cytotoxicity Assessment 70

4.3.8 In vitro Assessment of the Antiproliferative effect of Cur–FeONPs 72

4.4 Conclusions 73

CHAPTER 5

DEVELOPMENT OF A CONTROLLED-RELEASE IFN-LOADED NANOPARTICLE SYSTEM FOR SKIN CANCER

5.1 Introduction 75

5.2 Materials and Methods 77

5.2.1 Materials 77

5.2.2 Preparation and Statistical Optimization of the IFN-α-loaded PLGA NPs 77

5.2.2.1 Synthesis Validation of the IFNα-PLGANPs 78

5.2.2.2 SDS-Page Gel-Electrophoresis Assessment for IFNα-PLGANPs 78

5.2.3 Determination of Particle Size and Zeta Potential, of the DoE formulations 79

5.2.4 Drug Loading Capacity and Adsorption Efficiency of the DoE formulations 79

5.2.5 In vitro Release Analysis of the IFNα-PLGA NPs of DoE formulations 80

5.2.6 Optimization of the IFNα-PLGA NPs DoE formulations 81

5.2.6.1 Characterization of the Optimized IFNα-PLGANPs 82

5.2.6.2 Determination of Particle Size, Zeta Potential, and Morphology 82

5.2.6.3 Determination of the Thermal Characteristics of the optimized IFNα-PLGANPs 82

5.2.6.4 Crystallographic Structure 82

5.2.7 Cell culture and Cytotoxicity and Antiproliferation Assays 82

5.2.7.1 Evaluation of the Cytotoxicity and Antiproliferation Potential of the combined Cur-FeONPs and the Optimized IFNα-PLGANPs 82

5.2.8 Statistical analysis 83

5.3 Results and Discussion 83

5.3.1 Synthesis Validation of IFNα-PLGANPs 83

5.3.1.1 Evaluation of the Chemical Stability and Functional Transformation of the IFNα-PLGANPs 83

5.3.1.2 SDS-Page Gel-electrophoresis assessment for IFNα-PLGANPs 84

5.3.2 Evaluation of the Experimental Design 85

5.3.2.1 Particle Size Analysis 85

5.3.2.2 Release Dynamics 87

5.3.2.3 Statistical Validation and Model Fit 90

5.3.2.4 Data Analysis and Optimization of the Statistical Design 90

5.3.2.5 Constrained Statistical Optimization of the IFNα-PLGANPs 94

5.3.3. Analysis of Optimized IFNα-PLGANPs 96

5.3.3.1 Particle Analysis 96

5.3.3.2 SEM of the Optimized IFNα-PLGANPs 96

5.3.3.3 Thermal Analysis of the Optimized IFNα-PLGANPs 97

5.3.3.4 X-ray diffraction (XRD) analysis 99

5.3.3.5 Loading Capacity and Adsorption Efficiency within the IFNα-PLGANPs 100

5.3.4 Release Profile of the optimized IFNα-PLGANPs 100

5.3.5 The Cytotoxicity of the Optimized IFNα-PLGANPs and its Combination with Cur-FeONPs 102

5.3.5.1 The Antiproliferation of the Optimized IFNα-PLGANPs and its Combination with Cur-FeONPs 103

5.3.5.2 Therapeutic Dose Efficacy on A375 Melanoma Cells 105

5.4 Conclusions 104

CHAPTER 6

A NANOPARTICLE-LOADED HYDROGEL FOR THE TREATMENT OF SKIN CANCER

6.1 Introduction 107

6.2 Materials and Methods 108

6.2.1 Materials 108

6.2.2 Development of NP-loaded alginate-lecithin hydrogel topical system 108

6.2.2.1. Zeta Size and Zeta Potential Measurements of the NP-loaded hydrogel 109

6.2.2.2 Rheological Measurements of the NP-loaded hydrogel 110

6.2.2.3 Mechanical Properties of the NP-loaded hydrogel 110

6.2.2.3.1 *In vitro M*ucoadhesion Studies 110

6.2.2.4 Degradation Studies 111

6.2.3 Permeation Studies 111

6.2.4 Biocompatibility and Cytotoxicity Assessment of the NP-loaded hydrogel 113

6.2.5 Anti-Proliferative Activity of the NP-loaded hydrogel Topical System 114

6.2.6 Statistical analysis 114

6.3 Results and Discussion 114

6.3.1 Zeta Size and Zeta Potential Measurements of the hydrogel 114

6.3.2 Rheological Evaluation of the NP-loaded hydrogel Topical System 116

6.3.3 Mechanical Properties of the NP-loaded hydrogel 118

6.3.3.1 Ex Vivo Bioadhesion Properties 120

6.3.4 Degradation studies 124

6.3.5 Cur and IFNα Permeation 125

6.3.6 Biocompatibility and Cytotoxicity Assessment of the NP-loaded hydrogel 126

6.3.6.1 Cytotoxicity Assessment of the NP-loaded hydrogel and the Unloaded hydrogel 126

6.3.7 Anti-Proliferative Activity of the hydrogel Topical System 127

6.4 Conclusions 129

CHAPTER 7

CONCLUSION, LIMITATIONS, AND RECOMMENDATIONS

7.1 Conclusion 131

7.2 Limitations and Recommendations 132

REFERENCES 135

APPENDICES 158

LIST OF FIGURES

Figure 1.1: This illustration shows the two main layers of the skin: the outer epidermis, composed of stratified squamous epithelial cells arranged into distinct layers (including the stratum corneum, granulosum, spinosum, basale, and in thick skin, the stratum lucidum), and the underlying dermis, which is further divided into the papillary and reticular layers. The papillary dermis contains vascularized loose connective tissue and dermal papillae that interface with the epidermis, while the reticular dermis houses dense connective tissue along with blood vessels, lymphatics, nerves, sweat glands, and hair follicles. This structural organization is essential for protective, sensory, and regenerative functions of the skin. Disruptions in these layers can contribute to the development of skin pathologies, including cancer. Reproduced with permission from Akhtar and Khan [11]. 2

Figure 1.2: Schematic representation of the five-phase mechanism of bioactive release from the developed dual-delivery, NP -loaded topical patch system. After the patch is applied to the skin (Phase 1), the release of both Cur -loaded iron oxide NP s (Cur-FeONPs) and IFNα-loaded PLGA NP s is initiated (Phase 2). Cur is rapidly released from the FeONPs to exert an immediate therapeutic action (Phase 3), while the FeONPs penetrate the tumor tissue and induce apoptosis and oxidative effects (Phase 4). Simultaneously, the PLGA matrix degrades slowly to provide a sustained release of IFNα (Phase 5). This controlled release system enhances drug localization at the tumor site, minimizes systemic exposure, and combines both immunotherapeutic and chemotherapeutic dual-delivery strategies for effective melanoma treatment the topical patch system. 7

Figure 2.1: Nanocarrier-based drug delivery for melanoma therapeutics. This schematic illustrates how NPs exploit the enhanced permeability and retention (EPR) effect to deliver therapeutic agents to melanoma cells. Rapid tumor growth often leads to the formation of poorly structured and leaky blood vessels, allowing NPs to traverse these compromised vascular junctions and accumulate within the tumor microenvironment. Once localized, these nanocarriers can release their payload in a controlled manner, enhancing drug 13

efficacy while minimizing systemic side effects. This targeted approach improves therapeutic outcomes in melanoma treatment. Adapted from Dastgheib *et al.* [40].

Figure 2.2: An illustration of melanoma progression (Stages I-IV). This figure provides a visual representation of the progressive stages of malignant melanoma, detailing the tumor's advancement from localized growth to widespread dissemination: Reproduced with permission from Zeng *et al.* [4]. 14

Figure 2.3: The process of skin cell carcinogenesis involves three distinct stages: initiation, promotion, and progression. Each of these stages can be influenced by specific chemo-preventive agents. Blocking agents are employed to interfere with initiation, while suppressing agents are utilized to target the promotion and progression stages. Adapted with permission from Iqbal *et al*. [51]. 15

Figure 2.4: Nanomaterials improve cancer immunotherapy by facilitating the delivery of immunomodulatory drugs: (a), Nanomaterials can be targeted for delivery to tumor cells, with the ability for stimulus-responsive release at tumor sites and (b), Various types of nanomaterials such as implantable scaffolds (i), microneedle patches (ii) and hydrogels (iii), can be used to locally deliver immunomodulators directly to the surgical cavity, thus enhancing tumor eradication post-surgery. 25

Figure 2.5: Thermal effects on tumor and cell physiology. This figure illustrates the impact of thermal treatments on tumor cells and their microenvironment, highlighting the physiological responses to varying temperature ranges. These thermal effects are essential for optimizing hyperthermia-based cancer therapies, ensuring maximal tumor cell eradication while preserving normal tissue integrity. Reproduced with permission from Moyer and Delman [113]. 27

Figure 2.6: Schematic illustration of the formation of the Fe^{3+}@Au_1Ag_{24}@PbP nanoplatform and its imaging-guided synergistic anticancer therapy. This figure depicts the step-by-step synthesis and functionalization of the Fe^{3+}@Au_1Ag_{24}@PbP nanoplatform, highlighting its application in imaging-guided synergistic anticancer therapy. Reproduced with permission from Yang and Sun [123]. 30

Figure 3.1: A schematic representation of the basic action mechanisms of PTT, Ionizing RT and combining PTT/RT in cancer treatment based on functionalized AuNPs. This figure illustrates the fundamental mechanisms by which PTT and RT exert therapeutic effects on cancer cells, both individually and in combination. Reproduced with permission from Spyratou *et al*. [110]. 35

Figure 3.2: The experimental setup for the combination of (PT) with CT in an *in vivo* setting using MEO2MA@MEO2MA-co-OEGMA-CuS-DOX (G-CuS-DOX) NPs. This figure illustrates the experimental arrangement designed by Meng *et al*. for evaluating the synergistic effects of PTT and CT using G-CuS-DOX NP s in a live animal model. Reproduced with permission from Meng *et al.* [154]. 39

Figure 3.3: illustrates the types of nanomaterials employed in photoimmunotherapy for skin cancer. The primary categories include metallic, polymeric, lipid-based, and 2D NPs. This schematic illustration presents the major classifications of NPs employed in photoimmunotherapy, highlighting their structural diversity and functional potential in advanced cancer therapeutics, particularly for skin malignancies. The figure categorizes NPs into four main groups based on their composition and morphology. Reproduced with permission from Relvas *et al.* [177]. 46

Figure 3.4: A schematic representation of the mechanism of heating and cellular at elevated temperature in the presence of an alternating magnetic field (AMF). This illustration demonstrates the fundamental mechanism by which magnetic NPs, typically iron oxide-based (e.g., Fe_3O_4), generate localized heat within tumor tissues upon exposure to an external AMF. When subjected to AMF, these NPs undergo relaxation processes—Néel and Brownian relaxation—leading to the dissipation of energy in the form of heat. Reproduced with permission from Suneet *et al.* [17]. 47

Figure 3.5: Management of melanoma with FDA-approved immunotherapy agents. This figure provides a comprehensive schematic of the current immunotherapeutic strategies approved by the U.S.FDA for the treatment of melanoma, particularly advanced and metastatic forms. These therapeutic agents are primarily immune checkpoint inhibitors that enhance the body's 50

antitumor immune response by targeting regulatory pathways in T-cell activation and exhaustion. Reproduced with permission from Knight *et al*. [192].

Figure 4.1: Illustration of the relationship between Cur concentration and absorbance at 428 nm. The resulting data points were plotted to generate the standard curve, which demonstrates a linear correlation between concentration and absorbance within the tested range. This linearity confirms adherence to the Beer-Lambert law, indicating that absorbance is directly proportional to concentration. 59

Figure 4.2: FTIR spectra for the Cur-FeONPs, free Cur, and the uncoated FeONPs. FTIR spectroscopy is employed to identify characteristic functional groups and assess chemical interactions among these components. These spectral analyses confirm the successful conjugation of Cur onto the iron oxide NP s, a crucial step for developing targeted drug delivery systems. 62

Figure 4.3: The average size and zeta potential profiles of the prepared FeONPs, (a) and (b), respectively, and of the Cur-FeONPs, (c) and (d), respectively. The observed increase in hydrodynamic diameter and the more negative zeta potential upon Cur loading suggest successful functionalization of the FeONPs. The higher negative zeta potential indicates improved colloidal stability, which is crucial for minimizing aggregation and enhancing biocompatibility. These characteristics are anticipated to facilitate effective cellular uptake and targeted delivery of Cur to cancer cells, thereby enhancing therapeutic efficacy. 63

Figure 4.4: Digital images of samples with corresponding SEM images showing overall morphology of FeONPs (a & b) at 200 nm scales (82.34 KX magnification) and (c) of Cur-FeONPs at 200 nm scale (82.34 KX magnification) and (d) 100 nm scale (314.84 KX) (isolated particle), indicating a particle size of <100 nm. The SEM analyses confirm that both FeONPs and Cur-FeONPs possess spherical morphologies with sizes predominantly below 100 nm. The slight increase in size observed in Cur-FeONPs compared to FeONPs is indicative of successful Cur loading. These morphological characteristics are crucial, as NP size and shape significantly influence their biological interactions, cellular uptake, and overall efficacy in drug delivery 65

applications.

Figure 4.5: Visualization of the morphological attributes of the FeONPs: TEM images of FeONPs at (a) 100 nm scale and (b) 200 nm scale, and of Cur-FeONPs at (c) 100 nm and (b) 200 nm scales. The TEM analyses confirm that both FeONPs and Cur-FeONPs possess a predominantly spherical morphology with uniform size distributions. The observed increase in particle size upon Cur loading aligns with findings from similar studies, where TEM images demonstrated successful drug loading onto FeONPs without compromising their structural integrity. These characteristics are crucial for ensuring effective cellular uptake, targeted drug delivery, and minimizing potential cytotoxicity in biomedical applications. 66

Figure 4.6: DSC curves of the free Cur, FeONPs and Cur-FeONPs. The absence or shift of the characteristic melting peak of Cur in the Cur-FeONPs thermogram indicates successful encapsulation and possible molecular interactions between Cur and the NP matrix. These thermal analyses are crucial for understanding the stability and physicochemical properties of the formulated NP s, which are essential for their efficacy as drug delivery systems. 67

68

Figure 4.7: XRD spectra of free Cur, Cur-FeONPs, and free FeONPs. This figure presents the XRD patterns for free Cur, FeONPs, and Cur-FeONPs, providing insights into their crystalline structures and the effects of Cur loading on the NPs. The XRD analysis confirms the crystalline nature of free Cur and FeONPs. The diminished crystallinity of Cur in the Cur-FeONPs composite suggests effective loading onto the FeONPs, which may influence the dissolution rate and bioavailability of Cur in therapeutic applications.

Figure 4.8: Cur release profile of the synthesized Cur-FeONPs (SD≤ 0.38 in all cases). This figure illustrates the in vitro release kinetics of Cur from the synthesized Cur-FeONPs over a specified time period, with SD not exceeding 0.38 in all measurements. The low standard deviation across measurements indicates the reproducibility and consistency of the release profile, underscoring the reliability of the NP formulation. 69

Figure 4.9: Cytotoxicity assessments to evaluate the cell viability of Cur-FeONPs, free Cur and FeONPs at different concentrations on NIH-3T3 cells, where A, B, C and D represents 10, 5, 2.5 and 1.25 µg/, respectively. The experiments were undertaken for (a) 24 (b), 48 and (c) 72 hours (n=3). These findings suggest that Cur-FeONPs maintain a favorable cytotoxicity profile at lower concentrations, with enhanced cytotoxic effects at higher concentrations likely attributable to the therapeutic action of Cur. The results indicate that the NP formulations can modulate the cytotoxicity of encapsulated agents, potentially offering a controlled delivery mechanism that minimizes adverse effects on healthy cells. 71

Figure 4.10: Cell viability profile of A375 cells treated with varying concentrations of Cur-FeONPs, free Cur, FeONPs, negative control and positive control after 72 h, where A, B, C and D represents 10, 5, 2.5 and 1.25 µg/L, respectively. Data presented as mean ± SD, n = 3. These findings suggest that Cur-FeONPs effectively reduce the viability of A375 melanoma cells in a dose-dependent manner, with enhanced cytotoxic effects at higher concentrations likely attributable to the therapeutic action of Cur. 73

Figure 5.1: Standard curve of IFNα using the microBCA assay at 595 nm. The standard curve serves as a reference to determine the concentrations of IFNα in unknown samples by correlating their absorbance readings to the established curve. Accurate quantification of IFNα is crucial in various research and clinical contexts, including immunological studies and therapeutic monitoring. 81

Figure 5.2: Scheme of FTIR spectra of the IFNα-loaded PLGANPs, pure IFN-α 2b, and PLGA. The FTIR analysis confirms the successful incorporation of IFNα into the PLGA NP s, as evidenced by the presence of characteristic protein absorption bands alongside PLGA's peaks. These spectral features suggest potential intermolecular interactions between the polymer and the protein, which could influence the release profile and bioactivity of IFNα from the NPs. 84

Figure 5.3: Visualization of protein separation and characterization of the molecular weight properties of the IFN-PLGANPs and BSA. The resulting bands indicate successful loading and stability of IFN within the NP formulation. The migration pattern and band intensity provide insights into the integrity and encapsulation efficiency of the proteins, as well as potential interactions between IFN and the PLGA matrix. This analysis confirms the presence of the target proteins and validates the NP formulation as a carrier for therapeutic protein delivery 85

Figure 5.4: 3D plots portraying the influence of PEG-to-PLGA and the INFα-load on the (a) particle size, (b) cumulative release after one day (RD1), (c) cumulative release after three days (RD3), and (d) cumulative release after five days (RD5). These 3D plots were generated using statistical modeling techniques such as response surface methodology (RSM), enabling visualization of the interaction between formulation parameters and their effects on NP properties. The data help identify ideal formulation conditions that balance particle size, drug encapsulation efficiency, and stability for efficient therapeutic delivery of IFNα. 89

Figure 5.5: Release profiles of the prepared design formulations. This figure illustrates the cumulative in vitro release profiles of IFNα from various NP formulations designed using different PEG-to-PLGA ratios and drug loading concentrations. The release study was conducted under physiologically relevant conditions (e.g., pH 7.4, 37°C) over a specified time period to simulate systemic circulation and assess the sustained release behavior of the formulations. 90

Figure 5.6: Pareto Charts showing the t-Value |effect| of the dependent variables on (a) particle size, (b) cumulative release after one day, (c) cumulative release after three days, and (d) cumulative release after five days. This figure presents a series of Pareto charts summarizing the influence of formulation parameters—specifically the PEG-to-PLGA ratio and the IFNα loading concentration—on four critical NP performance metrics. The charts are based on standardized t-values derived from a factorial design analysis, representing the magnitude and statistical significance of the effect of each independent variable on the respective response. The vertical dashed line 93

indicates the minimum threshold for statistical significance; bars extending beyond this line represent variables with a statistically significant influence on the outcome.

Figure 5.7: Contour plot of numerical optimization (a) and overlay plot of graphical optimization (b). This figure illustrates the outcomes of both numerical and graphical optimization strategies applied to identify the optimal formulation conditions for IFNα-loaded PEG-PLGA NPs based on desired physicochemical properties and release characteristics. 95

Figure 5.8: The average size (a) and zeta potential (b) for the optimized IFNα-PLGANPs. This figure presents the results of dynamic light scattering (DLS) and phase-analysis light scattering measurements used to evaluate the key physicochemical characteristics of the optimized IFNα-PLGA NP formulation. 96

Figure 5.9: Scanning electron micrographs (SEM) of the IFNα-PLGANPs surface morphology. This figure displays high-resolution scanning electron microscopy (SEM) images used to assess the surface morphology and structural integrity of the optimized IFNα-PLGANPs. The micrographs reveal that the NP s exhibit a predominantly spherical shape with a smooth and uniform surface texture, indicative of successful encapsulation and stable NP formation. 97

Figure 5.10: DSC curves of free PLGA, and the optimized IFNα- loaded PLGANPs. This figure presents the DSC thermograms used to investigate the thermal behavior and possible physicochemical interactions between IFNα and the PLGA polymer matrix in the optimized NP formulation. The thermogram of the free PLGA polymer displays a characteristic endothermic peak corresponding to its glass transition temperature (Tg), indicating its amorphous nature. 99

Figure 5.11: The XRD spectrum for IFN loaded PLGANPs, free IFNα, and amorphous in nature of free PLGA. This figure displays the XRD spectra used to evaluate the crystalline or amorphous nature of the individual components free IFNα, free PLGA polymer, and the optimized IFNα-loaded PLGA NPs. The XRD pattern of free IFNα exhibits distinct sharp peaks, characteristic of its crystalline structure. These well-defined diffraction signals confirm the 100

presence of a highly ordered molecular arrangement in the native protein form in IFNα-PLGANPs.

Figure 5.12: Release Profile for Optimized IFNα-PLGANPs. This figure illustrates the cumulative in vitro release pattern of IFNα from the optimized PLGA-based NP formulation over a five-day evaluation period. The release profile demonstrates biphasic kinetic behavior, typical of polymeric delivery systems, with an initial burst release followed by a sustained release phase. 102

Figure 5.13: Cytotoxicity assessments to evaluate the cell viability of Cur–FeONPs, free Cur and IFNα-PLGANPs at different concentrations. The experiments will span 24, 48, and 72 hours, involving NIH-3T3 cells with a sample size (n=3). This figure presents that both Cur–FeONPs and IFNα-PLGANPs are promising candidates for therapeutic use, offering effective delivery of active agents with minimal toxicity to normal fibroblast cells under the tested conditions. 103

Figure 5.14: Cytotoxicity of MM (A375) under different concentrations of Cur-FeONPs, IFNα-PLGANPs, the combination of Cur-FeONPs and IFNα-PLGANPs, pure IFNα, negative control, and positive control after 72 h. Data shown as mean ± SD, n = 3. This figure presents the results of an in vitro cytotoxicity study conducted to evaluate the cell viability of A375 melanoma cells treated with varying concentrations of Cur -loaded iron oxide NP s (Cur–FeONPs), IFNα-loaded PLGA NP s (IFNα-PLGANPs), and their combination. The experiments were performed to assess the synergistic effects of combining the two NP formulations, with the aim of improving therapeutic efficacy in skin cancer treatment. 105

Figure 6.1: Development of NP-loaded alginate-lecithin hydrogel topical system. This figure outlines the formulation and development process of a NP-loaded alginate-lecithin hydrogel, designed as a topical delivery system for enhanced drug delivery. The formulation integrates the biocompatible and biodegradable properties of alginate, a natural polysaccharide, with the lipid-based properties of lecithin, forming a stable hydrogel matrix suitable for controlled, localized drug release. 109

Figure 6.2: Franz diffusion cell apparatus used for permeation study. This figure illustrates the Franz diffusion cell apparatus utilized for the in vitro evaluation of drug permeation through biological membranes, specifically designed for studying the release and absorption properties of the NP-loaded alginate-lecithin hydrogel topical system. The Franz diffusion cell is a well-established method for assessing the skin permeation and drug release kinetics of topical formulations. 113

Figure 6.3: Zeta size profile of the NP-loaded hydrogel platform. This figure presents the zeta size measurements of the NP-loaded alginate-lecithin hydrogel, which is crucial for assessing the stability, uniformity, and functional integrity of the NPs incorporated within the hydrogel matrix. Zeta size, also known as the hydrodynamic diameter, provides insight into the size distribution of the NPs, which directly impacts their permeability, stability, and controlled release behavior. 115

Figure 6.4: Zeta potential profile of the NP-loaded hydrogel platform. This figure illustrates the zeta potential of the NP-loaded alginate-lecithin hydrogel, an important parameter for assessing the colloidal stability and surface charge of the NPs within the hydrogel matrix. Zeta potential provides insights into the interparticle interactions and the stability of the NP dispersion in aqueous environments. It is a key indicator of the repulsive forces between NPs, which directly influences their tendency to aggregate or remain dispersed. 116

Figure 6.5: Viscosity versus shear rate force (N), where (a) represents the loaded gel at 25°C, (b) the loaded gel at 37°C, and (c) and (d) showed the influence of shear rate on the viscosity of NPs-loaded hydrogel at 25°C and 37°C. This figure illustrates the viscosity of a hydrogel as a key parameter for assessing its flow properties, spreadability, and ease of application, which are crucial factors in determining the practical suitability of a topical drug delivery system. 118

Figure 6.6: Adhesive force of the gels determined using cellulose membrane with a, b, c and d representing ratios 1:10, 2:10, 1:3, and 1:4, respectively, with a sample size of n = 3. This figure shows the adhesive force measurements of the NP-loaded alginate-lecithin hydrogel formulations, evaluated using a cellulose membrane to simulate the interaction between the gel and a 119

biological surface. Adhesive force is a critical parameter for assessing the skin adhesion properties of topical formulations, as it influences the gel's retention on the skin and its ability to deliver the active drug at the application site. The experiments were conducted using different gel ratios.

Figure 6.7: Represents the skin isolation procedure in the animal unit, utilizing hairless pig skin for evaluating the adhesive work of the gel formulation. This figure illustrates the ex vivo bioadhesion study process, where hairless pig skin was utilized as a model for assessing the adhesive properties of the NP-loaded hydrogel formulation. The use of porcine skin is particularly significant because its structural and physiological characteristics are closely aligned with human skin, making it a reliable and relevant model for evaluating mucoadhesive and detachment adhesion forces. 120

Figure 6.8: Adhesive force of gel determined using hairless porcine skin, for (a) the unloaded gel in a 1:4 ratio and (b) a 1:3 ration of crosslinker to polymer, respectively. This figure demonstrates the adhesive force measurements of two hydrogel formulations using hairless porcine skin, which serves as an ex vivo model to simulate the adhesion properties of the gels on human skin. The data provide important insights into how the gel formulations will adhere to the skin, influencing their performance in topical drug delivery applications. The two formulations tested are based on different crosslinker-to-polymer ratios: 1:4 and 1:3. 122

Figure 6.9: Adhesive work of gel determined using hairless porcine skin, for (a) the loaded-NPs in 1:4 ratio, (b) 1:3 ratio, (c) 2:10 ratio and (d) 1:10 ratio crosslinker to polymers, respectively. This figure illustrates the adhesive work of four different NP-loaded hydrogel formulations, each tested on hairless porcine skin. The adhesive work is a critical parameter for assessing the energy required to detach the gel from the skin, which directly influences the performance and retention of topical drug delivery systems. The gel formulations tested are based on varying crosslinker-to-polymer ratios, which alter the gel’s structure and adhesive properties. The different ratios are as follows: 1:4, 1:3, 2:10, and 1:10. Each ratio affects the adhesive work, demonstrating how formulation adjustments can impact the bioadhesive 123

behavior of NP-loaded hydrogels.

Figure 6.10: Profile representing the weight loss percentage of the NP-loaded gel versus days. This figure presents the degradation profile of the NP-loaded hydrogel system, which was designed to assess its dual-release capabilities and the role of the polymers (PEG and PLGA) in protecting the IFN from rapid degradation. The study aimed to evaluate how the polymer composition and the gel matrix design influence the stability of the encapsulated IFN while promoting its controlled release over time, which is vital for achieving an optimal therapeutic effect, particularly for melanoma treatment 124

Figure 6.11: Profile representing the permeability percentage of (a) Cur and (b) IFNα from the NP-loaded hydrogel. Data depicted as mean ± SD, n = 3. This figure illustrates the permeation profiles of two active pharmaceutical ingredients, Cur and IFNα, released from the combined NP-loaded hydrogel through a Strat-M membrane. The study evaluates the accumulation and release kinetics of Cur and IFNα in skin tissues, which are crucial for achieving therapeutic efficacy while ensuring safe drug levels for topical applications. 126

Figure 6.12: NIH-3T3 cell viability of the NP-loaded Gel (D), unloaded-gel (G) and the positive and negative controls. This figure presents the results from an MTT assay conducted to assess the cell viability of the NP-loaded hydrogel system, as well as the unloaded hydrogel, in terms of their cytotoxicity towards the NIH-3T3 fibroblast cell line. The study aimed to evaluate the biocompatibility and safety of the optimized IFNα-PLGANPs and Cur-FeONPs encapsulated within the hydrogel platform, focusing on their potential cytotoxic effects at varying concentrations over a 72-hour period. The findings demonstrate that the hydrogel system, whether loaded with therapeutic NPs or not, is biocompatible and non-toxic to NIH-3T3 cells at the tested concentrations. 127

Figure 6.13: % cell viability profiles of MM cells (A375) treated with the NP-loaded Gel (D), the unloaded gel and the negative positive controls after 72 h. Data depicted as mean ± SD, n = 3**.** This figure illustrates the cell viability results obtained from an MTT assay conducted on A375 MM cells after a 72-hour treatment with D, unloaded gel, and the negative and positive controls. The primary objective of this experiment was to assess the cytotoxic effects of 129

the gel formulations and to compare their efficacy in reducing the viability of MM cells.

LIST OF TABLES

Table 2.1: Comparison of recurrence-free survival rates between different pathologic types of non-melanoma skin cancer. 19

Table 3.1: Showcases the Collaborative Pairings of CI w immunotherapy h FDA-approved IT for the Effective Treatment of Various Skin Cancer Variants. Adapted from Nikolaou et al. [162]. 41

Table 3.2: Possible Association of CT with HT and Possible Potentiation of Drugs by HT on Oxygenated, Hypoxic and pH. 42

Table 3.3: Comparison of the Effects of HT, Radiotherapy, Chemotherapy, and Immunotherapy, on Several Cells and Tumor Structures. 48

Table 4.1: Average size and zeta potential of the synthesized FeONPs and Cur-FeONPs (n = 3). 64

Table 5.1: Formulation compositions as generated by the 2^2 FD. 78

Table 5.2: SDS-Page Gel-Electrophoresis Test Gel Components. 79

Table 5.3: 2^2 FD matrix and responses results for the DoE IFN-PLGANPs formulations (n=3, SD). 86

Table 5.4: Analysis of variance (ANOVA) for different responses of IFN-PLGANPs formulations. 92

Table 5.5: Model statistical fit parameters. 92

Table 5.6: The selected optimal configuration from numerical optimization. 94

LIST OF ABBREVIATIONS

2D	Two-Dimensional
3D	Three-Dimensional
AK	Actinic Keratosis
Alg	Alginate
ANOVA	Analysis of Variance
BCC	Basal Cell Carcinoma
CCD	Central Composite Design
CO_2	Carbon Dioxide
CPTT	Chemo-photothermal Therapy
CT	Chemotherapy
DCM	Dichloromethane
DMEM	Dulbecco's Modified Eagle Medium
DMSO	Dimethyl Sulfoxide
DoE	Design of Experiments
ECP	Extracorporeal Photopheresis
ECT	Electrochemotherapy
FBS	Fetal Bovine Serum
FD	Factorial Design
FDA	Food and Drug Administration

FDC	Franz Diffusion Cell
FTIR	Fourier Transform Infrared
GBD	Global Burden of Disease
IC50	Half maximal inhibitory concentration
MM	Malignant Melanoma
MTT	3-(4,5-Dimethylthiazole-2-yl)-2,5-diphenyl tetrazolium bromide
MW	Molecular Weight
NIH-3T3	Mouse Fibroblast Cells
NMSC	Non-melanoma Skin Cancer
NP	Nanoparticle
PBS	Phosphate Buffered Saline
PCL	Polycaprolactone
PDT	Photodynamic Therapy
OS	Overall Survival
R^2	Correlation Coefficient
Rpm	Revolutions per Minute
SCC	Squamous Cell Carcinoma
SD	Standard Deviation
SEM	Scanning Electron Microscopy
WRAF	Wits Research Animal Facility
XRD	X-Ray Diffraction

LIST OF EQUATIONS

Equation 4.1: The determination of the drug loading efficiency of NP s (NPs). 58

Equation 4.2: The determination of percentage of cell viability of NPs). 60

Equation 5.1: The Percentage of Adsorption Efficiency of the drug (%AE). 80

Equation 5.2: The Percentage of Drug Loading Capacity (%DLC). 80

Equation 5.3: Regression equation generated for particles size R1 influenced by responses. 92

Equation 5.4: Regression equation generated for cumulative R2 release from IFN-PLGANPs after day 1. 92

Equation 5.5: Regression equation generated for cumulative R3 release from IFN-PLGANPs after day 3. 92

Equation 5.6: Regression equation generated for cumulative R4 release from IFN-PLGANPs after day 5. 92

Equation 6.1: The percentage of mass loss due to degradation of NP-loaded hydrogel. 111

Equation 6.2: Linear regression generated for analysis of the permeation data. 112

CHAPTER 1

INTRODUCTION

1.1 Background of the Study

Skin cancers are classified into non-melanoma skin cancer (NMSC) and malignant melanoma (MM) and are primarily caused by the excessive exposure to ultra-violet (UV) radiation or the sun (UVA and UVB). Of these two types, NMSC is more prevalent globally, mainly among Caucasians, where the incidence has risen annually between 3-8% since the 1960s [1]. MM, however, results in a higher number of deaths due to metastasis [2], and includes rare skin cancers such as Merkel Cell Carcinoma (MCC), cutaneous lymphoma, Kaposi sarcoma [3]. In 2022, there were nearly 20 million new cancer cases, and approximately 9.5 million cancer-related deaths [4]. The incidence rates of cancer also varied significantly across different regions, with the United States, Australia and New Zealand reporting the highest incidence rates of skin cancer, with an average of 33 cases per 100,000 residents. This is followed by Northern European countries such as Norway and Denmark [5]. Recent fact sheets further provide a snapshot of the global cancer burden for specific types, including a new report on MM and NMSC. For MM, the incidence rates show 331,647 new cases, accounting for 1.7% of all cancers, while mortality statistics indicate 58,645 deaths, representing 0.6% of total cancer deaths. In contrast, NMSC had a reported incidence of 1,234,533 new cases, making up 10.4% of all cancers, with a mortality of 69,416 deaths, or 0.59% of total cancer deaths [6]. This prevalence extends to Southern and Eastern Africa, with the overall incidence of melanoma in South Africa being approximately 2.7 per 100 000 individuals. Among the 330,162 recorded NMSC cases, males accounted for a higher proportion (58%) compared to females. The highest incidence was observed in the White population group, comprising 81% of male cases (n = 156,058) and 79% of female cases (n = 106,766). In contrast, the Black population (n = 24,141) exhibited a different pattern [7]. Notably, the incidence varies significantly across different demographic groups, with a 23.2 per 100 000 incident rate occurring among the white population, with a much lower 0.5 per 100 000 among the black population [8, 9]. NMSC and MM therefore present significant global as well as local health risks and a deep understanding of its pathophysiology is needed for the development of effective treatment regimens to treat these conditions.

1.1.1 The Physiology of Skin Cancer

The skin consists of two primary layers: the superficial epidermis and the deeper dermis

(Figure 1.1). The epidermis serves as the skin's tough outer barrier, protecting the body from external threats, and is composed of stratified squamous epithelial cells, organized into four to five distinct layers. From the outermost to the innermost, these layers are the stratum corneum, stratum granulosum, stratum spinosum, and stratum basale. In areas where the skin is thicker, such as the palms and soles, there is an additional layer called the stratum lucidum, located between the stratum corneum and stratum granulosum. The epidermis regenerates through stem cells found in the basal layer, which gradually move upward toward the stratum corneum.

As the epidermis lacks its own blood supply, it relies on nutrients from the underlying dermis. The dermis, situated beneath the epidermis, provides structural support and nourishment. It is further divided into two layers: the superficial papillary dermis and the deeper reticular layer. The papillary layer, composed of highly vascularized loose connective tissue, forms finger-like projections called dermal papillae that extend into the epidermis. The reticular layer consists of dense connective tissue that forms a strong, supportive network. The dermis furthermore contains blood and lymph vessels, nerves, sweat glands, hair follicles, and other essential structures embedded within its connective tissue framework [10]. Skin function, sensitivity, location, and complex connections therefore make the skin a vital organ. Dysfunctions in these layers, combined with physiological changes, contribute to the development of abnormal skin conditions, potentially leading to various types of cancer [11].

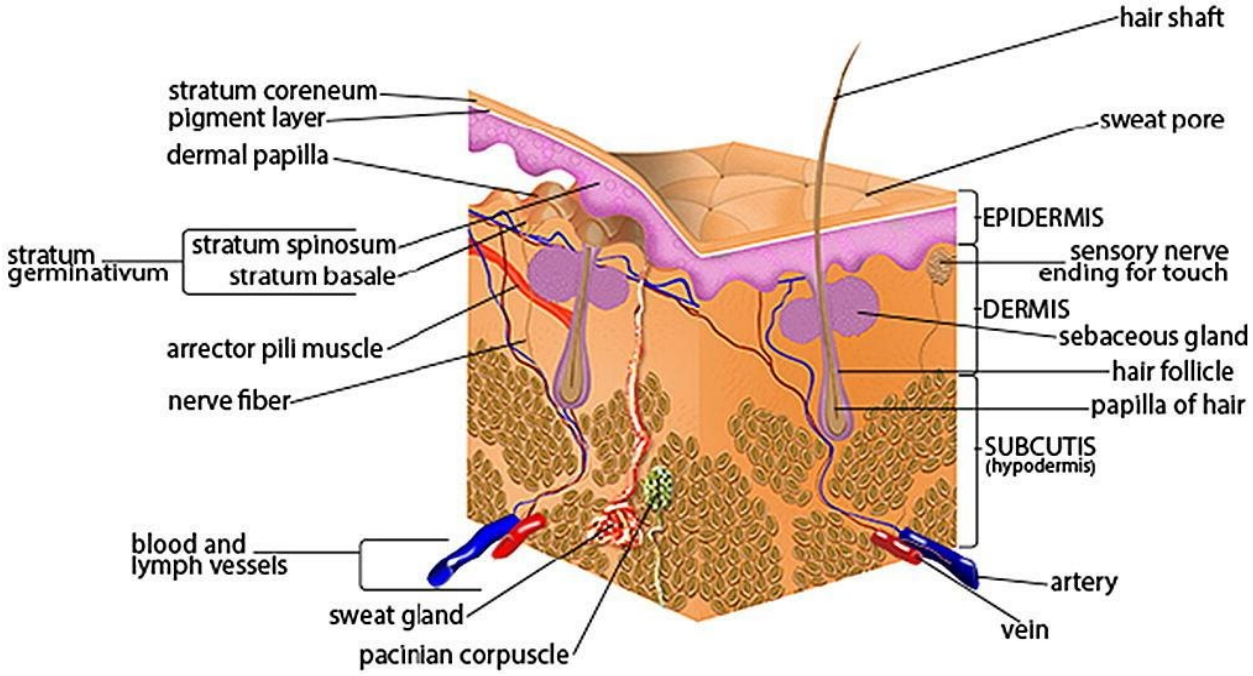


Figure 1.1: This illustration shows the two main layers of the skin: the outer epidermis, composed of stratified squamous epithelial cells arranged into distinct layers (including the stratum corneum, granulosum, spinosum, basale, and in thick skin, the stratum lucidum),

and the underlying dermis, which is further divided into the papillary and reticular layers. The papillary dermis contains vascularized loose connective tissue and dermal papillae that interface with the epidermis, while the reticular dermis houses dense connective tissue along with blood vessels, lymphatics, nerves, sweat glands, and hair follicles. This structural organization is essential for protective, sensory, and regenerative functions of the skin. Disruptions in these layers can contribute to the development of skin pathologies, including cancer. Reproduced with permission from Akhtar and Khan [11].

NMSC and MM are typically defined by the type of skin cell that is affected. NMSC starts in the basal cells or squamous cells, which are the two main types of cells that make up the epidermis, while MM starts in the melanocytes, which are the cells that produce melanin, the pigment that gives skin its color. NMSC is usually slow-growing and rarely spreads to other parts of the body. MM skin cancer, on the other hand, can be fast-growing and can spread to other parts of the body, even if it is small. This is why it is important to get regular skin checks, so that any melanomas can be detected early [12]. Squamous cell carcinoma (SCC) is a tumor originating from epidermal keratinocytes, commonly found in areas exposed to the sun. In individuals with darker skin tones, however, SCC can develop in areas not typically exposed to sunlight [13]. The appearance of SCC can vary but often presents as erythematous (red) papules, plaques, or nodules that may ulcerate or become hyperkeratotic (thickened). A biopsy is therefore required for definitive diagnosis and pathological confirmation. Basal cell carcinoma (BCC) is the most common type of skin cancer and is a locally invasive tumor arising from the basal layer of the epidermis. UV radiation is the primary risk factor, causing mutations in key tumor suppressor genes and proto-oncogenes [14]. BCC typically appears as a pink, pearly papule with visible blood vessels (telangiectasia), and a biopsy is also necessary to confirm the diagnosis. Compared to SCC and BCC, MM is highly aggressive due to its potential for rapid metastasis. It can be classified into four subtypes: superficial spreading, nodular, lentigo maligna, and acral lentiginous melanoma. Initially, MM begins as a superficial tumor confined to the epidermis, but may progress to a vertical growth phase, increasing the tumor's thickness. Tumor thickness, measured by Breslow's depth (starting from the granular layer of the epidermis), is the most critical prognostic factor. Clinically, MMs are often identified using the ABCDE criteria: asymmetry, border irregularity, color variation, diameter greater than 6 mm, and evolution over time [15]. Skin cancer arises when the tightly regulated balance of skin cell proliferation, differentiation, and apoptosis is disrupted, leading to uncontrolled cell growth. As mentioned, UV radiation, especially UVB and UVC, is the principal environmental risk factor that induces DNA damage in skin cells, notably forming pyrimidine dimers and other photoproducts. If this DNA damage is not effectively repaired, it can result in mutations in key genes such as p53, PTCH1, or BRAF, leading to carcinogenesis [16].

1.2 Rationale and Motivation for this Study

The treatment of NMSC and MM is the 5th and 9th most expensive treatment in inpatient care, respectively [17]. When skin cancer is diagnosed early, almost all cases of NMSC can be cured using simple techniques, such as scraping, burning, freezing, or surgically exercising the malignant tissue with local anaesthesia. MM can also be easily treated by excision if the tumor is not >1 mm in thickness [18]. The current treatment of larger MMs (> 1 mm) thickness is surgery, and/or followed by radiotherapy. Radiotherapy is also often used in conjunction with chemotherapy or a checkpoint blockade immunotherapy to treat both NMSC and MM. There are, however, several limitations in the current treatment of MM, such as acquired resistance, a nonadjacent dose that affects healthy tissue, the approved combined research clinically being unconvertable, as well as numerous systemic adverse effects [19].

Chemotherapy, including cytotoxic drugs (such as bleomycin, dacarbazine, and temozolomide), improves patients' life expectancy, but there are also several adverse effects due to the use of high doses of these drugs to reach an effective concentration, additionally increasing drug resistance. Immunotherapy, such as interferon alpha (IFNα), is also used in the treatment of MM and is administered in multiple intra-lesion or intravenous injections, with the high doses of IFN required in treating MM limiting its effectiveness. This is due to the side effects experienced such as myalgia and leukopenia. In addition, the current combinative methods used to treat MM often result in drug-drug interactions, due to the multiple drugs and high doses used. The current multidrug treatment regimens used in skin cancer are effective with death occurring in approximately only 4% of patients [19], with about 70% patient survival of more than 5-years after treatment [11]. There is, however, still the potential to increase the effectiveness of these strategies further as well as decreasing the numerous side effects experienced.

The use of nanoformulations is one such intervention and has been shown to significantly enhance drug delivery by improving penetration through skin layers, prolonging drug retention, and achieving higher effective concentrations at the tumor site while reducing systemic exposure and side effects. Specifically, advanced nanoscale drug delivery systems such as precision-guided NPs have been previously developed for treating skin melanomas to improve drug permeability into the skin's sub-layers, resulting in a reduction in tumor size and minimizing side effects [20]. Other nanostructures such as dendrimers, nanoliposomes, carbon-derived NPs, and inorganic nanomaterials are further examples that have been explored for a more targeted topical drug delivery, decreasing the amount of drug required for administration, thereby decreasing adverse effects, as well as diagnose dermatological

conditions [11]. These nanomaterials can incorporate a large spectrum of molecules including those for chemotherapy and immunotherapy, radiotherapy, hyperthermic therapy or a combination of these treatments. The use of synergistic nanosystems incorporating multiple active agents has therefore become a viable option for the enhanced treatment of skin cancer with limited adverse effects, increased patient quality-of-life and a decreased risk of relapses. Following this trend, this research aimed to develop a multicomponent, dual-release topical platform for the targeted treatment of MM skin cancer using a combination of Cur-loaded iron oxide NPs (Cur-FeONPs), co-administered with prolonged-release IFNα loaded PLGA NPs (IFNα-PLGANPs) delivered through a topical patch system. A patch-based topical delivery system has been used as it offers a non-invasive, patient-friendly, and localized platform for targeted and controlled drug delivery. This delivery method also enhances therapeutic efficiency, patient compliance, and minimizes systemic toxicity, thereby aligning with the shift toward personalized, targeted therapies in oncology. This approach was designed to optimize the treatment of Stage 0 (known as *melanoma in situ*), Stage 1 (the tumor is no more than 2mm) and Stage 2 (the tumor is more than 1 mm thick) skin cancer by incorporating the therapeutic aspects of both NP systems, while providing treatment targeting and decreased dosing. Treatments beyond these stages often require systemic interventions beyond the scope of this study.

The dual-combination approach that has been explored involves the delivery of IFNα (an immunotherapeutic agent) loaded within poly(lactic-co-glycolic acid) (PLGA), along with FeONPs coated with Cur. Immunotherapies, including IFNα, as described have been used clinically to treat NMSC and MM, with most routes of IFNα administration being parental (resulting in numerous side effects due to indiscriminate bioactive delivery) [21, 22]. Type I interferons (IFNs) function by signaling the IFNα receptor (IFNAR), initiating a cascade that involves the activation of receptor-associated Janus kinase 1 (JAK1) and tyrosine kinase 2 (TYK2). These kinases, in turn, activate downstream signal transducer and activator of transcription (STAT) factors, which drive the expression of IFN-stimulated genes (ISGs). Type I IFNs specifically activate the IFN-stimulated gene factor 3 (ISGF3) complexes, consisting of STAT1, STAT2, and IFNα regulatory factor 9 (IRF9). The ISGF3 complex then binds to IFN-stimulated response elements (ISREs), inducing the expression of antiviral genes [23]. While highly researched and known to be effective for MM treatment, IFNα however, has high degradation properties, which limit its use in topical platforms. For this reason, multiple doses are administered systemically in clinical practice. This property, however, can be overcome using a sustained release platform coated with a protective layer, for example through the encapsulation of IFNα within PLGA-coated NPs, which can retain the integrity of the IFNα prior to release, as used in this study.

The incorporation of IFNα in a controlled-release multi-component platform further offers a promising advancement for synergistic, non-surgical skin cancer treatment. By combining FeONPs with immunotherapy, this platform leverages the unique properties of each component. FeONPs are widely used in biological research due to their biocompatibility and safety and have garnered significant attention due to their straightforward synthesis, low toxicity when appropriately functionalized, and rapid magnetic separation capabilities [24]. They can furthermore absorb energy and convert it into harmful stimuli, effectively inducing cancer cell death [25]. One of the key benefits of this approach lies in the unique nature of FeONPs which have the potential to be coated with other bioactive agents such as Cur, while further allowing for accumulation at the tumor site for extended periods, inducing apoptosis in cancer cells.

Cur, a natural dietary polyphenolic compound, is well-documented for its antiseptic, anti-inflammatory, and anticancer properties [26, 27]. Recent studies suggest that coupling Cur with metal NPs may enhance its bioavailability and therefore its efficacy [28]. Curcumin's anticancer efficacy also lies in its ability to induce apoptosis and inhibit tumor proliferation and invasion by modulating various biochemical and signaling pathways [29]. The broad functionality of Cur therefore limits multiple pathways, which can have a negative effect on other anticancer treatments, including the use of IFNα [30]. This effect, however, can be overcome through the use of a controlled-release system for both bioactive molecules, circumventing this interaction, while leveraging the benefits of the individual agents. The developed platform has resultantly been designed to enable a sustained release of IFNα, while Cur is released more rapidly. This innovative multi-release system has the potential to revolutionize skin cancer treatment by providing a multifaceted, targeted therapeutic approach. The phases of bioactive release from the NP-loaded topical patch system (further depicted in Figure 1.2) are as follows:

Phase 1: Adherence of the topical patch system onto the affected skin surface
Phase 2: Release of Cur-FeONPs and IFNα loaded PLGA NPs from the topical patch system Phase 3: Immediate release of Cur from the Cur-FeONPs and degradation of the PLGA coating, leading to the release of IFNα.
Phase 4: Penetration of the FeONPs into the targeted tissue, inducing apoptosis.
Phase 5: Continued sustained-release of IFN-loaded from the PLGA nanoparticulate system.

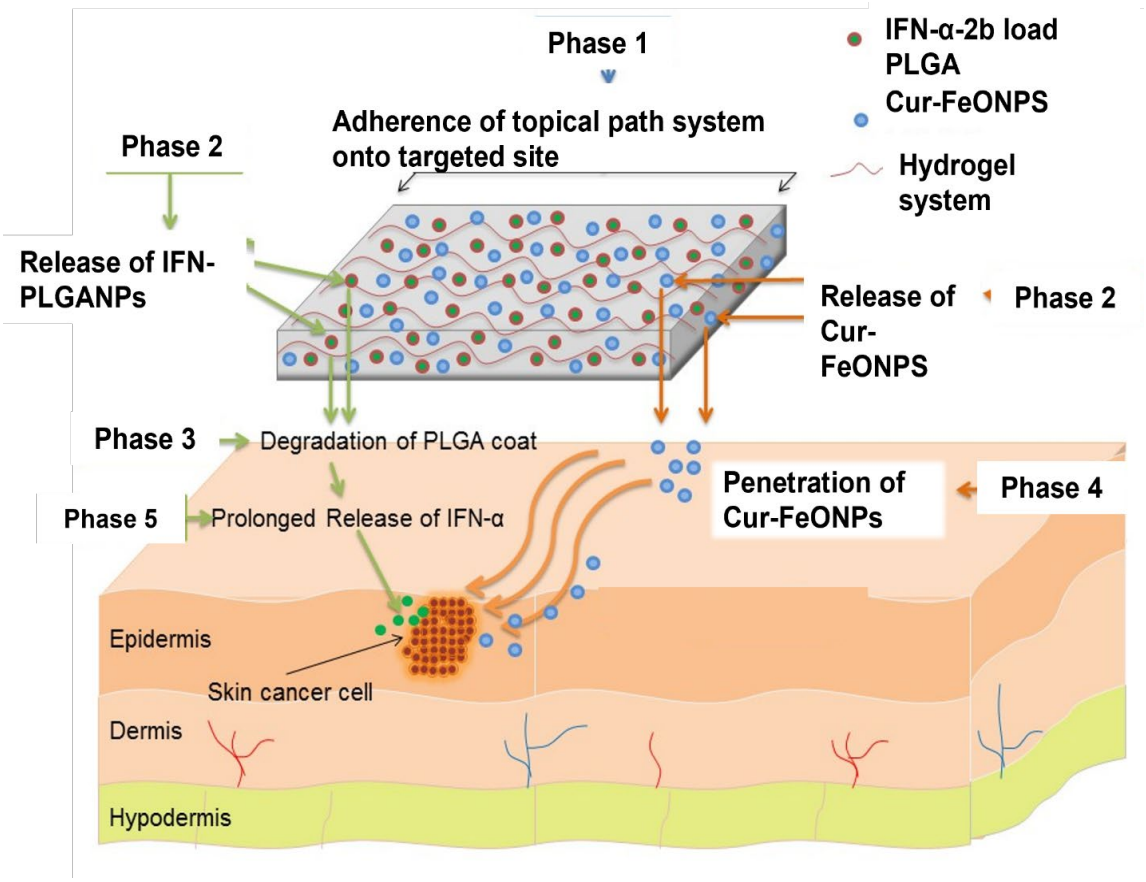


Figure 1.2: Schematic representation of the five-phase mechanism of bioactive release from the developed dual-delivery, NP -loaded topical patch system. After the patch is applied to the skin (Phase 1), the release of both Cur -loaded iron oxide NP s (Cur-FeONPs) and IFNα-loaded PLGA NP s is initiated (Phase 2). Cur is rapidly released from the FeONPs to exert an immediate therapeutic action (Phase 3), while the FeONPs penetrate the tumor tissue and induce apoptosis and oxidative effects (Phase 4). Simultaneously, the PLGA matrix degrades slowly to provide a sustained release of IFNα (Phase 5). This controlled release system enhances drug localization at the tumor site, minimizes systemic exposure, and combines both immunotherapeutic and chemotherapeutic dual-delivery strategies for effective melanoma treatment.

1.3 Novelty of This Research

This research introduces an innovative multicomponent, dual-release topical platform that incorporates Cur-FeONPs, and IFNα, delivered through a controlled-release mechanism using two distinct methods. The development of this topical patch system aims to mitigate the severe adverse effects associated with IFNα immunotherapy, offering a significant improvement over current treatment protocols for MM, while utilizing the synergistic effect of Cur and FeO for increased anticancer properties while overcoming the potential negative interaction between Cur and IFNα. By addressing the limitations of conventional MM treatments, this novel approach has the potential to enhance patient compliance and

survival, improve treatment adherence, and provide more effective control of malignant skin cancers. Additionally, this system could be applied to NMSC where complete excision of the affected tissue is not feasible, thereby decreasing the risk of metastasis in this condition.

1.4 AIM AND OBJECTIVES

This research aimed to design, develop and analyze a topical skin patch loaded with Cur-FeO and IFNα-PLGANPs for the enhanced treatment of MM skin cancer.

This aim was achieved by completing the following objectives:

1) Synthesis of Cur-FeONPs with a diameter ranging between 10-200 nm.

2) Characterization of the morphological structure of the Cur-FeONPs, using Scanning Electron Microscopy (SEM) and Transmission Electron Microscopy (TEM), and the physiochemical properties of the prepared NPs using zeta average and zeta potential.

3) Formulation of the IFNα-PLGANPs prior to the statistical optimization and conduction of *in vitro* characterization studies to determine drug entrapment, vesicle size-reduction, particle size, zeta potential, and release.

4) Development of a biocompatible hydrogel-based skin patch system using the solution gelation method, prior to the loading of the Cur-FeONPs and optimized IFNα-PLGANPs.

5) Characterization of the topical skin patch using SEM and TEM to determine the morphology and NP shape, X-ray diffraction (XRD) to ascertain the crystalline structure, and Differential Scanning Calorimetry (DSC), Fourier transform infrared (FTIR) Spectroscopy, and Rheological Studies to determine the thermal properties, structural characteristics, and rheological properties, respectively. *In vitro* drug permeation analysis was further undertaken on the topical platform system.

6) Assessment of the anticancer potential of the prepared topical platform system through cell studies.

1.5 OVERVIEW OF THE THESIS

This thesis has been presented as follows:

Chapter 1: This chapter provides an overview of skin physiology and anatomy, as well as the classification and types of skin cancer. It discusses the incidence rates, populations commonly affected (including morbidity and mortality statistics), and the underlying pathology of skin cancer and further highlights the conventional treatment methods and current therapeutic approaches, and the ongoing research landscape, emphasizing the

advanced synergistic strategies for skin cancer treatment, to which this study addresses. This chapter furthermore establishes the foundation for the study's aims and objectives and provides an overview of this thesis.

Chapter 2: This chapter examines the surgical synergistic and nano-based oncology treatments for skin cancer, which is mainly focused on conventional strategies such as chemotherapy, radiotherapy and immunotherapy in the treatment of MM. The chapter highlights the superior efficacy of combinatorial nano-based oncology therapies with surgery, such as dual, trimodality, and multicomponent treatments, compared to monotherapies. Additionally, the chapter explores the impact of these treatments on patient compliance, overall survival rates, and efforts to address relapses and metastasis and highlights the limitations of MM treatment using surgical interventions.

Chapter 3: This chapter explores the non-surgical combinative therapies for treating skin cancer and its potential to be an alternative to surgical interventions, focusing on both NMSC and MM. The chapter delves into the various drug delivery systems and oncology strategies aimed at improving survival rates, patient compliance, and addressing relapses and metastasis. It also discusses the recent advancements and the potential of combination non-surgical interventions in skin cancer treatment and advances on Chapter 2 by highlighting the potential benefits of synergistic nano-therapy with non-surgical interventions, thereby overcoming many of the shortcomings of conventional therapy, which underpins the rationale for this study.

Chapter 4: In this chapter, the Cur-FeONP system has been synthesized and evaluated for its potential in treating skin cancer, specifically MM. The synthesis and characterization of the Cur-FeONPs has been presented confirming the stability of the NP structure, its biocompatibility, and enhanced therapeutic efficacy. This chapter further highlights the potential of Cur-FeONPs as a promising nanoplatform for the treatment of MM.

Chapter 5: This chapter focuses on the synthesis and statistical optimization of the IFNα-PLGANPs. To ensure the IFNα-PLGANPs effectiveness and stability, an experimental design has been presented to optimize the platform particles size, stability by examining zeta potential and IFNα release. Furthermore, extensive characterization studies were conducted, including zeta sizing, zeta potential measurement, SEM, FTIR, DSC, and XRD analyses. This chapter further presents the use of Cur-FeONPs and optimized IFN-PLGANPs in combination as a novel strategy to enhance MM skin cancer treatment. It further emphasizes their potential as emerging biomaterials for responsive drug delivery and highlights the significance of detailed experimental design and characterization in overcoming the

limitations of conventional skin cancer therapies.

Chapter 6: This chapter outlines the formulation and characterization of the topical hydrogel system incorporating the Cur-FeONPs and optimized IFN-PLGANPs. This formulation included the optimal combinative formula of NPs and was composed of alginate and soy lecithin. The resulting formulation underwent thorough characterization to evaluate its physicochemical and physicomechanical properties. Additionally, *in vitro* cytotoxicity and anticancer activity were assessed to determine its effect on A375 cell proliferation.

Chapter 7: This chapter provides the conclusion for this thesis, offering a comprehensive summary of the various aspects explored regarding the multicomponent controlled-release system for MM skin cancer treatment. The chapter further outlines the limitations of this study and provides recommendations for future applications of the developed topical patch system, emphasizing the need to address the high costs of combination therapies and to integrate diverse mechanisms of action into multi-component drug delivery systems.

CHAPTER 2

SYNERGISTIC SURGICAL AND NANO-BASED ONCOLOGY TREATMENTS FOR SKIN CANCER

2.1 Introduction

The global incidence of skin cancer has risen significantly over the last decade. These cancers as previously described are mainly classified into MM, originating from melanocytes, and NMSC, which develop from epidermal cells [31]. Together, these two categories account for about 95% of all skin cancers, with a small percentage consisting of rare and aggressive types. Among NMSC, basal cell carcinoma (BCC) and cutaneous squamous cell carcinoma (SCC) constitute 99% of cases, with more than 5.4 million cases of NMSC are treated in the USA annually [32]. This number is expected to rise over the next 20 years due to more advanced diagnostic procedures and it is projected that during this period, the global incidence of skin cancer will increase by about 50%.

The treatment of skin cancer faces numerous challenges worldwide, particularly in low- and middle-income countries (LMICs). These regions often lack affordable care, cancer screening facilities, trained medical professionals, and comprehensive treatment and support service [33-36]. Standard treatment options for skin cancer consider multiple factors, including the cancer stage, genetic predispositions, patient age, tumor location, genodermatoses, HPV infection, tobacco and drug use, and the presence of other infections or inflammatory conditions. Given these complexities, there is an urgent need for more effective therapies. In this context, nanotechnology has emerged as a promising strategy that can be utilized alone or in combination with traditional interventions such as surgical resection for cancer treatment, as it allows for the efficient delivery of drugs and bioactive molecules to targeted tissues, while minimizing toxicity.

These nanosystems are typically administered via topical/transdermal, intratumoral (local), or systemic (intravenous) routes, or through a combination of these. Topical and transdermal applications are noninvasive, self-administered options, often recommended for elderly patients, those unsuitable for surgical treatment, or young patients with extensive lesions in cosmetically sensitive areas [37]. These methods are frequently employed for premalignant conditions, such as actinic keratosis (AK), superficial skin cancers like noninvasive SCC, BCC, and early-stage melanoma [38]. The stratum corneum (SC), the outermost layer of the epidermis, acts as the primary barrier influencing the penetration of anticancer agents into target cells, which subsequently affects the efficacy of topical or transdermal therapies. In

human skin, the SC typically consists of 15–30 layers of corneocytes, forming a thickness of about 10–20 μm. These layers are the result of prolonged epidermal maturation, differentiation, and keratinization processes initiated in the deeper epidermal layers resting on the basal lamina above the dermis, forming the basal layer [39]. Rapid tumor growth frequently results in the formation of poorly structured and leaky blood vessels. NPs, owing to their size, can traverse these compromised vascular junctions, leading to their progressive accumulation at the tumor site. This process is referred to as the enhanced permeability and retention (EPR) effect, as described in Figure 2.1 [40].

The properties of NPs therefore significantly affect their interactions with tumor cells, influencing how they bind to cellular components and respond to the cells' physiological traits. Key interactions between NPs and tumor cells include adsorption, cellular uptake, endosomal transport, followed by endosomal escape, metabolism, and eventual degradation [41]. Nanotechnology furthermore presents an innovative and promising solution for overcoming multidrug resistance (MDR). It facilitates the targeted, efficient, and orderly delivery of therapeutic agents, enabling the use of lower doses while minimizing toxic effects. Nanocarriers are especially effective for delivering a combination of molecules that work synergistically, providing potent and targeted treatment options against cancer types that are resistant to conventional therapies [42, 43].

Polymer NPs (PNPs) have garnered significant attention across various fields due to their ability to enhance drug activity, regulate and delay drug release, and improve drug adhesion or retention time in the skin. These features make them a preferred platform for NP-based drug delivery in cancer treatment applications [44]. PNPs typically have an average diameter of less than 1 μm and are categorized as nanocapsules or nanospheres, depending on their NP structural composition. Their preparation follows two primary methods: the dispersion of pre-formed polymers or the polymerization of monomers. PNPs are extensively utilized in targeted delivery systems as carriers for cancer therapeutics due to their key attributes, such as biodegradability, biocompatibility, nontoxicity, prolonged systemic circulation, and the ability to encapsulate a broad range of therapeutic agents [45].

Despite these clear advantages, in the realm of skin cancer treatment, there are currently not many commercially available nanosystems for the topical delivery of bioactive molecules. One notable example however is Doxil®, a PEGylated liposome encapsulating doxorubicin, used in treating conditions such as multiple myeloma and Kaposi sarcoma in HIV/AIDS patients [46]. Most other NP systems are still undergoing preclinical evaluation, with some advancing to clinical trials, demonstrating significant promises. For example, a recent clinical

trial was initiated to evaluate a topical NP formulation containing paclitaxel for the treatment of cutaneous metastases from non-melanoma cancers [47]. Additionally, the introduction of miR-34a mimics into *in vitro* cancer cell lines derived from solid tumors, including skin cancer, has shown a significant reduction in cell proliferation, migration, and invasion [48].

This chapter therefore reviews the nanotechnological advancements in conventional skin cancer therapies, specifically highlighting their synergistic potential with surgical interventions. The pathology and conventional treatment approaches have been reviewed, focusing on outcomes when conventional therapies are administered either before or after surgical procedures. The development of efficient nanosystems is also explored in subsequent sections, and the commonly used NPs described in the literature for skin cancer treatment presented. Furthermore, the integration of NPs for delivering CT agents, immune modulators, and PTT will be addressed, showcasing how these nanomaterials can complement surgical methods. Finally, multifunctional controlled-release systems, designed as anticancer agents with loaded or functionalized properties, have been discussed in detail.

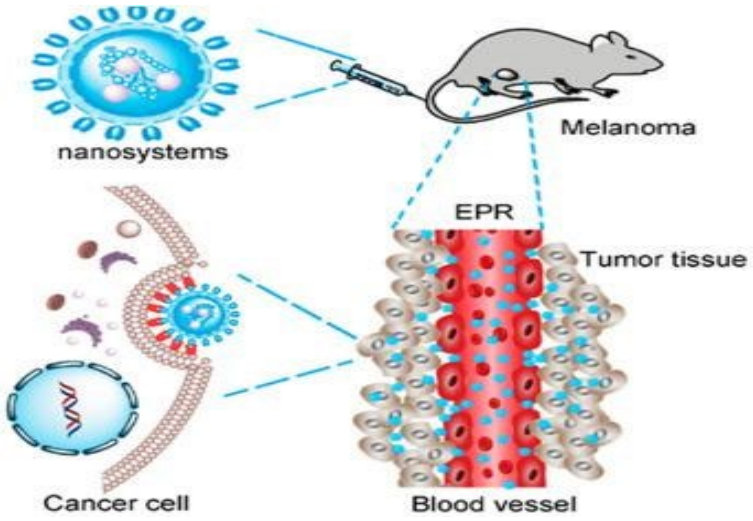


Figure 2.1: Nanocarrier-based drug delivery for melanoma therapeutics. This schematic illustrates how NPs exploit the enhanced permeability and retention (EPR) effect to deliver therapeutic agents to melanoma cells. Rapid tumor growth often leads to the formation of poorly structured and leaky blood vessels, allowing NPs to traverse these compromised vascular junctions and accumulate within the tumor microenvironment. Once localized, these nanocarriers can release their payload in a controlled manner, enhancing drug efficacy while minimizing systemic side effects. This targeted approach improves therapeutic outcomes in melanoma treatment. Adapted from Dastgheib *et al.* [40].

2.2 Treatment of Skin Cancer

2.2.1 Surgical Resection

Surgery is the primary treatment for early-stage skin cancer, for example in early-stage MM, where surgical removal of the tumor is an adequate method for many patients, however in

more advanced cases, excision alone is not possible, with relapse occurring in about 20% of patients [49, 50]. This is because in the early stages of MM, the lesion appears flat, pigmented, and irregularly shaped, confined to the epidermis. As the tumor progresses, it grows vertically, penetrating the dermal layer and infiltrating collagen fibers. In the final stages, the tumor extends into the subcutaneous tissue, forming nodules and papules [4]. This resultantly affects the efficacy of surgical monotherapy. The specific stages of melanomas are illustrated in Figure 2.2.

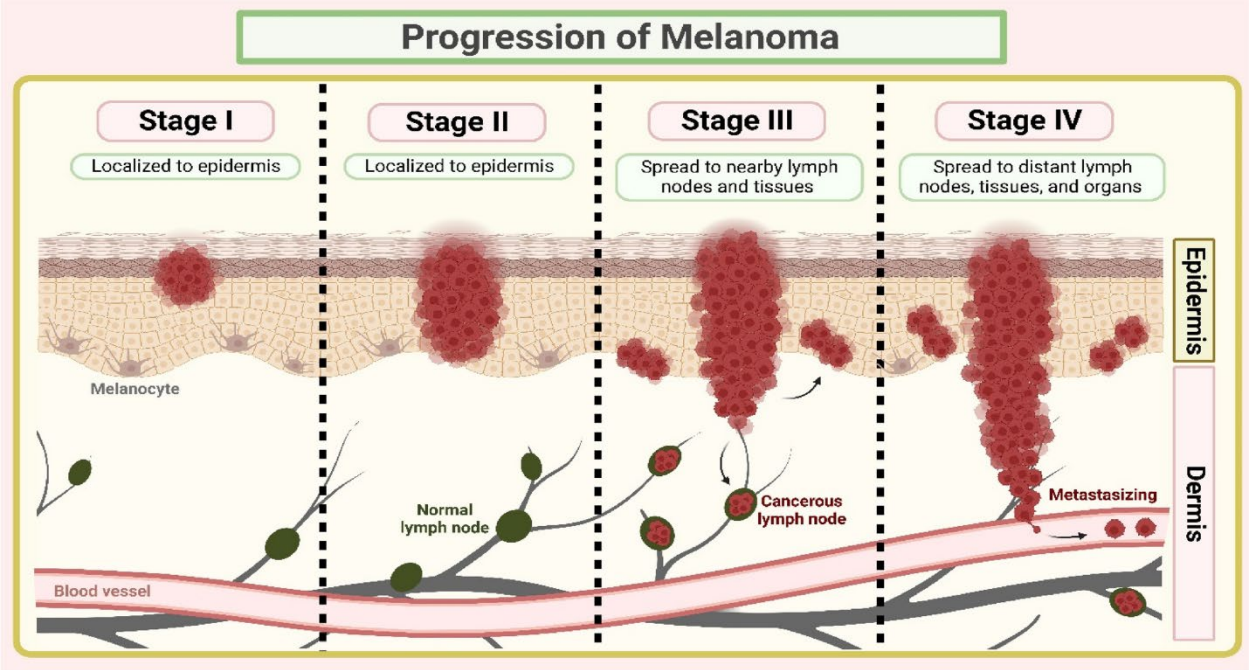


Figure 2.2: An illustration of melanoma progression (Stages I-IV). This figure provides a visual representation of the progressive stages of malignant melanoma, detailing the tumor's advancement from localized growth to widespread dissemination: Reproduced with permission from Zeng *et al.* [4].

According to a study by Iqbal *et al.* several factors contribute to skin carcinogenesis, which occur in three stages: initiation, promotion, and progression, as depicted in Figure 2.3. Anticancer interventions have been used to treat cancer cells during either of these stages. Skin cancer also has several progression stages, with Stage I involving a genotoxic effect due to tumor initiation, which is a quick process that occurs due to exposure to carcinogens, their delivery into the cells, and their interaction with DNA, while Stage II involves cancer promotion, which is a lengthy phase characterized by the proliferation of cancer cells, with Stage III resulting in tumor progression, accompanied by tumor growth, metastasis, and invasion into the surrounding cells [51].

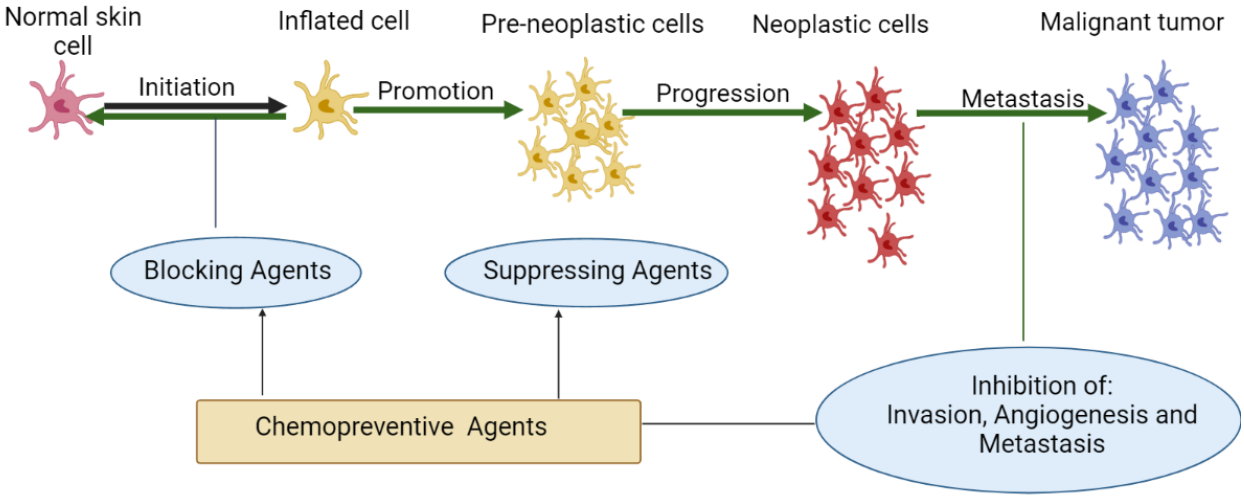


Figure 2.3: The process of skin cell carcinogenesis involves three distinct stages: initiation, promotion, and progression. Each of these stages can be influenced by specific chemo-preventive agents. Blocking agents are employed to interfere with initiation, while suppressing agents are utilized to target the promotion and progression stages. Adapted with permission from Iqbal *et al*. [51].

In therapeutic drug/gene delivery strategies, systems based on polymeric carriers emerge as the most promising approach. Polymers have been effectively utilized for the development of micro/nanoscale systems, facilitating the efficient delivery of anticancer genes and drugs, while overcoming all the barriers and limitations associated with conventional therapies [52]. Modern surgical techniques, when used, are now significantly less invasive and associated with lower morbidity while maintaining or improving accuracy and effectiveness compared to older methods. Historically, surgical approaches were more radical, involving the excision of 5-cm margins around the primary tumor and elective removal of regional lymph nodes for prophylaxis. However, randomized clinical trials have since demonstrated that less radical procedures can be equally effective. For thin melanomas (<2 mm), excision margins were first reduced to 2 cm and later to 1 cm. For intermediate-thickness melanomas (1 to 4 mm), 2-cm margins were found to be safe [53]. Recent studies have also shown that 2-cm margins are adequate for thicker melanomas (>2 mm) [54]. While surgical removal or destruction remains the preferred approach for treating skin cancer, it can also result in scarring and distortion and may not entirely eliminate the tumor [55]. Meanwhile, the decision of surgical excision should be achieved within 4–6 weeks of the first diagnosis, making surgical excision mainly for the primary melanoma margin (1–3 mm) [56].

A recent study has revealed that a biopsy is essential to determine whether excision is necessary before intervention. In fact, surgical treatment is more precise and requires less consultation for early-stage skin cancer than combination treatments after surgery in later

stages. Clinically suspicious pigmented lesions are usually biopsied, but a significant proportion of cutaneous melanomas are diagnosed through shave biopsy [57]. Synergistic therapy will thereafter be decided depending on the medications that can be used, the specific time of diagnosis, and the patient's characteristics and history to get a complete and persistent cure. Surgical and adjuvant interventions are therefore the principal approach for the treatment of skin melanoma [58]. The outcome of studies evaluating surgical and adjuvant interventions shows an increasing statistically significant use of combinative strategies treatments following surgical recovery with a lower recurrence and metastasis of the cancer tissue [59].

2.2.2. Combination Surgical Resection-Nanomaterial Interventions for MM

Various types of NPs have been extensively explored for NMSC and MM treatment due to their capacity to deliver therapeutic agents through multiple molecular pathways simultaneously and their adaptability for administration via less invasive routes. These nanomaterials include dendrimers, liposomes, carbon-derived NPs, protein-based NPs, and inorganic nanoformulations. Among these, liposomes have shown significant promise. Composing of a lipid bilayer, liposomes can encapsulate drugs and deliver them directly to cancer cells, increasing drug effectiveness and reducing side effects. Liposomes have further demonstrated efficacy in treating skin cancer in both animal and human studies, and they are currently undergoing clinical trials for melanoma treatment [3]. Dendrimers, which are branched polymers with a tree-like structure that can also encapsulate drugs and deliver them to cancer cells, such as in cases of actinic keratoses (AK) [60], while carbon nanotubes, which are long, thin tubes made of carbon atoms, can be used as a drug delivery system, allowing precise control over drug amounts reaching cancer cells [61]. Nanoemulsions, which are small droplets of oil suspended in water, and nanomicellesn, consisting of tiny spheres made of surfactants, are also being studied for their potential to deliver drugs to the skin [62]. While these nanomaterials are still in the developmental phase, they hold the potential to revolutionize skin cancer treatment.

2.2.2.1 Chemotherapy-Loaded Nanomaterials

CT has been used for decades as the mainstay of cancer treatments, after complete surgical resection, to ensure no residual cancer cells are present for the recurrence of the tumor. The approach of administering effective chemotherapies in the adjuvant setting has endured and led to progress in skin cancer treatment and other types of tumor therapies [63]. Multiple studies have shown good results when CT is administered after surgical resection treatment for patients with metastatic skin cancer and is used as the follow-up sequence of recovery [64]. This advantage has been confirmed in a study that applied adjuvant therapy of CT for

resected, node-positive of high-risk melanoma, relapsed tumors, in the eighth edition, patients with T1a N0 melanomas (primary tumor thickness <0.8 mm, nonulcerated) had a 5-year melanoma-specific survival (MSS) of 99% and a 10-year MSS of 98%, while patients with T4b N0 melanomas (primary tumor thickness >4.0 mm, ulcerated) had a 5-year MSS of 82% and a 10-year MSS of 75%. Generally, the presence of an ulcerated primary tumor was associated with an MSS like that of a patient with a nonulcerated primary tumor in the next highest tumor thickness category. The MSS for all T subcategories was significantly higher than that reported in the seventh edition, in which the 10-year MSS rates were 93% and 39% for patients with T1a N0 and T4b N0 melanomas, respectively, or in the sixth edition, and patients with stage III cancer who have undergone surgical excision with a curative intent including enhanced survival and low chances of acquiring a recurrence or metastasis [65].

CT has traditionally also been utilized as a post-surgery treatment for advanced MCC. Nonetheless, the response to CT is frequently brief, and its impact on the overall survival (OS) outcome remains uncertain. The current guidelines of the National Comprehensive Cancer Network (NCCN) recommend that for the treatment of localized disease, excision should be performed with margins of 1-2 cm and extended down to the fascia or periosteum. Although Villani *et al*. had shown a survival advantage in treatment of MCC due to their high sensitivity to CT. The initial response rates to CT for treating Merkel cell carcinoma range from 53% to 76%, but this high response rate tends to be temporary, with recurrence of tumors occurring within 4-15 months. A retrospective study of 6908 patients found that CT did not provide an OS benefit for patients with local or nodal MCC. Furthermore, CT is associated with a high risk of toxicity, especially in patients aged over 65 years. Therefore, the potential short-term benefits of CT must be weighed against the potential risks before making a treatment decision [66]. The best effects of CT when used in combination before surgery (neoadjuvant treatment) or after surgery (adjuvant treatment) led to a high efficacy acquired for melanoma treatment [67].

Recently, nanomaterial-based cancer therapy played a crucial role in enhancing therapeutic efficacy against cancer by combining nanomaterials with CT agents. This approach has demonstrated improved tumor control and reduced side effects by optimizing pharmacokinetics and enabling targeted drug delivery [68]. Combination therapy is a widely accepted strategy in conventional CT, designed to overcome cross-resistance and achieve synergistic therapeutic outcomes without significantly increasing toxicity. In contrast to monotherapy, which relies on a single drug and is often insufficient for inducing tumor regression, combination CT leverages the synergistic effects of two or more agents. These agents target distinct disease pathways, genes, or cell-cycle checkpoints, and when used

alongside surgical excision, significantly improve the likelihood of eradicating cancer [69].

Moreover, combining nanomaterials with surgical interventions has shown significant promise in the treatment of skin cancer. For instance, 5-fluorouracil (5-FU) is a widely used drug for conditions such as actinic keratosis and basal cell carcinoma; however, its hydrophilic nature limits its ability to penetrate the stratum corneum and effectively reach tumor tissues [70, 71]. Dacarbazine, a poorly soluble anticancer agent with a short half-life, is FDA-approved for chemotherapy against metastatic skin cancer (MSC) but often requires innovative delivery systems for improved efficacy [72]. For MSC treatment, dacarbazine has been encapsulated in lipid NPs for enhanced topical application [72]. Using a similar concept, Liu *et al*. advanced this field by designing a complex nanocarrier system comprising hollow mesoporous silica NPs coated with folic acid-grafted liposomes, offering a targeted delivery approach [73]. Additionally, carboplatin, a second-generation platinum compound FDA-approved for melanoma treatment, has been incorporated into poly(ε-caprolactone) NPs embedded in a chitosan-β-glycerophosphate gel for localized, intratumoral administration. In study done by Pallvi *et al*., Carboplatin (CBDCA) demonstrated a 19% response rate, similar to dacarbazine, in phase II melanoma trials. However, intravenous delivery often results in subtherapeutic tumor concentrations, prompting the development of alternative delivery systems. A novel formulation, CBDCA-loaded poly(ε-caprolactone) NPs in a chitosan-β-glycerophosphate gel (CBDCA-PCL-NPs-Gel), showed prolonged drug release, increased apoptosis (80.2%), and superior tumor suppression compared to conventional formulations in melanoma models. This system significantly improved therapeutic efficacy and reduced tumor volume more effectively than intravenous or intratumoral carboplatin solutions [74]. Similarly, Jian *et al*., developed temozolomide-loaded polyamide-amine dendrimers for their targeted efficacy against human melanoma cells *in vitro*, showcasing a promising NP-based delivery system [37].

2.2.2.2 Nanosystems for Phototherapy

PT is a treatment that uses light to activate drugs that are selectively absorbed by cancer cells. It can be used for superficial skin cancers, including melanoma, and is also known as photodynamic therapy (PDT). PDT is a medical treatment that uses a photosensitizing agent and a particular wavelength of light to treat cancerous and pre-cancerous cells. The photosensitizer is activated by light, leading to the formation of reactive oxygen species (ROS), which then damages the cancer cells. PDT can be an effective treatment for certain types of skin cancer, including melanoma [75]. Thus, it is of direct importance to construct an advantageous and useful combination and adjuvant following surgery to enhance PT efficiency in melanoma treatment, which showed advanced results [76].

Many synergistic strategies have been applied with PDT to elevate its efficacy and control limitations. PDT is a treatment for melanoma skin cancer that involves the use of a photosensitizing agent and light to destroy cancer cells. The specific method of administering PDT may vary depending on the patient and the stage of the cancer. In general, the first step in PDT for melanoma skin cancer involves the application of a photosensitizing agent to the area of the skin affected by the cancer. This agent is usually a topical cream or lotion that is applied to the skin and left in place for a certain period of time [77]. Once the photosensitizing agent has been absorbed by cancer cells, a specific wavelength of light is directed onto the affected area. This light activates the photosensitizing agent, causing it to release oxygen molecules that damage or destroy the cancer cells. The light may be delivered using a specialized lamp or laser, and the duration of the treatment will depend on the size and location of the melanoma. After the treatment, the patient's skin may be sensitive and prone to sunburn, so it is important to avoid exposure to sunlight and wear protective clothing and sunscreen [77]. Lucena *et al*. demonstrated that in the treatment of NMSC with PDT alone before surgical excision a tumor size reduction of 88% was achieved with a surgical intervention displaying excellent results and clear histological margins without recurrence after one year [78]. In another study by Yang *et al*. recurrence-free survival rates (FSR) were compared between different pathologic types of NMSC with a combination of surgery and PDT. The results provided good evidence that PDT is an effective treatment strategy for actinic keratosis and NMSC, particularly superficial BCC [79]. Nonetheless, the statistical analysis did not reveal significant differences between groups (Table 2.1), which may be due to the very small number of patients with extramammary Paget's disease (n = 3) and actinic keratosis (n = 7), making it difficult to detect the real differences between the study groups [79].

Table 2.1: Comparison of recurrence-free survival rates between different pathologic types of non-melanoma skin cancer. Reproduced with permission from [79].

Time after surgery	Squamous cell carcinoma (*n* = 66)	Basal cell carcinoma (*n* = 49)	Extramammary Paget's disease (*n* = 3)	Actinic keratosis (*n* = 7)	*p*-value
1 week	100%	100%	66.7%	100%	
4 weeks	98.5%	100%	66.7%	100%	
8 weeks	98.5%	98.0%	66.7%	100%	
12 weeks	98.5%	98.0%	66.7%	100%	
24 weeks	87.7%	93.9%	66.7%	100%	
					0.165

Note: Data are presented as *n* (%).

Monoclonal antibodies (mAbs), aptamers, antibody fragments, peptides, and DNA/RNA have also been utilized in various NP drug delivery platforms to enhance the active targeting of photosensitizer (PS) drugs in photodynamic therapy (PDT). Examples of such NP platforms include inorganic nanomaterials like quantum dots, solid lipid NPs, self-illuminating nanocrystals, theranostic agents, hydrogels, immune-conjugates, and metal-oxide-based or up conversion NPs. These platforms improve the precision and effectiveness of PS drug delivery to targeted cells during PDT [80]. Further research studies focused on the treatment of NMSC with surgery or curettage, and PDT has however been limited with few of these studies comparing clinical outcomes between surgical excision alone and surgery combined with PDT. The studies that do compare these clinical outcomes however are limited by their small sample sizes [79].

Carbon nanotubes are engineered nanomaterials renowned for their excellent near-infrared PDT capabilities, allowing them to elevate temperatures within tumors for effective treatment [81]. Water-soluble carbon nanotubes are currently being explored for gene and drug delivery because of their biocompatibility, efficient traversal of biological barriers, and ability to transport molecules directly into the cytoplasm [82]. The integration of dual plasmonic agents within hybrid constructs enhances the physicochemical properties of each agent, resulting in superior functionality by leveraging the combined effects of two distinct nanostructures [83]. For inorganic NPs, their applications in drug delivery and imaging have seen rapid advancements in recent years. These "nanotheranostic" systems are widely employed for cancer diagnosis and therapy. Although research specifically focused on skin cancer remains limited, existing studies have demonstrated promising results, particularly for melanoma treatment and detection, underscoring the need for further exploration in this field [84]. Notable examples include gold NPs functionalized with the anti-nucleolin aptamer (AS1411), and FeONPs modified with IR80, which have shown effectiveness as magnetic resonance imaging (MRI) probes and induced selective cytotoxicity in A375 melanoma cells upon near-infrared laser irradiation [85]. Another study highlighted cobalt ferrite oxide ($Co0.5Fe_2.5O_4$) nanotubes embedded in nanoemulsions, which exhibited significant time-dependent accumulation in a murine melanoma xenograft model, enhancing MRI imaging capabilities.

2.2.2.3 Nanosystems incorporating Radiotherapy

Even though radiation treatment is effective in approximately more than 75% of the early stages of some types of skin cancer, RT can be primarily used alone or with surgery for the treatment of advanced tumor cells [86]. RT is employed mainly after surgery to serve as an adjuvant therapy to kill the remaining cancer cells or to inhibit the recurrence of the tumor

[87]. RT is infrequently used after surgical interventions for the treatment of NMSC primary tumors. Nevertheless, in elderly, weak patients, or where the surgical approach is not required, RT can be used alone or as an alternative to surgery for skin metastases and adjuvant RT after the excision of lymph nodes [56]. For primary or loco-regional MCC, surgery followed by radiation therapy is regarded as the primary treatment option to prevent recurrences and lymph node metastasis [66]. The efficacy of surgery and radiation therapy in the management of primary or loco-regional MCC has been studied in several investigations.

Veness *et al*. conducted a retrospective study on 48 patients with primary MCC who underwent surgery followed by radiation therapy, revealing a 5-year OSR of 58%, and the local recurrence-FSR was 76% [88]. Another retrospective study of 48 patients with primary MCC who were treated with surgery and adjuvant radiation therapy found a 5-year local control rate of 82% and a 5-year OSR of 53% [89]. These findings suggest that the risk of relapse in lymph-node affected patients would be lowered by adjuvant RT after resection. Some studies found that synergistic RT with surgery increases the OS, as The ANZMTG 01.02/TROG 02.01 randomized controlled trials investigated the efficacy of adjuvant RT in reducing the risk of relapses in melanoma patients with high risk of relapse. A total of 250 patients who had undergone complete lymphadenectomy for metastases to cervical, inguinal, or axillary lymph nodes and were at high risk of relapse were randomly assigned to receive adjuvant RT or observation. At a median follow-up of 73 months, the adjuvant RT group had a lower rate of relapse in the lymph-node field (21%) compared with the observation group (36%), but there was no difference in OS or relapse-free survival (RFS) between the two groups. Adjuvant RT was associated with skin or subcutaneous tissue fibrosis, pain, nerve damage, and increased lower limb volume as the predominant toxic effects; 22% of patients in the adjuvant RT group had grade 3-4 toxic effects [90].

Dendrimers are increasingly being utilized in radionanotherapy, an innovative approach designed to enhance the effectiveness of radiotherapy through nanovectorization, a well-established technique in drug delivery and diagnostic applications. The incorporation of radionuclides into dendrimers aims to minimize the required dose of radiolabeled materials, thereby reducing toxicity and tumor resistance. This chapter highlights examples of radiolabeled dendrimers featuring alpha, beta, and Auger electron emitters, as well as their application in boron neutron capture therapy (BNCT). Additionally, the conjugation of radiolabeled dendrimers to monoclonal antibodies for improved targeting and their potential role in gene delivery radiotherapy are discussed. NPs play a significant role in advancing radiation therapy, serving as therapeutic agents or carriers for therapeutic compounds.

Among the various nanosensitizers investigated, gadolinium-based nanoprobes have garnered significant attention. These agents serve as dual-purpose theranostic tools, enhancing both diagnostic imaging and therapeutic efficacy. By promoting radiosensitization, they amplify the radiation damage in tumor tissues while simultaneously reversing radiation resistance, a common challenge in advanced cancers. Furthermore, these nanoprobes protect healthy tissues through increased radioresistance [91]. Their high X-ray absorption coefficients enable efficient energy deposition within tumors, leading to localized enhancement of radiation-induced cytotoxicity. Additionally, gold NPs are biocompatible and demonstrate immune evasion capabilities, allowing them to circulate in the body without eliciting significant immune responses. Their tunable size and surface modifications ensure optimal tumor tissue penetration and retention, while their stability facilitates ease of pharmaceutical evaluation and clinical translation.

Beyond gold, other nanosensitizers such as titanium oxide (TiO_2) and silver NPs (AgNPs) also hold promise. Titanium oxides NPs, for instance, generate reactive oxygen species (ROS) under X-ray irradiation, amplifying DNA damage in tumor cells. Silver NPs, on the other hand, possess inherent antimicrobial and anti-inflammatory properties, alongside their ability to enhance radiation-induced apoptosis in tumor cells. These nanosensitizers contribute to a multifaceted improvement in radiotherapy outcomes, offering a blend of enhanced tumor targeting and reduced off-target effects. Collectively, these studies show the potential of radionanotherapy to revolutionize cancer treatment by integrating diagnostic and therapeutic capabilities, minimizing radiation toxicity, and improving patient outcomes [92].

2.2.2.4 Immunomodulating Nanosystems

Immunotherapy is divided into the following major classes to treat cancer: cytokine therapy; immune checkpoint blockers; oncolytic viruses; cellular Immunotherapy; and polysaccharides. These pathways are further divided into two categories: activating agents and inhibition agents [93]. Adjuvant systemic therapy is recommended for high-risk patients with resected melanoma to lower the likelihood of melanoma recurrence following surgery [94]. A study conducted by Eggermont *et al*., investigated the use of pembrolizumab in the adjuvant setting for patients with resected stage III melanoma. The study included 1,019 patients who had undergone complete resection of stage III melanoma and were randomly assigned to receive pembrolizumab or placebo. The study found that the 12-month recurrence-free survival rate was significantly higher in the pembrolizumab group compared to the placebo group [95]. Another study also found that the 18-month distant metastasis-free survival rate was significantly higher in the pembrolizumab group compared to the

placebo group (71.4% for pembrolizumab vs. 53.2% for placebo). Based on these results, the study concluded that adjuvant therapy with pembrolizumab after complete resection of stage III melanoma resulted in significantly longer recurrence-free and distant metastasis-free survival [96]. While cytokines serve as the initial form of immune therapy, specific agents have shown efficacy in treating certain types of skin cancer such as MCC. These treatments enhance the OS duration of patients by directly promoting the growth and activity of immune cells. One such agent is IFNα (Intron A), which has been shown to be an excellent adjuvant treatment for MSC following surgical resection. Inducing the maturation of immune cells and enhancing tumor-associated antigens (TAAs) expression on tumor cells, IFNα can promote antitumor immunity. Despite being used in clinical settings for a long time, the short half-life of cytokines in circulation often requires high-dose administration, leading to various unwanted side effects, such as potentially fatal capillary leakage and cytokine release syndrome.

To overcome these limitations, long-circulating versions of these cytokines have been investigated including PEGylated forms of IFN (peginterferon-alfa-2b) [97]. IFNα is an adjuvant therapy for malignant MSC following surgical resection and enhances antitumor immunity by stimulating the maturation of immune cells and increasing the expression of tumor-associated antigens (TAA) on tumor cells. However, prolonged administration of this cytokine has been linked to the production of neutralizing antibodies against both the natural protein and its therapeutic form, as noted by Borgheti-Cardoso *et al*. [37]. The U.S. Food and Drug Administration approved PEG-Interferon alfa-2b (PEG-IFN) as an adjuvant therapy for melanoma patients with microscopic or gross nodal involvement following complete lymphadenectomy. This decision was based on a multicenter, open-label trial involving 1,256 patients who had undergone surgical resection and were randomized (1:1) to receive either PEG-IFN or observation over five years. PEG-IFN was administered subcutaneously (s.c.) with an initial dosage of 6 μg/kg per week for eight doses, followed by 3 μg/kg per week for up to 252 weeks. The primary endpoint was recurrence-free survival (RFS), which was significantly longer in patients treated with PEG-IFN. Median RFS was 34.8 months for the PEG-IFN group compared to 25.5 months in the observation group. which utilized there was no significant difference in OS between the two groups [97].

According to a 2020 study by Tarhini *et al*. the study enrolled adult patients with histologically confirmed cutaneous or unknown primary origin melanoma, at American Joint Committee on Cancer (AJCC) 7th edition stage IIIB, IIIC, or IV (M1a or M1b), who had undergone successful surgical resection and were determined to be disease-free by physical examination and imaging studies within four weeks prior to randomization. Complete lymph

node dissection was mandatory for patients with stage IIIB or IIIC disease. Randomization had to occur within 84 days of resection. Ipilimumab was compared with IFN, but no statistical difference in OS was found [98]. The KEYNOTE-054 trial for stage III resected melanoma showed that pembrolizumab, used in combination therapy, led to a 20% absolute increase in 3-year RFS compared to placebo (63.7% vs. 44.1%, respectively) [99]. Trials of neoadjuvant Immunotherapy in stage III melanoma showed an impressive response rate of almost 80% [100]. With the introduction of new immune checkpoint agents (such as relatlimab, [101]) and innovative approaches (such as neoantigen-driven T-cell stimulation), there is promising and steady progress in achieving long-term survival and potentially cures for patients with melanoma, including those with advanced disease [102].

Twenty-five years ago, high-dose IFNα (HDI) was the standard of care for adjuvant therapy in locally advanced melanoma after surgical resection. The pivotal role of HDI was established by the E1684 trial, which randomly assigned 287 patients to receive 52 weeks of HDI or undergo observation. Initially, with a median follow-up of 6.9 years, the trial showed improved RFS and OS in patients with AJCC 6th edition stages IIB, IIC, and III who received adjuvant HDI compared to those who underwent observation. However, with longer follow-up, the OS benefit was no longer evident (99). Another trial, EORTC 18991, evaluated pegylated interferon-α (PEG-IFN) in patients with resected stage III melanoma, randomizing 1,256 patients to observation or PEG-IFN after lymphadenectomy. EORTC 18991 demonstrated a positive improvement in RFS in the PEG-IFN arm, but no significant improvement in OS [103]. Patients with stage III or IV melanoma who undergo surgical excision remain at a high risk for relapse. Three randomized trials demonstrated that adjuvant therapy with a programmed death-1 (PD-1)–blocking antibody, such as nivolumab or pembrolizumab, provides significant benefit compared to no treatment or previous standard therapies like IFNα-α2b or ipilimumab. Moreover, event-free survival was notably longer in patients who received pembrolizumab both before and after surgery compared to those who received it only as adjuvant treatment after surgery [104]. The combination of NP-induced ferroptosis and the inhibition of programmed cell death effectively suppresses the progression of B16-F10 melanoma tumors, highlighting the potential of ferroptosis induction as a strategy to enhance cancer immunotherapy [105].

The use of smart nanomaterials in drug delivery systems therefore enables targeted immune-drug delivery and controlled payload release in response to various stimuli such as acidic/hypoxic environments, enzyme levels, glutathione, and metabolic changes (Figure 2.4a). Nanomaterials can also be locally administered with immunomodulators to improve their antitumor activities by controlled release, especially against tumor recurrence and

metastasis, as depicted in Figure 2.4b [106]. One example of this is a bio-responsive hydrogel that is formed by the interaction of thrombin and fibrinogen, incorporated with CaCO3 NPs coated with anti-CD47 antibodies and applied into the surgery cavity. This hydrogel significantly suppresses local tumor recurrence and metastatic spread through M1-type macrophage-activated innate and adaptive immunity [107].

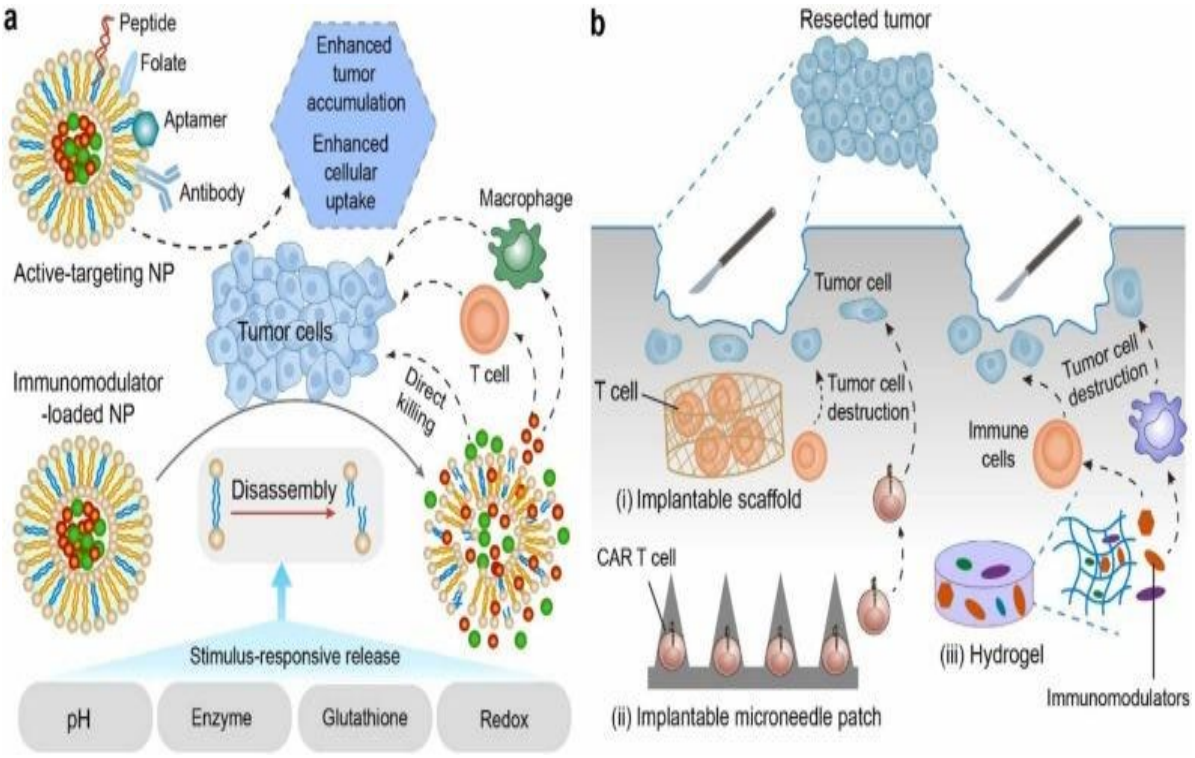


Figure 2.4: Nanomaterials improve cancer immunotherapy by facilitating the delivery of immunomodulatory drugs: (a), Nanomaterials can be targeted for delivery to tumor cells, with the ability for stimulus-responsive release at tumor sites and (b), Various types of nanomaterials such as implantable scaffolds (i), microneedle patches (ii) and hydrogels (iii), can be used to locally deliver immunomodulators directly to the surgical cavity, thus enhancing tumor eradication post-surgery. Reproduced with permission from Luo and Liu [106].

Several studies have also highlighted the efficacy of self-adjuvanted nanomaterials in suppressing tumor growth and preventing post-operative recurrence and metastasis across various tumor models. For instance, self-adjuvanted, pH-sensitive polymeric NPs (PEG-PC7A) loaded with tumor antigens demonstrated significant tumor inhibition *in vivo* in melanoma. This success is attributed to enhanced cytosolic antigen delivery and the STING-activating properties of the PC7A segment [108]. Additionally, a nanovaccine composed of fluorinated polyethyleneimines (PEIs) mixed with ovalbumin (OVA) has shown the ability to induce dendritic cell (DC) maturation via the toll-like receptor (TLR) 4 signaling pathway. This system facilitates the release of loaded antigens into the cytosol of DCs, promoting efficient MHC-I antigen presentation and eliciting robust antigen-specific cytotoxic T

lymphocyte (CTL) responses *in vivo* [109]. These enhanced CTL responses significantly suppress established B16-OVA tumors. Furthermore, fluoropolymer-based personalized cancer vaccines, when combined with immune checkpoint blockade, effectively prevent post-operative tumor recurrence and metastasis, demonstrating a promising approach to advanced cancer immunotherapy [106].

2.2.2.5 Nanomaterial-induced Hyperthermia

Hyperthermia therapy (HTT) has been applied for decades in the treatment of skin cancer, with magnetic hyperthermia (MHT) introduced as one of the important thermal treatment methods to induce hyperthermia (HT) for the destruction of malignant cells [110]. Several studies have been conducted to investigate the effectiveness of combining surgery with HT in the treatment of various cancers, including melanoma. These studies have shown promising results in terms of improving local tumor control and OSR. For example, a study by Hildebrandt *et al*. (2004) demonstrated that adjuvant HT following surgery for high-risk soft tissue sarcoma significantly improved local recurrence-free survival and OSR compared to surgery alone [111]. In the context of melanoma, a study by Lutgens *et al*. (2001) showed that the addition of hyperthermic isolated limb perfusion to surgery for in-transit melanoma metastases resulted in a significantly higher complete response rate and prolonged disease-free survival compared to surgery alone [112].

According to Moyer *et al*. [113], HT destroys cancer cells by targeting the disorganized and irregular neo-vascularization found in tumors. The blood vessels in tumors are often twisted, compacted, and filled with cancer cells, leading to reduced blood flow. As the temperature increases in the tumor, the blood vessels collapse due to a preferential increase in red blood cell rigidity, swelling of the endothelial cells, hemorrhage into capillary lumens, and adherence of leukocytes to vessel walls. This process starts at 42°C and affects all human tissue at 45°C (as illustrated in Figure 2.5) [113]. Following the combination of surgery with HT, no tumor growth was observed. Six patients with SCC and skin melanoma in this study stabilized tumor growth, while two patients with BCC achieved a complete and permanent cure with Blood Flow Restriction Training (BFRT) and local HT. In most cases (41.4%), the tumor regressed to 75% of its original size. In the second stage, the remaining tumor was removed within healthy tissue, with 1-1.5 cm from the clinically identifiable tumor margin to account for possible "subclinical" spread. The excision was performed in a single block, and the specimen was histologically evaluated to confirm the final diagnosis. The study found that the addition of HTT to surgery led to a significant improvement in disease-FSR and OS rates compared to surgery alone [114]. The application of regional hyperthermia (RHT) further aimed to increase the body temperature above 42°C, and after this treatment,

patients who were deemed operable underwent surgery, with the tumor exhibiting a positive response. Thus, post-surgical HT may be critical for local control [115]. Recent studies on nanomaterials for post-surgical HT have shown promising results. One example is the development of multifunctional polymeric NPs loaded with gold nanorods (Au-NRs) and liquid perfluorocarbon, which were conjugated with a monoclonal MAGE-1 antibody. These theranostic NPs demonstrated targeted delivery to melanoma tumor cells, exhibiting high persistence at the tumor site *in vivo* [116]. In another study, gold NPs conjugated with elastin-like polypeptides (ELPs) displayed photothermal capabilities. A single intratumoral injection of these ELP-gold NPs enabled simultaneous photothermal, photoacoustic, and X-ray computed tomographic imaging, in addition to effective PTT of melanoma tumors [117].

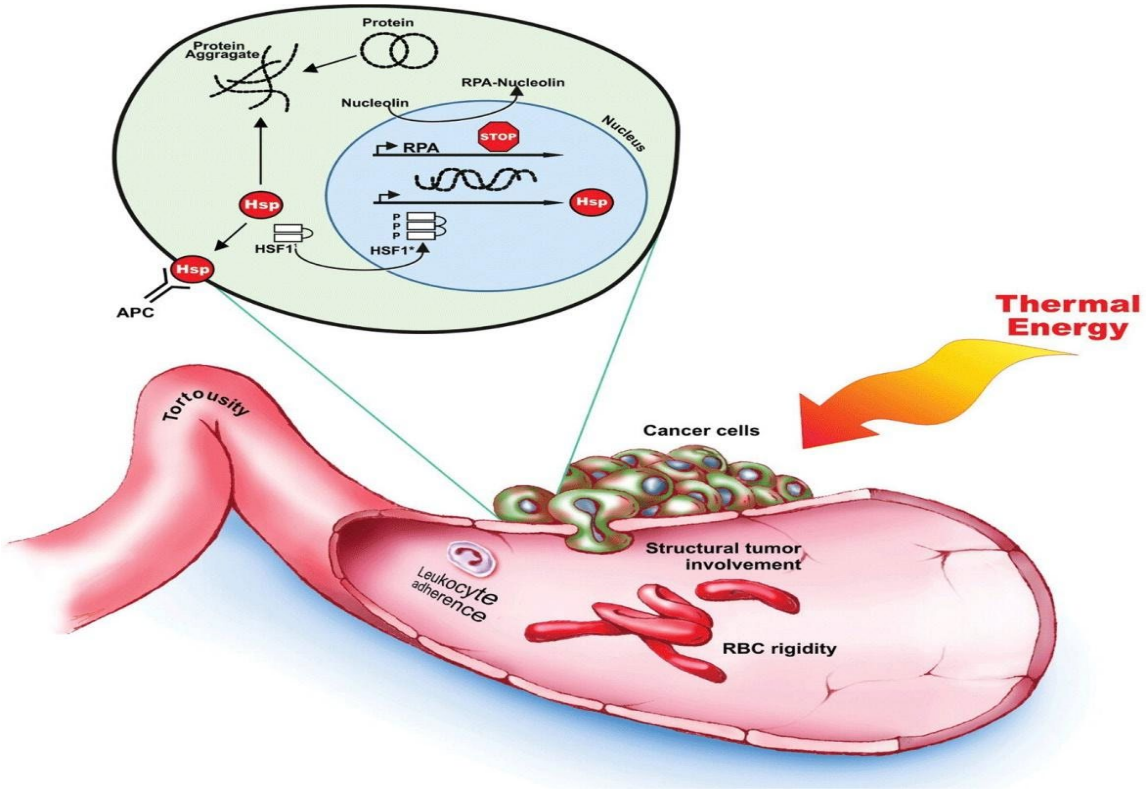


Figure 2.5: Thermal effects on tumor and cell physiology. This figure illustrates the impact of thermal treatments on tumor cells and their microenvironment, highlighting the physiological responses to varying temperature ranges. These thermal effects are essential for optimizing hyperthermia-based cancer therapies, ensuring maximal tumor cell eradication while preserving normal tissue integrity. Reproduced with permission from Moyer and Delman [113].

2.2.2.6 Nanomaterial-regulated Extracorporeal photopheresis

Extracorporeal photopheresis (ECP) has been explored as an adjuvant treatment option in melanoma, although it is not as widely established in melanoma management as in cutaneous T-cell lymphoma (CTCL). ECP works by modifying the immune system's response through the exposure of leukocytes to UVA light combined with a photosensitizing

agent. This immune-modulating effect can help in controlling metastatic melanoma in some cases, especially in patients with immune-related conditions or as part of combination therapies with other systemic treatments like checkpoint inhibitors [118]. Furthermore, ECP is a recommended treatment for erythrodermic cutaneous T-cell lymphoma (CTCL) according to the guidelines of the European Organisation for the Treatment and Research in Cancer (EORTC) for mycosis fungoides/Sézary syndrome, where it has shown efficacy as monotherapy and as an adjuvant therapy. Its mechanism involves immune modulation by exposing leukocytes to ultraviolet A light, potentially enhancing anti-tumor immunity. It is also endorsed by the Joint British Association of Dermatologists and the UK Cutaneous Lymphoma Group guidelines. Moreover, ECP is highlighted in the National Institute for Health and Care Excellence (NICE) 2006 Improving Outcomes Guidance in Skin Cancer, affirming its role in managing CTCL [119].

Although ECP is not a standard first-line treatment for melanoma, some studies have suggested potential benefits in advanced melanoma cases, particularly when combined with other therapies, such as immunotherapy or post-surgical interventions. Its efficacy is still under evaluation, and further research is needed to confirm its broader applicability specifically for melanoma. Additionally, ECP may help reduce the risk of recurrence and improve survival outcomes for skin cancer patients when used after surgery in combination with systemic therapies like CT or immunotherapy. Further studies will determine its full potential in the broader management of skin cancers, including melanoma. In the pursuit of novel therapeutic strategies for advanced and metastatic sarcoma, various drug delivery systems (DDS) have been explored. One such approach involves magnetic drug targeting, which utilizes an applied magnetic field to direct drug-loaded NPs to the tumor site [120].

2.2.3 Multicomponent combinations

The combination of surgical intervention with multi-component therapeutic approaches has been widely explored in melanoma treatment to enhance effectiveness and reduce recurrence rates. By incorporating more than two methods alongside surgery, such as immunotherapy, CT, and targeted therapy, the outcomes for patients can be significantly improved.

Combining surgery with immune checkpoint inhibitors (e.g., nivolumab or pembrolizumab) and BRAF/MEK inhibitors have shown notable results in advanced melanoma. The surgical removal of the tumor is supplemented with immunotherapy to bolster the immune response against residual cancer cells, while targeted therapies (e.g., vemurafenib and dabrafenib for BRAF-mutated tumors) work to block molecular pathways driving tumor growth. This multi-

pronged approach helps tackle microscopic cancer remnants that surgery alone might miss and addresses resistance mechanisms [98]. Another study by Issels *et al.* (2010) found that the addition of regional HT to neoadjuvant CT and surgery significantly improved disease-free survival and OSR in patients with high-risk soft tissue sarcoma compared to neoadjuvant CT and surgery alone [121]. To counteract resistance mechanisms in cancer, combining different therapeutic strategies following surgical excision has proven effective. Approaches like CT, immunotherapy, and targeted therapies can be used synergistically, focusing on different pathways to enhance treatment outcomes.

Another combination of surgery, CT, and PDT has also been employed particularly for difficult-to-treat or recurrent cases of melanoma. Surgery removes the bulk of the tumor mass, while CT targets residual cancer cells systemically. PDT, which activates photosensitizers with light to generate ROS, is employed to further damage cancer cells at the local site. This approach enhances overall tumor eradication and reduces the likelihood of recurrence [80].

Among the emerging therapeutic strategies, nanotechnology plays a multifaceted role in cancer management, including cancer detection, treatment, biomarker identification, understanding of cancer progression, and guiding the development of novel diagnostic and imaging agents [122]. While targeting treatments against solid tumors using various modalities often results in significant initial tumor regression, these effects are frequently short-lived due to the development of therapeutic resistance. As a result, utilizing multiple anticancer agents in combination with NPs presents a promising strategy to address drug-resistant cancers. Combination therapy, particularly when facilitated by NPs, offers an effective alternative to improve treatment outcomes. NP-mediated combination therapy allows the simultaneous delivery of multiple therapeutic agents with diverse physicochemical and pharmacological properties within a single NP. This approach ensures that the optimal synergistic drug ratio is preserved all the way to the intracellular uptake by the target cancer cells past two decades [69], nanotechnology has garnered significant attention in clinical therapeutics, especially with advancements in biocompatible nanoscale drug carriers like liposomes and polymeric NPs, enhancing the safe and efficient delivery of a wide range of drugs.

Multivalent metal ions, such as Fe^{3+}/Fe^{2+}, Cu^{2+}/Cu^{+}, and Mn^{4+}/Mn^{2+}, are GSH-responsive through redox reactions. These ions facilitate chemodynamic therapy (CDT) by reacting with H_2O_2 to produce cytotoxic $^{\cdot}OH$. Composite NPs with dual pH and GSH responsiveness enable synergistic PTT and PDT under near-infrared light. Additionally, Fe^{3+} ions deplete GSH, preventing $^1O_2$ quenching, while Fe^{2+} ions from the reaction promote ferroptosis via

·OH generation. This multimodal nanoplatform has demonstrated efficacy *in vitro* and *in vivo* for cancer therapy (Figure 2.6) [123].

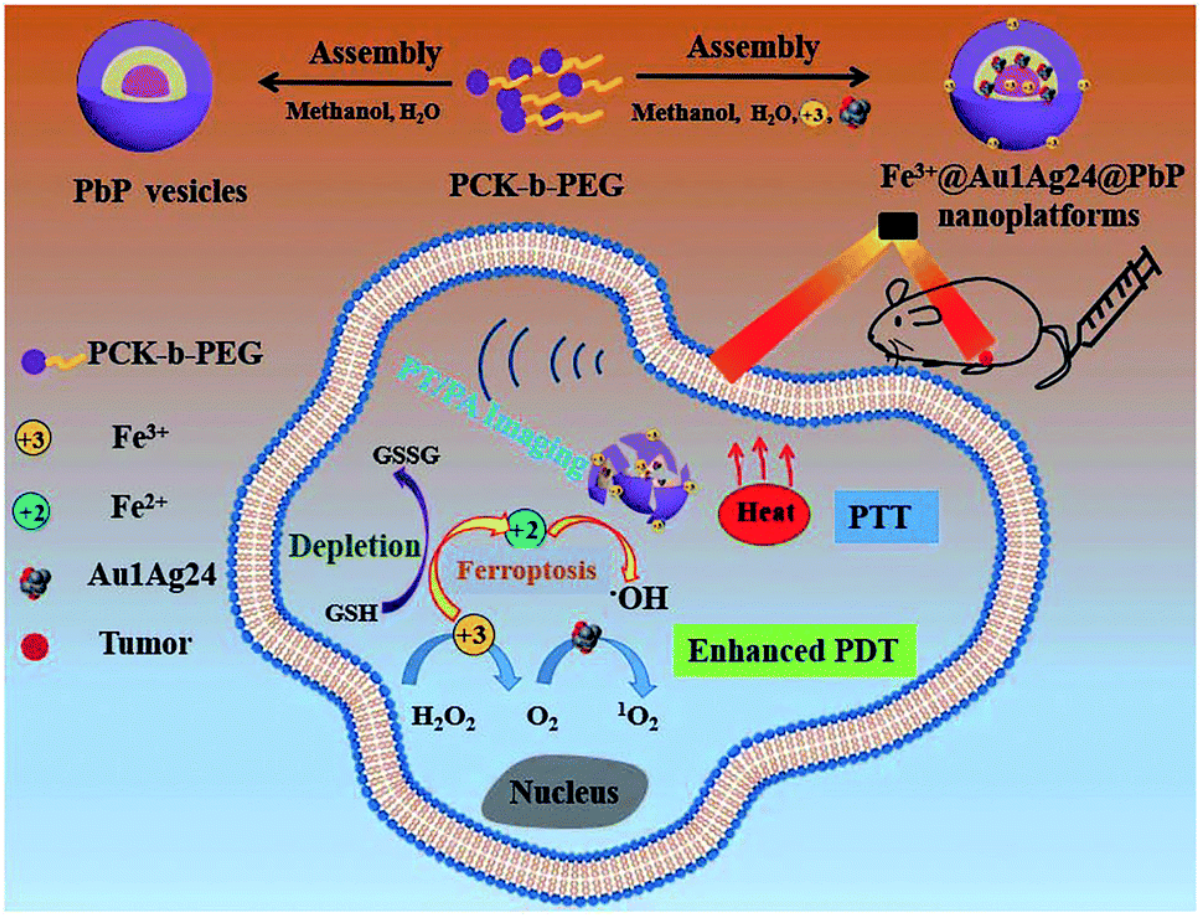


Figure 2.6: Schematic illustration of the formation of the Fe^{3+}@Au_1Ag_{24}@PbP nanoplatform and its imaging-guided synergistic anticancer therapy. This figure depicts the step-by-step synthesis and functionalization of the Fe^{3+}@Au_1Ag_{24}@PbP nanoplatform, highlighting its application in imaging-guided synergistic anticancer therapy. Reproduced with permission from Yang and Sun [123].

2.3 Conclusion

The future of skin cancer treatment, particularly melanoma, will likely see a continued integration of multi-modal approaches that combine surgical interventions with other advanced therapeutic strategies. The need for innovative therapies is crucial. The treatment landscape is shifting towards using combinatorial therapies involving surgery with such as CT, immunotherapy, targeted therapies to counteract resistance mechanisms and improve outcomes. Recent advancements have demonstrated the potential benefits of combining surgery with immunotherapy and hyperthermia therapy. The development of more personalized treatment options using gene therapy and nanomaterials such as liposomes, dendrimers, and carbon nanotubes is expected to grow. These nano-based therapies, when

used alongside surgery, may reduce adverse effects, improve precision in drug delivery, and enhance patient compliance. Future efforts will focus on optimizing nano-based, multimodal therapies for specific skin cancer types and stages. Rigorous research and clinical trials are essential to confirm the efficacy of these therapies, aiming to improve survival rates and minimize relapse risk. Nanotechnology-based systems have emerged as transformative tools for cancer therapy, designed to overcome biological barriers and target tumor sites with enhanced precision. These nanosystems reduce drug dosages while maintaining high therapeutic efficacy and minimizing side effects.

Looking forward, future research may focus on optimizing these combinations for specific cancer types and stages. Further clinical trials will be essential to evaluate the efficacy of these multi-component systems, with the goal of improving long-term survival rates and reducing relapse and metastasis in skin cancer patients. Additionally, the use of biomarkers for early detection and real-time monitoring during treatment could help tailor therapies for individual patients, maximizing therapeutic success. Overall, the field is evolving toward more targeted, less invasive, and highly effective treatment approaches that could revolutionize skin cancer care in the coming decades.

This chapter has highlighted the synergistic potential of nanotechnological advancements when combined with surgical interventions for skin cancer therapy. Conventional treatments paired with nanosystems have demonstrated improved outcomes in both pre-clinical and clinical studies. For example, carbon nanotubes and dual plasmonic agents exhibit remarkable efficacy in PTT and gene delivery. Additionally, innovative techniques like extracorporeal high-pressure therapy (EHPT) provide novel solutions for addressing large skin defects post-surgery by preserving native tissue structure and eliminating cancer cells, allowing for the re-implantation of tissue as an autologous matrix.

In summary, nanotechnology has introduced transformative advancements in enhancing conventional skin cancer therapies. The integration of nanomaterials into both surgical and systemic approaches has demonstrated synergistic potential for improving outcomes. Although many nanotechnology-based strategies are still under development, the progress achieved thus far underscores their potential to revolutionize skin cancer management. Continued research and clinical trials are vital to fully realize these advancements. The next chapter of this thesis will explore non-surgical synergistic interventions to assess the role of combination therapies without surgical involvement in the treatment of skin cancer. This focus will address the gaps identified in current approaches, shaping the primary research direction of this study.

CHAPTER 3

NON-SURGICAL SYNERGISTIC INTERVENTIONS FOR THE TREATMENT OF SKIN CANCER

3.1 Introduction

Building on Chapter 2, which emphasized the transformative advancements in nanotechnology and its synergistic integration with surgical approaches for skin cancer treatment, this chapter focuses on non-surgical combination therapies. While surgical intervention remains a cornerstone in managing skin cancer, particularly MM, the exploration of non-invasive alternatives is critical to addressing the limitations associated with surgical procedures, such as extensive tissue damage, recovery time, and challenges in treating advanced or metastatic cases. Nanotechnology has demonstrated immense potential in revolutionizing skin cancer management by enhancing drug delivery precision and reducing systemic toxicity. The integration of nanomaterials into surgical and systemic approaches has showcased its ability to improve therapeutic outcomes, particularly when used in combination with conventional therapies. However, as highlighted in the previous chapter, many nanotechnology-based strategies remain in the development phase, necessitating further research and clinical validation.

This chapter explores the potential of non-surgical synergistic interventions as viable alternatives to surgery in treating skin cancer. The focus extends to both NMSC and MM, examining the efficacy of innovative drug delivery systems and oncology strategies in improving survival rates, patient compliance, and managing relapses and metastases. By delving into recent advancements, including nano-based chemotherapeutics, immunotherapy, PDT, and gene therapy, this chapter aims to highlight their transformative role in skin cancer treatment without surgical involvement. Furthermore, the chapter addresses the gaps identified in conventional and surgical approaches, emphasizing the need for targeted and patient-centric therapies. Through the exploration of cutting-edge non-surgical techniques, this chapter underscores the potential of these interventions to not only complement but also potentially replace surgical methods, paving the way for more effective and less invasive treatment paradigms.

3.2 Non-Surgical Combination Treatments for Skin Cancer

Combination therapy uses two or more standard therapeutic agents with the aim of integrating distinct treatment mechanisms of action to enhance the sensitivity of cancer cells

[124]. Recent studies have found that non-surgical combinatorial cancer treatments have delivered more favorable results compared with monotherapies [125]. The primary objective of these interventions is to enhance survival rates and reduce the risk of cancer recurrence or metastasis by specifically targeting residual microscopic carcinoma [63]. Although these approaches can elevate the cost of treatment compared with monotherapy, synergetic combinations and platforms can lower side effect profiles, increase quality-of-life during and after treatment, and have a higher efficacy compared to traditional strategies. Provided below are the different synergistic non-surgical interventions for the treatment of skin cancer, subclassified into combinations with traditional treatment strategies including CT and RT, as well as more advanced therapies such as PT, immunotherapy, and thermal therapy.

3.2.1 Synergistic Radiotherapy Interventions

Despite surgery being the method of choice in the early stages of skin cancer, RT is considered a popular strategy for controlling skin melanoma. Regardless of the favorable developments in RT techniques, there are limitations when it is applied alone, with its effectiveness not more than 23% [126]. Additionally, the main mechanism of RT depends on the existence of oxygen molecules in the tissue site, so hypoxia disorders and inefficient absorption of radiation rays restrict RT effectiveness in skin cancer treatment [127].

3.2.1.1 Chemotherapy

RT is now commonly used as a primary non-surgical treatment option for various types of skin cancers, including low- and high-risk cases. When combined with CT, RT has shown significant efficacy in treating skin carcinoma [128]. According to a recent publication by NCCN, the NCCN recommended RT as a first-line therapy for non-surgical candidates at low and high risk of BCCs and with local localized and high risk of SCC. For those at highest risk in cases involving SCCs, a combination of RT and CT may be considered. Though, due to concerns about potential long-term side effects, RT is typically reserved for patients over the age of 60. Additionally, patients with genetic conditions that increase their risk for skin cancer or connective tissue diseases are generally not recommended for RT [127]. Studies in the field of medical research have indicated that the use of adjuvant, platinum-based, postoperative chemoradiotherapy (CRT) can lead to improved outcomes in individuals with high-risk mucosal SCC of the head and neck. Specifically, the combination therapy has been shown to enhance locoregional control, development of free survival, and increased OS compared to the use of RT alone [129]. In an initial study, patients with locally advanced cutaneous squamous cell carcinoma (la-cSCC) who were not suitable for surgery received definitive RT (70 Gy in 35 fractions) along with concurrent weekly cisplatin. The study included 19 patients, and it reported an overall complete response rate of 63% [130].

However, as discussed by Porceddu *et al*. a recent randomized phase III trial called TROG 05.01, conducted in la-cSCC, which compared postoperative concurrent CRT with RT alone, the trial did not demonstrate any added benefit from the inclusion of weekly carboplatin. Furthermore, a combined treatment approach involving cetuximab and RT has been described for the treatment of cSCC. Additionally, there have been case reports showcasing the use of RT in combination with vismodegib for recurrent or la-BCC [129, 131]. In another study conducted by Her *et al*. it was revealed that the administration of 1.9 nm gold NPs (AuNPs) as novel radiosensitizers along with 30 Gy irradiation using 250 kVp X-rays led to a significant improvement in the one-year survival rate of mice with subcutaneous EMT-6 mammary carcinoma. The survival rate increased from 20% when treated with X-rays alone to 50% when combined with 1.35 g of AuNPs per kilogram of body weight, and further increased to 86% with a higher dose of 2.7 g of AuNPs per kilogram of body weight [132].

3.2.1.2 Immunotherapy

Current research focusing on RT with synergistic immunotherapy, has shown favorable effects in cancer therapy, with recent findings suggesting that RT can be used in conjunction with the host immune system to identify novel mechanisms that could potentially upgrade the effectiveness of RT, particularly in skin cancers such as MM [133-135]. Furthermore, the synergy between radiation and immunotherapy involves the enhancement of the mechanism of these immunotherapies by increasing a tumor's sensitivity to radiation or vice versa, thereby improving cytotoxicity to cancer with low doses of radiation, additionally improving the efficacy of the combination strategy [110]. The combination of immunotherapy and RT has further shown preclinical proof and indicated a promising impact on mutated melanomas [136]. A recent study by Domingues *et al*. has concluded that adjuvant IFNα can lower the risk of relapse and improve survival of melanoma patients when used in combination with RT [137]. Immunotherapy with IFN exhibits immunomodulatory effects, such as stimulating the most histocompatibility complex class I expression in melanoma and immune cells, inhibiting melanoma cell proliferation, and causing proapoptotic effects in a manner dependent on the dosage. Despite the emergence of newer and more effective immunotherapies, IFNs continue to be studied in combination with RT and other immunotherapies and targeted therapies in clinical trials [137]. One such study was by Gonzalez *et al*. where the use of adjuvant immunotherapy and radiation in the treatment of high-risk resected melanoma was investigated. The treatment protocol consisted of intravenous administration of induction IFNα-2b at a dosage of 20 MU/m² per day for 5 consecutive days every week for duration of 4 weeks. Following this, RT was administered (30 Gy in five fractions) concurrently with subcutaneous administration of IFNα-2b at a dosage of 10 MU/m², three times per week on alternating days. Maintenance therapy included adjuvant subcutaneous administration of

IFNα-2b at a dosage of 10 MU/m², three times per week, for a total of one year. The results of this study noted that the probability of regional control (within the regional nodal basin) was 78% at 12 months, and the median follow-up was 80 months among the 10 surviving patients (43%). The median OS was 35 months, and the median failure-free survival was 20 months [138]. While this study did not confirm a significant improvement in OS when comparing the combination of RT with immunotherapy to other synergistic treatment methods for skin cancer, these findings could prove valuable in the formulation of new trials involving radiation and bioimmunotherapy.

3.2.1.3 Photothermal therapy

The dual method of PTT improves RT effectiveness by enhancing the flow of blood and oxygen to the tissue, thereby settling any hypoxic crisis and reducing radioresistance in cancerous tissue . Figure 3.1 illustrates a schematic depiction of the mechanisms involved in cancer treatment using functionalized AuNPs in PT, RT, and PTT combined with RT (PTT/RT) [110].

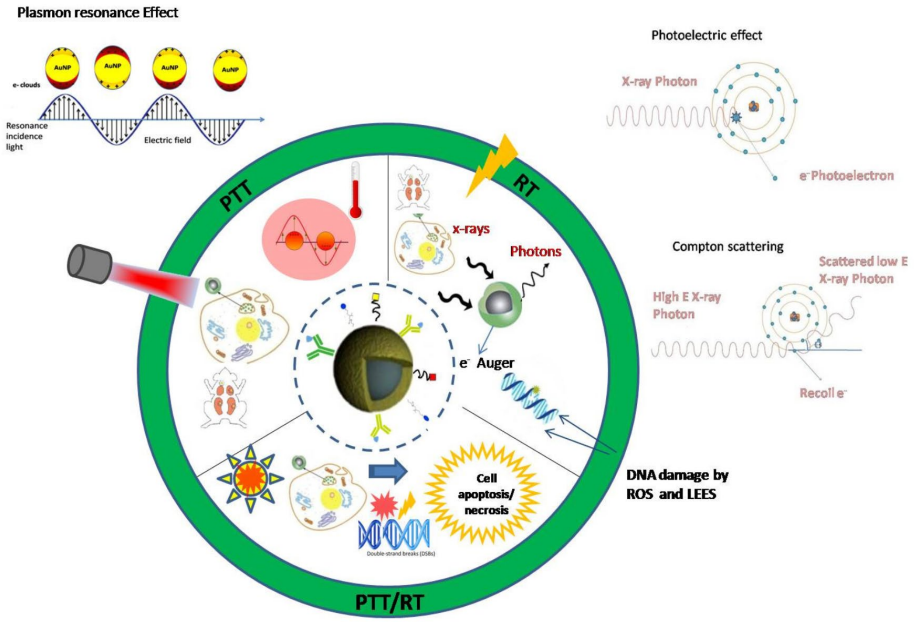


Figure 3.1: A schematic representation of the basic action mechanisms of PTT, Ionizing RT and combining PTT/RT in cancer treatment based on functionalized AuNPs. This figure illustrates the fundamental mechanisms by which PTT and RT exert therapeutic effects on cancer cells, both individually and in combination. Reproduced with permission from Spyratou *et al*. [110].

In a study by Daneshvar *et al*. a novel approach to treat melanoma cancer cells by combining X-ray RT and laser PTT using PtNPs was explored to maximize the effectiveness

by sensitizing the cancer cells to both treatments simultaneously. This was achieved by modifying the PtNPs (≈12.2 ± 0.7 nm) with photosensitizing agents (PSs), which allowed the NPs to absorb laser energy and convert it into heat, resulting in localized hyperthermia. The study involved vitro experiments using MM cells. The researchers demonstrated that the combination of X-ray radiation and laser-induced hyperthermic effect using PtNPs resulted in synergistic cytotoxic effects. The dual-sensitization approach led to increased cell death and enhanced tumor regression compared to the individual treatments alone. This research concluded that the combination of X-ray RT and laser PTT using PtNPs holds promise for improved treatment outcomes in melanoma. However, further research is needed to validate these findings and evaluate the approach in preclinical and clinical settings [139].

3.2.1.4 Hyperthermia Therapy

HTT provides a good synergistic combination with RT and has been approved clinically for the treatment of various cancers [140], with combinational therapy using HTT utilized in pre-clinical and clinical experiments to overcome the radioresistance of tumors [141]. Baronzio *et al*. [142] observed that several clinical trials have reported an enhanced response when combining radiation and HT. However, many authors have noted a significant variability in the improvement of perfusion and oxygenation. This variability can be attributed, in part, to the heterogeneous regulation of the carcinoma neo-vasculature and the uneven distribution of regional regulatory mechanisms within it [142]. Starting from 1975, clinical trials were undertaken to examine if the combination of RT with localized HTT can improve tumor inhibition when compared to using RT alone. The HTT of local tumors were accomplished by employing radiofrequency inductive heating at 27.12 MHz, and for larger lesions (over 100 cm^3), radiofrequency conductive heating at 13.56 MHz was also utilized. A total of 100 lesions of 38 affected individuals underwent treatment, either with RT or in adjuvant with HTT. The treatment frequency varied, with almost all lesions receiving treatment two times a week or one per week, as per the radiation dose fractionation scheme employed. These findings indicate that the combined therapy resulted in a superior tumor control rate compared to radiation therapy alone (75% versus 46%; statistically significant with a P-value of less than 0.01). Additionally, there were no observable adverse effects on normal tissue after the synergistic treatment. After data analysis of the therapeutic outcomes, it was observed that the efficacy of tumor control is influenced by the initial tumor volume, the total dose and the dose per fraction. When RT was administered alone at high level doses per fraction, it achieved control of 80% of the lesions if the tumor volume was less than 10 cm^3, whereas the control rate dropped to 30% for larger tumor volumes. Regardless of the tumor volume, the combination therapy achieved an 80% local tumor control rate [143].

In recent research, both *in vitro* and *in vivo* studies have suggested a unique potential of HTT for immunomodulation when administered with RT [144], with the combinative intervention observed to enhance the tumor cells sensitiveness to ionizing radiation. One noteworthy finding was in the research undertaken by Vujaskovic *et al*. which subjected R3230 tumors to temperatures of 40.5°C or 41.58°C for durations of 30 to 60 minutes in combination with RT. The results of this study noted that the post-heating increase in tumor blood flow observed 24 hours later was notably higher than what was observed immediately after heating. As illustrated in R3230 tumors, the blood flow increased by approximately 1.5 times immediately after heating, whereas it rose by 2.5 times 24 hours after heating at 41.58°C for 60 minutes. [145]. This synergy led to an increased effect of HTT to re-oxygenate hypoxic carcinoma cells by boosting blood flow, thereby eliminating the protective hypoxic environment during HTT treatment.

It is well-established that hypoxia is associated with radioresistance, and elevating the oxygen level in the hypoxic tumor tissues can enhance tumor radiosensitivity. However, this influence of HTT is temperature-dependent, and only the right temperature can result in improved oxygenation and vascular perfusion of tumors, ultimately lead to enhanced radiosensitivity [146]. Additionally, some studies suggest that HT can sensitize cells to X-rays in further treatment phases, resulting in concepts such as thermoradiotherapy (TRT). In TRT, cancer cells may be destroyed due to their insensitivity to radiation, and the process of repairing DNA damage under ionizing radiation is inhibited. This synergistic approach offers a more effective treatment outcome for cancer patients [147]. Overall, clinical trials have demonstrated the success of combining HT and RT in the treatment of melanoma.

3.2.2 Chemotherapeutic Combinations

In the past, CT served as the initial treatment choice for advanced melanomas, with cytotoxic drugs such as doxorubicin (DOX), methotrexate, and 5-FU commonly used. A significant concern, however, with the use of CT is that it significantly lowers the patient's immune system by affecting bone marrow cells, thereby increasing the potential for acquired diseases. CT, however, remains a critical component in providing effective care for patients with advanced, treatment-resistant, or recurrent melanomas [148, 149]. The main advantage of CT is that it provides consistent results with a decreased risk of relapse.

3.2.2.1 Phototherapy

In current years, the integration of CT and PTT has appeared as an effective and favored strategy method for different types of cancer cells line. This was demonstrated by Yu, N. *et al*. where blue tellurium (Te) nanoneedles exhibited superior characteristics compared to

purple Te nanorods. The nanoneedles were noted to possess higher photothermal conversion efficiency when subjected to a 915 nm laser, and they also demonstrate laser-enhanced antioxidative activity in scavenging free radicals. The developed nanoneedles displayed significant selectivity in their cytotoxicity towards different cell lines and effectively induced anticancer activity by causing mitochondrial dysfunction. Moreover, the injection of blue Te nanoneedles into mouse tumors enables the detection of tumors using thermal/photoacoustic imaging techniques. When employed in synergistic thermo-chemotherapy (TCT), these nano-needles exhibit satisfactory therapeutic effects, surpassing the limited efficacy observed with treatment by Te alone. Consequently, these blue Te nanoneedles hold promise as an innovative theranostic nanoagent, facilitating simultaneous multimodal imaging and synergistic TCT for various tumor types, which could enhance the efficiency of cancer treatment and reduce the adverse effects [150].

There are further increased benefits in the synergistic therapy of PDT with CT due to the mechanism of action that destroys cell cancer and along with the effect on blood vessels at the cancer tissue site [151]. Song, J. *et al*. demonstrated the positive efficacy of synergistic chemo-photothermal therapy (CPTT) for treating melanoma *in vitro*. The researchers combined near-infrared (NIR) laser irradiation with free DOX to induce cytotoxicity in branched nanoporous gold nanoshells (BAuNSP) and generated DOX-loaded BAuNSPs (BAuNSP–DOX). *In vitro* experiments showed a significant increase in overall toxicity with this combination. For instance, when DOX was used alone at a concentration of 1.6 μg/ml, it inhibited cell growth by 39%. Surprisingly, when both DOX and laser irradiation were applied, cell viability remained similar to DOX treatment alone. However, upon NIR laser irradiation following the addition of BAuNSP-DOX to the cell culture medium, heating was induced, resulting in a remarkable cell growth inhibition of 83.5% at the same DOX concentration. Notably, for non-irradiated U87MG cells, the rate of cell death caused by BAuNSP-DOX was almost negligible, indicating that no DOX was released without NIR laser irradiation [152].

Chemo-photothermal cancer therapy additionally leads to outstanding photothermal results and regulated drug release, showing marked synergistic outcomes in destroying skin carcinoma cells in both *vitro* and *vivo* testing. In a study conducted by Yu, Q. *et al*. a scaffold incorporating copper silicate hollow microspheres (CSO HMSs) was fabricated for drug-loaded (Trametinib) photothermal agents (PTAs) to treat MM, as well as for localized wound recovery. The drug-loaded CSO HMSs, referred to as Tra-CSO HMSs, were incorporated into a poly(ε-caprolactone)/poly(D,L-lactic acid) (PP) template using an electrospinning technique to form Tra-CSO-PP scaffolds. Subsequently, the matrix was subjected to laser

irradiation for 1, 2, and 3 times, at 808 nm and 45 °C for 15 minutes. The experimental results demonstrated that after irradiation the viability of B16F10 cells in the Tra-CSO-PP + Laser group significantly decreased to approximately 40.9%, 14.0%, and 0.1%, respectively. In contrast, in the PP group's cell viability showed no significant difference with increasing irradiation times. The findings demonstrated that the Tra-CSO-PP scaffolds, which combined drug release and hyperthermia induced through PDT, resulted in the highest mortality rate among all tumor cell groups. Further *in vivo* studies were conducted with the view that the tumor cells could be entirely eradicated with single PT at power intensity of 0.85 W/cm_2 [153]. In conclusion, this study indicated the exceptional potential of CPTT effectiveness both *in vitro* and *in vivo* for the treatment of MM.

In another study by Meng *et al*., CT and near-infrared photoacoustic imaging and therapy (NIR-PAT) was investigated using MEO2MA@MEO2MA-co-OEGMA-CuS-DOX (G-CuS-DOX) nanocapsules which demonstrated the ability to increase tumor temperatures from 37 °C to 57 °C via photothermal effects when irradiated with a 915-nm laser (Figure 3.2). It was noted that once the temperature elevated over 42 °C, the PTT of G-CuS-DOX was activated, raising temperatures further, resulting in volume shrinkage of G-CuS-DOX *in vivo*, with a controlled release of the anticancer CT DOX achieved. It was further noted, that in case the NIR laser was turned off, both therapy effects were immediately interrupted [154].

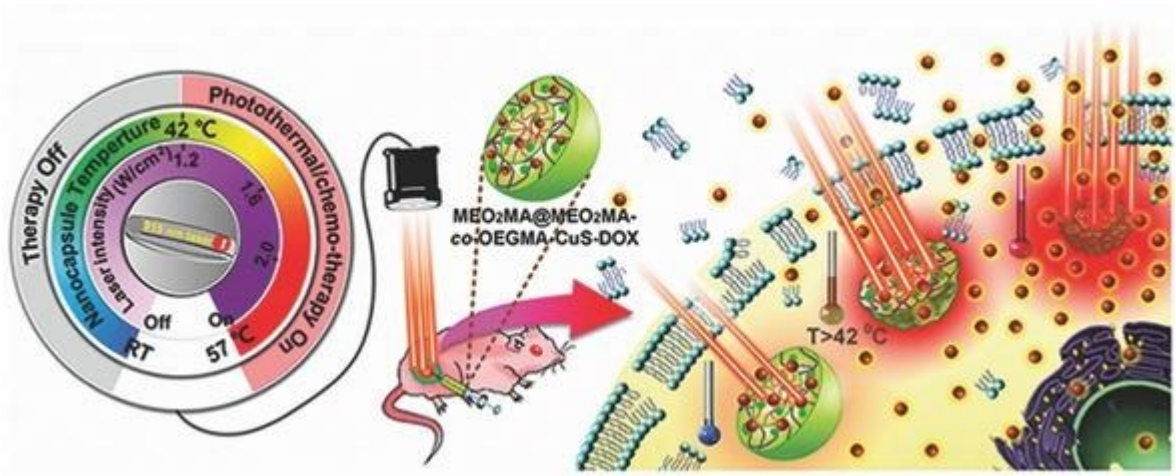


Figure 3.2: The experimental setup for the combination of (PT) with CT in an *in vivo* setting using MEO2MA@MEO2MA-co-OEGMA-CuS-DOX (G-CuS-DOX) NPs. This figure illustrates the experimental arrangement designed by Meng *et al*. for evaluating the synergistic effects of PTT and CT using G-CuS-DOX NP s in a live animal model. Reproduced with permission from Meng *et al.* [154].

3.2.2.2 Immunotherapy

The synergistic combination of CT with immunotherapy heightens the therapeutic potential of CT alone by generating inflammation and cell death, thereby leading to an increased immune response without metastasis [155, 156]. This hypothesis was tested by van der Most *et al*. where CT was combined with immunotherapy targeting the antigen-presenting cell (APC) by stimulating the CD40 molecule, which mimics a robust CD4+ T helper response and activates antigen-presenting cells to activate CD8+ T cells. The researchers discovered that APC-directed immunotherapy did not provide any survival benefits when administered before CT. Nevertheless, when this immunotherapy was administered after CT, an unprecedented 80% of the experimental animals were cured. The use of CT with immunotherapy was further explored in a clinical trial on patients with metastatic melanoma who underwent lymphodepleting CT, followed by the transfer of *in vitro* expanded tumor-specific CD8+ T cells. This treatment approach elicited notable clinical effects in 18 out of 35 patients, including those with large tumors, leading to tumor regression. Importantly, these responses were linked to a high frequency of tumor-specific T cells found in the blood of these patients [157]. Significantly, the therapeutic effects of CT have been obtained when combined with immunotherapy (checkpoint inhibitors) for metastasis MM [158, 159]. The explanation for the double-combined system is that CT can debulk the primary cancer tissue, whilst immunotherapy has the potential to completely destroy disseminated cancer by altering the response of the immune system [160].

According to Lao *et al.'s* research, the concept of using effective chemotherapies in the adjuvant setting has persisted and has led to better outcomes in terms of RFS and OS for various types of cancers [63]. However, Simon and Norton highlighted in 2006 that as new therapies are being introduced, tumor modeling and clinical trial design would need to evolve as well [63]. Luke *et al.* demonstrated that the most used agents in combination with CT were INF-α and IL-2. These agents were administered alongside various CT cocktails in different treatment schedules, but the results were not as promising as anticipated. Although they often led to improved response rates ranging from 27% to 64%, more than 10 chemoimmunotherapy regimens were compared to CT, with none demonstrating a significant improvement in OS compared to dacarbazine alone. Moreover, the addition of immunotherapy to CT, particularly combination CT, increased toxicity, makes it challenging to justify the improvement in response rate. Despite several attempts to address this issue, no successful strategies have been identified. Some experts further argue that reducing the dose of immunologics, specifically IL-2, to make it more tolerable with CT renders them ineffective. According to this hypothesis, the effectiveness of high-dose IL-2 treatment is dose-dependent, and when combined with CT, it becomes difficult to reach the critical dose

threshold necessary for its therapeutic advantage in selected patients. Some data supports this reasoning, as patients who did not respond to prior chemoimmunotherapy regimens have shown responses to high-dose IL-2 treatment [161]. Table 3.1 provides for some of the synergistic combinations of CI with immunotherapy approved by FDA.

Table 3.1: Showcases the Collaborative Pairings of CI w immunotherapy h FDA-approved IT for the Effective Treatment of Various Skin Cancer Variants. Adapted from Nikolaou *et al.* [162].

Category	Drug	Type of Cancer	Doses
CTLA-4	Ipilimumab	Metastatic melanoma	3 mg/kg every 3 weeks for a maximum of 4 doses
		Adjuvant therapy for melanoma stage III (TNM)	10 mg/kg every 3 weeks for 4 doses, followed by 10 mg/kg every 12 weeks for up to 3 years
PD-1	Nivolumab	Adjuvant therapy for melanoma stage III	240 mg (flat dose) once every 2 weeks or 480 mg (flat dose) once every 4 weeks until disease recurrence or unacceptable toxicity for up to 1 year
	Pembrolizumab	Metastatic melanoma	200 mg once every 3 weeks
PD-L1	Avelumab	Merkel cell carcinoma	10 mg/kg once every 2 weeks
CTLA-4 + PD-1	Ipilimumab + nivolumab	Metastatic melanoma	Nivolumab (1 mg/kg every 3 weeks) plus ipilimumab (3 mg/kg every 3 weeks for 4 doses) followed by nivolumab 3 mg/kg every 2 weeks

Abbreviations: FDA, Food and Drug Administration; CTLA-4, cytotoxic T lymphocyte-associated protein 4; TNM, tumor, node, and metastases; PDL-1, programmed death-ligand 1.

3.2.2.3 Hyperthermia Therapy

CT drugs which have a shortage of specificity toward tumors and can cause severe side effects in patients due to their high toxicity. A combination strategy of CT with HTT, however, has been noted to be the most suitable to decrease tumor proliferation [163-165]. In the study by Baronzio *et al*. [142] it was demonstrated that combining HTT with CT drugs can increase CT efficiency through three mechanisms, which mostly result in an additive effect that becomes more pronounced at higher temperatures. The study utilized a potent combination, as detailed in Table 3.2 that targeted whole types of cells found within the

tumor site, encompassing hypoxic, oxygenated, and cells of an acidic microenvironment. This finding has been supported by various studies over the last few decades, which have shown that when CT drugs are used in combination with HTT, they exhibit three different types of behavior. The first type is characterized by drugs that slightly increase their activity with temperature, such as Carmustine, Thio-TEPA, methyl-CCNU and lomustine, while the second type involves drugs that become more effective at temperatures above 42°C, such as Bleomycin. The third type involves drugs, as seen with Amphotericin B, which are inactive CT agents at body temperatures but become more effective when temperatures reach 42°C [142].

Table 3.2: Possible Association of CT with HT and Possible Potentiation of Drugs by HT on Oxygenated, Hypoxic and pH Reproduced from Baronzio *et al.* [142].

Chemotherapy	HT	Oxygenated Cells	Hypoxic Cells	pH ≤ 7
Adriamycin	↑ ↑	↑↑	ND	ND
Cyclophosphamide	↑↑	↑↑	ND	ND
Bleomycin	↑↑↑	↑↑	↑↑↑	↑↑↑
Mitomycin –C	↑↑	↑↑↑	↑↑↑	↑↑↑
BCNU/TMZ	↑↑	↑	↑↑	↑↑
Carboplatin	↑↑	↑	↑↑↑	↑
Vincristine	↑	↑	ND	ND
Methotrexate	↑	↑	ND	ND
5FU	↑	↑	ND	ND

ND: not determined; ↑: association strength, BCNU/TMZ: Carmustine (bischloroethylnitrosourea)/ Temozolomide.

Cheng *et al.* further studied the potential benefits of combining HTT with CT agents to increase the effectiveness of drug cytotoxicity. They found that artificially raising the temperature of the tumor tissue can enhance the fluidity of the phospholipid bilayer in cancer cells, making it easier for drugs to permeate. Additionally, the cell membrane structure changes, leading to a decrease in viscosity, which improves cellular uptake of drugs in the tumor tissue. Overall, the combination of HTT and CT agents may result in improved drug efficacy in skin cancer treatment [146].

In another study by Issels *et al*. which focused on neo-adjuvant CT, a total of 341 patients

were randomly distributed into two groups, with 169 patients receiving ifosfamide, etoposide and (EIA) doxorubicin, while the rest were given EIA in combination with RHT. All patients were part of the primary endpoint analysis, and the safety assessment comprised of 332 patients who were administered at minimum of a single cycle of CT, following a median follow-up of 34 months (with an interquartile range of 20-67). The results noted 132 patients experienced local progression, with 56 patients from the EIA plus RHT group and 76 from the EIA-alone group. The relative hazard (RH) of experiencing local progression or death was significantly lower in the EIA plus regional HT group compared to the EIA-alone group (RH 0.58, 95% CI 0.41-0.83; p=0.003), resulting in a 15% absolute difference in local progression-free survival (LPFS) at 2 years (95% CI 6-26; 76% for EIA plus regional HT vs. 61% for EIA). The relative hazard for DFS was also favorable for the EIA plus RHT group (RH 0.70, 95% CI 0.54-0.92, p=0.011) compared to the EIA-alone group. Furthermore, the treatment response rate was significantly higher in the EIA plus RHT category (28.8%) compared to the CT-alone category (12.7%, p=0.002). In a pre-specified per-protocol investigation among patients carried out, EIA plus RHT induction therapy compared to those who received EIA alone, the OS was superior in the category that received combined treatment, with a hazard ratio (HR) of 0.66, a 95% CI of 0.45-0.98, and a p-value of 0.038. Additionally, the incidence of leucopenia class 3 or 4 was higher in the EIA plus RHT category compared to the EIA-alone category (128 out of 165 vs. 106 out of 167, p=0.005) [166].

3.2.2.4 Extracorporeal photopheresis (ECP)

The synergistic therapy of ECP with CT in treatment of skin cancer such as Mycosis Fungoides (MF) and Sézary syndrome (SS) utilized significant outcomes as reported by Ninosu N *et al*. . The mechanism of action of ECP in cutaneous T-cell lymphoma (CTCL) is believed to be a result of 8-MOP covalently binding to DNA in separated leukocytes, causing cell cycle arrest and apoptosis. The apoptotic leukocytes are reintroduced into the peripheral circulation, where antigen-presenting cells phagocytose them, leading to the generation of specific tumor suppressor cells against malignant lymphocytes [167]. Bexarotene, a chemotherapy drug, inhibits the growth of cancerous T-cells [168], and methotrexate can be considered as an alternative. ECP is also recommended as a combination therapy with total skin electron therapy, bexarotene, and methotrexate. The diverse range of available combinations highlights the relative safety and tolerability of ECP [119, 169].

3.2.3 Synergistic Phototherapy

PTT depends on oxygen therapy that converts an external NIR light source into HTT, which can deliver a significant impact on tumor development with fewer adverse effects [170, 171].

While PDT radical oxygen is a common anti-tumor intervention that has been used alone or in a combinative strategy, PSs have an effective action on different forms of cancers. The mechanism of PDT to damage and kill cancer cells therefore depends on a dual response to light energy and a PS [124]. The main sources are lasers and incandescent light, which give the same effect applied to PDT [172], while PSs are administered to the body, topically, intravenously, or orally. In brief, PSs in carcinoma therapy depend on the type of tumor tissue, and the depth of light of a long wavelength used, such as NIR and red light [173]. In contrast, PDT is a good choice for the treatment of non-pigment skin cancers as a monotherapy (NMSC) because of its excellent selectivity to tumor tissues, meanwhile it is more effective in a synergistic combination for the treatment of pigmented melanoma [80, 174].

3.2.3.1 Immunotherapy

Photothermal immunotherapy (PTIT) is a novel strategy merging PTT with immunotherapy. This strategy has been noted to have a highly beneficial action, especially on primary tumors and is also effective in advanced and metastatic melanoma [175]. This treatment protocol was studied by Qi *et al*. that proposed personalized cancer therapy through an adjuvant intratumoral injection of an immunostimulant called N-dihydrogalactochitosan (GC) in synergism with local PTT, known as Laser Immunotherapy (LIT) [167]. The adjuvant treatment resulted in the generation of triggered systemic antitumor immunity involving neutrophils. This practical method was used for creating lasting immune memory in solid malignant tumors to prevent the recurrence and metastasis of tumors. Additionally, combining LIT with a checkpoint inhibitor was found to enhance the therapy's effectiveness in preventing the recurrence and metastasis of melanoma.

GC further demonstrated the ability to stimulate immature dendritic cells (DCs) in laboratory settings and recruit T cells *in vivo* to eradicate tumors cells when combined with laser irradiation [176]. LIT was utilized in the treatment of variant tumor template, employing different cell lines as A431 cancer cells derived from cSCC. Moreover, preliminary clinical trials have employed LIT to treat patients with melanoma cancer. Melanoma-bearing mice were in this study subjected to an intratumoral injection of GC, followed by local irradiation using a 980-nm laser after a 2-hour interval. The researchers then conducted immune assays and intravital imaging to examine the timelines of antitumor immune responses in the primary treated tumors, TDLNs (tumor-draining lymph nodes), and rechallenged tumors after laser LIT. Combining LIT with PTT led to a significant recruitment of neutrophils to the treated tumors during the early stages of LIT. This acceleration contributed to the cohort of a whole-cell vaccine, triggering a systemic anti-tumor immune response. Furthermore, the

combination approach of LIT with checkpoint blockade resulted in a reduction of PD-L1 expression on tumor cells [167].

3.2.3.2 Nanomaterials Therapy

In recent years, there has been growing interest in the biomedical field regarding the application of nanomaterials, particularly in areas such as drug delivery, tissue engineering, diagnosis, and theragnostics. For the specific context of nanomaterials used in skin cancer photoimmunotherapy, the primary categories include metallic, polymeric, lipid-based, and 2D nanomaterials, as depicted in Figure 3.3 [177]. In addition, Nag *et al.* developed an intriguing nanosystem, known as a hybrid nanomaterial, has shown promise as a synergistic nanosystem in conjunction with PTT. This nanosystem involves combining two or more organic or inorganic components [178]. Targeted drug delivery, a promising and advanced system, is commonly utilized for the efficient delivery of drugs to specific sites. This approach not only reduces drug dosage but also prevents damage to non-targeted tissues [179]. Moreover, inorganic nanomaterials facilitate supplementary treatment modalities like hyperthermal ablation and enhancement of radiotherapy, due to their distinctive magnetic and photoelectric properties. Hence, inorganic nanocarriers can facilitate combinatorial antitumor therapies not only by concurrently delivering various therapeutics but also by leveraging their inherent properties to harness external energy for therapeutic advantages [126].

The utilization of photoresponsive nanomaterials, combined with near-infrared (NIR) light irradiation, has demonstrated the ability to induce hyperthermia and trigger tumor cell death. However, many photoresponsive nanomaterials are typically composed of inorganic metals (e.g., gold nanomaterials), carbon-based materials, or light-absorbing organic molecules [180]. In contrast, Kato *et al.* demonstrated NIR-PIT (Illuminox™) has exhibited selective cytotoxicity against target cells through a photo-induced ligand release reaction, as opposed to relying on reactive oxygen species (ROS), following the systemic intravenous injection of IR700-based antibody–photoabsorber conjugates. Furthermore, NIR-PIT represents a hybrid therapy involving direct cancer cell killing induced by NIR light exposure, coupled with a rational immune activation. Therefore, NIR-PIT differs significantly from traditional "photoimmunotherapy" and is now defined as Illuminox™ [181].

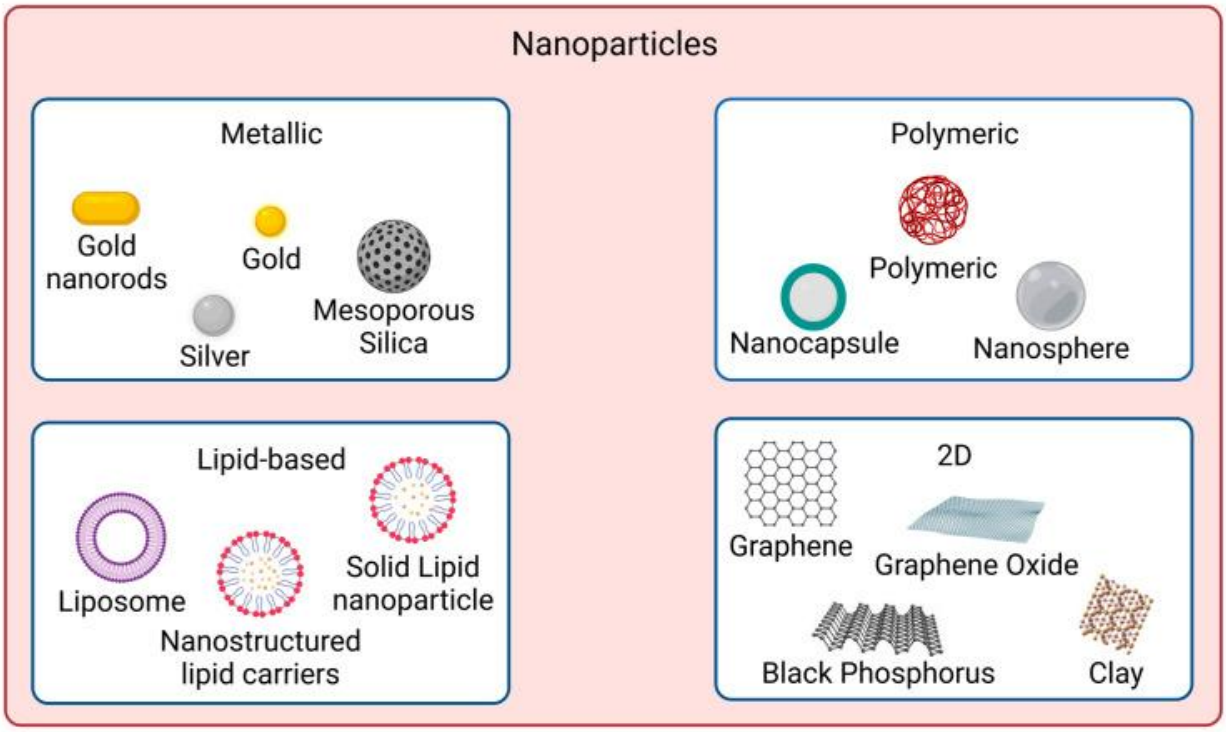


Figure 3.3: illustrates the types of nanomaterials employed in photoimmunotherapy for skin cancer. The primary categories include metallic, polymeric, lipid-based, and 2D NPs. This schematic illustration presents the major classifications of NPs employed in photoimmunotherapy, highlighting their structural diversity and functional potential in advanced cancer therapeutics, particularly for skin malignancies. The figure categorizes NPs into four main groups based on their composition and morphology. Reproduced with permission from Relvas *et al.* [177].

The combination of HTT and PDT is increasingly being used in cancer treatment due to their relatively lower adverse effects compared to CT or RT. The effectiveness of these therapies depends greatly on the dosage administered. Compared to conventional methods, PDT and HTT are less toxic, less harmful, and more secure, offering many advantages such as selectivity, precision, increased blood flow in tumors, targeting, and more [182]. Magnetic hyperthermia (MHT) NPs with PTT is an example, which showed a strong effect compared to other synergistic methods on melanoma as well as other types of cancers [183]. The results of this study highlighted the importance of exploring neglected strategies such as PDT and HTT in the fight against cancer and provided new perspectives for the development of improved cancer treatment strategies. Spyratou *et al*. further demonstrated that PTT when applied through the photon energy of laser-activated photo absorbers generated enough thermal energy to kill cancer cells. Furthermore, HTT showed good results when used with radiofrequency, microwave, ultrasound, and laser [110].

3.2.4 Hyperthermic Interventions

HTT is the induction of high temperature on the tumor target cells from 39-45 °C, which has

evolved into a viable technique for cancer therapy. The mechanism of HT to kill cancer cells is by changing the metabolism of tumor cells, inducing apoptosis, leading to activation of an immune response [184]. HTT can further be used to kill tumor tissue depending on the side and method of administration such as (local, regional, and whole-body HT) [146]. The primary methods for NP-induced HTT include excitation with light, magnetic domains, or radiofrequency radiation [185]. Thus, these methods have been used depending on specific NPs applied by a certain route of administration on the cancer site tumor, under an external stimulus to induce localized HTT [186]. Meanwhile, the intensity of HTT depends on the strength of the stimuli, which can be difficult clinically, or the use of a rather extensive dosage of NPs [187]. In contrast to *in vitro* conditions, where protein denaturation and DNA damage occur directly due to heat exposure, the dissipation of heat *in vivo* is influenced by various factors such as blood tissue density, tissue thermal conductivity, the temperature of the heat source and tissue-specific heat [17]. As shown in Figure 3.4, the tumor's surrounding vasculature is thick and irregular, creating an acidic microenvironment that provides nutrients for rapid tumor growth, unlike close healthy cells. By raising the surrounding temperature, blood flow to the tumor tissue increases, causing the compact vasculature to rupture, thereby obstructing nutrient supply to growing cells and ultimately leading to kill the cells. Conversely, organized vasculature in healthy tissue enables it to effectively regulate its temperature by dissipating heat, resulting in no observed irreversible damage to healthy cells [17].

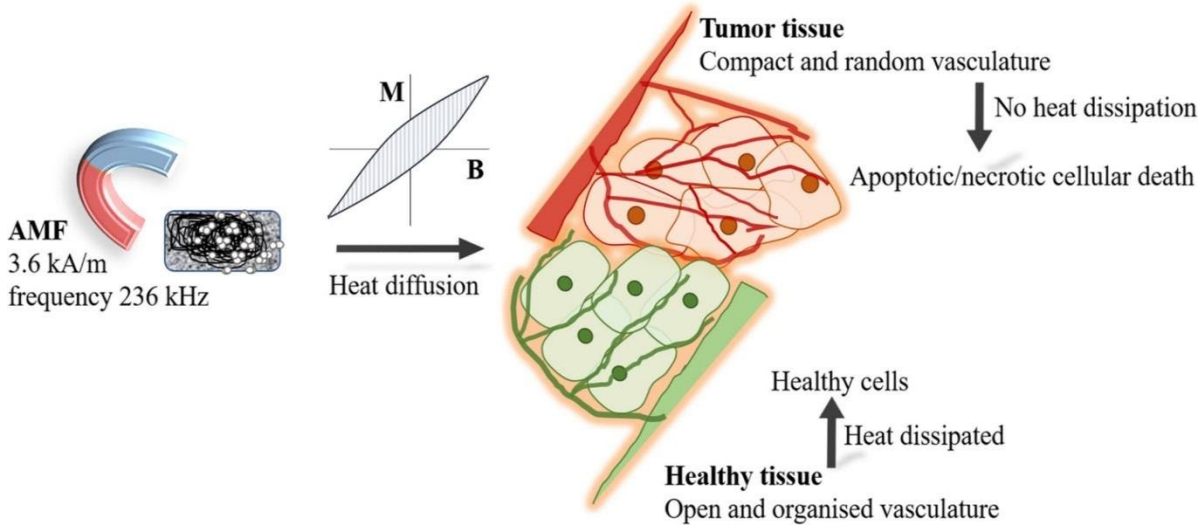


Figure 3.4: A schematic representation of the mechanism of heating and cellular at elevated temperature in the presence of an alternating magnetic field (AMF). This illustration demonstrates the fundamental mechanism by which magnetic NPs, typically iron oxide-based (e.g., Fe_3O_4), generate localized heat within tumor tissues upon exposure to an external AMF. When subjected to AMF, these NPs undergo relaxation processes—Néel and Brownian relaxation—leading to the dissipation of energy in the form of heat. Reproduced with permission from Suneet *et al.* [17].

Previous studies have confirmed that the negative effects of an acidic and hypoxic environment on CT and RT do not seem to affect HTT, which exhibits an excellent effect, particularly on cells experiencing acute hypoxia as opposed to those under chronic hypoxia. Additionally, research has demonstrated that heat sensitivity is increased in the presence of metabolic states and energy deprivation. In another study, it was further suggested that the use of HT in combination with Trans Arterial Chemoembolization (TACE) is more effective due to changes in membrane composition [142]. Clinical trials utilizing appropriate statistical methods have also investigated the safety and efficacy of therapeutic approaches for a specific disease. Multiple studies have been conducted on HT using radiofrequency (RF) and microwave (MW) methods, as well as oncothermia. It is crucial to acknowledge that the available data is not comprehensive, which consists of a compilation of findings demonstrated by various researchers. Upon analyzing these results, it becomes evident that HTT serves as an additive treatment method, as its standalone effectiveness is comparatively lower. While a few successful cases have been reported, they appear to be isolated instances or fortunate outcomes. In the context of treating MM, specifically considering tumor histology, a total of 19 patients were involved in a research study by Baronzio *et al*. The results obtained indicate a complete response (CR) rate of 21% and OR rate of 32% when HTT was combined with RT. Moreover, this combined approach demonstrated an increase in OS [142]. Additionally, this study provided a comparison of the effects of HT, RT, CT, and immunotherapy on several cells and tumor structures, as described in Table 3.3.

Table 3.3: Comparison of the Effects of HT, Radiotherapy, Chemotherapy, and Immunotherapy, on Several Cells and Tumor Structures. Reproduced with permission from Baronzio *et al.* [142].

Tumor Structure Cells Affected	Chemotherapy	Radiotherapy	HT	Immunotherapy
Oxygenated Cells	+++	+++	+++	+++
Hypoxic cell	+ -	- - -	+++	++
Vascular Structure	+	++	+++	+ -
Stroma	+	+	++	++
Microcirculation	-	+	++	+

3.2.4.1 Immunotherapy

Researchers have been widely interested in immunotherapy over the last few years, with research undertaken on its mechanism and ability to activate the body's innate protection to

determine, kill, and or destroy cancer cells. HTT has resultantly been applied to activate an immune response against cancer cells [183, 188]. Crucially, HTT has the ability to generate an immunogenic tumor microenvironment (TME), significantly enhancing cancer cell immunotherapy. According to recent studies, there are now two advanced types of highly effective systemic therapeutic agents that are widely used in clinical practice. These include immunotherapies, such as programmed death (1PD-1), checkpoint inhibitors targeting or/and cytotoxic T lymphocyte antigen (4CTLA-4). These treatments amplify the inherent immune response against tumors and also target specific molecules involved in tumor growth and progression, such as (BRAF) inhibitors (B-Raf proto-oncogene, serine/threonine kinase), either alone or in combination with mitogen-activated protein kinase-kinase (MEK inhibitors), which have been used to treat approximately 40%-50% of individuals affected with BRAF V600-mutant melanoma.

Previous studies have emphasized the significance of temperature in enhancing the effectiveness of immunotherapy. The mounting evidence indicates that hypoxia in tumors contributes to an immunosuppressive tumor microenvironment. Hence, it becomes essential to leverage the potential of heat in modulating tumor tissue reoxygenation when combining it with immunotherapy. Moreover, raising the temperature can provoke a significant immune response to the tumor tissue. Immune checkpoint inhibitors (ICIs) are a promising new treatment for cancer, but they can also cause serious side effects. In one study, in individuals who were diagnosed with advanced melanoma, and treated with ipilimumab and nivolumab, 96.8% experienced immune-related adverse events (irAEs), with 59% of them being grade 3 or grade 4 irAEs. These irAEs can pose life-threatening risks and may lead to discontinuation of treatment. However, a retrospective trial of 131 stage IV melanoma patients revealed that the addition of systemic or local HTT significantly reduced the incidence of grade 3 and grade 4 irAEs to 6.11% and 2.29%, respectively. This indicates that mild HTT combined with ICIs is a safer approach compared to ICIs alone [189]. In another prospective phase I clinical trial, the combination of HTT with anti-PD-1 treatment and adoptive cell therapy (ACT) demonstrated safety and feasibility. Additionally, this therapeutic combination led to an enrichment of the T-cell receptor (TCR) library among the clinical immune responders and induced favorable changes in serum levels of IL-2, IL-4, TNF-α, and IFN-γ. These findings suggest that HTT may be a safe and effective way to reduce the risk of serious side effects associated with ICI therapy. More research is, however, needed to corroborate these findings and to determine the optimal dose and schedule of HTT for the treatment of cancer [190].

3.2.5 Immunotherapy Interventions

Immunotherapy utilizing IFNα demonstrates immunomodulatory effects, including the stimulation of major histocompatibility complex class I expression in melanoma and immune cells, inhibition of melanoma cell proliferation, and induction of proapoptotic effects, dose-dependently [137]. In 1995, IFNα-2b became the first agent to receive FDA approval for adjuvant therapy, demonstrating its efficacy in reducing disease recurrence and mortality in high-risk patients. Although interleukin-2 (IL-2) was the initial immunotherapy approved for advanced metastatic melanoma, its widespread use was hindered by substantial toxicity [191]. Knight *et al*. reported that in 2011, ipilimumab, the first CTLA-4 immune checkpoint inhibitor, received approval for the treatment of advanced, inoperable metastatic melanoma. Since then, it has also been approved for adjuvant therapy in high-risk, node-metastatic resected melanoma. Additionally, monoclonal antibodies targeting programmed cell death protein 1 (PD-1), such as pembrolizumab and nivolumab, have been approved for both metastatic and adjuvant settings. In March 2022, a combination of the anti-LAG-3 monoclonal antibody, relatlimab, in a fixed-dose combination with nivolumab, received approval for the treatment of metastatic melanoma. Figure 3.5 illustrates the timeline of these approvals [192].

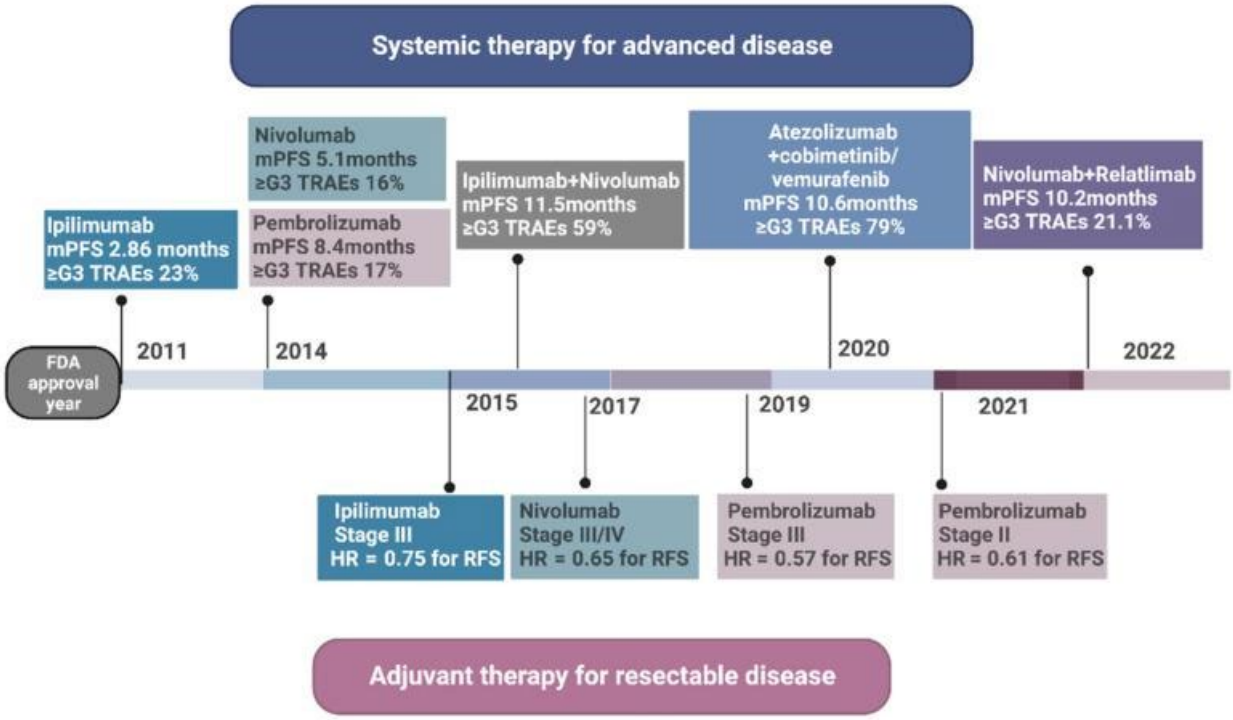


Figure 3.5: Management of melanoma with FDA-approved immunotherapy agents. This figure provides a comprehensive schematic of the current immunotherapeutic strategies approved by the U.S.FDA for the treatment of melanoma, particularly advanced and metastatic forms. These therapeutic agents are primarily immune checkpoint inhibitors that enhance the body's antitumor immune response by targeting regulatory pathways in T-cell

activation and exhaustion. Reproduced with permission from Knight *et al*. [192].

3.2.5.1 Extracorporeal photopheresis

ECP in combination with immunotherapy additionally stands out as an effective treatment protocol for conditions such as cutaneous T-cell lymphoma and SS [193, 194]. ECP involves a cell-based immuno-modulatory therapy that includes the separation of leucocyte-rich plasma, followed by ex-vivo administration of a photosensitizer and UVA radiation before re-infusion. The European Organisation for the Treatment and Research in Cancer (EORTC) mycosis fungoides/Sézary Guidelines recommend ECP as therapy for erythrodermic CTCL [195]. Excellent responses are reported in those with SS when treated with a combination of IFNα and ECP [119]. ECP is suggested as a first-line single agent in SS and a treatment option with IFNα, showcasing high efficacy with response rates reaching up to 80%, particularly in those with a high tumor burden. Immunomodulatory therapies, including ECP and IFN-α, may lead to durable remissions, as observed in anecdotal cases. These findings, coupled with the substantial expression of PD-L1 in a minority of patients, strongly support the rationale for checkpoint blockade (CPB) in CTCL [196].

3.2.6 Multicomponent Non-Surgical Combination Therapies

Multifunctional therapies have been widely used in recent research in the treatment of cancer compared to conventional methods to improve safety, and effective drug delivery systems [197]. Multicomponent combination is an interesting protocol in anticancer research focused on overcoming unwanted effects, relapses, and metastasis. In MM treatment, the current research indicates that the concomitant use of multi-component combinations may provide more effective treatment and prevention of relapses [136]. In a study conducted for the treatment of skin cancer using multicomponent combinations, an important synergy, known as trimodality therapy, between RT, CT, and HT. The local control of the tumor, in fact, built on the order in which the treatments was administered, for Bleomycin, HT, and RT. Baronzio *et al.* further demonstrated that combining Bleomycin with HT increases its toxicity to hypoxic cells, and the most effective sequence to achieve a stronger killing effect is administering Bleomycin first, followed by HT, and then RT. Choosing the correct sequence not only improves the local control of the tumor and reduces adverse effects but may also impact the immune response. The right sequence trimodality therapy could also control many suppressive cells and decrease the suppressive arm of immunity [136]. In another recent study by Datta *et al.* [144] positive clinical outcomes were observed in various tumor sites with the use of TRT or thermoradiochemotherapy. Furthermore, HTT was safely used with low or moderate doses of reirradiation for retreatment of previously treated and recurrent tumors, resulting in significant tumor regression. In this evaluation, the response

rate was 71% (17 out of 24 patients), and a total of 16 centers participated. Recently, HTT was introduced for the treatment of skin cancers in multi-strategic therapies via various combined techniques. One such study looked at metallic nanostructures, which destroyed skin cancer cells and then transformed light energy into HTT via a PTT method. The effectiveness of the PTT was improved by combining gold and other metallic NPs with RT using protons and other ions [110].

3.3 Conclusion

Combination therapy for skin cancer has the potential to be a valuable addition in broadening the number of patients benefiting from treatment strategies. The ultimate objective of such a strategy is to develop a more potent dual or trimodality therapy, possibly involving multiple components, to achieve greater anti-tumor efficacy and effectively prevent tumor recurrence and metastasis. Nevertheless, while combination therapy offers several advantages, there are still several issues that require careful consideration. Furthermore, the treatment of skin cancer has made significant progress with the discovery of synergistic oncology treatments. This has led to several revolutionary therapeutic advances, which have improved the standard of care. Therefore, the use of rationale-based combinatorial strategies is crucial for overcoming resistance, interactions, and achieving a long-term response.

Non-surgical synergistic interventions therefore offer several advantages over surgical approaches combined with conventional therapies in the treatment of MM and skin cancer. These non-invasive treatments reduce the risks and complications associated with surgery while offering greater flexibility in tailoring therapies to individual patients. Combination therapy for skin cancer, especially non-surgical options, holds immense potential in expanding the number of patients who can benefit from comprehensive treatment strategies.

In conclusion, Chapters 2 and 3 have explored the various treatment modalities for skin cancer, highlighting both surgical and non-surgical approaches, including the integration of nanotechnology and combination therapies. While these strategies offer promising avenues for enhanced therapeutic outcomes, it is imperative to acknowledge the current limitations and challenges associated with these approaches. The concurrent use of multiple therapeutic agents can lead to overlapping toxicities, potentially exacerbating adverse effects compared to monotherapies. This necessitates careful selection and dosing of agents to balance efficacy with patient safety.

Implementing combination therapies often involve complex protocols, which can pose challenges in clinical management and patient adherence. While not all therapeutic

combinations result in synergistic effects; some may exhibit antagonism, reducing overall treatment efficacy. Robust preclinical evaluations are therefore essential to identify and mitigate such interactions. Ensuring that NPs effectively reach and penetrate tumor tissues remains a significant hurdle, while factors such as the tumor microenvironment and biological barriers can impede targeted delivery. Additionally, the long-term effects and safety profiles of various nanomaterials are not yet fully understood. There is a risk of unforeseen toxicities, and extensive research is required to establish their biocompatibility. Additionally, producing NPs with consistent quality and functionality on a large scale presents technical and economic challenges, potentially hindering widespread clinical application.

Addressing these limitations is crucial for the advancement and successful integration of these innovative therapies into standard skin cancer treatment protocols. Ongoing research, clinical trials, and interdisciplinary collaborations are essential to overcome these challenges and realize the full potential of combination and nanotechnology-based therapies in improving patient outcomes. Building on this and the mentioned potential of alternate interventions for skin cancer treatment, the next chapter explores the development of non-surgical, multicomponent platforms that enable dual or multi-release mechanisms within a single system for treating skin cancer. These advanced systems are designed to enhance anti-tumor efficacy and effectively prevent tumor recurrence and metastasis. By synthesizing such platforms, this study aims to present innovative strategies for addressing the complexities of skin cancer treatment, offering a multifaceted solution that aligns with the transformative advancements that have been reviewed.

CHAPTER 4

SYNTHESIS OF CURCUMIN-FUNCTIONALIZED IRON OXIDE NANOCOMPLEX SYSTEM FOR THE TREATMENT OF SKIN CANCER

4.1 Introduction

Through the extensive evaluation of the currently utilized non-surgical synergistic interventions for the treatment of skin cancer, as provided in Chapter 3, it can be concluded that these regimens present significant promise in enhancing therapeutic outcomes for skin cancer, particularly through their potential to improve patient responses, reduce treatment-related complications, and minimize the risk of recurrence and metastasis. These findings emphasized that a combinative, non-invasive strategy might address some of the limitations associated with surgical interventions, thereby broadening the spectrum of effective treatment options available for skin cancer patients, especially those with MM.

As addressed in previous chapters, skin cancer ranks among the most prevalent diseases worldwide, prompting the utilization of various treatment approaches alongside the ongoing search for novel strategies to enhance treatment of the condition and prevent its recurrence. The existing approach for treating thicker MM (≥ 1 mm) involves surgical intervention, often followed by RT. Existing conventional treatment therapies fall short of achieving the desired therapeutic efficacy primarily because of a notable drug resistance phenomenon. These treatments, characterized by their inability to completely cure ailments, also inflict considerable adverse effects on patients. Additionally, the efficacy of current conventional is disadvantages due to their lack of precision in targeting drugs, resulting in unfocused actions. Moreover, these treatments frequently impact healthy cells, inducing unintended toxicity [198, 199]. To overcome the shortfalls of traditional treatment monotherapies, recently, the use of multiple therapeutic agents in combination, known as combination therapy, has gained significant attention as a means of enhancing efficacy and minimizing side effects. For example, in certain cases, RT is combined with CT or immunotherapy utilizing checkpoint blockade to address both NMSC and MM [19].

In recent years, the use of metal NPs and Cur -based therapies has also been explored to fill critical gaps in the current treatment landscape. Metal NPs, known for their unique physical and chemical properties, such as high surface reactivity and ability to generate reactive oxygen species (ROS), have demonstrated significant potential as targeted delivery systems and therapeutic agents for cancer. These NPs can be engineered to enhance the selectivity

and bioavailability of anticancer compounds, providing a robust platform for treating aggressive skin cancers with greater precision. Additionally, metal NPs facilitate controlled drug release, improve tumor penetration, and can be functionalized for multimodal imaging and therapy, making them highly versatile in oncological applications [200, 201].

Resultantly, FeONPs have garnered significant attention due to their uncomplex synthesis processes and low toxicity when appropriately functionalized [24]. FeONPs have additionally shown potential in various applications such as ferrofluids, hyperthermia treatment, magnetic resonance imaging (MRI), high-density information storage, and targeted drug delivery labeling, often achieved through appropriate surface modification [202]. These surface-altered FeONPs, carrying functional groups on their surfaces, have the potential to be affixed to bioactive compounds, offering targeting capabilities to specific sites as required for various applications. Additionally, the FeONPs on their own have shown anticancer effects, especially when used with external stimuli to produce cellular necrosis, apoptosis and protein denaturation [203].

In the application of surface-modified FeONPs, among several functional groups interacting with NP surfaces, Cur, a natural dietary constituent and polyphenolic compound, has received extensive attention in scientific literature [27]. Known for its antiseptic anti-inflammatory, and various therapeutic properties, including anticancer activity [26]. Recent studies suggest that coupling Cur with metal NPs (FeO) might enhance its bioavailability and the stability of Cur in biological media [28, 204]. This is due to Cur's poor water solubility, rapid metabolism, and low bioavailability. By incorporating Cur into NP-based delivery systems, these limitations can therefore be overcome, allowing for more effective localization and sustained release at the tumor site. The anticancer efficacy of Cur is contained in its ability to trigger apoptosis and inhibit tumor proliferation and invasion by influencing various biochemicals and signaling pathways [30].

This chapter builds on the advances discussed previously, focusing on the development and application of non-surgical combinative synergistic treatments for MM and NMSC. It explores how the strategic integration of FeONPs and Cur can address the challenges faced by surgical skin cancer therapies and improve the outcomes of non-surgical interventions. This platform was developed to be part of a more potent, multi-component treatment platform for skin cancer, which maximizes therapeutic impact while minimizing adverse effects. By employing this rationale-based combinatorial strategy, this research seeks to achieve longer-term tumor control, the overcoming of resistance mechanisms, and the improvement of overall patient quality of life.

4.2 Materials and Methods

4.2.1 Materials

Iron (III) chloride hexahydrate (FeCl3·6H2O), iron (II) chloride (FeCl2·4H2O), and dimethyl sulfoxide (DMSO) were purchased from Thermo Fisher Scientific (Johannesburg, South Africa), ammonium hydroxide (NH_4OH) from EMD Chemicals (Modderfontein, South Africa) and Cur powder from Chem-Impex Int'l Inc, (Wood Dale, IL, USA). NIH-3T3 mouse fibroblast cells (ATCC CRL-1658) were obtained from the ATCC (American Type Culture Collection, Manassas, VA, USA), the model malignant melanoma cell line (A375) from Cellonex (Johannesburg, South Africa), the MTT Cell Proliferation Kit I from Roche (Basel, Switzerland), Dulbecco's Modified Eagle Medium (DMEM) from Life Technologies Limited “Gibco” (Paisley, UK) and Fetal bovine serum from PAN Biotech (Aidenbach, Germany). All other chemicals were utilized as received without further modification.

4.2.2 Synthesis of the Cur-FeONPs

The Cur-FeONPs were synthesized, using the method described by Bhandari *et al.,* with modifications, by first preparing an aqueous solution containing Fe (III) and Fe (II) salts in a molar ratio of 2:1, with the reaction initiated under an inert nitrogen atmosphere. In a specific setup, 2.2 g of $FeCl_3.6H_2O$ and 0.8 g of $FeCl_2.4H_2O$ were dissolved in 40.0 mL of water in a three-neck round-bottom flask, and the reaction conducted under a continuous nitrogen flow. As the reaction progressed, 10.0 wt% of Cur (dissolved in DMSO) was gradually added dropwise to the reaction system at approximately 40 °C. The reaction temperature was then adjusted to 85 °C, with 5.0 mL of 28% (w/w) ammonium hydroxide introduced into the reaction mixture while maintaining vigorous stirring. The reaction was allowed to continue stirring at 85 °C for approximately one hour, followed by magnetic decantation and a series of washing steps employing ethanol, a 50:50 mixture of acetonitrile/dichloromethane, and water [202]. As a comparison, FeONPs were prepared without the addition of Cur, as described above.

4.2.3 Chemical Structure Validation

The analysis of the chemical structure of the synthesized Cur-FeONPs was conducted to detect the distinctive functional groups of free Cur, Cur-FeONPs, and FeONPs using an FTIR spectrophotometer (Spectrum 100, PerkinElmer Inc, Waltham, MA, USA). For each analysis, dried powder samples were positioned on a diamond ATR crystal, and an infrared spectrum was captured within the range of 650 to 4000 cm^{-1}, utilizing 32 scans for the analysis.

4.2.4 Determination of Particle Size, Zeta Potential, and Morphology

Dynamic light scattering and phase-analysis light scattering measurements were conducted on a Zeta Sizer instrument (NanoZS, Malvern Panalytical, Malvern, UK) to determine the average hydrodynamic diameter and zeta potential of the synthesized Cur-FeONPs and FeONPs. For the analysis, dried samples (10 mg) of FeONPs and Cur-FeONPs were suspended in 10 mL distilled water and sonicated for 15 minutes (Sonics Vibra Cell, Newtown, Newtown, CT, USA). The samples were then transferred into disposable cuvettes for hydrodynamic size and polydispersity index (PDI) analysis, followed by zeta potential cuvettes (DTS 1070) for surface charge analysis at 25 °C.

Samples of Cur-FeONPs and FeONPs were further subjected to morphology analysis using SEM (ZEISS Electron Microscopy, Carl Zeiss Microscopy Ltd., Cambridge, UK) and Transmission Electron Microscopy (TEM). For the SEM analysis, an aliquot of the respective sample was meticulously placed on an aluminum specimen stub and air-dried before undergoing gold palladium (AuPd) coating (applied twice). The sample was then observed and imaged under both low (82.34 KX) and high (314.84 KX) magnifications.

TEM was also employed to confirm the morphology and size of the NPs. The analysis was conducted using an FEI Tecnai T12 TEM (operating at 60–120 kV, Hillsboro, OR, USA), where 1 mg sample of NPs was dispersed in double-deionized water, and a drop of the suspension placed onto a Form Var®-coated 200-mesh copper grid (TAAB Labs Equipment Ltd., Aldermaston, England). The grid was left to dry at room temperature before TEM imaging.

4.2.5 Differential Scanning Calorimetry

DSC was performed on the synthesized Cur-FeONPs and FeONPs using a DSC822E Differential Scanning Calorimeter (PerkinElmer, USA) to investigate the thermal properties of the various formulations. Prior to analysis, the samples were precisely weighed and placed in a crucible, with an empty crucible serving as the reference. The temperature varied from 10 to 500 °C at a heating rate of 10 °C/min, under a dynamic air atmosphere of 50 ml/min.

4.2.6 Crystallographic Analysis

XRD analysis was conducted using a RIGAKU MiniFlex instrument (RIGAKU Inc., Tokyo, Japan) to evaluate the crystallinity of Cur before and after modifications of dried samples. Prior to the XRD study, Cur, FeONPs, and Cur-FeONPs were mounted on aluminum sample holders and analyzed to obtain diffractograms. The following measurement conditions were set for the analysis: a 2θ range of 10°–90° and a scan rate at 10 deg/min, with a current and

voltage of 15 mA and 40 kV, respectively.

4.2.7 Drug Loading and *In vitro* drug release analysis

The drug loading of the Cur-FeONPs was determined by analysis of the supernatant after magnetic decantation using a Thermo Evolution 600 double-beam UV-Vis spectrophotometer (Thermo Fisher Scientific, Waltham, MA, USA). The amount of unloaded Cur in the supernatant was quantified at a fixed wavelength (λ = 428 nm) using a standard cuvette with a 1 cm optical path (ε = 0.0031; R^2 = 0.996, Figure 4.1). All experiments were conducted in triplicate, with the drug loads calculated as the mass of the detected drug relative to the total mass of the sample, reported as mean values with standard deviation (SD). Drug loading efficiency was determined using the following Equation 4.1:

$$\text{Drug loading efficiency (\%)} = \frac{\text{Total amount of drug} - \text{Free amount of drug}}{\text{Total amount of drug}} \times 100 \quad (4.1)$$

Finally, Cur release was investigated in a PBS: ethanol = 3:2 (v/v) solutions as described by Chircov *et al.,* [205]. For each sample, 100 mg of NPs were placed into a filter bag enclosure and immersed in 25 mL of the solution, with continuous stirring at 37 °C. Measurements were thereafter at predetermined intervals over 24 h and analyzed by UV spectrophotometry, as previously described.

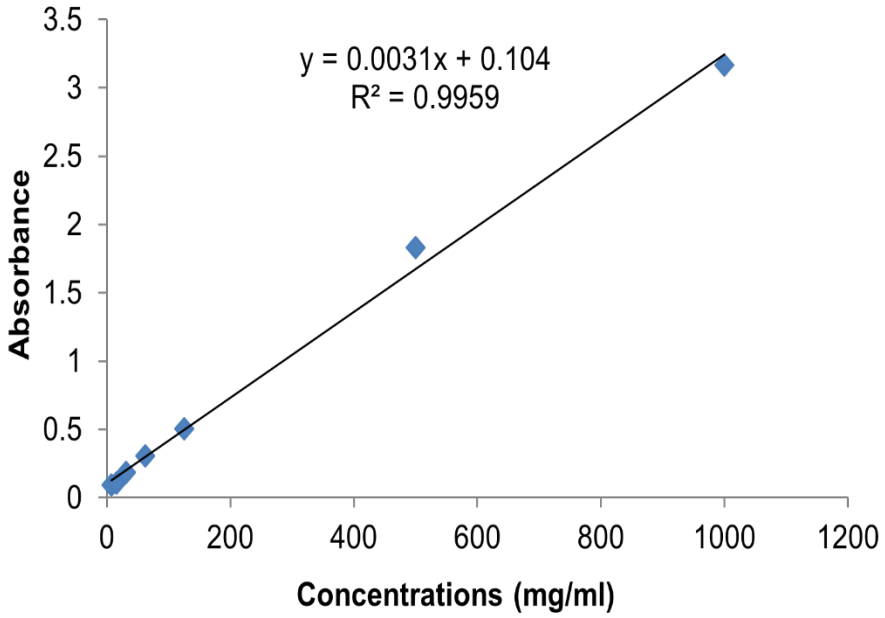


Figure 4.1: Illustration of the relationship between Curconcentration and absorbance at 428 nm. The resulting data points were plotted to generate the standard curve, which demonstrates a linear correlation between concentration and absorbance within the tested range. This linearity confirms adherence to the Beer-Lambert law, indicating that absorbance is directly proportional to concentration.

4.2.8 Cytocompatibility and Antiproliferation Activity Analyses

The cytotoxicity and antiproliferation of the synthesized Cur-FeONPs and FeONPs were evaluated using the MTT assay, as outlined [206]. NIH-3T3 cells were used for the cytocompatibility studies and were cultured in DMEM media supplemented with 10% FBS and 1% P/S at a density of 5 × 10^5 cells/well in a 96-well plate. Once the cells reached confluency, they were treated with FeONPs, Cur and functionalized Cur-FeONPs at concentrations of 10, 5, 2.5 and 1.25 µg/µL. After 24, 48, and 72 hours, the supernatants were removed, a 10 µL aliquot of MTT solution (5 mg/mL) was added to each well, and the plate incubated for 4 h under humid conditions at 37 °C with 5% CO_2. After incubation, 100 µL of solubilizing agent (acid-isopropanol; 0.04 N HCl in isopropanol) was added to dissolve the formed formazan crystals, followed by overnight incubation at 37 °C with 5% CO_2. Wells containing only the solubilizing agent and growth medium served as blanks. The absorbance of the solution was thereafter measured at 570 nm with a reference wavelength of 620 nm using a multimodal microplate reader (Victor X3, PerkinElmer, Waltham, MA, USA). The absorbance data (mean ± standard deviation) were used to calculate the percentage of cell viability using Equation 4.2:

Cell Viability % =AT /AC X100 (4.2)

Where, AT and AC are absorbance of the treated and untreated cells, respectively.

The antiproliferation analysis was undertaken on A375 melanoma cells using the method above. Prior to each analysis, the cells were cultured in DMEM medium supplemented with 10% fetal bovine serum (FBS) and 1% penicillin-streptomycin (P/S) at a density of 5×10^5 cells per well in a 96-well plate. Upon reaching confluency, the cells were treated with FeONPs, free Cur, and functionalized Cur-FeONPs at concentrations of 10, 5, 2.5 and 1.25 µg/µL. After 24, 48, and 72 hours of treatment, the supernatant was removed, and 10 µL of MTT solution (5 mg/mL) was added to each well. The plates were incubated for 4 hours under humidified conditions (NUAIRE, Radobio, China) at 37 °C with 5% CO_2. Subsequently, 100 µL of solubilizing agent (acidified isopropanol; 0.04 N HCl in isopropanol) was added to each well to dissolve the formazan crystals, followed by overnight incubation under the same conditions.

Control wells containing only the solubilizing agent and growth medium served as blanks. The absorbance of the resulting solution was measured at 570 nm, with a reference wavelength of 620 nm, using a multimodal microplate reader (Victor X3, PerkinElmer, Waltham, MA, USA). The absorbance data (mean ± standard deviation) was utilized to calculate the percentage of cell viability.

4.2.9 Statistical analysis

All results were reported as mean ± standard deviation (SD) from triplicate measurements. Statistical analyses were conducted utilizing SPSS software (SPSS 29, IBM, SPSS Inc, Chicago, IL, USA) with a one-way analysis of variance carried out. Differences between means were compared using Tukey HSD multiple range test at a significance level of $p < 0.05$.

4.3 Results and Discussion

In the various methods reported for synthesizing FeONPs, thermal decomposition stands out as an efficient approach, carried out at room temperature and atmospheric pressure. This method provides precise control over NP size, composition, morphology, and distribution. Typically, the synthesized metallic NPs are surface-modified with hydrophobic ligands. This modification strategy helps prevent oxidation, reduce agglomeration, and minimize polydispersity in organic solvents. However, it often results in instability in aqueous

suspensions, which restricts their use in biomedical applications [22]. In this study, FeONPs were functionalized with Cur to improve their biocompatibility and bioavailability in affected tissues with the aim of integrating this platform, with other combinative therapies within a topical drug system for enhanced skin cancer treatment.

4.3.1 Evaluation of the Chemical Stability and Functional Transformation of the Cur-FeONPs

FTIR spectroscopy was employed to examine the characteristic functional groups of Cur on the surface of Cur-FeONPs, providing insights into the chemical stability and functional transformations of the NP platform. This technique enabled a comparative analysis of vibrational transitions in the chemical structures of Cur and iron oxide, both as individual and as combined components.

Figure 4.2 displays the FTIR spectra for the uncoated FeONPs, free Cur, and the Cur-coated FeONPs. The uncoated FeONP spectrum, consistent with previous literature, exhibited an absorption peak at 541 cm^{-1}, corresponding to the Fe-O bond, thereby confirming the successful synthesis of FeONPs. This peak serves as a distinct indicator of iron oxide formation.

In contrast, the Cur-FeONPs spectrum revealed new peaks were present in the uncoated NPs, signifying interactions with Cur. The disappearance of the peak at 963 cm^{-1} in the free Cur spectrum, associated with in-plane bending of the hydroxyl group in the enolic moiety, suggests functionalization through the keto-enol functionality of Cur. This interaction aligns with earlier studies where Cur functionalized metal NP s (e.g., Au, Ag) through similar mechanisms in aqueous solutions.

Additional features in the Cur-FeONPs spectrum, such as a broad peak around 3290 cm^{-1} and a sharp peak around 3470 cm^{-1}, correspond to the –OH groups observed in the free Cur spectrum. The strong peak at 1605 cm^{-1} in the free Cur spectrum, indicative of mixed C=C and C=O character, appears shifted to 1573 cm^{-1} with reduced intensity in the Cur-FeONPs spectrum, further evidencing interactions between Cur and the NP surface.

Furthermore, the peak at 1023 cm^{-1} in free Cur, attributed to C-O-C stretching, persists in the Cur-FeONP spectrum, albeit with lower intensity, indicating the retention of intact C_6H_5-O-CH_3 moieties. These findings confirm the successful functionalization of the NP surface with Cur, with Cur also serving as a stabilizing agent for the FeONPs.

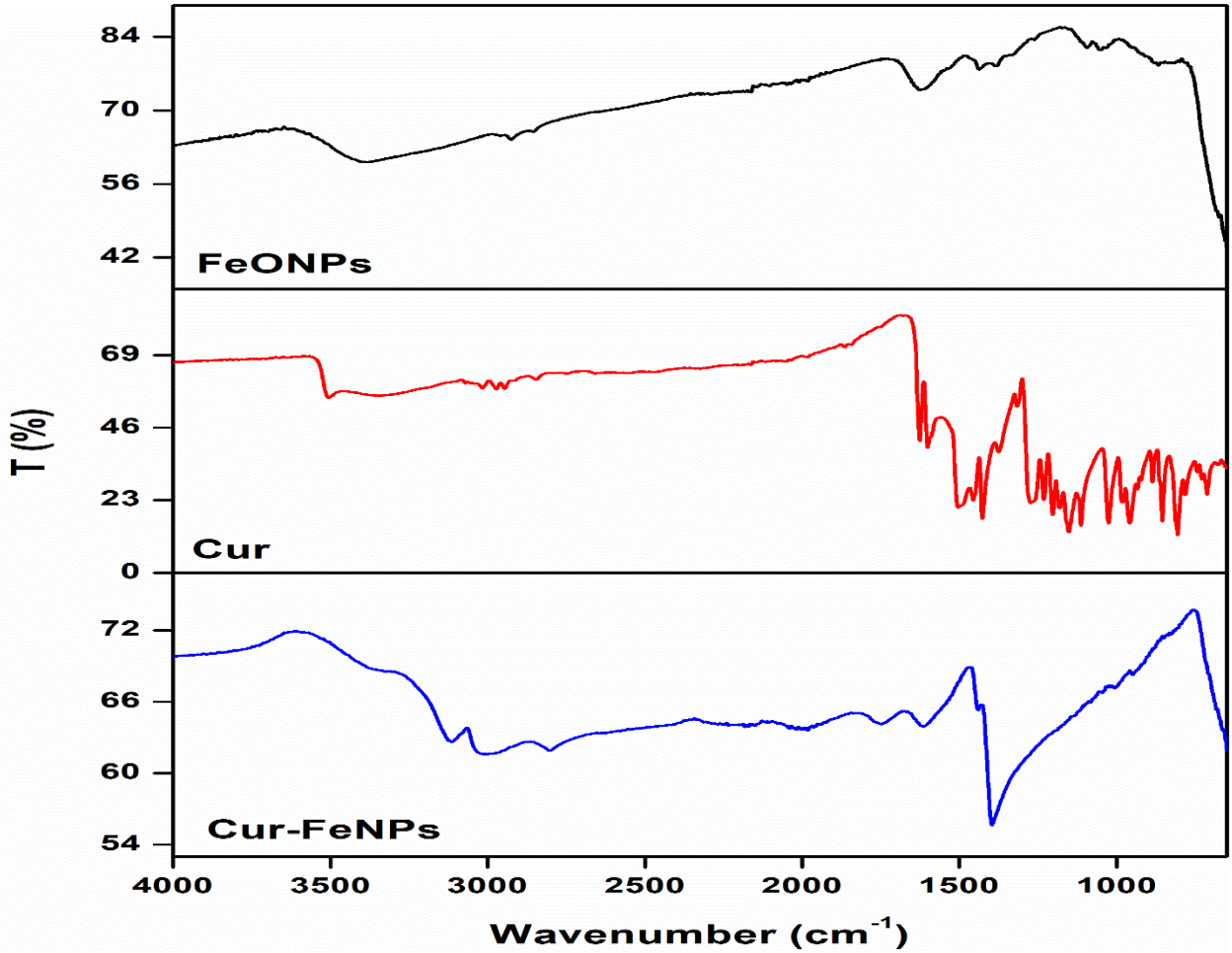


Figure 4.2: FTIR spectra for the Cur-FeONPs, free Cur, and the uncoated FeONPs. FTIR spectroscopy is employed to identify characteristic functional groups and assess chemical interactions among these components. These spectral analyses confirm the successful conjugation of Cur onto the iron oxide NP s, a crucial step for developing targeted drug delivery systems.

4.3.2 Particle Sizing and Morphological analysis of the Cur-FeONPs

4.3.2.1 Particle analyses

Dynamic light scattering (DLS) and zeta potential analyses were performed on the FeONPs. The results indicated a general trend of increase in hydrodynamic diameter and decreased zeta potential values with the addition of Cur. This suggests that the polymer functionalizing Cur-loading significantly reduced the surface charge of the drug delivery system, thereby diminishing their interactions with the surrounding solvent (distilled H_2O) [205]. Zeta average and zeta potential are additionally key indicators of sample stability. A high absolute value of zeta potential suggests strong colloidal stability of the NPs in solution. Figure 4.3a indicates that the average hydrodynamic diameter (zeta size) of the FeONPs obtained is approximately 95.37 nm with a SD = 5.28, while in Figure 4.3b, the mean zeta potential of the FeONPs was -23.5 mV, while SD was 7.43 Figure 4.3c shows the average

hydrodynamic diameter (zeta size) of Cur-FeONPs as 105 nm with SD = 1.3 and in Figure 4.3d, the mean zeta potential of Cur-FeONPs was found to be −29.6 mV with a SD of 9.51. This high negative value indicates the non-aggregate nature of the prepared Cur-FeONPs, minimizing the tendency to absorb plasma proteins and providing stability [206]. Table 4.1 represents the particle size analysis zeta average and zeta potential of the synthesized FeONPs and Cur-FeONPs (n = 3).

These characteristics are anticipated to enhance the potential for significant cellular uptake of Cur-FeONPs by human endothelial cells [207]. Furthermore, the NP size facilitates the penetration of Cur-FeONPs through the cancer cell membrane, aiding in the accumulation of Cur within cancer cells [208]. The findings by Larese *et al*. indicate a key distinction between metal and non-metal NPs, emphasizing the impact of NP size after interacting with physiological media, which influences size-dependent skin penetration [209]. Specifically, NPs smaller than 100 nm are generally considered to be in the optimal size range for deep skin penetration, however this may expose healthy tissue not affected by the skin cancer to potentially toxic bioactives, leading to unwanted adverse effects. Based on this size range, the average size of the NPs developed in this study (≈100nm) may remain localized at the skin cancer site, targeting affected cells to enhance the therapeutic efficacy of the platform while minimizing diffusion into healthy tissue and systemic circulation.

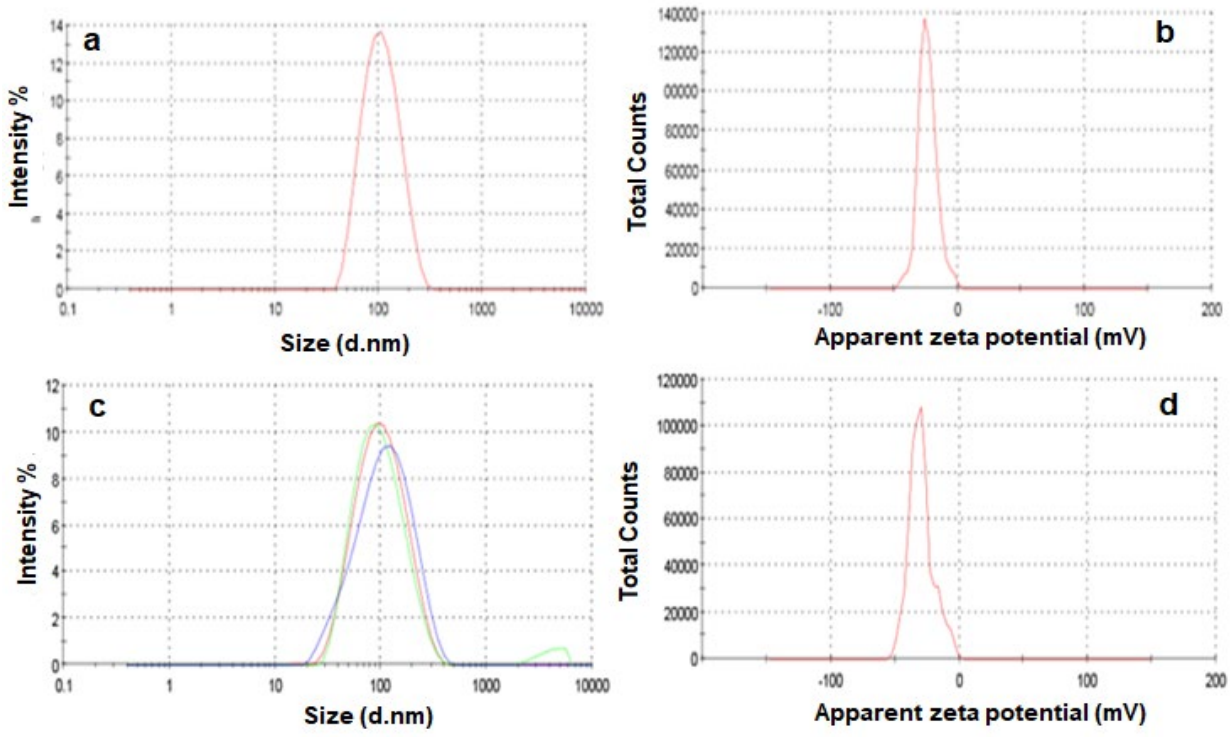


Figure 4.3: The average size and zeta potential profiles of the prepared FeONPs, (a) and (b), respectively, and of the Cur-FeONPs, (c) and (d), respectively. The observed increase in

hydrodynamic diameter and the more negative zeta potential upon Cur loading suggest successful functionalization of the FeONPs. The higher negative zeta potential indicates improved colloidal stability, which is crucial for minimizing aggregation and enhancing biocompatibility. These characteristics are anticipated to facilitate effective cellular uptake and targeted delivery of Cur to cancer cells, thereby enhancing therapeutic efficacy.

Table 4.1: Average size and zeta potential of the synthesized FeONPs and Cur-FeONPs (n = 3).

System	Particle size (nm) in water	Average Polydispersity Index ± SD	Zeta potential (mV)	SD
FeONPs	95.37	5.28 ± 0.02	-23.5±3.2	7.43
Cur-FeONPs	105	1.30 ± 0.02	-29.6±4.5	9.51

4.3.2.2 SEM and TEM Analysis

Among the various methods reported for synthesizing NPs, co-precipitation was chosen as the most suitable in this study. This method is conducted in an inert atmosphere with alkalinity and elevated temperatures to prevent oxidation, ensuring control over particle size, distribution, and morphology [210]. The synthesis of the FeONPs in this study successfully produced a black-colored powder, characteristic of free FeONPs. Precipitation in an inert nitrogen (N_2) environment effectively inhibited the oxidation and decrease of iron II/III salts, as well as the degradation of FeONPs. SEM imagery (Figure 4.4a and 4.4b) confirmed that the Cur-functionalized FeONPs (Cur-FeONPs) were spherical with a relatively rugged surface and average particle size of less than 100 nm. These findings align with previous research indicating that co-precipitation produces spherical NPs, which are advantageous in enhancing bio-distribution and cellular uptake in cancer nanomedicine applications [210]. High-resolution TEM further provided detailed insights into the morphology of FeONPs. The images, as depicted in Figure 4.5, confirmed their spherical shape and revealed clear atomic planes. Notably, the particle sizes observed in TEM were smaller compared to those measured by DLS with a zeta sizer. This discrepancy arises because TEM measures the core size of individual NPs in a dry state, whereas DLS accounts for the hydrodynamic diameter, including surface-bound water and potential particle aggregation in suspension.

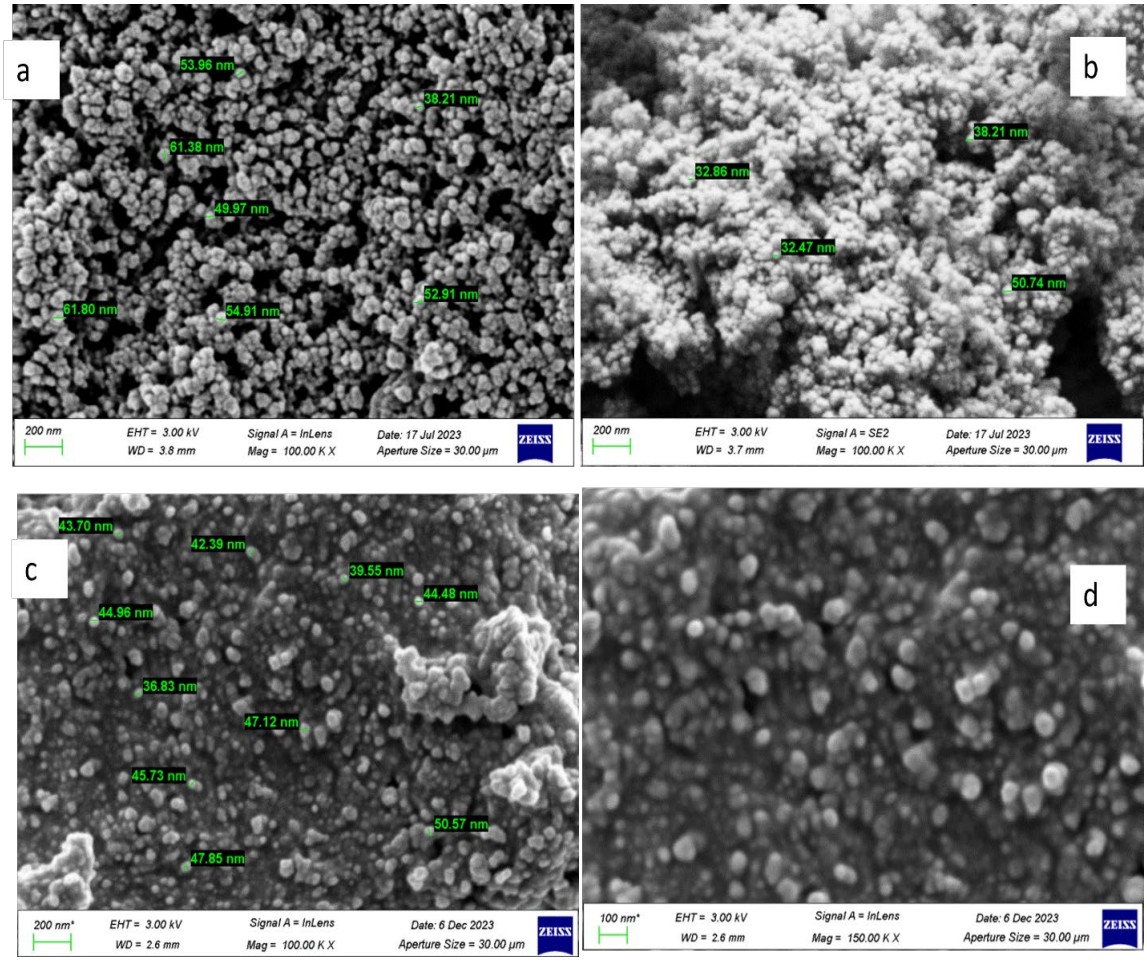


Figure 4.4: Digital images of samples with corresponding SEM images showing overall morphology of FeONPs (a & b) at 200 nm scales (82.34 KX magnification) and (c) of Cur-FeONPs at 200 nm scale (82.34 KX magnification) and (d) 100 nm scale (314.84 KX) (isolated particle), indicating a particle size of <100 nm. The SEM analyses confirm that both FeONPs and Cur-FeONPs possess spherical morphologies with sizes predominantly below 100 nm. The slight increase in size observed in Cur-FeONPs compared to FeONPs is indicative of successful Cur loading. These morphological characteristics are crucial, as NP size and shape significantly influence their biological interactions, cellular uptake, and overall efficacy in drug delivery applications.

TEM images also confirmed the successful synthesis of Cur-FeONPs. Cur-NPs exhibited a monodisperse distribution, displaying a spherical shape with an average size 90 to 140 nm, as illustrated in Figure 4.5. These findings are aligned with a result undertaken by Elbialy, *et al.,* where the NPs were mono-dispersed and spherical in shape [211]. The size and surface charge of NPs are critical factors influencing their penetration into the skin, with NPs of a size of around 100 nm preferable for skin penetration with larger particles able to diffuse effectively through hair follicles.

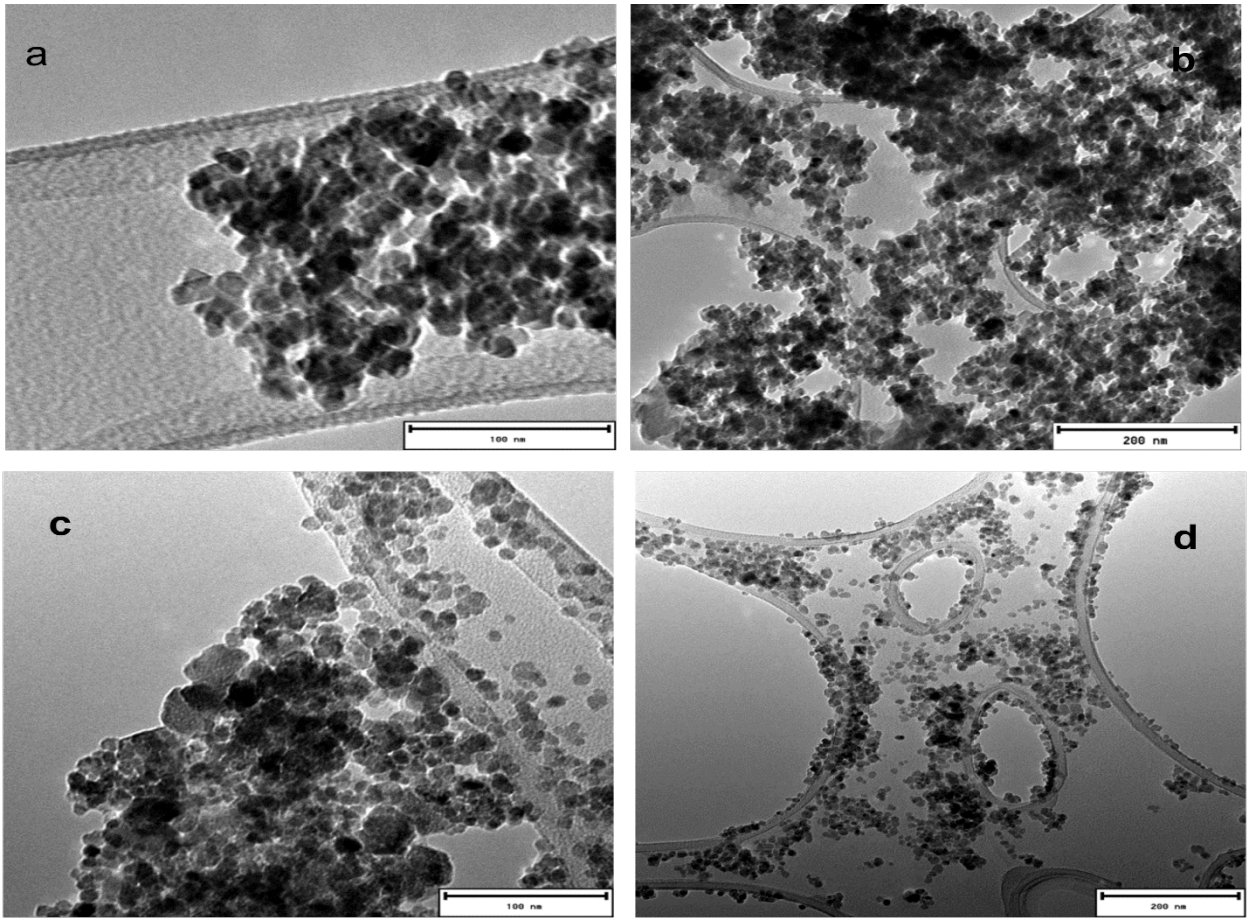


Figure 4.5: Visualization of the morphological attributes of the FeONPs: TEM images of FeONPs at (a) 100 nm scale and (b) 200 nm scale, and of Cur-FeONPs at (c) 100 nm and (b) 200 nm scales. The TEM analyses confirm that both FeONPs and Cur-FeONPs possess a predominantly spherical morphology with uniform size distributions. The observed increase in particle size upon Cur loading aligns with findings from similar studies, where TEM images demonstrated successful drug loading onto FeONPs without compromising their structural integrity. These characteristics are crucial for ensuring effective cellular uptake, targeted drug delivery, and minimizing potential cytotoxicity in biomedical applications.

4.3.3 Thermal Analysis

Figure 4.6 illustrates the DSC curves of free Cur, FeONPs and Cur-FeONPs. The results of the DSC analysis noted that the unfused Cur displayed a distinct endothermic peak with a melting point at 186.2 °C [212], whereas the melting point of Cur-FeONPs ranged between 285 and 300 °C. Notably, the melting point of FeONPs exceeded the specified range due to iron physical properties, and the Cur-functionalized FeONPs exhibited a forward shift with a considerable decrease in peak intensity. This shift could be attributed to the interactions between Cur and iron oxide, which increased the stability of the system. The exothermic peak observed in the DSC analysis of FeONPs at approximately 480 °C corresponds to the phase transition from maghemite to hematite, a transformation typically occurring around 500 °C [213, 214].

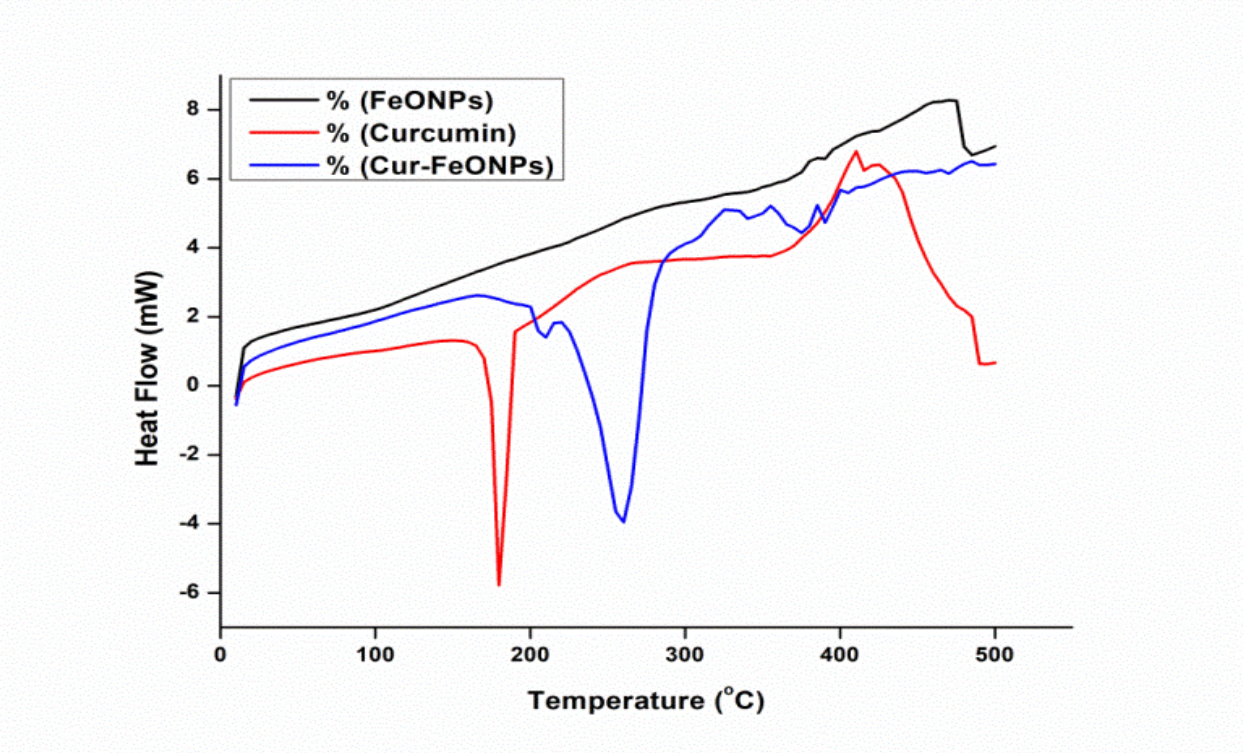


Figure 4.6: DSC curves of the free Cur, FeONPs and Cur-FeONPs. The absence or shift of the characteristic melting peak of Cur in the Cur-FeONPs thermogram indicates successful encapsulation and possible molecular interactions between Cur and the NP matrix. These thermal analyses are crucial for understanding the stability and physicochemical properties of the formulated NP s, which are essential for their efficacy as drug delivery systems.

4.3.4 Crystallinity studies

In Figure 4.7, the XRD pattern of Cur-FeONPs displayed characteristic peaks at 2θ = 30.2, 35.5, 43.2, 53.6, 57, 62.75. From this, it is evident that the diffraction peaks of Cur-FeONPs aligned with the typical diffraction peaks of Fe3O4. The observation confirms that the fabrication of Cur-FeONPs did not impact on the crystalline structure of Fe3O4, which is consistent with studies demonstrating that Fe3O4 retains its crystalline integrity even after modifications or functionalization with Cur, as shown in Figure 4.7. For instance, in the synthesis and coating of Fe3O4 with silica (SiO2), XRD analysis confirmed the preservation of characteristic diffraction peaks, indicating that the structural framework of Fe3O4 remained intact. This reinforces the conclusion that the functionalization processes, including the development of Cur-FeONPs, do not compromise the core crystalline properties of either Cur or Fe3O4. Maintaining this structural stability is crucial for applications where the crystalline characteristics of Fe3O4 are essential for performance and functionality. The variation in peak intensity between FeONPs and Cur- FeONPs was attributed to the Cur coating process which resulted in a reduction in peak intensity, as both samples displayed high-intensity peaks within the 10–30° range of the 2θ diffraction angle, this indicated the crystalline nature of Cur in its pure form and around the NPs. Consistent with prior studies

(e.g., Peng *et al*., Taghavifar *et al*.), the similarity in peak patterns confirms that the Cur molecule remained intact without degradation during NP synthesis, preserving its structural integrity in the formulation [215, 216].

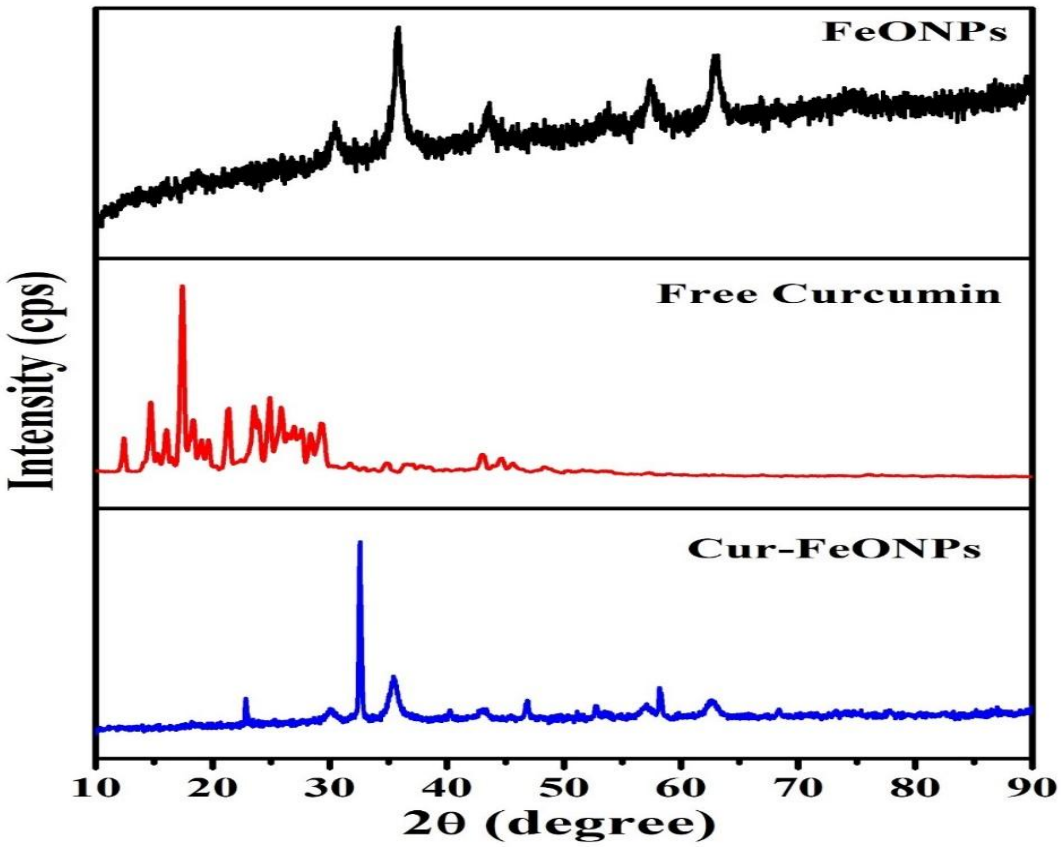


Figure 4.7: XRD spectra of free Cur, Cur-FeONPs, and free FeONPs. This figure presents the XRD patterns for free Cur, FeONPs, and Cur-FeONPs, providing insights into their crystalline structures and the effects of Cur loading on the NPs. The XRD analysis confirms the crystalline nature of free Cur and FeONPs. The diminished crystallinity of Cur in the Cur-FeONPs composite suggests effective loading onto the FeONPs, which may influence the dissolution rate and bioavailability of Cur in therapeutic applications.

The XRD analysis confirms the crystalline nature of free Cur and FeONPs. The diminished crystallinity of Cur in the Cur-FeONPs composite suggests effective loading onto the FeONPs, which may influence the dissolution rate and bioavailability of Cur in therapeutic applications.

4.3.5 Determination of the Cur-Loading of the Cur-FeONPs

The Cur loading efficiency assessment showed that about 93% of the total Cur was successfully loaded onto the FeONPs, noting a high loading capacity and percentage

entrapment efficiency (%EE) for the Cur-FeONPs. This result is consistent with that found in the study by Chircov *et al*., where no significant differences were observed between the metal nanocarriers, with a notable decrease in loading efficiency observed in samples containing 10% Cur, compared to those loaded with 5% Cur, confirming that Cur loading is controlled by the available surface area [205]. Due to the amount of Cur used in the synthesis process, this explained that most of the Cur included in the reaction was loaded onto NP platform.

4.3.6 *In vitro* Cur release

The release profile of Cure-FeONPs in PBS: ethanol revealed that 100% of Cur was rapidly released within the first 24 hours, as depicted in Figure 4.8. Comparatively, a study by Chirkov *et al*. revealed that specimens exposed to prolonged reaction times exhibited slightly faster release rates, likely attributed to the larger size of the nanocarriers. However, the samples synthesized under lower-pressure conditions in this study demonstrated higher loading efficiency, resulting in a greater overall release of Cur. Notably, sustained release was observed between 8 and 24 hours, demonstrating the system's potential for extended drug delivery, when needed [205].

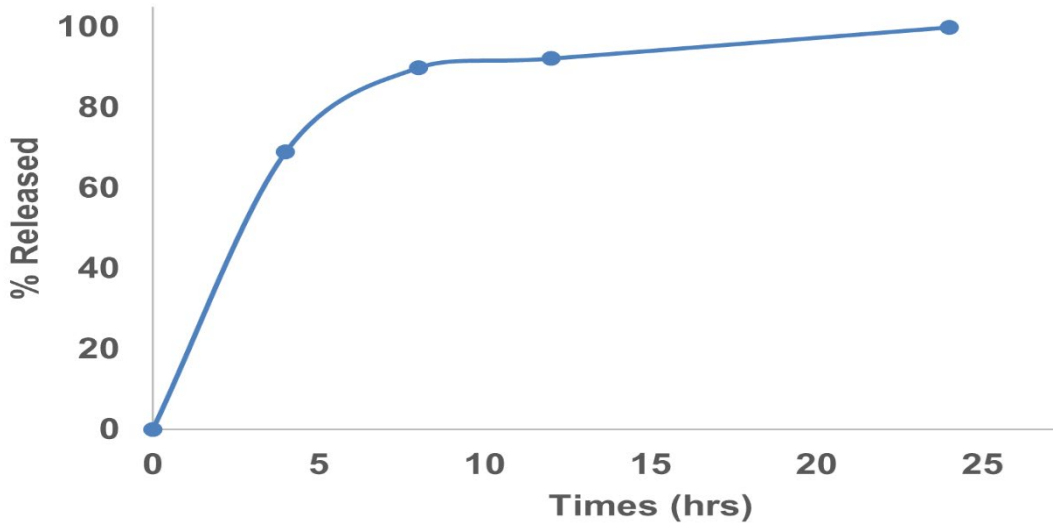


Figure 4.8: Cur release profile of the synthesized Cur-FeONPs (SD≤ 0.38 in all cases). This figure illustrates the in vitro release kinetics of Cur from the synthesized Cur-FeONPs over a specified time period, with SD not exceeding 0.38 in all measurements. The low standard deviation across measurements indicates the reproducibility and consistency of the release profile, underscoring the reliability of the NP formulation.

4.3.7 Cell culture and cytotoxicity Assessment

The MTT assay was utilized to evaluate the cytotoxic effects of Cur-FeONPs, free Cur, and

FeONPs on the NIH-3T3 cell line, seeded at a density of 5×10^5 cells. Cell viability was measured after 72 hours of treatment with varying concentrations of the compounds, represented as A, B, C, and D, in Figure 4.9, as 110, 5, 2.5 and 1.25 µg/µL, respectively. DMSO was used as a negative control.

The percentage of cell viability indicated that NIH-3T3 cells maintained viability above 70% across all tested concentrations, with Cur-FeONPs showing relatively high biocompatibility, even at the highest concentration of 10 µg/µL. This trend was consistent for free Cur and FeONPs, affirming their non-toxic nature under these experimental conditions. Cell viability was measured at 24, 48, and 72 hours, and the results demonstrated that all tested compounds were biocompatible with normal fibroblast cells. This is a critical attribute for potential anticancer applications, as maintaining biocompatibility with normal cells is a primary consideration in developing therapeutic interventions.

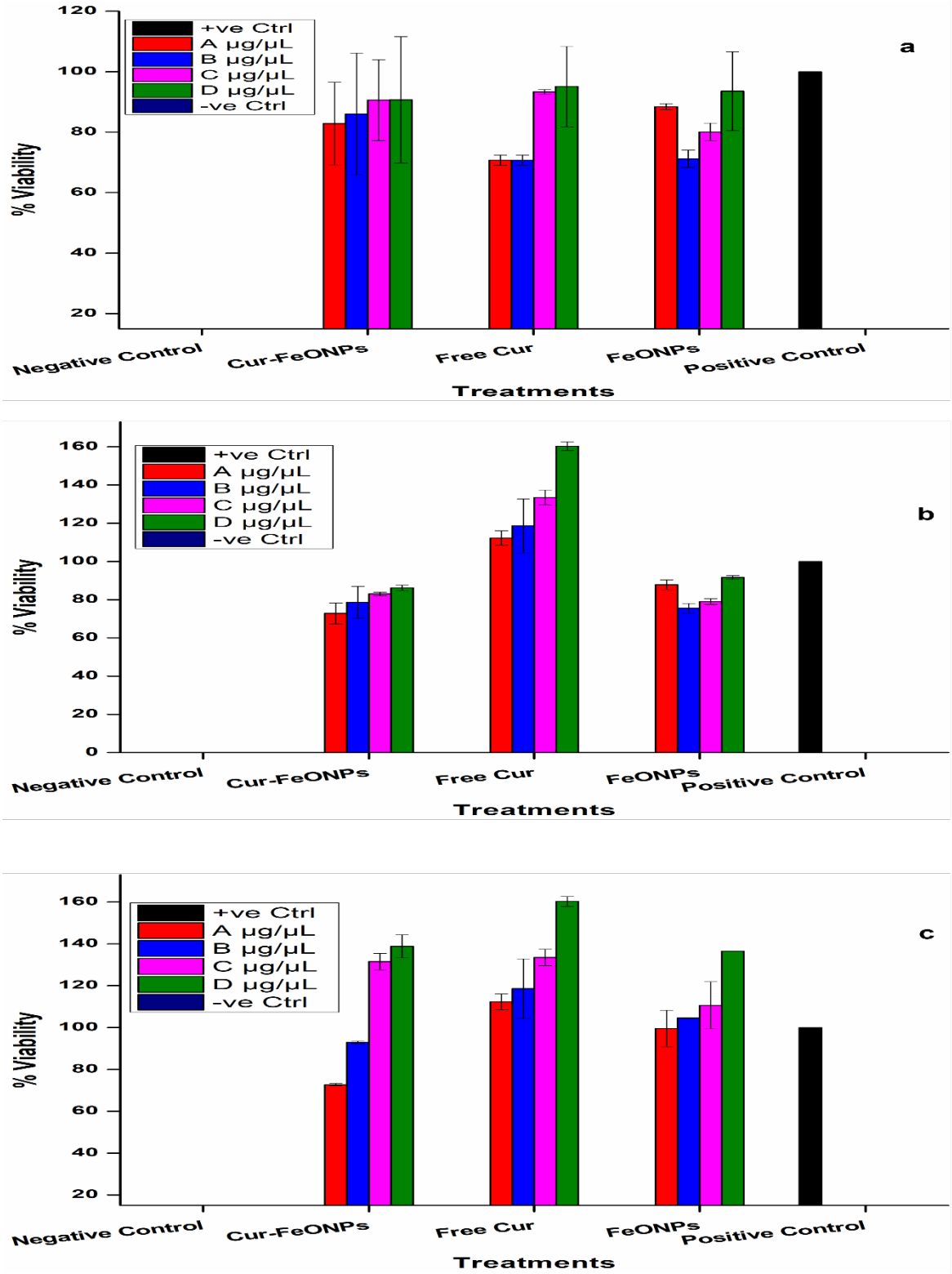


Figure 4.9: Cytotoxicity assessments to evaluate the cell viability of Cur-FeONPs, free Cur and FeONPs at different concentrations on NIH-3T3 cells, where A, B, C and D represents 10, 5, 2.5 and 1.25 µg/, respectively. The experiments were undertaken for (a) 24 (b), 48 and (c) 72 hours (n=3). These findings suggest that Cur-FeONPs maintain a favorable cytotoxicity profile at lower concentrations, with enhanced cytotoxic effects at higher concentrations likely attributable to the therapeutic action of Cur. The results indicate that the NP formulations can modulate the cytotoxicity of encapsulated agents, potentially offering a controlled delivery mechanism that minimizes adverse effects on healthy cells.

4.3.8 *In vitro* Assessment of the Antiproliferative effect of Cur–FeONPs

The potential toxicity of the NPs is a critical consideration in their biomedical and pharmaceutical applications, necessitating a thorough assessment to ensure they do not harm healthy cells. In this context, the tumor growth inhibition effects of Cur-FeONPs, free Cur, and FeONPs were evaluated on an A375 melanoma cell line. The MTT assay was employed to track metabolic changes over a 72-hour treatment period to determine whether the cells underwent apoptosis or proliferation, as addressed in Figure 4.10. A comparison of the efficacy of Cure-FeONPs and free Curl revealed dose-dependent cytotoxic effects against A375 cells, with concentrations ranging from A, B, C and D µg/µL, while FeONPs showed low toxic effect compared with Cur-FeONPs at the same concentration of Cur-FeONPs, this finding demonstrated Cur coated Fe_3O_4 enhanced the efficacy of each other.

The tested Cur-FeONPs samples significantly inhibited A375 cell proliferation (% viability was less than 70%) except for concentration C and D, the lowest doses tested exhibited more than 70% cell viability. These findings demonstrate selective toxicity toward skin cancer cells when compared to exposure to NIH-3T3 cells. It was noted that the Cur-FeONPs exhibited greater cytotoxicity than free Cur (17% vs 68%) after 72 hours, likely due to enhanced cellular penetration resulting from functionalization, whereas FeONPs demonstrated low anticancer activity on the melanoma cell line at higher concentrations. In a recent study by Mi *et al.* on folic acid-conjugated superparamagnetic iron oxide NPs (SPIONs-FA), the researchers reported no significant differences in cell viability between the experimental and control groups at SPIONs-FA concentrations of 0.1 and 0.2 mg/mL, with SPIONs-FA promoting cell growth at lower concentrations [217]. In this study, Cur-FeONPs demonstrated a significantly higher ability to suppress A375 cells, achieving less than 5% cell viability at the highest doses tested compared to free Cur and FeONPs. It also confirmed that Cur-FeONPs induced apoptosis in A375 cells, with an IC50 value of 0.47 µg/µL after 72 hours of treatment. These results align with prior outcomes by Zhang [218]*et al.* and Liao *et al*. [219]. These findings highlight the potential of Cu-FeONPs as powerful agents for treating melanoma and potentially other skin cancers.

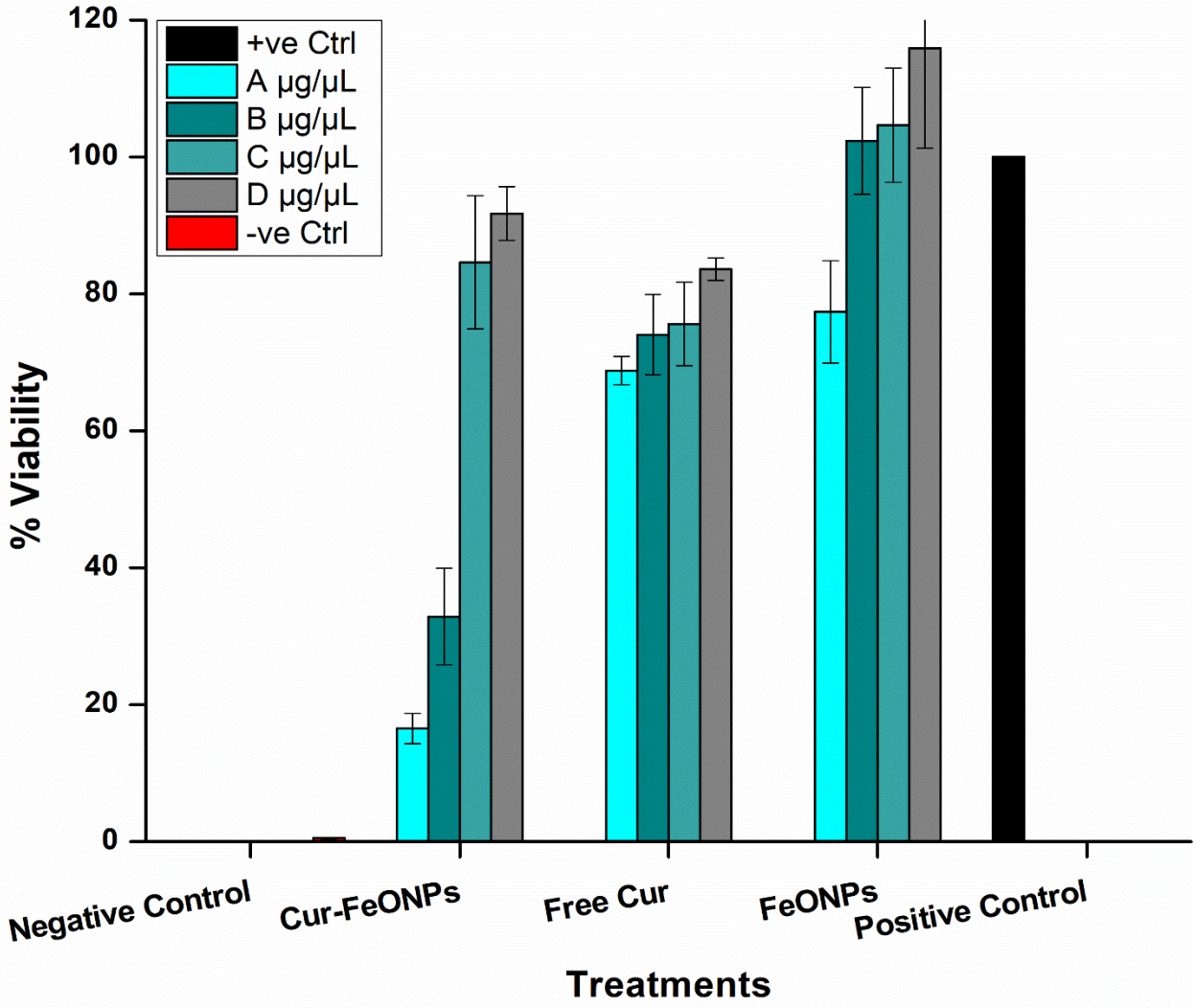


Figure 4.10: Cell viability profile of A375 cells treated with varying concentrations of Cur-FeONPs, free Cur, FeONPs, negative control and positive control after 72 h, where A, B, C and D represents 10, 5, 2.5 and 1.25 µg/L, respectively. Data presented as mean ± SD, n = 3. These findings suggest that Cur-FeONPs effectively reduce the viability of A375 melanoma cells in a dose-dependent manner, with enhanced cytotoxic effects at higher concentrations likely attributable to the therapeutic action of Cur.

The cytotoxicity studies (Figures 4.9 and 4.10) revealed that Cur-FeONPs exhibit significant anti-proliferative effects against A375 melanoma cells while maintaining biocompatibility with normal NIH-3T3 fibroblast cells. This selective cytotoxicity underscores the platform's potential to provide safer treatment alternatives, especially when compared to non-targeted conventional therapies. The improved therapeutic index suggests a promising role for Cur-FeONPs in reducing off-target effects, a major hurdle in existing cancer treatment regimens.

4.4 Conclusions

In this chapter, the Cur-FeONP system was successfully synthesized and evaluated for its potential in treating skin cancer, specifically MM. The synthesis and characterization of Cur-

FeONPs confirmed their stable structure, biocompatibility, and enhanced therapeutic efficacy. Morphological analysis revealed well-formed NPs with an average size of less than 100 nm, providing optimal conditions for cellular uptake and bioavailability. *In vitro* studies demonstrated that Cur-FeONPs showed significantly higher cytotoxicity toward A375 melanoma cells compared to free Cur or FeONPs alone, achieving cell death at the highest concentration tested. Importantly, Cur-FeONPs exhibited minimal cytotoxicity toward normal NIH-3T3 fibroblast cells, indicating selective toxicity toward cancer cells and improved safety over traditional treatments. The enhanced anti-proliferative activity observed in Cur-FeONPs is likely attributed to the functionalization with Cur, which facilitated greater cellular penetration and apoptosis induction at lower doses, compared to free Cur.

These results therefore highlight the potential of Cur-FeONPs as a promising nanoplatform for the treatment of MM. The incorporation of Cur into FeONPs not only enhanced the therapeutic effects but also improved the safety profile, minimizing adverse effects on healthy cells. These findings support further investigation into Cur-FeONPs for clinical applications in cancer treatment, with the potential for use in combination therapies to overcome resistance and enhance treatment efficacy in skin cancer patients. The subsequent Chapter 5 explores the formulation and assessment of the immunotherapy agent IFN, loaded in sustained-release PLGA NPs, prior to the assessment of the combinative strategy between Cur-FeONPs and the optimized IFNα-PLGANPs.

CHAPTER 5

DEVELOPMENT OF A CONTROLLED-RELEASE IFN-LOADED NANOPARTICLE SYSTEM FOR SKIN CANCER

5.1 Introduction

IFNα is a potent cytokine protein and is an effective immunotherapy against MM. IFNα possesses angiostatic, immunomodulatory and antiproliferative properties, rendering it crucial for the management and prevention of conditions such as MCC, renal cell carcinoma, and Kaposi's sarcoma [220, 221]. IFNα, exhibits anti-tumor properties through several mechanisms such, direct anti-proliferative effects by binding to receptors on tumor cells, which leads to the expression of genes that inhibit cell proliferation and induce apoptosis. IFNα therefore promotes initial cancer elimination in three ways: (a) expression of anti-tumour ISGs in malignant and host cells, (b) enhancement of innate immune cell cytotoxicity; (c) prevention of angiogenesis and metastasis [222]. Additionally, through immunomodulatory actions, it enhances the activity of immune cells, such as natural killer cells and cytotoxic T-lymphocytes, promoting the recognition and destruction of tumor cells [223].

The synergistic utilization of IFNα-2b alongside surgical interventions, targeted therapy regimens, and conventional chemotherapy markedly enhances the efficacy of tumor cell elimination and addresses the limitations of each individual treatment approach [224]. This is evident in the use of temozolomide, an alkylating agent, which has exhibited advantages in controlling multiple metastases when combined with IFNα-2b. This treatment regimen has proven to be relatively straightforward, safe, and effective, enabling potential outpatient or home-based application [224].

Despite the therapeutic potential of IFN treatment in skin cancer, its toxicity profile often hinders the completion of treatment and limits its broader clinical application. Specifically, IFNα has been used as a standard of care in advanced MM; however, its use is restricted by several challenges, including high administration costs, limited efficacy in monotherapy, and adverse side effects. The most serious side effects of IFNα are typically associated with the higher doses administered systemically. These include hematologic toxicities, such as cytopenia (neutropenia, lymphopenia, and thrombocytopenia), gastrointestinal issues (nausea, vomiting, and anorexia), and neurological symptoms (fatigue, depression, and suicidal ideation). These adverse effects significantly reduce patient adherence and curtail

the drug's clinical therapeutic effectiveness, making its long-term use difficult to justify in many cases [225].

The limitations linked to conventional cancer therapies have boosted the exploration and advancement of innovative drug delivery platforms, primarily rooted in nanotechnology, and is a potential solution for limitations associated with IFNα therapy. These pioneering drug delivery systems encompass a diverse range of NPs (for both targeted and controlled release), such as PNPs, solid-lipid NPs, nanostructured lipid carriers and polymeric micelles. The development of controlled-release formulations, however, requires a meticulous and systematic approach to optimize various parameters, such as the composition of the polymer matrix and the ratio of the drug to matrix-forming polymer. Conventional trial-and-error methods often demand extensive resources, including numerous experimental trials, to achieve a satisfactory outcome. This process becomes increasingly inefficient and resource-intensive when multiple factors are involved. As a result, innovative strategies are needed to improve efficiency and precision in the formulation of controlled-release systems [226].

Statistical Design of Experiments (DoE) methodologies have emerged as a solution to these challenges, offering a structured approach to streamline the optimization process. DoE minimizes the experimental burden while addressing the complexity of formulation development. Its widespread adoption in the pharmaceutical industry highlights its ability to generate statistically robust insights and cost-effective solutions for the optimization of drug formulations [226, 227]. In pharmaceutical research, Response Surface Methodologies (RSMs) like the Central Composite Design (CCD) and Box–Behnken Design (BBD) are commonly employed for optimizing independent variables. The CCD, introduced by Box and Wilson in 1951, is particularly noteworthy. It combines two-level factorial design points, star points to extend the design space for estimating quadratic terms, and central points to assess experimental error [228]. By incorporating rotatable star points with extreme values, CCD provides greater flexibility and more accurate predictions than BBD, making it advantageous for optimizing complex formulations [229]. Following this trend, this chapter showcases the fabrication and statistical optimization of biodegradable IFNα-loaded-PLGA NPs (IFNα-PLGANPs) for the controlled release of IFNα 2b for the treatment of skin cancer. These controlled-release NPs have been developed to decrease the dose and dosing intervals required for treatment, potentially decreasing adverse effects and cost of treatment. Statistical optimization of the formulated IFNα-PLGANPs has been undertaken to produce NPs of an adequate size for skin permeation, a preferable zeta potential to ensure particulate stability and an ideal release profile to allow for the controlled release of IFNα over a period of 5 days.

Once the optimized IFNα-PLGANPs have been developed and characterized, these NPs have been combined with the Cur-FeONPs presented in Chapter 4 to develop a synergistic anticancer combination therapy for MM. This combination is intended to mitigate side effects due to high systemic doses, further improve patient compliance, shorten treatment durations, and address issues such as recurrence and metastasis. Cytotoxicity and antiproliferation studies have further been presented in this chapter highlighting the benefits of using the proposed combination therapy and its potential for targeted administration to the affected skin cancer site.

5.2 Materials and Methods

5.2.1 Materials

Iron (III) chloride hexahydrate (FeCl3·6H2O), iron (II) chloride (FeCl2·4H2O), and dimethyl sulfoxide (DMSO) was purchased from Thermo Fisher Scientific (Johannesburg, South Africa), ammonium hydroxide (NH_4OH) from EMD Chemicals (Modderfontein, South Africa), Cur powder from Chem-Impex Int'l Inc. (Wood Dale, IL, USA) and IFNα-2b, Bovine Serum Albumin (BSA) Chondroitin Sulphate, PEG, and PLGA, from Merck Life Science (Pty) Ltd (Modderfontein, South Africa). NIH/3T3 mouse fibroblast cells (ATCC CRL-1658) were obtained from the ATCC (American Type Culture Collection, Manassas, VA, USA), Dulbecco's Modified Eagle Medium (DMEM) from Life Technologies Limited “Gibco” (Paisley, UK) and Fetal bovine serum from PAN Biotech (Aidenbach, Germany). The model malignant melanoma cell line (A375) was procured from Cellonex (Johannesburg, South Africa), Human IFNα Kits, from Thermo Fisher Scientific (Vienna Austria) and the MTT Cell Proliferation Kit I from Roche (Basel, Switzerland). All other chemicals were utilized as received without further modification.

5.2.2 Preparation and statistical optimization of the IFNα-loaded PLGANPs

IFNα-loaded NPs were prepared using a double emulsion solvent evaporation method. In brief, PEG and PLGA were dissolved in 2 mL of dichloromethane (DCM), which was thereafter mixed with a protein solution consisting of IFNα diluted 20-fold with PBS. The mixture was then emulsified for 30 seconds using a probe sonicator (Model W-220, Heat Systems Ultrasonics) at 70 W powers and a frequency of 20 kHz. This primary emulsion was then added to 3.5 mL of 2 wt% aqueous PVA solution and sonicated for 60 seconds to form a water/oil/water (w/o/w) double emulsion. The DCM was thereafter evaporated by continuous stirring at 800 rpm for 3 hours using a magnetic stirrer (IKA RET B). After complete evaporation of DCM, the solid NPs (IFNα-PLGANPs) were collected, dried and stored at -20°C for further analysis.

Statistical optimization of the IFNα-PLGANPs was conducted using Design-Expert® DoE software (Version 8, StatEase, Inc., Minneapolis, MN, USA) through a factorial design (FD). For the DoE the IFNα-loaded NPs (IFNα-NPs) formulations (n=7) were prepared using the modified double emulsion solvent evaporation method mentioned above. For the DoE, the PEG content was varied in ratios of 33%, 61.5%, and 90% relative to PLGA to leverage PEG's superior hydrophilicity for enhancing and optimizing IFNα release, with IFNα solutions of 20 to 40 µL also investigated. All other formulation parameters were maintained as previously described. Control formulations without IFNα were prepared in parallel to match the design formulations for comparative studies. The detailed DoE IFNα-PLGANP formulations are provided in Table 5.1.

Table 5.1: Formulation compositions as generated by the 2^2 FD.

Formulation code	**Point type**	**PEG-to-PLGA ratio**		**INF load**	
		Coded	**Actual (%)**	**Coded**	**Actual (µl)**
F1	Factorial	-1	33	-1	20
F2	Factorial	+1	90	-1	20
F3	Factorial	-1	33	+1	40
F4	Factorial	+1	90	+1	40
F5	Center	0	61.5	0	30
F6	Center	0	61.5	0	30
F7	Center	0	61.5	0	30

5.2.2.1 Synthesis Validation of the IFNα-PLGANPs

FTIR analysis was conducted to detect the distinctive functional groups of the optimized IFNα PLGANPs, pure PLGA and IFNα as described in Chapter 4, Section 4.2.3.

5.2.2.2 SDS-Page Gel-Electrophoresis assessment for IFNα-PLGANPs

SDS-PAGE analysis was performed on the IFNα-PLGANPs samples using a Bio-Rad vertical electrolysis cell Criterion system (Bio-Rad Laboratories Pty Ltd., California, USA) to ascertain the integrity of IFNα during the NP formulation process. The apparatus setup, sample loading and gel visualization for this analysis were conducted in accordance with the SDS-PAGE protocol, as outlined by the system manufacturer. The test gels were prepared as per Table 5.2.

Briefly, after preparation, the gel solution was poured into the gel-casting casing and allowed

to polymerize. Isobutanol (100µL) was used to overlay on top of the casted resolving gel and allowed to stand for 3 minutes before removal and rinsing with double distilled water (ddH_2O; resistivity between 15 and 18 MΩ cm^{-1}). A paper towel was used to dry the casing before adding onto the resolving gel, the 4% stacking gel solution. A 10-well comb was thereafter inserted into the stacking gel to allow formation of wells during polymerization. A volume of 10µL of each sample was then added into respective wells. A Tris-HCl running buffer was used with a standard voltage applied for 60 minutes. The gels were thereafter removed from the cassettes and washed three times with ultrapure water (MilliQ water; resistivity >18.2 MΩ cm^{-1}). Gel staining was conducted by immersing the gels in a staining solution (Coomassie Brilliant Blue R-250) for 1 hour in an orbital shaker (50rpm, 25°C). After washing out with MilliQ water a destaining solution was added. MilliQ water was used for rinsing prior to gel visualization. As controls, BSA and Chondroitin Sulphate were added into separate wells and run as per the protocol.

Table 5.2: SDS-Page Gel-Electrophoresis Test Gel Components.

Chemical	**4% sample gel (stacker)**	**10% sample gel (separator)**
	2 gels	2 gels
Acrylamide/ bisacrylamide solution (ml)	0.5	3
Gel buffer (3X) (ml)	1.5	5
Glycerol (ml)		1.5
Add water to final V (ml)	6 (4)	15 (5.5)
Polymerise by adding		
APS (10%) (µl)	45	75
TEMED (µl)	9	7.5

5.2.3 Determination of Particle Size and Zeta Potential of the DoE formulations

DLS and phase-analysis light scattering measurements were conducted on a Zeta Sizer instrument (NanoZS, Malvern Panalytical, Malvern, UK) to determine the mean hydrodynamic diameter and zeta potential of the synthesized IFNα-PLGANPs DoE formulations as outlined in Chapter 4, Section 4.2.4.

5.2.4 Drug Loading Capacity and Adsorption Efficiency of the DoE formulations

For the drug loading analysis, 10 mg of IFNα-PLGANPs underwent hydrolysis with 1N NaOH

(2 mL) under moderate stirring for 20 min to 1 h at room temperature (25 ºC) as outlined by Saez *et al*. [230]. The resulting solution was neutralized with 1N HCl and the concentration of IFNα thereafter determined using the bicinchoninic acid method and microBCA protein assay reagent kit (Pierce, Rockford, IL, USA). The encapsulation efficiency (EE) of IFNα was calculated as the ratio of experimental to theoretical IFN loading, expressed as a percentage. The experimental loading level of IFNα was thereafter determined by dividing the mass of IFNα recovered from the NPs by the mass of the hydrolyzed NPs, expressed as a percentage (w/w). The theoretical IFN loading parameter was defined as the initial mass of IFNα introduced in the process divided by the initial mass of PLGA, assuming that the mass of IFNα is negligible compared to that of PLGA. As an additional control, for all studies quantifying IFNα, a Human IFNα ELISA Kit (Thermo Fisher Scientific, Vienna, Austria) was used to confirm the stability of the loaded IFNα during formulation and through the analysis procedure.

The Adsorption Efficiency (%AE) and Drug (IFN) Loading Capacity (%DLC) were determined by quantifying free IFN in the supernatant after the loading procedure. %AE and %DLC were computed using Equations 5.1 and 5.2, respectively.

%AE (Percent Encapsulation Efficiency): Represents the percentage of the drug successfully encapsulated within the NP formulation relative to the initial drug amount.

$$\%AE = \frac{D_l - D_s}{Dl} \times 100\% \qquad (5.1)$$

Where Dl is the initial drug amount (ng), and Ds is the free drug amount in the supernatant (ng).

%DLC (Percent Drug Loading Capacity): Represents the percentage of the drug loaded into the formulation relative to the total weight of the NPs formulation.

$$\%DLC = \frac{\text{Amount of drug loaded}}{Wf} \times 100\% \qquad (5.2)$$

Where Wf is the total weight of NPs formulation in ng.

5.2.5 *In vitro* Release Analysis of the IFNα-PLGANPs of DoE formulations

To determine the drug release of IFNα from the IFNα containing NPs, 10mg of the respective NPs were suspended in a dialysis membrane within 2.5 mL of release medium

(PBS, pH 7.2, with 0.001% Tween 80 and 0.1% sodium azide) [230]. This setup was thereafter incubated in an orbital shaking incubator (YIHDER LM-530, YIHDER Co., Ltd., Taipei, Taiwan) at 37 ºC rotating at 35 rpm. At specified time intervals (8h, 12h and 1, 2, 3, 4 and 5 days), samples (60 µl) were removed and analyzed using the microBCA assay on a multimodal microplate reader (Victor X3, PerkinElmer, Waltham, MA, USA) at 595 nm in three separate instances. The amount of IFNα-2b released was then calculated, using a standard curve, with respect to the total mass of IFNα-2b contained in the suspended NPs. At all time-points, the volume extracted was replaced with an equal volume of fresh release medium to maintain sink conditions. The standard curve for the quantification of IFNα has been provided in Figure 5.1.

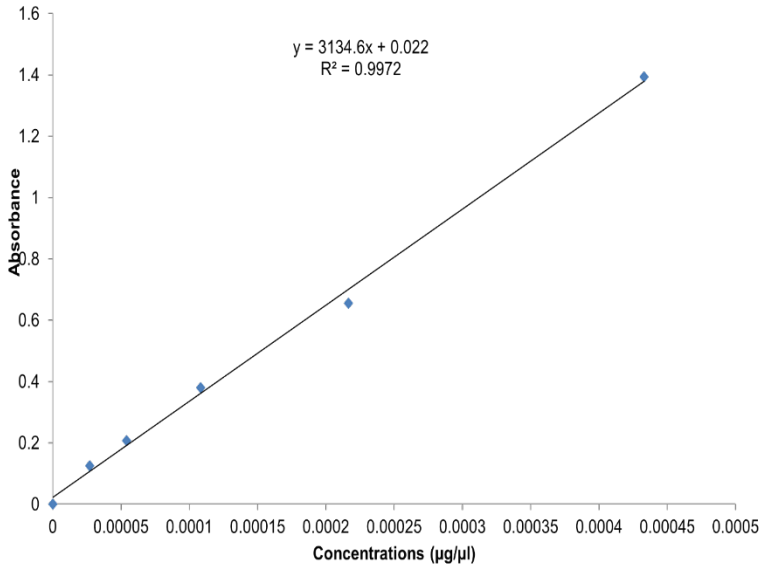


Figure 5.1: Standard curve of IFNα using the microBCA assay at 595 nm. The standard curve serves as a reference to determine the concentrations of IFNα in unknown samples by correlating their absorbance readings to the established curve. Accurate quantification of IFNα is crucial in various research and clinical contexts, including immunological studies and therapeutic monitoring.

5.2.6 Optimization of the IFNα-PLGANPs DoE formulations

To systematically evaluate and optimize the IFNα-PLGANP formulation, the factorial design was used. The optimal mathematical models were selected based on an assessment of statistical parameters such as, p-value, R^2, adjusted R^2, predicted R^2, CV, and predicted residual sum of squares (PRESS). Second-order polynomial equations were derived to express the relationship between responses and input parameters. The response

optimization was performed using numerical and graphical techniques, employing the desirability approach and overlay plots, respectively, to achieve an optimized formula with desirable drug load and polymeric proportions. The criteria used for optimization was a minimized size and drug release after 5 days (RD5).

5.2.6.1 Characterization of the Optimized IFNα-PLGANPs

5.2.6.2 Determination of Particle Size, Zeta Potential, and Morphology

Particle size, zeta potential, and morphology analysis of the optimized IFNα-PLGANPs were determined using the same methods and equipment, as described in the previous Chapter 4, Section 4.2.4.

5.2.6.3 Determination of the Thermal Characteristics of the optimized IFNα-PLGANPs

DSC was performed on the optimized IFNα-PLGANPs using a DSC822E instrument (PerkinElmer, USA) to investigate the thermal properties of the formulation in reference to PLGA using the method as described in Chapter 4, Section 4.2.5.

5.2.6.4 Crystallographic Structure

XRD analysis was conducted on the pure IFNα-2b, PLGA and the optimized IFNα-PLGANPs using a RIGAKU MiniFlex instrument (RIGAKU Inc., Tokyo, Japan) to evaluate the crystallinity of IFNα before and after synthesis of the IFNα-PLGANPs, using the method as described in Chapter 4, Section 4.2.6.

5.2.7 Cell culture and Cytotoxicity and Antiproliferation Assays

The cytotoxicity and antiproliferation of the optimized IFNα-PLGANPs were evaluated on NIH-3T3 and A375 cells using the MTT assay, as described in Chapter 4, Section 4.2.8. For the analyses, IFNα-PLGANPs at concentrations of 10, 5, 2.5 and 1.25 µg/µL were evaluated, with the cell studies undertaken for 24, 48, and 72 hours.

5.2.7.1 Evaluation of the Cytotoxicity and Antiproliferation Potential of the combined Cur-FeONPs and the Optimized IFNα-PLGANPs

In accordance with the focus of this study, the combination of the Cur-FeONPs synthesized in Chapter 4 and the optimized IFNα-PLGANPs, each at concentrations of 10, 5, 2.5 and 1.25 µg/µL were evaluated, with the cell studies undertaken for 24, 48, and 72 hours, as described previously. This was undertaken to ascertain the synergistic potential of the two NP platforms, as well as their potential to be incorporated into a non-surgical intervention for MM skin cancer. Additionally, as a comparison, the combination of Cur-FeONPs and

optimized IFNα-PLGANPs were subjected to *in vitro* drug release analyses, as previously described, to ascertain the effect of combining the NPs on their independent drug release.

5.2.8 Statistical analysis

All results were reported as mean ± standard deviation (SD) from triplicate measurements. Statistical analyses were performed using the SPSS software (SPSS 29, IBM, SPSS Inc, Chicago, IL, USA), with One-way analysis of variance carried out. Differences between means were compared using Tukey HSD multiple range test at a significance level of $p < 0.05$.

5.3 Results and Discussion

5.3.1. Synthesis Validation of IFNα-PLGANPs

5.3.1.1. Evaluation of the Chemical Stability and Functional Transformation of the IFNα-PLGANPs

The mean FTIR spectrum of PLGA, as shown in Figure 5.2, featured characteristic bands at 1080 cm^{-1} (C-O-C stretching), 1750 cm^{-1} (C=O stretching), 1400–1450 cm^{-1}, 2940–3000 cm^{-1} (C-H vibrations in methyl groups), 1270 cm^{-1} (OH vibrations), and 1170^{-1} (C-O stretching). This band profile aligns with the reported FTIR spectrum for PLGA, as confirmed by a study conducted by Paragkumar *et al.,* While PLGA and the IFNαPLGANP exhibited similarities, some variations in peak intensity were observed. For instance, the carbonyl and C–O–C stretching peaks at approximately 1750 and 1080 cm^{-1}, respectively, were noted to shift towards lower wavenumbers in the ATR spectrum for both polymers [231],. In the single bond region (4000–2500 cm^{-1}), the wavenumber range for CH_3 vibrations in PLGA and IFNα is 2940–3000 cm^{-1}. Specifically, IFNα displayed bands at 2920 cm^{-1} (asymmetric CH stretching) and 2870 cm^{-1} (symmetric CH stretching). In the double bond region (2000–1500 cm−1), PLGA is characterized by a representative band at 1750 cm^{-1}, while IFNα-2b exhibits bands in the range of 2950–3507 cm^{-1}. These findings provided insights into the molecular interactions and bond characteristics of the PLGA-IFNα system and proved successfully synthesized of IFNα-2b-loaded PLGANPs [221].

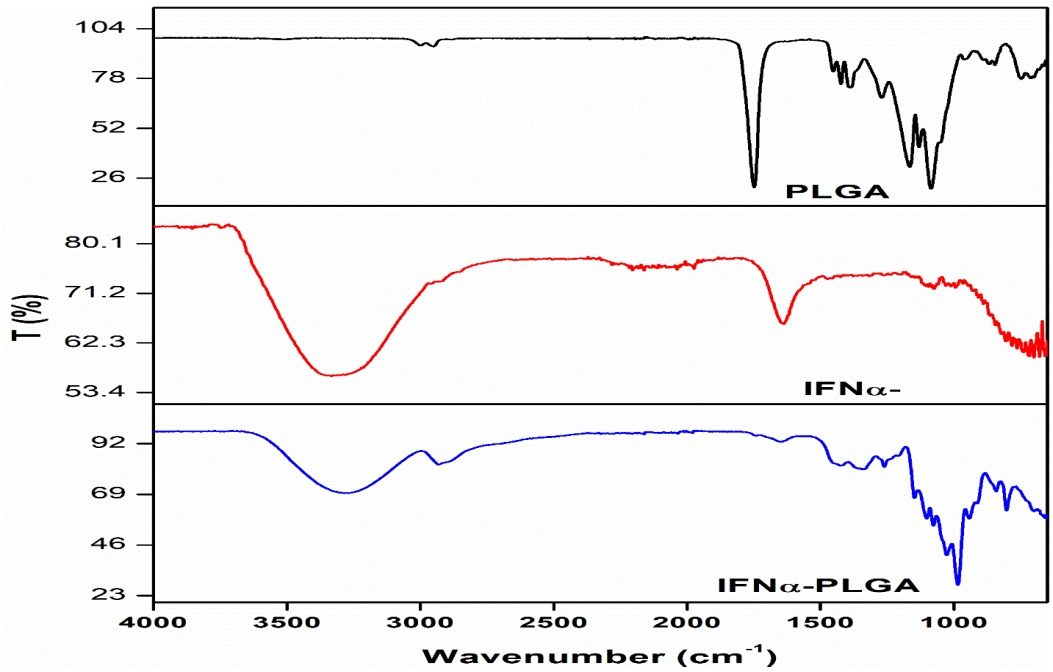


Figure 5.2: Scheme of FTIR spectra of the IFNα-loaded PLGANPs, pure IFN-α 2b, and PLGA. The FTIR analysis confirms the successful incorporation of IFNα into the PLGA NP s, as evidenced by the presence of characteristic protein absorption bands alongside PLGA's peaks. These spectral features suggest potential intermolecular interactions between the polymer and the protein, which could influence the release profile and bioactivity of IFNα from the NPs.

5.3.1.2 SDS-Page Gel-electrophoresis assessment for IFNα-PLGANPs

Human IFNα-2a, with a molecular weight of approximately ~19.4 kDa, and BSA, with a molecular weight of ~66.5 kDa, is often compared in SDS-PAGE analysis. BSA is commonly used as a molecular weight marker and a stabilizing agent in biochemical assays.

SDS-PAGE migration patterns in human IFNα-2a band appear at ~19 kDa on the SDS-PAGE gel, due to its smaller size, it migrates faster and forms a band in the lower region of the gel. While BSA band appears at ~66 kDa, migrating slower because of its larger size, forming a distinct band in the upper region of the gel.

Both proteins are typically visualized after electrophoresis using stains such as Coomassie Brilliant Blue or Silver Stain. The band intensity reflects the amount of protein loaded and the efficiency of the staining process. Evaluation of the IFNα-PLGA-NPs, as shown in Figure 5.3, depicted that IFNα migrated fast through the gel to the bottom area comparative to pure IFNα, with no additional bands forming, noting that the molecule was intact and that no degradation occurred during the formulation process.

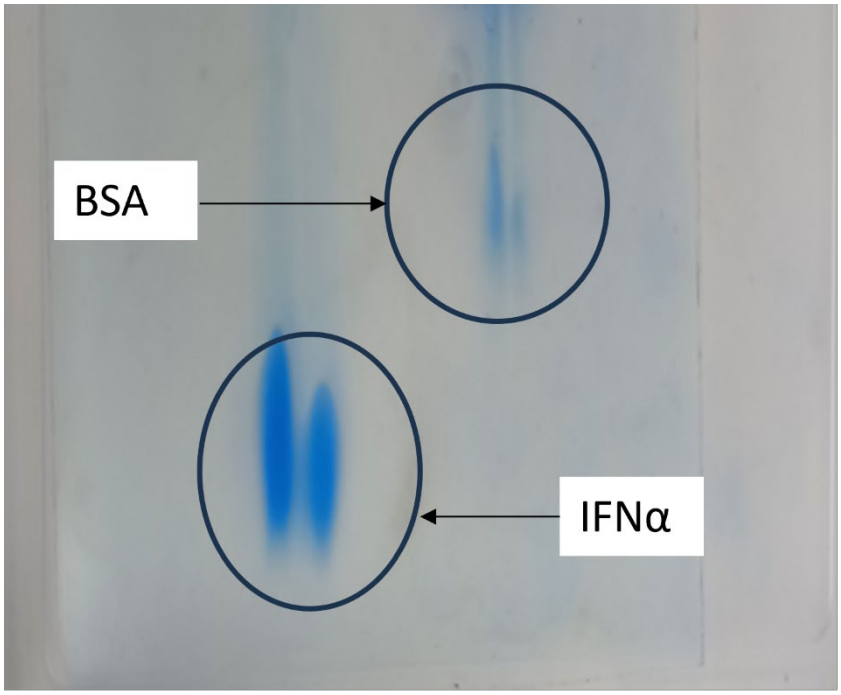


Figure 5.3: Visualization of protein separation and characterization of the molecular weight properties of the IFN-PLGANPs and BSA. The resulting bands indicate successful loading and stability of IFN within the NP formulation. The migration pattern and band intensity provide insights into the integrity and encapsulation efficiency of the proteins, as well as potential interactions between IFN and the PLGA matrix. This analysis confirms the presence of the target proteins and validates the NP formulation as a carrier for therapeutic protein delivery

5.3.2 Evaluation of the Experimental Design

5.3.2.1 Particle Size Analysis

The optimization process for IFN-loaded PLGANPs involved a two-level FD with the ratio of PEG to PLGA (factor A) and IFNα concentration (factor B) as independent variables. The particle size (R1) and release dynamics (R2, R3, R4 corresponding to Day 1, Day 3, and Day 5 release rates) were analyzed as response variables.

The particle size (R1) ranged from 59.54 nm to 127.3 nm across the formulations, as described in Table 5.3. The mean particle size was 90.73 nm, which is suitable for drug delivery applications as particles within this size range exhibit favorable biodistribution and tumor penetration.

The particle size of IFN-PLGANPs formulations, as presented in Table 5.3 and visualized in Figure 5.3.a, was influenced by two key factors, PEG-to-PLGA ratio (A) and IFNα loading (B). The trend observed on formulations with higher PEG-to-PLGA ratios (e.g., F2) demonstrated smaller particle sizes, as evidenced by F2 (62.31 nm) and F3 (59.54 nm) although the ratio of PEG-to-PLGA was in low in F3. Conversely, formulations with lower

PEG content, such as F1 (127.3 nm), exhibited significantly larger particle sizes. This could be attributed to PEG enhancing the hydrophilicity, reducing NPs aggregation during the emulsion process. This therefore resulted in smaller, more stable particles. Likewise, lower PEG ratios increased the dominance of PLGA, leading to larger particles due to the slower emulsification and higher viscosity of the polymeric matrix. It was however seen that a higher PEG-to-PLGA ratio facilitated the formation average of less than 100 nm NPs, ideal for enhancing drug diffusion and cellular uptake. However, an excessively high PEG ratio might compromise structural integrity, necessitating a balance between the polymers.

Like PEG-PLGA rations, variable B (IFN-load) displayed those formulations with higher IFNα loading, such as F3 and F4 (59.54 nm and 93.17 nm, respectively), exhibited smaller particle sizes compared to lower IFNα-loaded formulations like F1 (127.3 nm). This can be due to higher IFNα concentrations promoting a tighter packing of NPs due to B-polymer interactions, reducing particle size. Increased IFN-loading may also reduce the overall polymer density, leading to reduced particle sizes, enhancing bioavailability and cellular interaction. The combined influence and interaction of Variables A and B) therefore plays a critical role in determining particle size. This was further seen in balanced levels of both factors (e.g., F5, F6, and F7, with sizes around 96–99 nm) result in moderately sized, uniform particles.

Analysis of variance (ANOVA) showed that the model was statistically significant for particle size ($p = 0.0013$), with significant effects from factors A (PEG-to-PLGA ratio, $p = 0.0045$) and B (IFNα load, $p = 0.0040$). The interaction between A and B (AB) was also significant ($p = 0.0007$), indicating that both polymer composition and drug loading play key roles in determining particle size.

Table 5.3: 2^2 FD matrix and responses results for the DoE IFN-PLGANPs formulations (n=3).

Formulation code	Size (nm)	SD	RD1 (%)	SD	RD3 (%)	SD	RD5 (%)	SD
F1	127.3	83.35	40.8038	1.60	45.9942	1.81	62.9295	2.30
F2	62.31	49.62	40.0548	2.12	57.4147	4.76	89.4213	3.77
F3	59.54	48.27	48.2765	2.54	62.5379	1.82	100.652	1.86
F4	93.17	71.61	49.7825	3.06	67.6185	2.99	100.601	1.30
F5	99.99	78.42	44.9205	0.83	60.0473	4.81	91.9394	5.38

F6	96.6	69.72	45.32	2.09	61.4214	9.19	93.0821	12.81
F7	96.2		42.2068	0.87	61.4171	8.29	90.7683	4.43

5.3.2.2 Release Dynamics

The release dynamics of IFN-PLGANPs DoE formulations, as evaluated over Days 1 (RD1), 3 (RD3), and 5 (RD5), provide a comprehensive understanding of the release profiles and their dependence on formulation parameters (Figure 5.3b-d and Table 5.3).

On Day 1 (RD1; (Figure 5.3b); Initial Release Stage), the release rates ranged from 40.05% (F2) to 49.78% (F4), with an average of 44.48%. Formulations with higher PEG content, such as F2, exhibited lower initial release while lower PEG ratios (e.g., F1) led to higher burst release. This trend reflects the interplay between PEG's hydrophilicity, which promotes faster degradation, and the protective effect of PLGA, which slows drug diffusion. The model indicated that initial release is primarily influenced by IFNα loading (B), reflecting diffusion-based mechanisms. A higher burst release (e.g., low PEG content) can also be detrimental by causing off-target effects. ANOVA analysis revealed significant model fitting for RD1 ($p = 0.0010$), with Factor A the most influential determinant of dynamic release on Day 1, emphasizing PEG's critical role in modulating initial drug diffusion.

At Day 3 (RD3; (Figure 5.3c). Sustained Release Phase), the release ranged from 45.99% (F1) to 67.62% (F4), with a mean of 59.49%. Formulations with balanced PEG-to-PLGA ratios, such as F5, F6, and F7, demonstrated controlled and sustained release, highlighting the synergistic effect of PEG and PLGA in modulating release kinetics. The trend underscored that balanced PEG-to-PLGA ratios and IFNα loading both contributed to sustained mid-term release. This stage represents the transition from initial burst release to steady-state drug diffusion, critical for maintaining therapeutic levels. These formulations provided steady drug availability, crucial for maintaining therapeutic activity over time. Interestingly, the factorial model for RD3 was highly significant ($p = 0.0011$), with both Factor A and Factor B contributing to release behavior.

At Day 5 (RD5; Figure 5.3d; Complete Release Dynamics), the release percentages extended up to 100.652% (F3), indicating complete drug release for high-PEG formulations. Formulations with moderate PEG content (e.g., F6 and F7) showed sustained release (~93–90%), achieving an optimal balance between rapid and controlled drug delivery. The model highlights that long-term release is influenced by both factors, with higher PEG-to-PLGA ratios and IFNα volume promoting sustained release. The negative AB interaction suggests

a potential for fine-tuning cumulative release by adjusting PEG and IFNα loading to prevent excessive degradation or burst release. Statistical evaluation of these results determined that the release dynamics on Day 5 were strongly influenced by both Factor A ($p = 0.0008$) and Factor B ($p < 0.0001$), with their interaction (AB) also showing significance ($p = 0.0013$). Figure 5.5 provides for the cumulative IFNα release profiles for each of the design formulations. Each curve represents a distinct formulation from the experimental design matrix, allowing for comparative analysis of release kinetics. The profiles demonstrate a biphasic release pattern characterized by an initial burst release followed by a more controlled and sustained release phase. This behavior is indicative of surface-associated IFNα being released rapidly, followed by the diffusion of encapsulated drug from within the polymer matrix. The results provide insight into how formulation parameters influence the release characteristics, with certain combinations promoting more sustained and controlled delivery. These findings are crucial for optimizing the therapeutic performance of IFNα-loaded PLGA NP s, particularly in enhancing bioavailability and reducing dosing frequency.

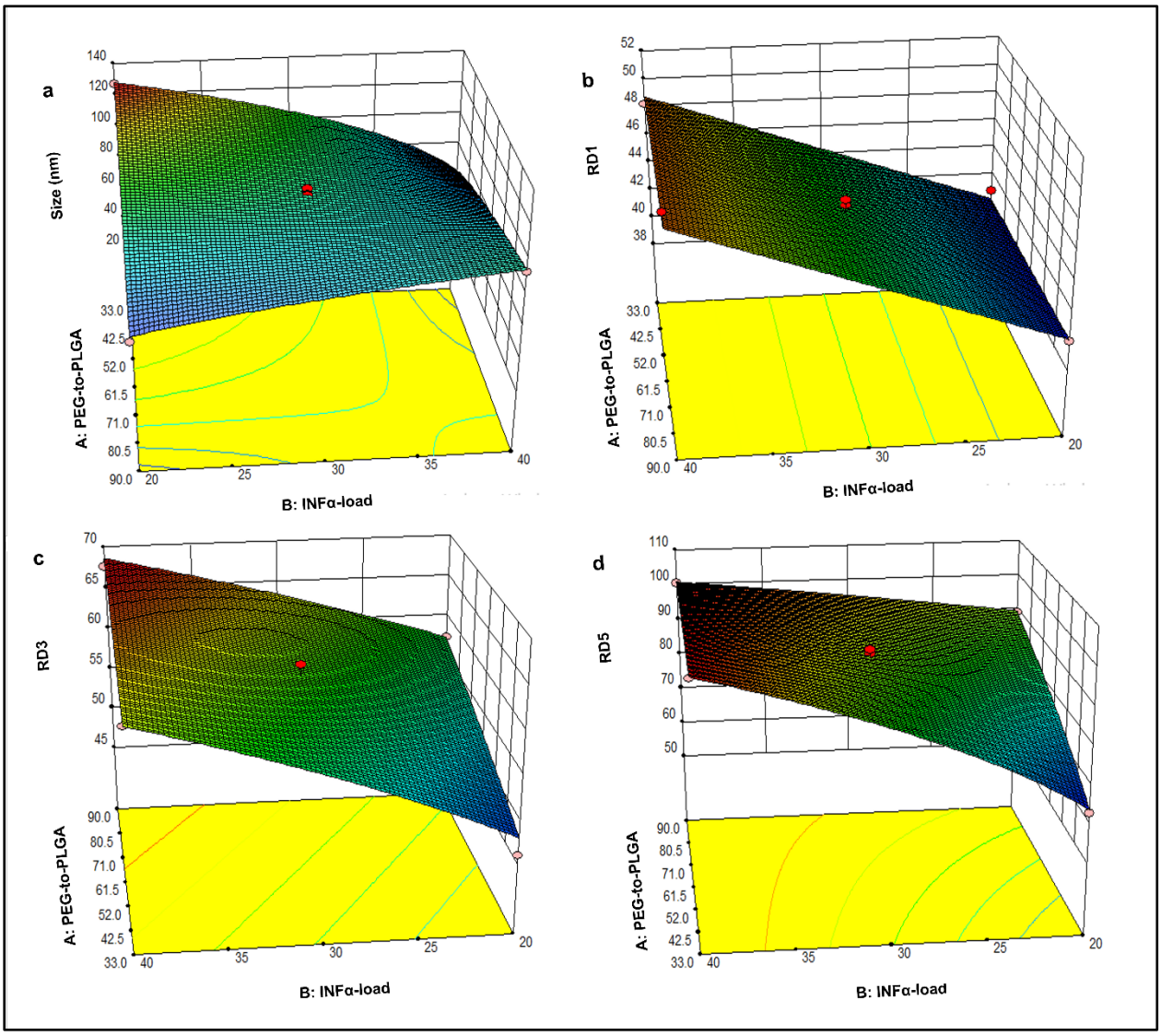


Figure 5.4: 3D plots portraying the influence of PEG-to-PLGA and the INFα-load on the (a) particle size, (b) cumulative release after one day (RD1), (c) cumulative release after three days (RD3), and (d) cumulative release after five days (RD5). These 3D plots were generated using statistical modeling techniques such as response surface methodology (RSM), enabling visualization of the interaction between formulation parameters and their effects on NP properties. The data help identify ideal formulation conditions that balance particle size, drug encapsulation efficiency, and stability for efficient therapeutic delivery of IFNα.

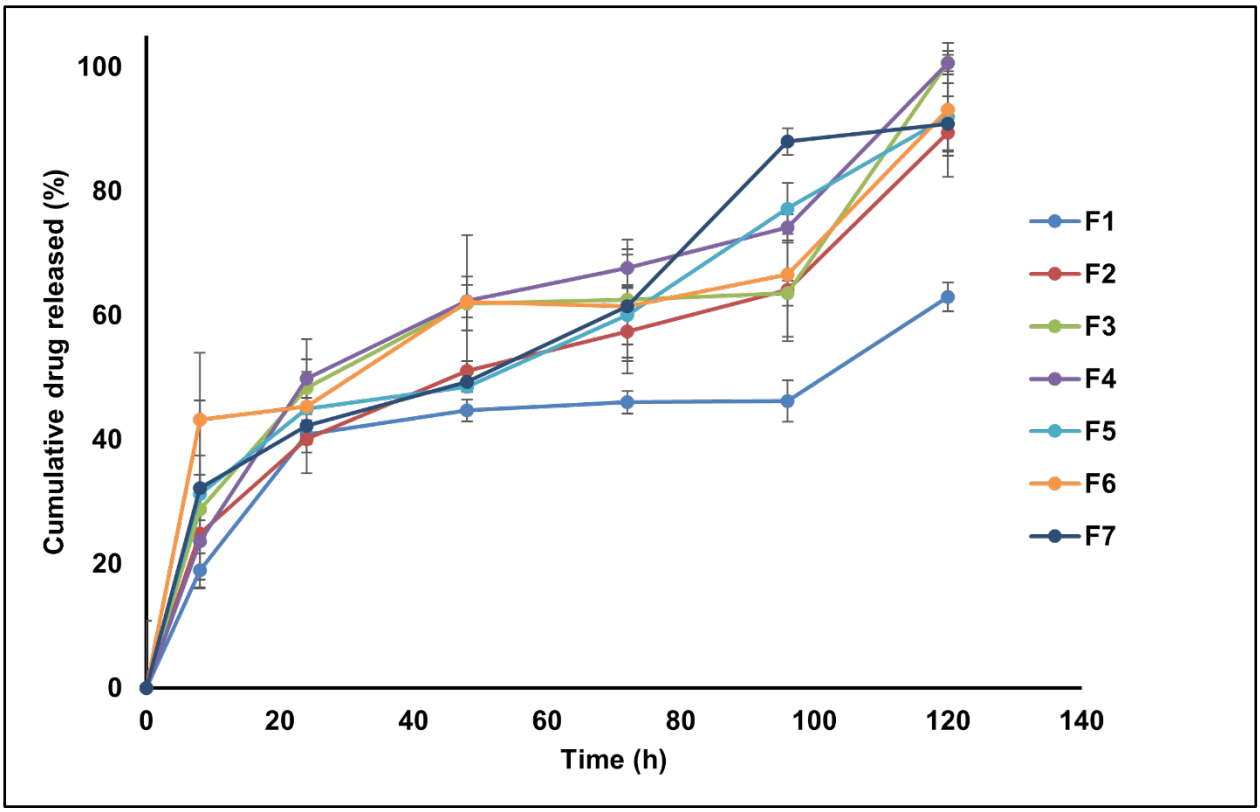


Figure 5.5: Release profiles of the prepared design formulations. This figure illustrates the cumulative in vitro release profiles of IFNα from various NP formulations designed using different PEG-to-PLGA ratios and drug loading concentrations. The release study was conducted under physiologically relevant conditions (e.g., pH 7.4, 37°C) over a specified time period to simulate systemic circulation and assess the sustained release behavior of the formulations.

5.3.2.3 Statistical Validation and Model Fit

The ANOVA results confirmed the statistical significance of the models for all responses, with R^2 values ranging from 0.90 to 0.99. High Adj R^2 values further validated the model's robustness, while non-significant lack of fit indicated excellent compatibility between experimental data and the factorial design. The key observations from these findings demonstrated that for PEG-to-PLGA Ratio (A), higher PEG content enhanced hydrophilicity, leading to faster degradation and higher release rates. This also contributed to reduced particle size, facilitating better cellular uptake. While for IFNα Loading (B), Increased IFNα loading slightly enlarged particle size and influenced release, particularly on Day 5, due to structural modifications in the NP core.

5.3.2.4 Data Analysis and Optimization of the Statistical Design

A FD was employed to systematically investigate the effects of two independent factors, PEG-to-PLGA ratio (A) and IFNα volume (B), on the properties of the IFN-PLGANPs. The design matrix allowed for evaluation of their individual and interaction effects on the

prepared NPs crucial parameters including NPs size (R1), cumulative release after day 1 (R2), day 3 (R3), and day 5 (R4).

The principles of experimental design were applied to conduct a 2^2 full FD, resulting in seven formulations of IFN-loaded PLGANPs. The experimental data underwent mathematical transformation, and linear regression models were developed. These models were evaluated using ANOVA, with statistical significance determined based on p-values. Using ANOVA, the statistical significance of the models and factors (A, B, and AB) was determined based on p-values. Above all, the low probability values ($p < 0.0013$, < 0.0010, $= 0.0011$, and $= 0.0002$ for R1, R2, R3, and R4, respectively) emphasize the strong statistical significance of the constructed models for all responses, confirmed with a 95% confidence interval. The absence of a significant lack-of-fit, indicated by p-values of 0.2075, 0.8692, 0.1895, and 0.6029 for R1, R2, R3, and R4, respectively, further supports the models' excellent predictive ability, suggesting that the lack-of-fit has minimal impact compared to random error. The results also show that variations in the PEG-to-PLGA ratio significantly influence all the investigated responses, indicating a consistent impact of the PEG-to-PLGA ratio on NP properties, while INFα load significantly affects the release kinetics over time. Furthermore, the interaction between the independent variables variation exhibited significant impact on the size of the prepared particles and the cumulative release after day 5, demonstrating the interplay between PEG content and IFNα loading in controlling these outcomes.

The findings confirm that the PEG-to-PLGA ratio (Factor A) consistently impacts NP properties, particularly particle size and drug release rates. Meanwhile, the IFNα volume (Factor B) exerts its influence primarily on extended-release profiles. The significant interaction between factors underscores the importance of NP formulation optimization. The high predictive accuracy and reliability of the models affirm their utility in guiding future formulation strategies for IFN-PLGANPs.

Tables 5.4 and 5.5 present a comprehensive set of fitness statistics. The strong correlation between the anticipated and observed responses is reflected in the high R^2 values, exceeding 0.90. Additionally, all responses demonstrated excellent precision, with the predicted R^2 values closely matching the adjusted R^2 values. Lack of Fit, non-significant for all responses, confirming that the linear models are a good fit for the experimental data. Additionally, model selection considerations were directed towards the minimization of Prediction Error Sum of Squares (PRESS) values, reinforcing the efficacy of the selected models.

Table 5.4: Analysis of variance (ANOVA) for different responses of IFN-PLGANPs formulations.

	Size (Y1)	**RD1 (Y2)**	**RD3 (Y3)**	**RD5 (Y4)**
Sources	**P value**	**P value**	**P value**	**P value**
Model	0.0013	0.0010	0.0011	0.0065
A	0.0045	0.0010	0.0053	0.0156
B	0.0040		0.0007	0.0030
AB	0.0007			0.0154
Lack of Fit	0.2075	0.8692	0.1895	0.3563

Table 5.5: Model statistical fit parameters.

Parameters.	**Size (Y1)**	**RD1 (Y2)**	**RD3 (Y3)**	**RD5 (Y4)**
R^2	0.99	0.9054	0.9673	0.9926
Adj R^2	0.98	0.8864	0.9509	0.9853
Pred R^2	0.79	0.8437	0.8539	0.8780
Adeq Precision	30.4	12.940	22.731	32.571
C.V.%	9.78	2.80	6.56	4.11
PRESS	3.703E+11	12.77	3.622E+009	4.873E+010

Furthermore, the analysis of the FD results resulted in the derivation of the following first-order linear equations, which are expressed in terms of the coded factors as mentioned earlier:

$$(Y1-6)^3 = +7.267 \times 10^5 - 2.743 \times 10^5 \times A - 2.869 \times 10^5 \times B + 5.288 \times 10^5 \times A\,B \quad (5.3)$$

$$Y3\ (RD1) = +44.48 + 4.30\,B \quad (5.4)$$

$$(Y4)^3 = +2.172 \times 10^5 + 39137.62 \times A + 66797.75 \times B \quad (5.5)$$

$$(Y5)^3 = +7.619 \times 10^5 + 1.161 \times 10^5 \times A + 2.684 \times 10^5 \times B - 1.168 \times 10^5 \times A\,B \quad (5.6)$$

In Equation 5.3, both main effect terms, A and B, are shown to have statistically significant impacts on the cubic particle size responses, suggest that increasing PEG content or IFNα volume reduces particle size. While the AB interaction terms showed a positive effect, countering the individual reductions effect of each independent variable. In Equation 5.4,

release after Day 1 is mainly influenced by Factor B (IFNα volume), with a positive influence indicating that higher loading increases the initial release. Additionally, both main effects exhibit significant positive impacts on the cubic release responses observed on Day 3 (Equation 5.5). Moreover, as shown in Equation 5.6, the interaction term AB demonstrates a significant negative influence on the release responses during Day 5., whereas both factors A and B individually demonstrated a statistically significant positive effect by enhancing release on Day 5. Figure 5.6 presents the Pareto Charts showing the t-Value effect of the dependent variables on particle size, cumulative release after one day, cumulative release after three days, and cumulative release after five days, in correlation with the statistical data generated for the DoE. These Pareto charts provide essential insight into the formulation design space and help prioritize variables for optimization to achieve the desired particle size and drug release profile for effective IFNα delivery.

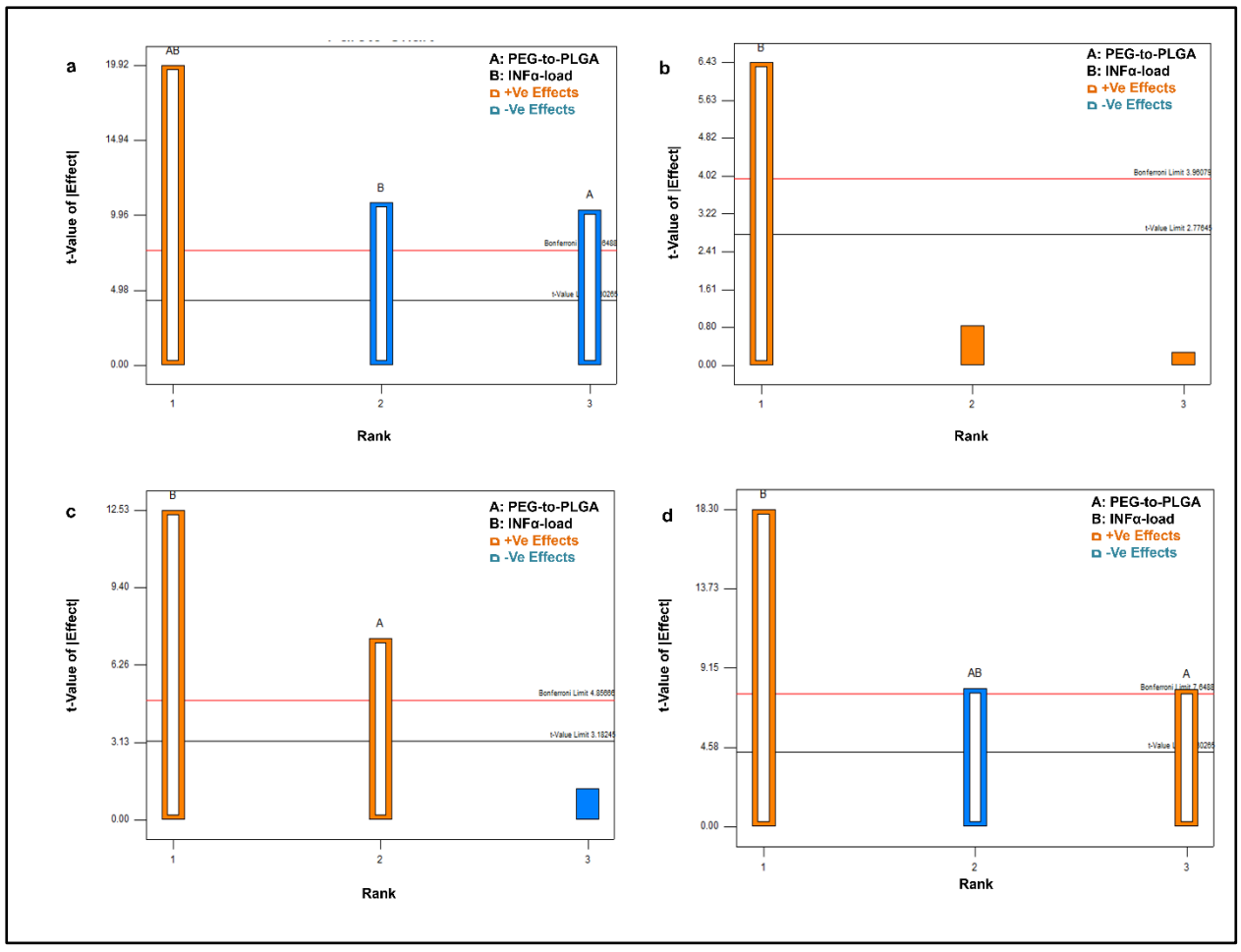


Figure 5.6: Pareto Charts showing the t-Value |effect| of the dependent variables on (a) particle size, (b) cumulative release after one day, (c) cumulative release after three days, and (d) cumulative release after five days. This figure presents a series of Pareto charts summarizing the influence of formulation parameters—specifically the PEG-to-PLGA ratio and the IFNα loading concentration—on four critical NP performance metrics. The charts are

based on standardized t-values derived from a factorial design analysis, representing the magnitude and statistical significance of the effect of each independent variable on the respective response. The vertical dashed line indicates the minimum threshold for statistical significance; bars extending beyond this line represent variables with a statistically significant influence on the outcome.

5.3.2.5 Constrained Statistical Optimization of the IFN-PLGANPs

The primary objective of utilizing the CCD-based optimization approach was to determine the optimal formulation parameters for preparing IFN-loaded PLGA NPs. To accomplish this, constraints were applied to both independent and dependent variables. The independent variables were constrained within a defined range ("in-range"), while the dependent variables, particle size and drug release percentage, were set to be minimized.

Table 5.6 presents the numerical optimization formula, offering a detailed overview of the specific values and conditions identified as optimal for the study. Figure 5.7a depicts the contour plot of numerical optimization, highlighting the selected optimal solution. Additionally, Figure 5.7b illustrates the desirability landscape, an optimal design space created by superimposing contour plots and main effect plots using the graphical optimization module of the CCD. The bright yellow regions in the design space signify areas that meet the specified optimization criteria.

The CCD model ultimately provided an optimized formulation, recommending a drug load of 20% volume and a PEG-to-PLGA ratio of 90%. This formulation was predicted to achieve ideal results, with a particle size of 65.68 nm and a 5-day drug release percentage of 89.95%. Together, these plots serve as critical tools in formulation development, enabling the identification of robust and reproducible NP designs for efficient and sustained delivery of IFNα.

Table 5.6: The selected optimal configuration from numerical optimization.

No	PEG-to-PLGA	IFNα load	Particle size	RD1	RD3	RD5	Desirability
1	90.00	20.08	65.68	40.22	57.50	89.95	0.764

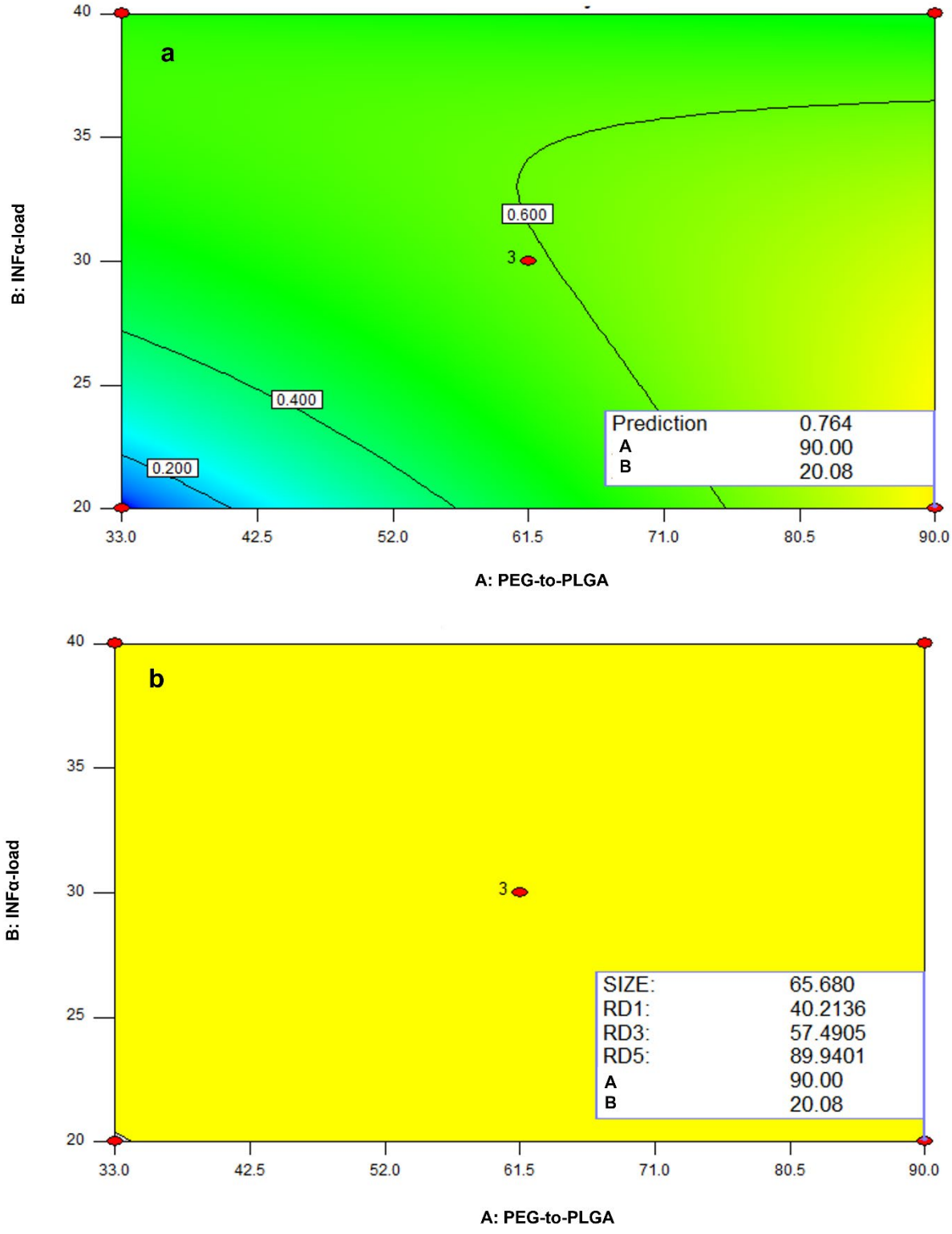


Figure 5.7: Contour plot of numerical optimization (a) and overlay plot of graphical optimization (b). This figure illustrates the outcomes of both numerical and graphical optimization strategies applied to identify the optimal formulation conditions for IFNα-loaded PEG-PLGA NPs based on desired physicochemical properties and release characteristics.

5.3.3 Analysis of the Optimized IFNα-PLGANPs

5.3.3.1 Particle Analysis

DLS and phase-analysis light scattering were employed to determine the mean diameter size and zeta potential of IFNα-PLGANPs. The average hydrodynamic diameter for IFN-loaded PLGA NPs was determined to be 90.73 nm, and the zeta potential was found to be in average of optimized formula -34.1 ± 4.5 mV (Figure 5.8). The results from DLS and zeta potential analysis highlight key physicochemical properties of optimized IFN-PLGANPs, critical for their stability and therapeutic efficiency. A hydrodynamic diameter of IFN-PLGANPs indicates a suitable size for enhanced penetration into tumor tissues, while a zeta potential ensuring good colloidal stability by preventing aggregation. Overall, these measurements confirm that the optimized IFNα-PLGANPs possess physicochemical attributes conducive to enhanced in vivo performance, including improved stability, bioavailability, and targeted delivery potential.

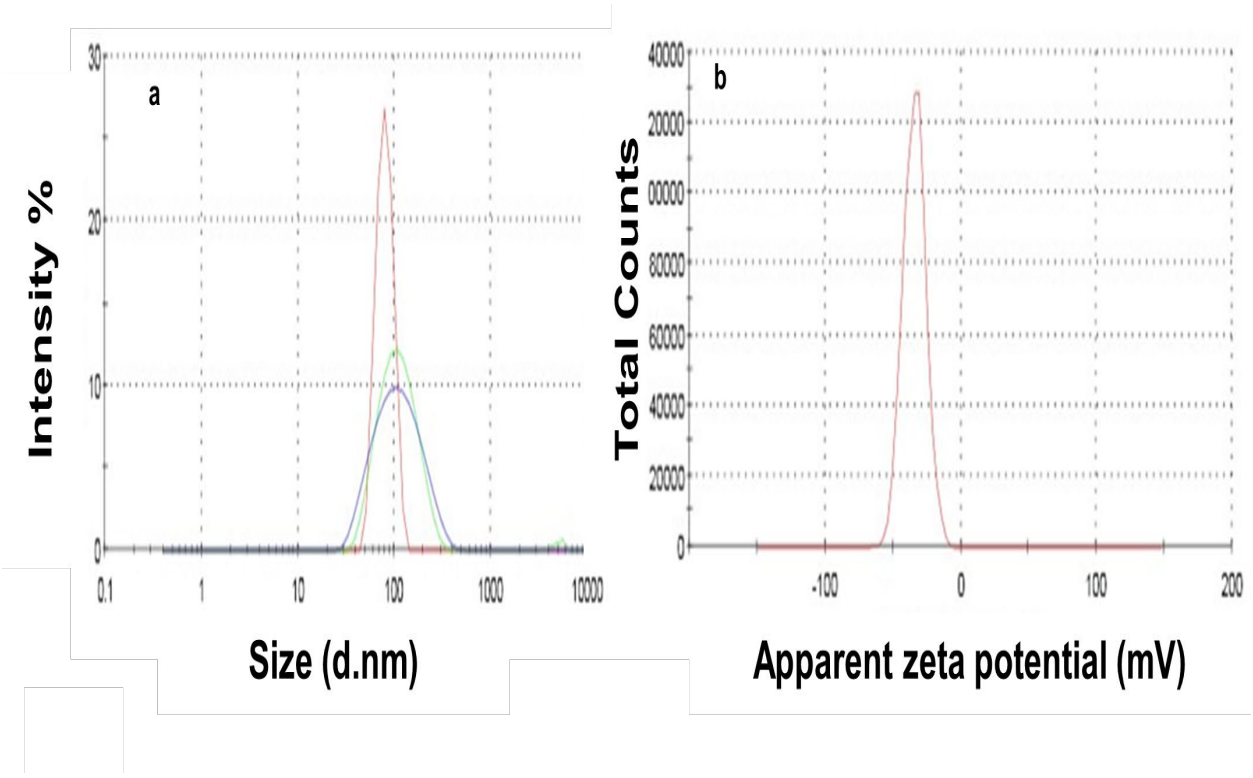


Figure 5.8: The average size (a) and zeta potential (b) for the optimized IFNα-PLGANPs. This figure presents the results of dynamic light scattering (DLS) and phase-analysis light scattering measurements used to evaluate the key physicochemical characteristics of the optimized IFNα-PLGA NP formulation.

5.3.3.2 SEM of the Optimized IFNα-PLGANPs

Representative SEM of NPs surface morphology has been shown in Figure 5.9. SEM images of the optimized IFNα-PLGANPs revealed that most of the NPs were spherical in

shape with a smooth surface and ≤ 100 nm in size. The organic solvent used in the preparation of IFN-PLGANPs in this study had a minimal impact on the NPs' properties. However, a study by Wan *et al*. highlighted that the choice of organic solvent and the feeding rate ratio of the outer to inner feed solution during the spray-drying process can significantly affect particle morphology. SEM analysis, depicted in, revealed that the NPs had a spherical shape with a wrinkled and porous surface [232]. These findings suggest that the synthesized system enhances IFN release from the polymer, enabling optimized and controlled release through precisely adjusted particle sizes. The consistent morphology and well-defined nanoscale architecture observed under SEM confirm the reproducibility and quality of the NP synthesis process, aligning with the intended design for effective drug delivery and biological interaction.

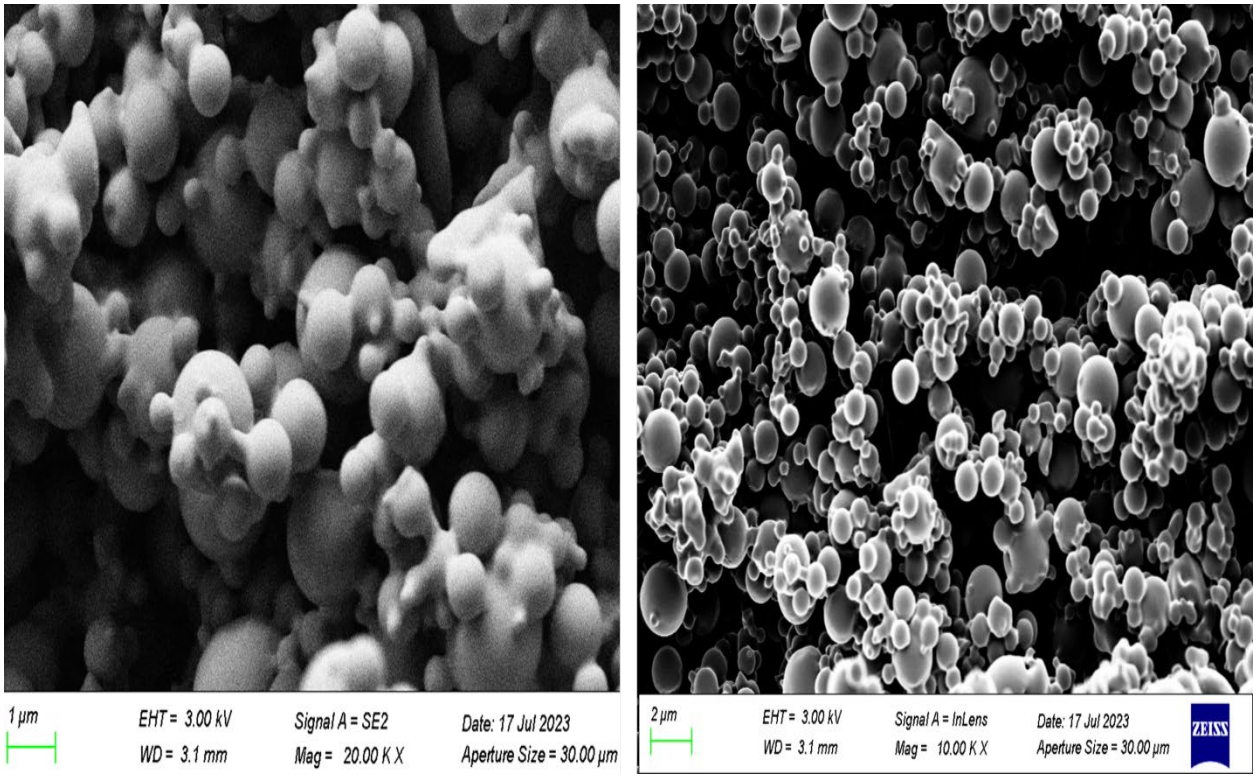


Figure 5.9: Scanning electron micrographs (SEM) of the IFNα-PLGANPs surface morphology. This figure displays high-resolution scanning electron microscopy (SEM) images used to assess the surface morphology and structural integrity of the optimized IFNα-PLGANPs. The micrographs reveal that the NP s exhibit a predominantly spherical shape with a smooth and uniform surface texture, indicative of successful encapsulation and stable NP formation.

5.3.3.3 Thermal Analysis of the Optimized IFNα-PLGANPs

DSC analysis confirmed the chemical interaction between PLGA and IFN when focusing on the comparison of the thermal behavior of IFN loaded in the IFNα-PLGANPs. This evaluation highlighted structural differences between free PLGA and IFNα-encapsulated PLGANPs.

Figure 5.10 displays the thermogram of free PLGA, which does not exhibit a distinct melting point, confirming its amorphous nature. The free PLGA polymer showed a small peak at 50°C, corresponding to the relaxation peak following the glass transition. Another peak at 340°C relates to the thermal decomposition of the polymer. The DSC curves indicate that free PLGA is thermally stable up to 250°C, aligning with the study by Mukerjee & Vishwanatha [233].

The results show that the NPs preparation method did not alter the polymer structure. The thermogram of IFN-loaded PLGA NPs additionally showed peaks at 130°C, 160°C and 300°C, confirming the successful entrapment of the drug within the PLGA matrix. This suggests that the incorporated drug exists in an amorphous or disordered crystalline state, forming a molecular dispersion or solid solution within the polymer. Additionally, the similarity in melting transition properties between loaded and unloaded NPs demonstrates that the encapsulation process did not impact on the integrity of the PLGA polymer.

In contrast, the thermogram of the optimized IFNα-PLGANPs shows a shift or broadening of the Tg peak and the absence of any sharp endothermic peak corresponding to free IFNα-2b. This suggests successful encapsulation of the protein within the polymer matrix and indicates molecular dispersion or entrapment of the drug rather than simple physical mixing. The absence of distinct thermal events related to crystalline IFNα-2b implies that the drug is either in an amorphous state or molecularly dispersed within the PLGA matrix, which can enhance drug release uniformity and bioavailability. These findings confirm the compatibility of IFNα-2b with PLGA and provide evidence of successful NP formulation at the molecular level.

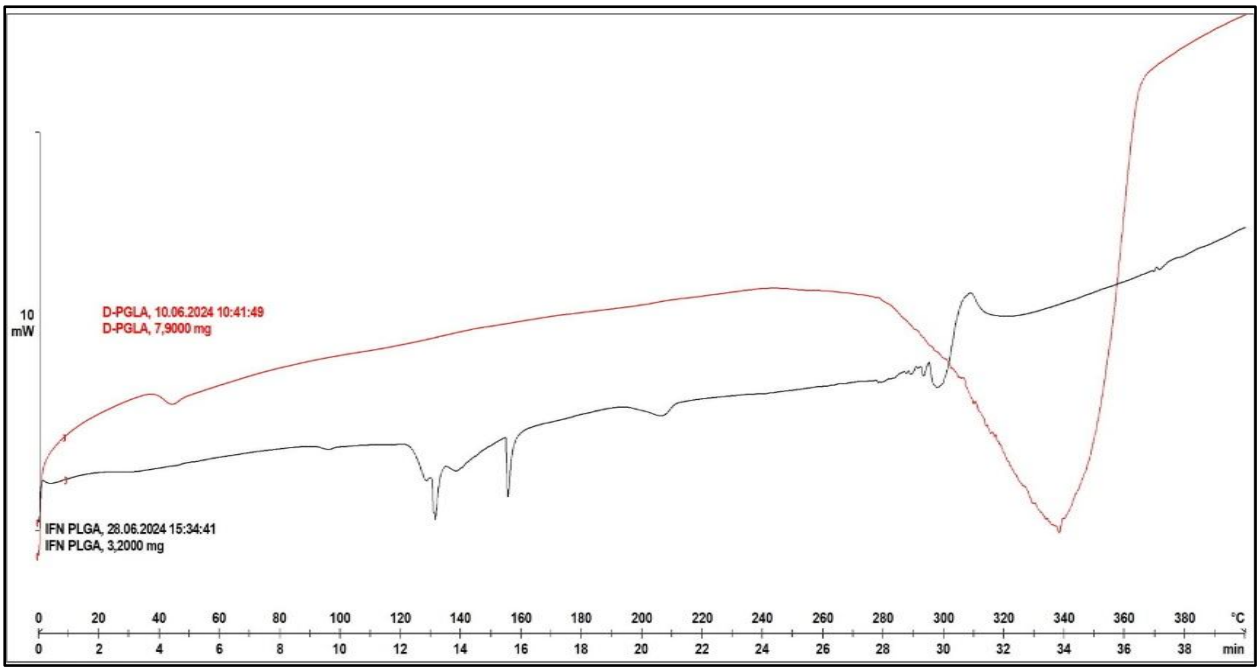


Figure 5.10: DSC curves of free PLGA, and the optimized IFNα- loaded PLGANPs. This figure presents the DSC thermograms used to investigate the thermal behavior and possible physicochemical interactions between IFNα and the PLGA polymer matrix in the optimized NP formulation. The thermogram of the free PLGA polymer displays a characteristic endothermic peak corresponding to its glass transition temperature (Tg), indicating its amorphous nature.

5.3.3.4 XRD analysis

XRD was employed to distinguish between crystalline and amorphous phases of NPs. The XRD analysis of IFNα, PLGA, and IFNα-PLGANPs was conducted using XRD. Figure 5.11 illustrates the XRD data within the 2θ range of 10°–90°. The XRD pattern of PLGA demonstrates the crystalline nature of IFNα-PLGANPs NPs after loading IFN into the PLGA polymer. The XRD patterns of IFNα-PLGANPs revealed numerous sharp peaks indicative of crystalline phases. Specifically, the XRD data, recorded in the 2θ range of 10°–90°, showed high-intensity peaks at 2θ angle values of 14.558°, 15.363°, 17.481°, 21.925°, 21.12°, and 23.9° for IFNα–PLGANPs. These peaks closely resemble those reported by Singh *et al.,* [234]. The presence of sharp, intense peaks suggests the presence of the crystalline form of the drug. In contrast, the XRD spectrum of free PLGA displayed no peaks but a broad amorphous band between 10° and 90°, indicating the amorphous nature of PLGA as a copolymer.

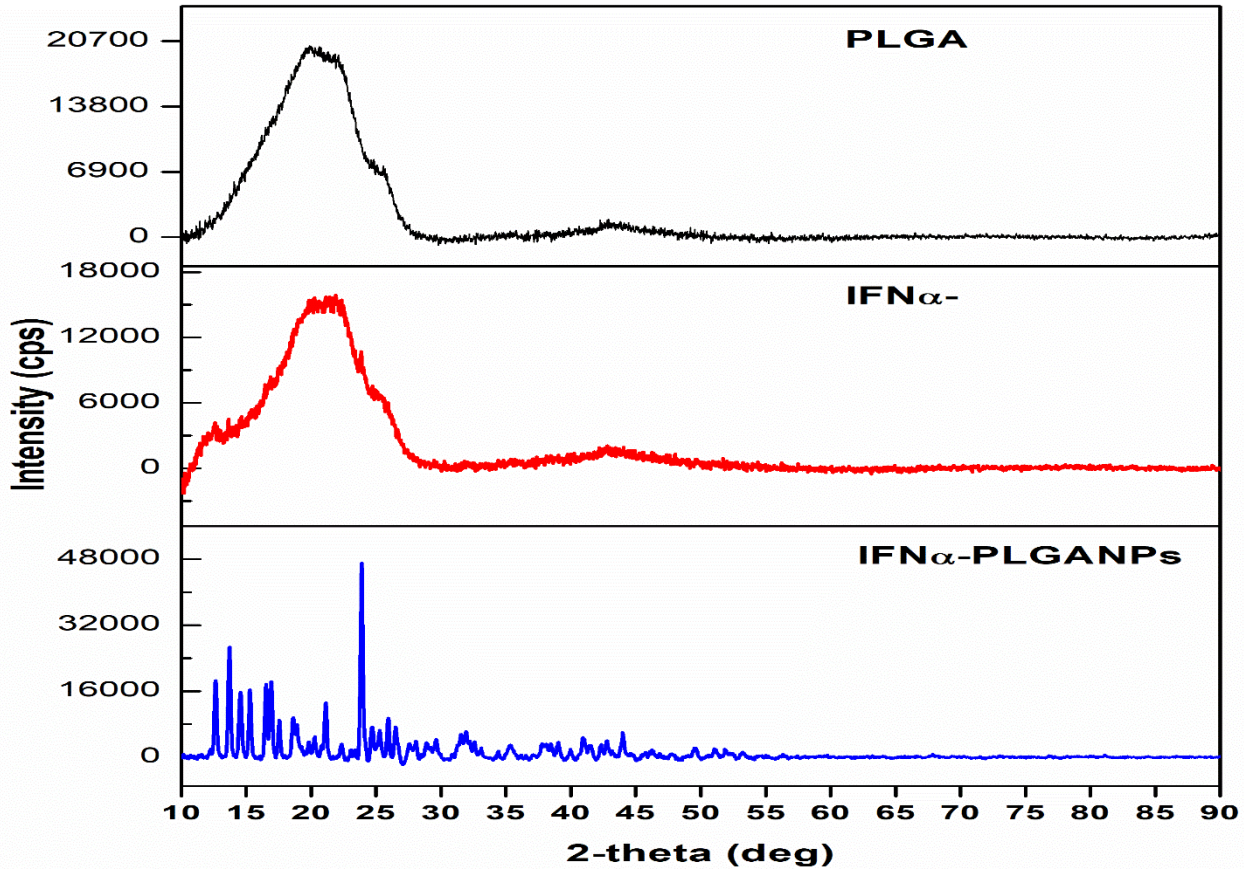


Figure 5.11: The XRD spectrum for IFN loaded PLGANPs, free IFNα, and amorphous in nature of free PLGA. This figure displays the XRD spectra used to evaluate the crystalline or amorphous nature of the individual components free IFNα, free PLGA polymer, and the optimized IFNα-loaded PLGA NPs. The XRD pattern of free IFNα exhibits distinct sharp peaks, characteristic of its crystalline structure. These well-defined diffraction signals confirm the presence of a highly ordered molecular arrangement in the native protein form in IFNα-PLGANPs.

5.3.3.5 Loading Capacity and Adsorption Efficiency within the IFNα-PLGANPs

The formation of NPs is influenced by various experimental conditions, including the volume and concentration of protein in the inner aqueous phase, the polymer concentration in the organic phase, the type of polymer used, the emulsification times, and any additives included in different phases of NPs assembly. These factors significantly affect EE% [235]. IFN-recovery experiments can indicate the impact of the current NPs encapsulation conditions on the cytokine. In this study the EE% of IFNα-2b was calculated as the ratio of experimental to theoretical IFN loading and expressed as a percentage. EE%, indirectly determined from supernatants obtained by ultracentrifugation, was as high as 78.9% for IFN-PLGA.

5.3.4 Release Profile for Optimized IFNα-PLGANPs

Precise control of drug release remains a critical challenge in drug delivery, as it significantly

influences treatment outcomes. It is essential to ensure that drug dosages remain within a predefined range, exceeding the therapeutic threshold while staying below toxic levels. Drug release kinetics in polymeric systems are influenced by various factors, including the properties of the polymer, environmental conditions, and drug characteristics and structural parameters such as the system's size, shape, and drug loading within the polymer matrix play a significant role in modulating release kinetics. Drug release from polymeric systems occurs primarily through diffusion, erosion, or swelling mechanisms. In hydrophilic matrices, drug release is driven by water penetration, leading to swelling and diffusion as the dominant mechanisms. Conversely, hydrophobic matrices rely predominantly on diffusion or erosion, which are governed by the properties of the drug and excipients.

The optimized formulation demonstrated a selective sustained release manner, with a cumulative release of approximately 24.8% after 4 hours of evaluation. An initial burst release of 40.22% is observed on Day 1, followed by a slower, sustained release over the subsequent 4 days, as shown in Figure 5.12. This burst release likely results from the release of surface-bound drug, influenced by physical, chemical, and processing parameters. Specifically, drug migration to the matrix surface during cooling and drying, coupled with the formation of surface cracks, may enhance surface erosion and contribute to the initial release.

The pronounced burst release on the first day can also be attributed to the hydrophilic properties of PEG, which is present in the highest concentration ratio (90:10) to the hydrophobic PLGA polymer. This is followed by a more gradual release, likely due to a decrease in the drug concentration gradient in the outer layers of the PEG/PLGA matrix. At the second detection point on Day 3, the cumulative release was reported at 57.50%. The slower release rate from the inner layers is attributed to the longer diffusion path for the aqueous release medium to penetrate deeper into the polymer matrix and the reduced drug concentration gradient in the outer layers. By Day 5, the study achieved a cumulative release of 89.95%, showcasing a successful controlled release profile aligned with the dual nanosystem platform designed for skin cancer treatment. The experimental data closely aligned with the predictions of the best-fit models, as presented in Figure 5.12. Importantly, the experimental data shown in this figure aligned well with the theoretical predictions of the best-fit kinetic models, reinforcing the formulation’s potential for effective and sustained delivery of IFNα in skin cancer therapy.

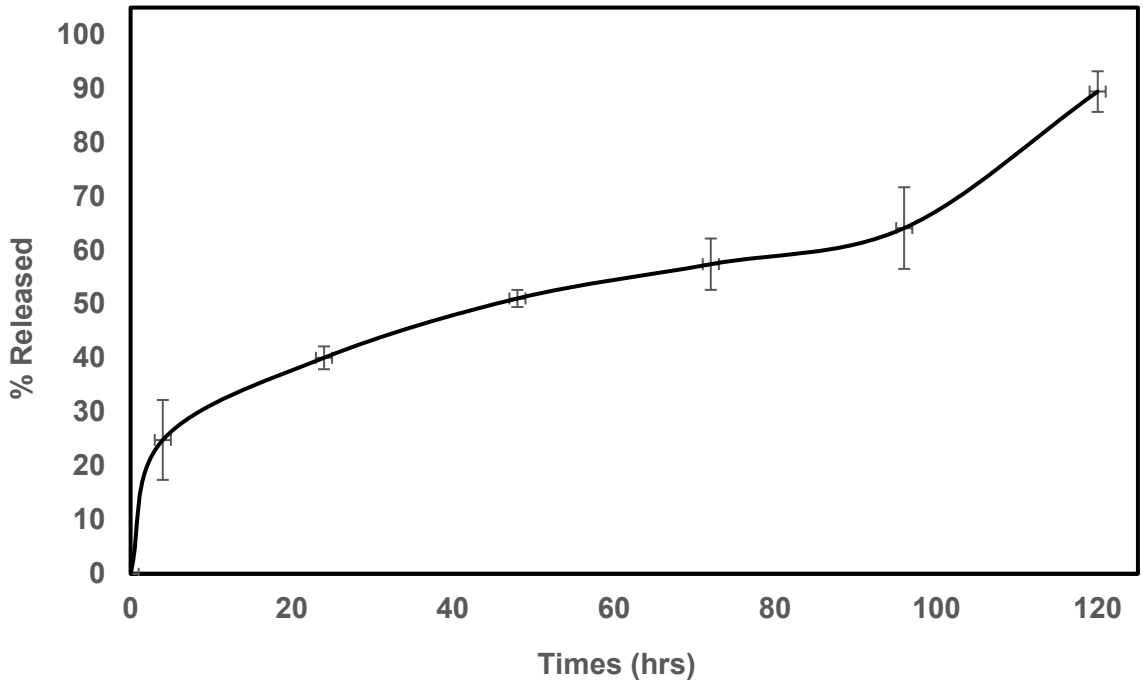


Figure 5.12: Release Profile for Optimized IFNα-PLGANPs. This figure illustrates the cumulative in vitro release pattern of IFNα from the optimized PLGA-based NP formulation over a five-day evaluation period. The release profile demonstrates biphasic kinetic behavior, typical of polymeric delivery systems, with an initial burst release followed by a sustained release phase.

5.3.5 The cytotoxicity of the Optimized IFNα-PLGANPs and its combination with Cur-FeONPs

MTT was employed to assess the cell viability of the IFNα-PLGANPs on the NIH-3T3 cell line at a seeding density of 5×10^5 by measuring the % viability after 72 hours of treatment. The cells were exposed to different concentrations of IFNα-PLGANPs, presented as A, B, C in Figure 5.12, with DMSO serving as a negative control. After 72 hours, the percentage of cell viability for cells treated with IFNα-PLGANPs was <90% for the highest dose for IFNα-PLGANPs, whereas the unloaded PLGANPs (control) showed 98.8% and 89% viability at the lowest and highest treatment concentrations, respectively. These results indicate that IFNα-PLGANPs did not exhibit significant cytotoxicity on NIH-3T3 cells.

The cytotoxicity after 72 hrs treatment in various concentrations exhibited more than 70% cell viability of Cur-FeONPs (the high dose % viability from 74 to 86% in average 80%), while IFNα-PLGANPs (the high dose % viability from 82 to 96% in average 88%) was additionally investigated to assess their biocompatibility with NIH-3T3 cells. Using the MTT assay, the combination demonstrated negligible toxicity toward the fibroblast cells, confirming their safety for normal tissues. Evaluation of the release properties of the combination of Cur-

FeONPs and the optimized IFNα-PLGANPs displayed properties similar to the individual NP release properties with maximum Cur release achieved in 24 hours and a 90.64± 0.35% IFN release after 5 days. This result confirmed that the release profiles of the individual NPs were not impacted by their combination.

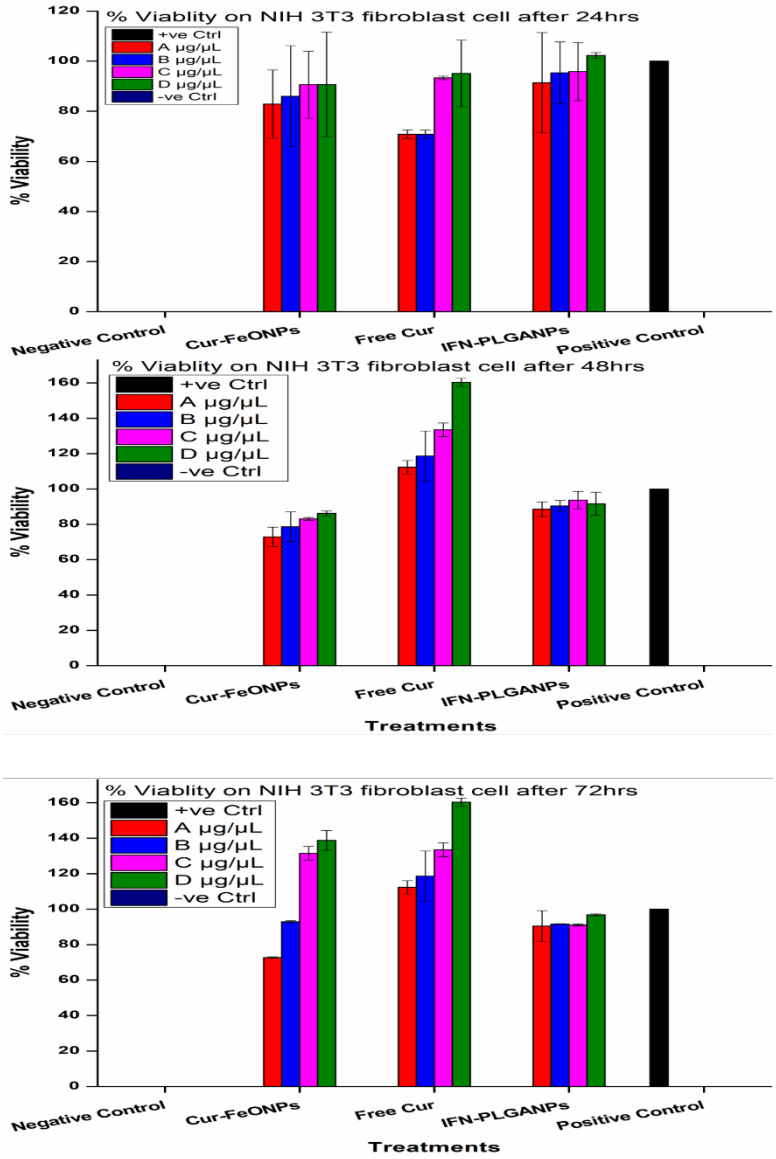


Figure 5.13: Cytotoxicity assessments to evaluate the cell viability of Cur–FeONPs, free Cur and IFNα-PLGANPs at different concentrations. The experiments will span 24, 48, and 72 hours, involving NIH-3T3 cells with a sample size (n=3). This figure presents that both Cur–FeONPs and IFNα-PLGANPs are promising candidates for therapeutic use, offering effective delivery of active agents with minimal toxicity to normal fibroblast cells under the tested conditions.

5.3.5.1 The antiproliferation of the Optimized IFNα-PLGANPs and its combination with Cur-FeONPs

The potential toxicity of NPs is a key consideration in their biomedical and pharmaceutical

applications, requiring a careful assessment to ensure that they do not adversely affect healthy cells. To this end, the tumor growth inhibition properties of IFNα-PLGANPs was evaluated on the A375 melanoma cell line. Using the MTT assay, the metabolic changes of the A375 cells were monitored over a 72-hour treatment period to determine apoptosis or proliferation in response to the NPs as shown in Figure 5.13.

All tested compounds significantly inhibited A375 cell proliferation compared to controls, demonstrating selective toxicity to cancerous cells with minimal impact on normal 3T3 cells. At higher concentrations, IFNα-PLGANPs, when compared to Cur-FeONPs presented in Chapter 4 and showed no significant difference in suppressing A375 cells, with both achieving <5% cell viability at the highest doses tested. The study also confirmed that IFNα-PLGANPs induced apoptosis in A375 cells, with IC50 values of 0.47 and 0.31 μg/μL, after 72 hours of treatment. Additionally, IFNα-PLGANPs protected IFNα from degradation and allowed controlled release, enabling lower doses to be used effectively in melanoma treatment by promoting A375 apoptosis. These findings highlight the potential of IFNα-PLGANPs as a potent therapeutic agent for melanoma and other skin lesions.

The subsequent approach investigated the dual controlled release of IFNα-PLGANPs alongside Cur-FeONPs, focusing on maintaining effective individual therapeutic doses. This strategy aimed to demonstrate the efficacy of combining control release mechanisms within a single therapeutic platform, offering a promising avenue for the advanced treatment of skin cancer. Both NPs, however, showed cytotoxic activity against A375 melanoma cells in the highest concentration dose with no effect in the lowest concentration (D) and time-dependent manner, when used individually, as discussed in 5.3.4 above.

When combined, Cur-FeONPs and IFNα-PLGANPs demonstrated a synergistic effect, significantly reducing A375 melanoma cell viability more effectively than either formulation alone, at the same concentration (D). This enhanced therapeutic efficacy is attributed to the complementary mechanisms of the two NPs: Cur-FeONPs induced targeted oxidative stress through a rapid release, while IFNα-PLGANPs provided sustained immunomodulatory and anticancer activity. The combined treatment remained selectively toxic to melanoma cells while sparing healthy 3T3 fibroblast cells, highlighting its specificity and safety.

This synergistic cytotoxicity underscores the potential for combination therapy to overcome limitations of single-agent treatments. Additionally, the high biocompatibility of the combination with normal cells highlights its potential as a safe and effective therapeutic approach. The success of this dual NPs system in achieving synergistic effects not only

confirms the novelty of the approach but also fulfills the study's objective to develop an advanced multi-component, dual-release therapeutic platform. This innovation paves the way for more effective and safer treatment strategies for skin cancer, demonstrating the potential to overcome the limitations of single-agent therapies.

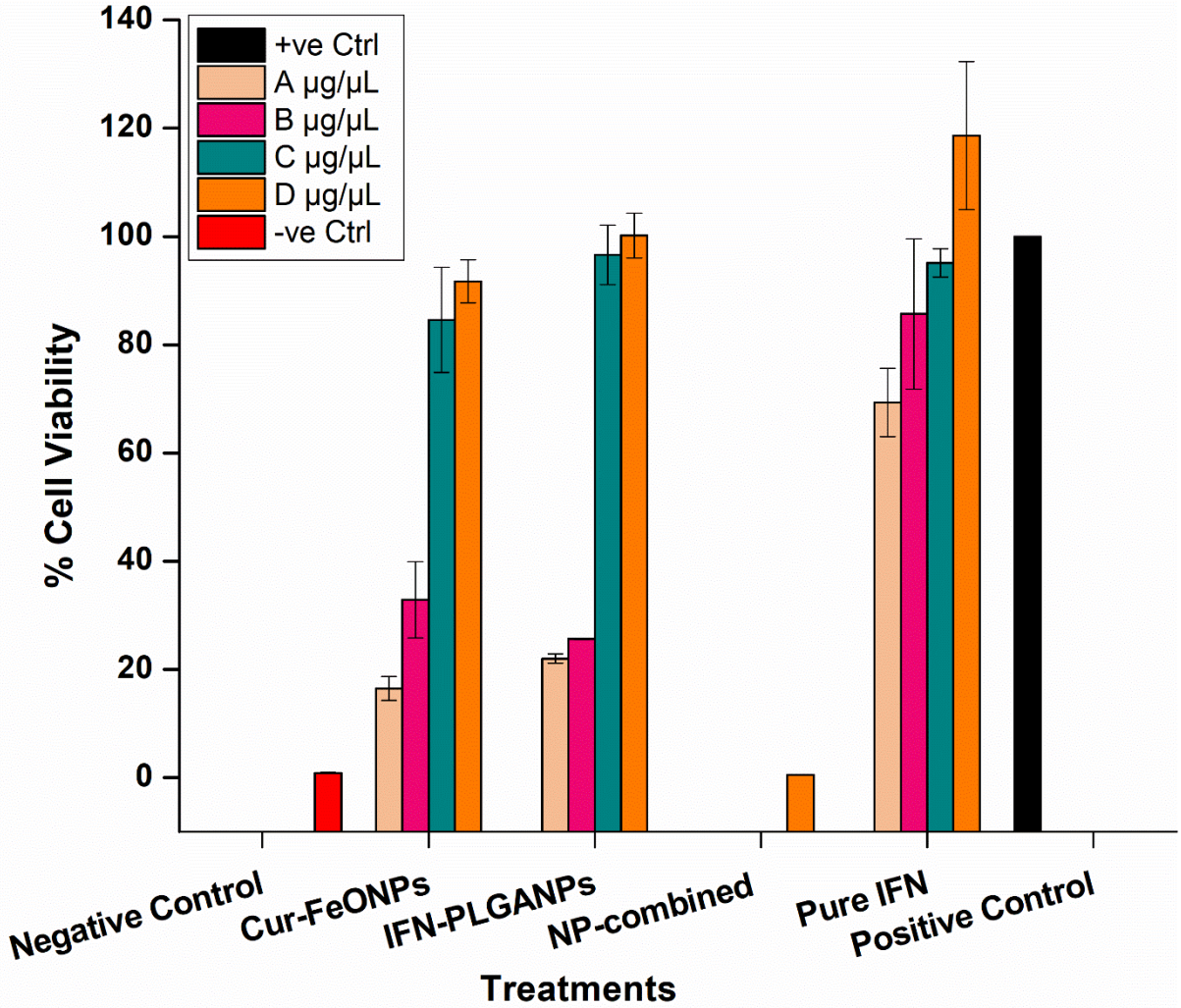


Figure 5.14: Cytotoxicity of MM (A375) under different concentrations of Cur-FeONPs, IFNα-PLGANPs, the combination of Cur-FeONPs and IFNα-PLGANPs, pure IFNα, negative control, and positive control after 72 h. Data shown as mean ± SD, n = 3. This figure presents the results of an in vitro cytotoxicity study conducted to evaluate the cell viability of A375 melanoma cells treated with varying concentrations of Cur -loaded iron oxide NP NP s (Cur–FeONPs), IFNα-loaded PLGA NP s (IFNα-PLGANPs), and their combination. The experiments were performed to assess the synergistic effects of combining the two NP formulations, with the aim of improving therapeutic efficacy in skin cancer treatment.

5.3.5.2 Therapeutic Dose Efficacy on A375 Melanoma Cells

The low-concentration combination of Cur-FeONPs and IFN-PLGANPs exhibited no cytotoxicity to 3T3 fibroblast cells as depicted in Fig, 5.14, demonstrating excellent biocompatibility. However, it showed significant efficacy in inducing apoptosis in A375

melanoma cells, attributed to its synergistic action as a multicomponent, dual-release platform system as reported in Figure 5.14. In contrast, the individual low concentrations of each NPs alone did not demonstrate a significant anticancer effect on A375 melanoma cells. This outcome underscores the safety of the formulation for normal cells at subtherapeutic doses while maintaining the potential for enhanced anti-cancer effects through optimized, synergistic combinations.

These findings underscore the selective biocompatibility of Cur-FeONPs and IFN-PLGANPs with normal cells, reinforcing their safety and applicability in biomedical contexts. This approach offers a high therapeutic efficacy against melanoma while minimizing off-target toxicity, highlighting its potential as a safe and effective treatment strategy.

5.4 Conclusions

This chapter focused on the design and optimization of IFN-PLGA NPs and the preparation of IFNα-2b-coated PLGANPs. Using the CCD model, an optimized formulation was developed, recommending a 20% drug load by volume and a PEG-to-PLGA ratio of 90%. Material characterization confirmed the successful and efficient encapsulation of IFNα-2b within the PLGA matrix. The optimized IFN-loaded PLGA NPs demonstrated an average hydrodynamic diameter of 90.73 nm and a zeta potential of -34.1 ± 4.5 mV.

The nanosystem exhibited notable anti-cancer activity, showing cytotoxic effects on melanoma (A375) cells while maintaining the viability of fibroblast cells (NIH-3T3), thus highlighting its biocompatibility and safety. Additionally, it demonstrated enhanced anti-proliferative activity, effective protection of IFNα-2b from degradation, and controlled release properties. The PLGA coating safeguarded IFNα-2b and enabled sustained release, enhancing its anticancer potential. The therapeutic efficacy of IFNα-2b in this dual-release delivery system underscored the platform's synergistic benefits. This multiphasic delivery system represents a significant advancement in the development of targeted treatment strategies for melanoma skin cancer, offering a promising approach for clinical applications.

The subsequent Chapter 6 explores the integration of Cur-FeONPs and optimized IFN-PLGA NPs into a hydrogel system for topical application. It further includes the characterization of the hydrogel platform and examines the cytotoxicity and proliferation effects of NP-loaded and unloaded gels on NIH-3T3 and A375 melanoma cells, respectively.

CHAPTER 6

A NANOPARTICLE-LOADED HYDROGEL FOR THE TREATMENT OF SKIN CANCER

6.1 Introduction

Skin cancer remains one of the most prevalent forms of cancer worldwide, requiring innovative approaches for effective treatment. Conventional therapies, such as surgical resection, chemotherapy, and radiation, come with significant drawbacks, including non-specific targeting, toxicity to healthy tissues, and poor patient compliance [236]. In recent years, hydrogel-based topical systems have gained significant attention due to their potential to improve anticancer drug delivery by offering localized treatment, controlled drug release, and minimized systemic side effects. They additionally offer several advantages over traditional ointments or creams due to their unique properties, including viscoelasticity, flexibility, superabsorbency, softness, and ease of spreadability. Their hydrophilic nature furthermore makes them comfortable to apply, as they spread smoothly on the skin without leaving a greasy residue and can be easily washed off. Hydrogels made from biodegradable and biocompatible polymers with bioadhesive properties are particularly appealing, as they enhance contact time with the skin surface, improving the effectiveness of topical applications [237].

Topical hydrogels on their own, however, do face several limitations due to poor drug permeation through the skin, especially for substances with low water solubility. To address these challenges, modern drug carriers like NPs have been integrated into traditional hydrogels enhancing solubility, permeation and bioavailability [238]. This chapter provides for the development and evaluation of a hydrogel patch, prepared from sodium alginate and soy lecithin, incorporating the Cur-FeONPs and optimized IFNα-PLGANPs developed in Chapters 4 and 5 respectively, for topical administration directly to the MM site, circumventing the need for systemic delivery of the NP platforms.

Alginate (Alg) is a natural hydrogel, a polysaccharide polymer, which has garnered significant attention in pharmaceutical and medical applications due to its notable properties, including biocompatibility, biodegradability, low cost and non-toxicity [239]. This naturally occurring anionic biopolymer forms hydrogels upon the addition of divalent cations, such as Ca^{2+}, with various cross-linking techniques possible to create Alg-hydrogels, resulting in a structure that closely mimics the extracellular matrix of biological tissues [240]. In a previous study, lecithin, a naturally occurring substance found in human tissues, was used to modify

the internal structure of hydrogels and was therefore included in the formulated topical patch. Lecithin, a mixture of phospholipids with both hydrophobic and hydrophilic properties, enhances the bioavailability of co-administered drug therapies. The functionality and effectiveness of multi-component hydrogel systems can therefore be improved by adjusting the lecithin content, while alterations in the internal structure of materials can significantly influence their transport and mechanical properties [241]. The interactions of the polymeric materials in the hydrogel therefore significantly impact its structure, improving its water retention capacity [241], which, in turn, facilitates the targeted release of NPs from the hydrogel nanocarrier system. Hydrogels, which are also known for their ability to maintain a moist microenvironment and absorb wound exudates, can play a crucial role in promoting wound healing, making Alg -based hydrogels are well-suited for skin cancer treatment [242].

6.2 Materials and Methods

6.2.1 Materials

L-α-Lecithin (soybean), sodium alginate, and calcium chloride were obtained from Sigma-Aldrich (Germany), GEL type A (from porcine skin) from Sigma-Aldrich (USA), and sodium hydroxide pellets from Merck Chemicals (Modderfontein, South Africa). The materials used for preparing, releasing, and evaluating the cytotoxicity and cell proliferation (% viability) of Cur-FeONPs and IFNα-PLGANPs are detailed in Chapter 4 (Section 4.2.1) and Chapter 5 (Section 5.2.1). The porcine skin used in the analysis of the topical hydrogel was sourced from the Wits Research Animal Facility (WRAF, Johannesburg, South Africa) under an approved ethics waiver (waiver number AREC-101210-002). All other chemicals used were of analytical grade and applied without further purification.

6.2.2 Development of NP-loaded alginate-lecithin hydrogel topical system

The NP-loaded alginate-lecithin hydrogel topical system was prepared by first dissolving an 8% w/v solution of sodium alginate in deionized water, followed by the addition of soy lecithin to achieve a final concentration of 0.5% w/v. The mixture was then stirred slowly for one hour at 40°C to ensure complete dispersion of the alginate-soy lecithin blend as present in Figure 6.1a. After cooling to room temperature (25°C), the conditioned medium containing Cur-FeONPs and optimized IFNα-PLGANPs was added (Figure 6.1b), resulting in a final formulation of 2% w/v sodium alginate, 0.5% w/v lecithin, and Cur-FeONPs (5µg/ml) and optimized IFNα-PLGANPs (5µg/ml) in the final gel, as depicted in Figure 6.1c). The mixture was then crosslinked using 0.1 M $CaCl_2$ as reported in Figure 6.1d, at room temperature dried in a fume-hood and thereafter stored at 4°C for later use. As controls, hydrogels without the addition of the Cur-FeONPs and optimized IFNα-PLGANPs were prepared as

stated.

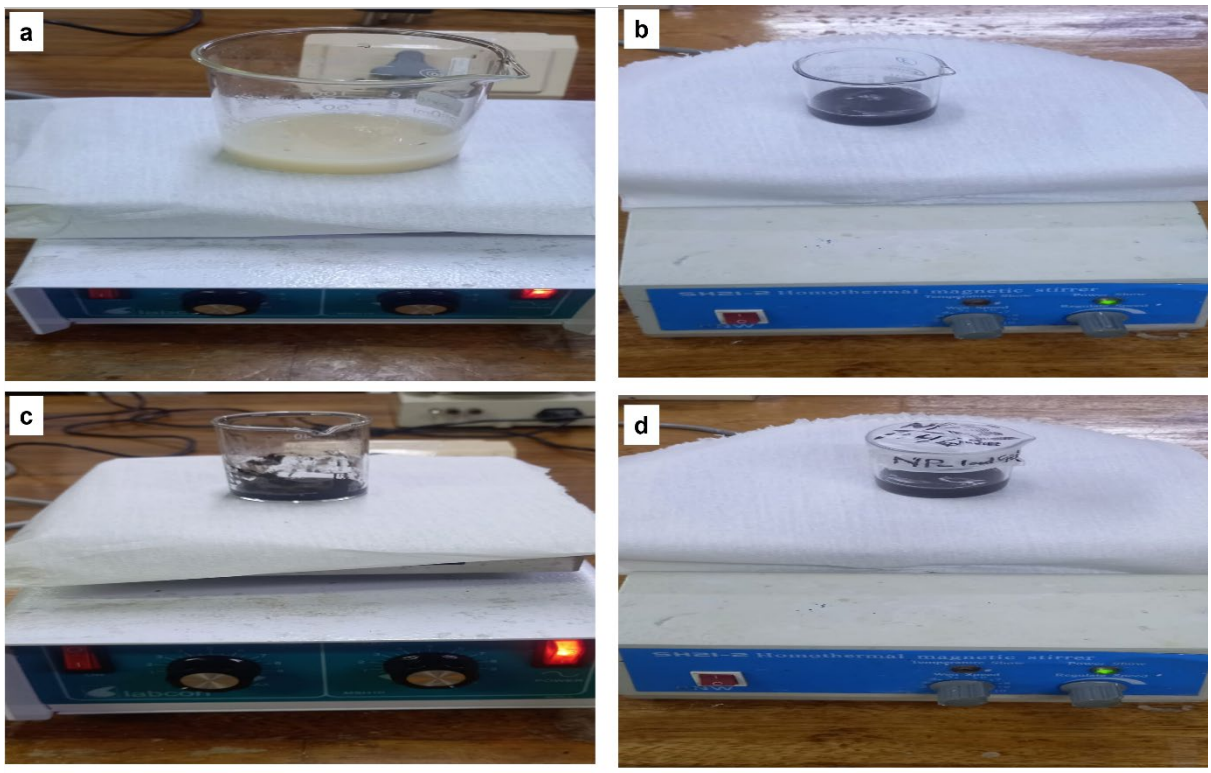


Figure 6.1: Development of NP-loaded alginate-lecithin hydrogel topical system. This figure outlines the formulation and development process of a NP-loaded alginate-lecithin hydrogel, designed as a topical delivery system for enhanced drug delivery. The formulation integrates the biocompatible and biodegradable properties of alginate, a natural polysaccharide, with the lipid-based properties of lecithin, forming a stable hydrogel matrix suitable for controlled, localized drug release.

6.2.2.1. Zeta Size and Zeta Potential Measurements of the NP-loaded Hydrogel

DLS was conducted on a Zeta Sizer instrument (NanoZS, Malvern Panalytical, Malvern, UK) to determine the average hydrodynamic diameter and zeta potential of the synthesized IFNα-PLGANPs DoE formulations as outlined in Chapter 4, Section 4.2.4.

To measure the zeta potential of the NP-loaded hydrogel, a Zeta sizer NanoZS from Malvern Instruments (Worcestershire, UK) was used. This technique monitors the electric potential within the double-layer structure of particles. For the analysis, the samples were sonicated in distilled water, filtered, and then placed in a zeta potential cell for analysis at 25°C. This analysis provided important insights into the surface charge of the dispersion and therefore its stability within the colloidal system.

6.2.2.2 Rheological Measurements of the NP-loaded Hydrogel

The rheological properties of NP-loaded and unloaded hydrogels were evaluated using a ThermoHaake MARS Modular Advanced Rheometer (Thermo Fisher Scientific, Karlsruhe, Germany). This analysis aimed to assess the compatibility of various cross-linker-to-polymer ratios (1:10, 2:10, 1:3, and 1:4) with respect to viscosity. Measurements were conducted at room temperature (25°C) to examine the hydrogel's behavior during storage and at physiological temperature (37°C) to assess its performance during application on the skin.

The rheometer was equipped with a temperature-controlled bath, ensuring precise temperature regulation within the sample chamber. The analysis included strain sweep, shear rate ramp, frequency sweep, and temperature ramp measurements. All tests were performed in triplicate using a parallel plate configuration with a gap size of 0.052 mm. This comprehensive evaluation provided critical insights into the hydrogels' viscoelastic behavior and their suitability for topical applications.

6.2.2.3 Mechanical Properties of the NP-loaded Hydrogel

The mechanical properties of the NP-loaded hydrogels were assessed using a texture analyzer (TA.XT Plus, Stable Micro System, Godalming, UK) immediately after the preparation of both unloaded and NP-loaded gels. This evaluation aimed to determine the impact of varying cross-linker concentrations of Ca^{2+} at polymer ratios of 1:10, 2:10, 1:3, and 1:4 under controlled room temperature conditions.

During the analysis, a 35 mm diameter disc was moved at a speed of 1 mm/s and immersed in the hydrogel samples. The analyzer measured key mechanical attributes, including firmness (g), cohesiveness (g x·s), and consistency (g). To evaluate the bioadhesive properties, adhesive force (mN) and adhesive work (µJ) were measured. These tests were conducted at a physiological temperature of 32 ± 0.5°C, applying a force of 0.5 N for 60 seconds as reported by Czajkowska [243].

The study utilized two materials: cellulose for *in vitro* tests and porcine skin for *ex vivo* analysis. This approach provided critical insights into the hydrogels' ability to adhere effectively to skin, a crucial factor for developing topical formulations designed to maintain prolonged contact with the application site, enhancing therapeutic efficacy.

6.2.2.3.1 *In vitro* Mucoadhesion Studies

The assessment of the mucoadhesive ability of the prepared NP-loaded hydrogel was performed by using a TA.XT.Plus Texture Analyzer (Stable Micro Systems, Surrey, UK). The

parameters of the analysis included a pretest speed of 60 mm/s, test and post-test speed of 0.1 m/s, a time of contact of 180 sec, a return distance 15 mm and a force of 1 N. The mucoadhesive properties were expressed in terms of work of mucoadhesion (Wad) and the maximum detachment force (Fmax) [244].

6.2.2.4 Degradation Studies

The NP-loaded hydrogel was subjected to a degradation study in a simulated *in vitro* exudative environment using phosphate-buffered saline (PBS) as the simulated fluid using the method as outlined by Nokoorani *et al.* [245]. For the experiment, pre-weighed samples of the gel-loaded NPs were dispersed in 2 mL of the simulated fluid. The samples were then incubated in an orbital shaking incubator (LM-530-2, MRC Laboratory Instruments Ltd., Hahistadrut, Holon, Israel) set at 37°C and 50 rpm. The degree of degradation was assessed on Days 1, 3, and 5. After each time-point, the samples were dried in an oven at 40°C to ensure complete moisture removal, allowing the dried mass to be accurately measured. The percentage of mass loss due to degradation was calculated using Equation 6.1:

$$\boldsymbol{Degradation}\ (\%) = (\boldsymbol{Mo} - \boldsymbol{Md}) / \boldsymbol{Mo}\ \boldsymbol{x}\ \mathbf{100} \qquad (6.1)$$

Where:
Mo = Initial mass of the sample before immersion in the simulated fluid.
Md = Dried mass of the sample after each time-point.

6.2.3 Permeation Studies

The Strat-M® membrane was utilized to evaluate the permeation of Cur and IFNα across a simulated membrane. Permeation studies were conducted using a Franz Diffusion Cell (FDC) apparatus (PermeGear Inc., Bethlehem, PA, USA), as depicted in Figure 6.2. The FDC setup comprised a 12-mL receptor compartment, a clamp, and a magnetic stirrer bar. The Strat-M® membrane was carefully positioned between the donor and receptor compartments, with its shiny side facing the donor compartment. The receptor compartment was filled with 10.5 mL of phosphate-buffered saline (PBS, pH 7.4) and maintained at 37°C using a water bath to ensure a stable environment. Continuous stirring was achieved with a magnetic stirrer bar to promote uniform mixing. The Strat-M® membrane, served as the barrier for assessing drug diffusion.

In the donor compartment, a specific weight of NP-loaded gel was applied, overlaid with 1 mL of simulated artificial sweat fluid, and analyzed for drug permeation across the

membrane into the receptor compartment containing PBS. Aliquots of 0.2 mL were withdrawn at predetermined intervals over three days from the receptor compartment for quantitative analysis as previously described. Fresh PBS was replenished after each sampling to maintain sink conditions.

The permeation study was conducted in triplicate. Drug flux ($\mu g \cdot cm^{-2} \cdot h^{-1}$) across the membrane was calculated at a steady state per unit area using linear regression analysis of the permeation data and the following Equation 6.2.

$$Js = Qr/A.t \qquad (6.2)$$

Where: Js is the drug flux ($\mu g \cdot cm^{-2} \cdot h^{-1}$), Qr is the quantity of drug (μg) that diffused through the Strat-M® membrane into the receptor compartment, A (cm^2) is the effective cross-sectional area for drug permeation, and t (h) is the duration of drug exposure to the membrane.

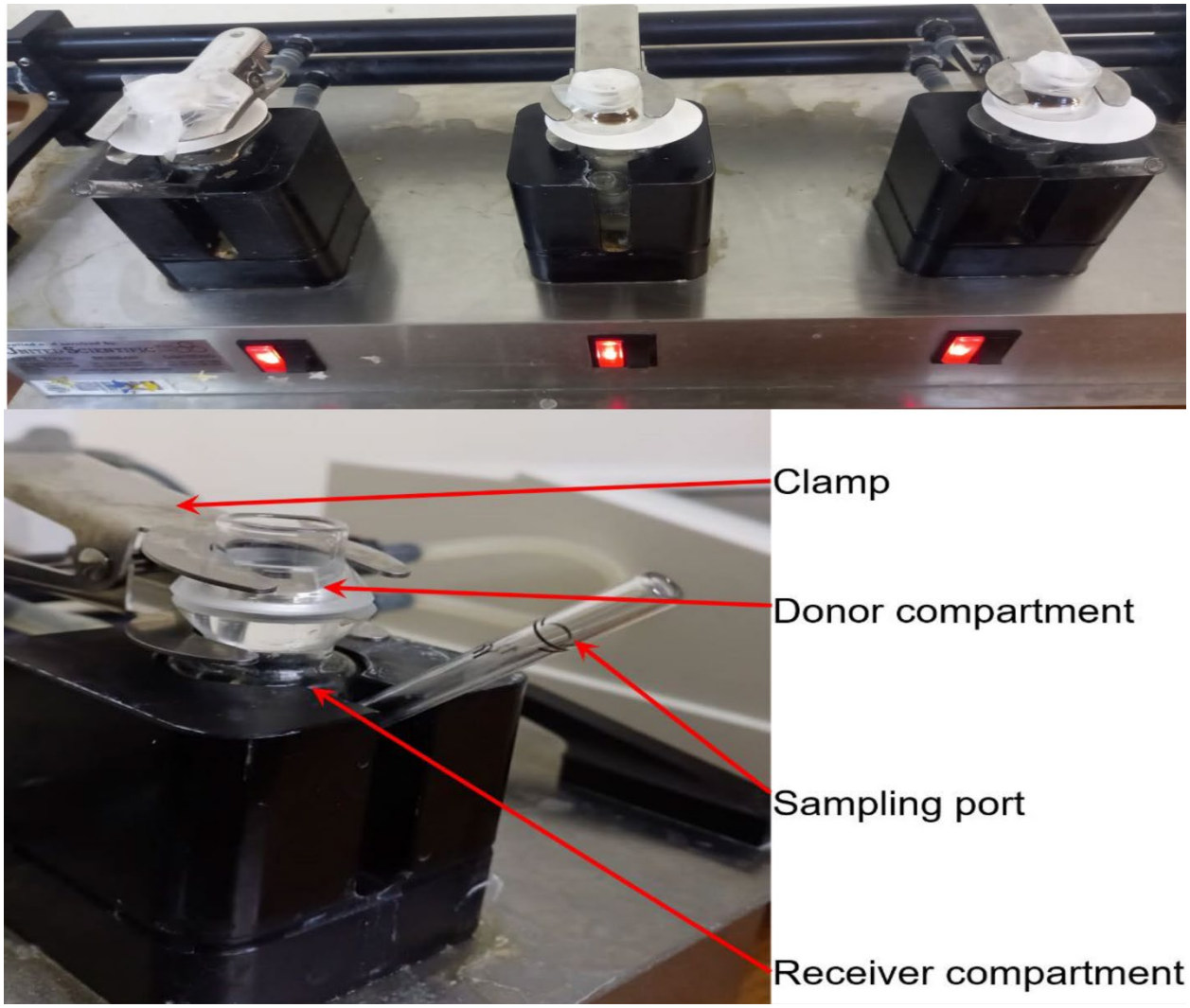


Figure 6.2: Franz diffusion cell apparatus used for permeation study. This figure illustrates the Franz diffusion cell apparatus utilized for the in vitro evaluation of drug permeation through biological membranes, specifically designed for studying the release and absorption properties of the NP-loaded alginate-lecithin hydrogel topical system. The Franz diffusion cell is a well-established method for assessing the skin permeation and drug release kinetics of topical formulations.

6.2.4 Biocompatibility and Cytotoxicity Assessment of the NP-loaded Hydrogel

To assess the cytocompatibility of the hydrogels, particularly focusing on the non-toxicity and antiproliferative efficacy of the NPs-loaded hydrogel system, the NIH-3T3 fibroblast cell line was employed. The cytotoxicity of the synthesized NPs loaded topical hydrogel system was assessed via the MTT assay, as detailed in Chapter 4 (Section 4.2.8). For the analysis, the NIH-3T3 cells were treated with the NP-loaded hydrogel system, dissolved in sterile PBS, at varying concentrations (µg/µL) for 72 hours to evaluate their effect of hydrogel exposure on the cell viability of non-cancerous cells.

6.2.5 Anti-proliferative Activity of the NP-loaded Hydrogel Topical System

The antiproliferation of the synthesized NP-loaded topical hydrogel system was assessed on A375 melanoma cell line using the MTT assay as detailed in Chapter 5, Section 5.2.7.1. For the analysis, the A375 cells were treated with the NP-loaded hydrogel system, dissolved in sterile PBS, at varying concentrations (µg/µL) for 72 hours to evaluate the effect of hydrogel exposure on the cell viability of skin cancer cells.

6.2.6 Statistical Analysis

All results were reported as mean ± standard deviation (SD) from triplicate measurements. Statistical analyses were performed using SPSS software (SPSS 29, IBM, SPSS Inc, Chicago, IL, USA), with one-way analysis of variance carried out. Differences between means were compared using Tukey HSD multiple range test at a significance level of $p < 0.05$.

6.3 Results and Discussion

The hydrogel prepared in this study's unique structure, composed of NP-loaded alginate-lecithin, provides several critical potential advantages in cancer therapy. Firstly, the hydrogel's ability to encapsulate and release NPs in a controlled manner allows for localized drug delivery, minimizing systemic toxicity while enhancing the effectiveness of the therapeutic agents at the tumor site. This feature is crucial for targeted therapy in cancer management, where precision and minimizing side effects are paramount. Secondly, the hydrogel's bioadhesive properties ensure it can remain in place for extended periods, ensuring continuous and localized treatment. This sustained release feature can improve the therapeutic efficacy over time, reducing the need for frequent dosing. Lastly, the inclusion of lecithin may offer additional benefits, such as improved cellular uptake of NPs, which can contribute to the enhanced delivery of chemotherapeutic agents or other synergistic drugs to cancer cells.

6.3.1 Zeta Size and Zeta Potential Measurements of the Hydrogel

Analyzing zeta size is a key step in assessing NP-loaded hydrogels for their consistency and functionality. Figure 6.3 illustrates the zeta size measurements, revealing a uniform particle size of approximately 100 nm, aligning with the platform's design specifications. The NP-loaded hydrogel showed an average hydrodynamic diameter of 106.4 nm, closely matching the 105 nm observed for Cur-FeONPs (Chapter 4) and the 90.73 nm reported for the optimized IFN-PLGA NPs (Chapter 5). These findings underscore the hydrogel's effectiveness as a nanocarrier, supporting its role in targeted melanoma therapy and

enabling controlled therapeutic release.

By achieving a suitable NP size, the NP-loaded alginate-lecithin hydrogel platform is well-suited for targeted drug delivery, especially in applications like melanoma therapy, where localized drug release is essential to maximizing therapeutic efficacy and minimizing systemic exposure.

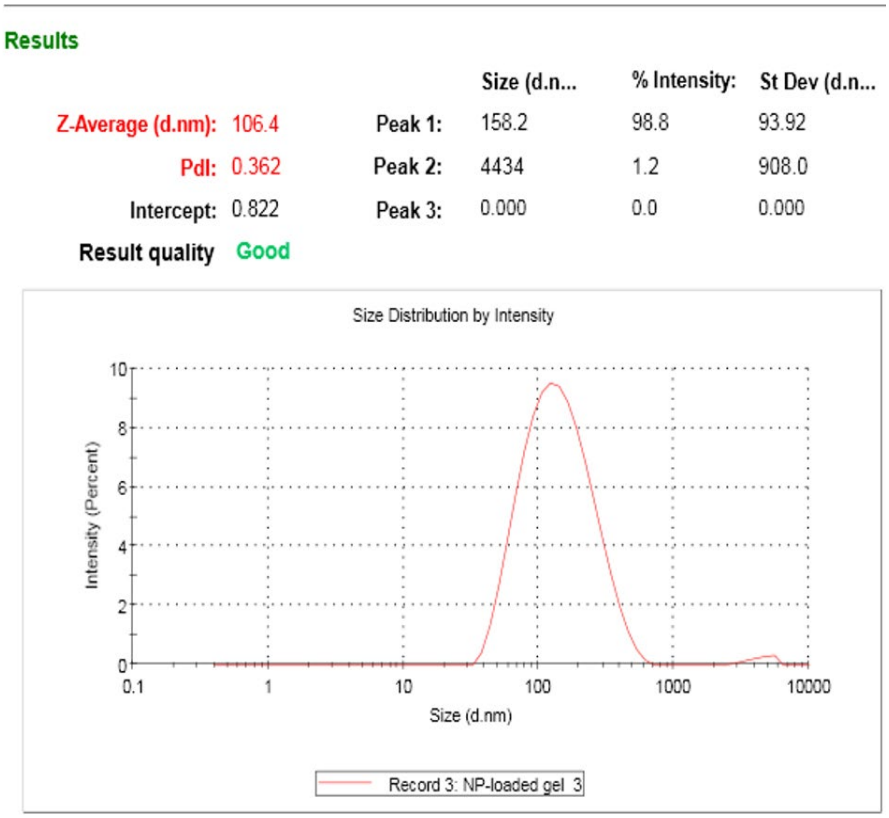


Figure 6.3: Zeta size profile of the NP-loaded hydrogel platform. This figure presents the zeta size measurements of the NP-loaded alginate-lecithin hydrogel, which is crucial for assessing the stability, uniformity, and functional integrity of the NPs incorporated within the hydrogel matrix. Zeta size, also known as the hydrodynamic diameter, provides insight into the size distribution of the NPs, which directly impacts their permeability, stability, and controlled release behavior.

Analyzing surface charge is essential for understanding particle stability, especially concerning ionic interactions between polymers and salts. The hydrogel system loaded with the NPs demonstrated a favorable average zeta potential of -30.8 mV, as depicted in Figure 6.4, thereby confirming the physical stability of the NPs loaded within the hydrogel matrix. The observed zeta potential of the NP-loaded hydrogel is consistent with other NP systems designed for controlled drug delivery, where stability is achieved by maintaining sufficient electrostatic repulsion. This feature makes the NP-loaded hydrogel platform suitable for use in topical delivery applications, where consistency and stability are critical for ensuring that the formulation performs as intended throughout the treatment process.

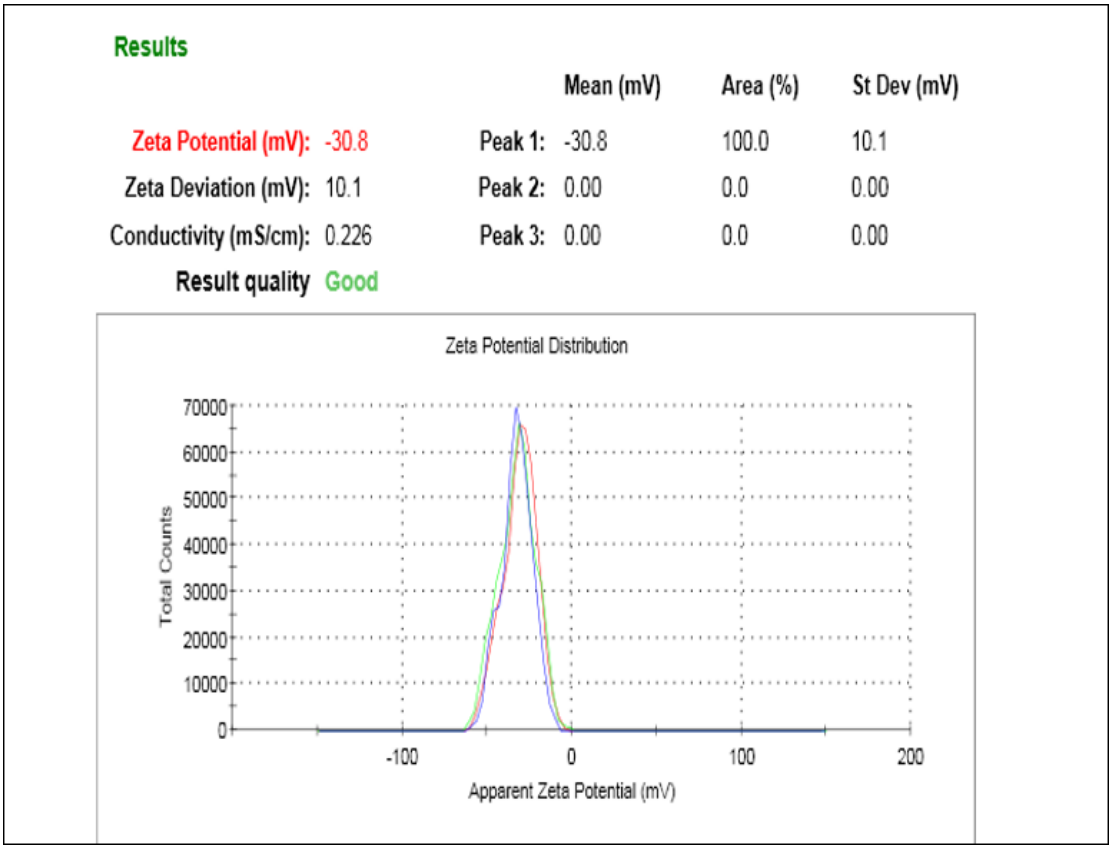


Figure 6.4: Zeta potential profile of the NP-loaded hydrogel platform. This figure illustrates the zeta potential of the NP-loaded alginate-lecithin hydrogel, an important parameter for assessing the colloidal stability and surface charge of the NPs within the hydrogel matrix. Zeta potential provides insights into the interparticle interactions and the stability of the NP dispersion in aqueous environments. It is a key indicator of the repulsive forces between NPs, which directly influences their tendency to aggregate or remain dispersed.

6.3.2 Rheological Evaluation of the NP-loaded Hydrogel Topical System

The rheological analysis of NPs-loaded hydrogels based on alginate-soy lecithin with 1:4% $CaCl_2$ as a crosslinker was performed to understand how temperature and shear stress influence the viscosity of the topical formulation.

At a temperature at 25°C (Figure 6.5a), the viscosity of the hydrogel was higher, indicating a more structured gel network at lower temperatures. This can be attributed to reduced molecular mobility and less disruption of the crosslinked matrix at room temperature, which supports a firmer gel suitable for storage and initial application. In contrast, at 37°C (Figure 6.5b), the viscosity decreased significantly. This reduction suggests that at body temperature, the hydrogel network becomes less rigid, promoting better spreadability and ease of application on the skin. This temperature-responsive behavior is advantageous for a topical system, allowing for ease of administration while maintaining adequate stability at lower temperatures.

Evaluating the effect of shear stress/rate (Figure 6.5c and 6.5d), the hydrogel exhibited shear-thinning behavior, where viscosity decreased with an increasing shear rate. This property is desirable for topical applications as it ensures the gel flows smoothly under applied stress (e.g., during spreading) and regains its viscosity when at rest, enhancing its mucoadhesive and retention properties. Furthermore, unlike cryogels, which can lose viscosity rapidly at physiological conditions, the NP-loaded hydrogel maintained functional viscosity, ensuring better adherence and performance on the skin. Shear-thinning cryogels furthermore tend to have fixed viscosity and may break down under stress, whereas the shear-thinning property of the alginate-soy lecithin hydrogel ensures a more dynamic response to application forces.

Mucoadhesion and detachment force and the bioadhesive properties of the hydrogel were also superior to cryogels, as evidenced by higher adhesive force and work values. This improvement is crucial for retaining the formulation on the skin, especially under dynamic conditions such as movement. Furthermore, crosslinking efficiency of the $CaCl_2$ (1:4) ratio provided a stable network in the hydrogel, overcoming the fragility observed in cryogels. This ensures prolonged stability and functionality of the gel under physiological conditions.

The alginate-soy lecithin hydrogel loaded with NPs demonstrated enhanced viscosity characteristics and bioadhesion compared to conventional cryogels, making it a more effective platform for the treatment of skin cancer. Its temperature responsiveness and shear-thinning behavior further add practical advantages for clinical use allowing for easy application and spreading on irregular skin surfaces. Additionally, these properties ensure that the hydrogel adheres well to the affected area, providing sustained release of therapeutic agents and prolonged contact time, which are critical for achieving optimal treatment efficacy in skin cancer therapy. These viscosity profiles are crucial for ensuring that the NP-loaded hydrogel exhibits optimal flow properties, enhancing the ease of application, spreadability, and skin penetration while maintaining stability and controlled drug release upon application. This makes the formulation highly suitable for topical drug delivery systems, especially for melanoma treatment and other dermatological applications.

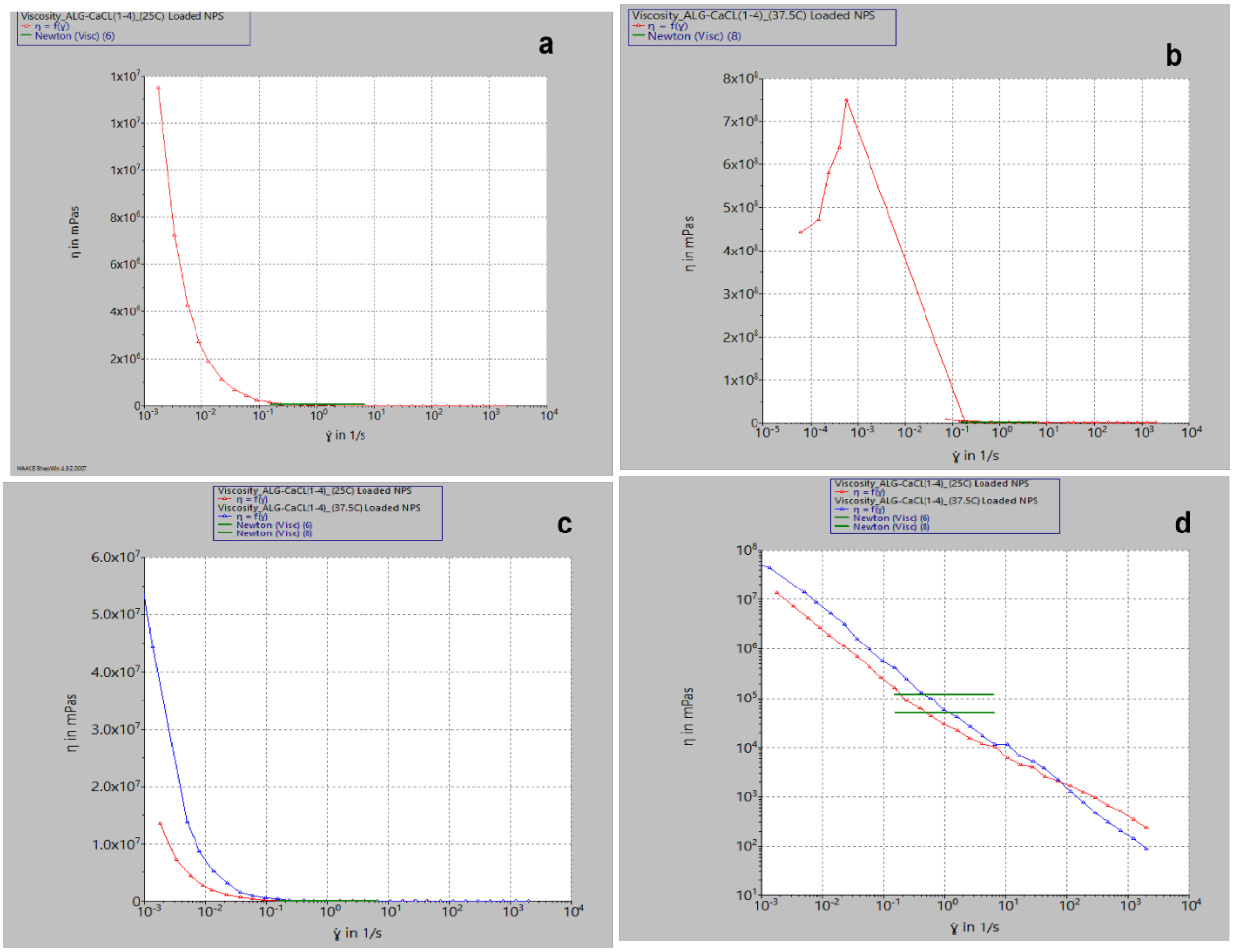


Figure 6.5: Viscosity versus shear rate force (N), where (a) represents the loaded gel at 25°C, (b) the loaded gel at 37°C, and (c) and (d) showed the influence of shear rate on the viscosity of NPs-loaded hydrogel at 25°C and 37°C. This figure illustrates the viscosity of a hydrogel as a key parameter for assessing its flow properties, spreadability, and ease of application, which are crucial factors in determining the practical suitability of a topical drug delivery system.

6.3.3 Mechanical Properties of the NP-loaded Hydrogel

The conception of the mechanical value of cation-alginate complexes is crucial, especially for applications that require strong and durable materials. This technique yields valuable information on the mechanical stability of materials when subjected to stress. This data can also be interpreted through various models to gain a deeper understanding of the network structure, shedding light on the material's performance under different conditions. Tensile and compression tests are also fundamental for assessing the strength, elasticity, and durability of these complexes. These evaluations are particularly crucial for applications such as tissue scaffolds, where mechanical robustness is paramount. As the scope of functional materials expands into new areas like wound healing patches, sensors, and artificial skin, adhesion testing has become increasingly significant. This type of testing assesses the material's ability that were performed on two different materials *in vitro* test cellulose

membrane and *ex-vivo* study on porcine skin, to adhere effectively to various surfaces, ensuring optimal performance in real-world applications.

Figure 6.6 illustrates the maximum detachment force and adhesion work on the cellulose membrane, influenced by varying cross-linker concentrations of Ca^{2+} ratios range to polymer (1:10, 2:10, 1:3, and 1:4). The 1:4 ratio displayed the highest detachment force of 72.6 mN (Figure 6.6a), with the 2:10 ratio demonstrating 69.4 mN (Figure 6.6b), while in Figure 6.6c, the 1:3 ratio measured at 70.5 mN, and the 1:10 ratio reported the lowest detachment force at 47.3 mN as show in Figure 6.6d, due to the minimal cross-linker concentration.

The results indicate that Ca^{2+} as a cross-linker significantly impacts the mucoadhesive strength and detachment force of the hydrogel platform. This effect is particularly notable when the hydrogels are loaded with NPs, emphasizing the role of cross-linking in enhancing the adhesiveness and efficacy of topical patch systems.

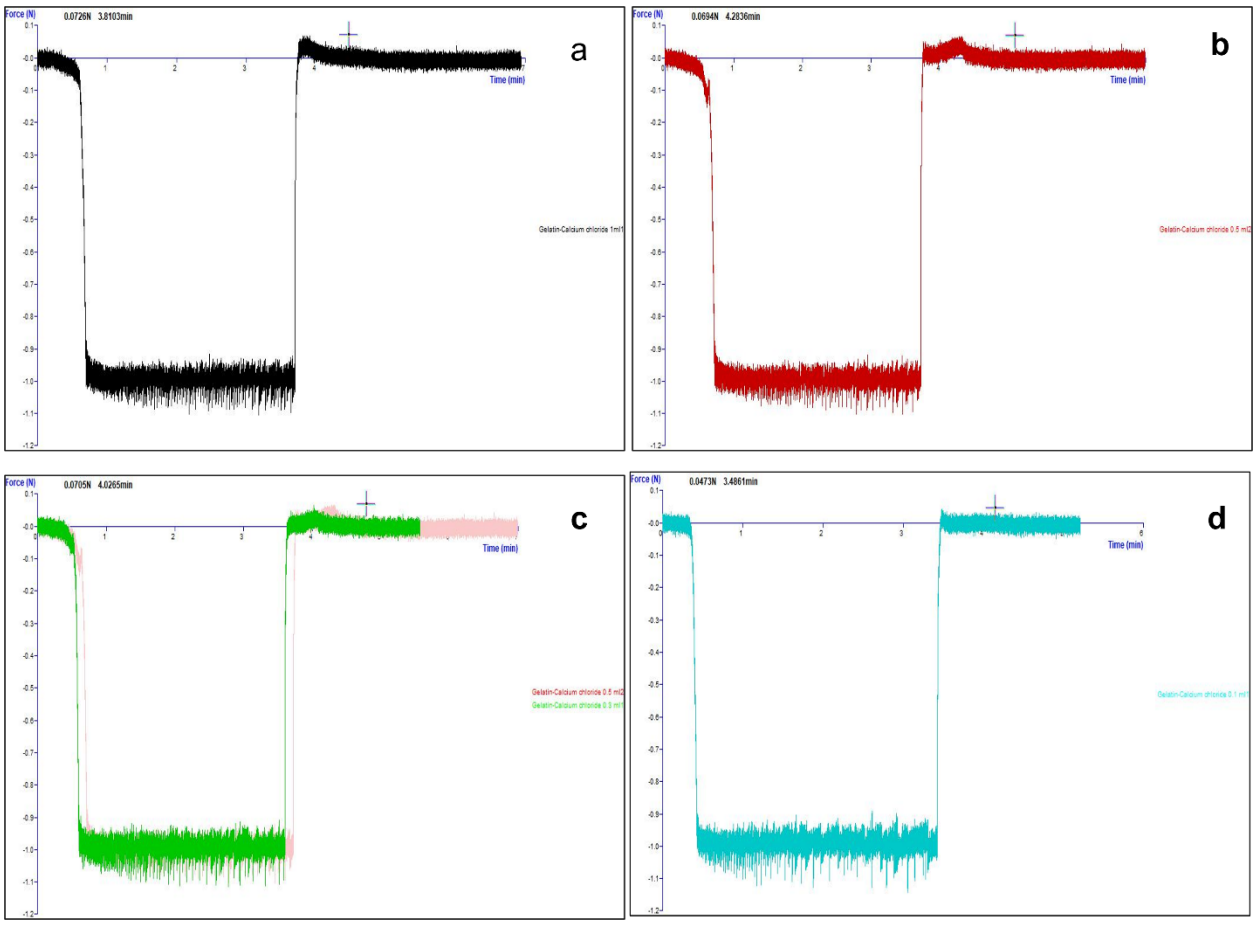


Figure 6.6: Adhesive force of the gels determined using cellulose membrane with a, b, c and d representing ratios 1:10, 2:10, 1:3, and 1:4, respectively, with a sample size of n = 3. This figure shows the adhesive force measurements of the NP-loaded alginate-lecithin hydrogel formulations, evaluated using a cellulose membrane to simulate the interaction between the gel and a biological surface. Adhesive force is a critical parameter for assessing the skin

adhesion properties of topical formulations, as it influences the gel's retention on the skin and its ability to deliver the active drug at the application site. The experiments were conducted using different gel ratios.

6.3.3.1 *Ex Vivo* Bioadhesion Properties

The use of porcine skin in this study is significant due to its structural and physiological similarity to human skin, making it a reliable model for assessing mucoadhesive and detachment adhesion forces. This ensures the evaluation of the unloaded gel and NP-loaded formulations mimic real-world conditions for topical patch systems. The porcine skin was obtained from the WRAF, University of the Witwatersrand, South Africa as depicted in Figure 6.7. Prior to examination, the skin samples were thawed (previously stored at -20°C), sectioned into suitable pieces, and immersed in a PBS solution.



Figure 6.7: Represents the skin isolation procedure in the animal unit, utilizing hairless pig skin for evaluating the adhesive work of the gel formulation. This figure illustrates the ex vivo bioadhesion study process, where hairless pig skin was utilized as a model for assessing the adhesive properties of the NP-loaded hydrogel formulation. The use of porcine skin is particularly significant because its structural and physiological characteristics are closely aligned with human skin, making it a reliable and relevant model for evaluating mucoadhesive and detachment adhesion forces.

Figure 6.8 represented the *ex vivo* tensometric analysis demonstrated that the mucoadhesive properties of hydrogels vary based on the polymer-to-$CaCl_2$ crosslinker ratio and the presence of NPs. The unloaded gels showed that a 1:4 crosslinker-to-polymer ratio exhibited a higher adhesive force (148.3 mN), suggesting stronger bioadhesion due to a balanced gel network (Figure 6.8a), while in Figure 6.8b, the 1:3 ratio displayed comparable

adhesive force (130.5 mN) with slightly enhanced flexibility but no significant difference from the 1:4 ratio. The ratios with reduced crosslinker concentrations (e.g., 2:10 and 1:10) demonstrated weaker adhesive properties 69.4 mN and 65.2 mN), respectively, likely due to inadequate crosslinking. The 1:4 ratio for unloaded gels therefore provided the optimal balance between adhesive strength and ease of detachment.

Figure 6.9 depicts the adhesive force of the gel ratios loaded with Cur-FeONPs and IFN-PLGANPs compared to an unloaded hydrogel. The incorporation of NPs modified the gel's adhesive performance. The 1:4 ratio hydrogel exhibited superior adhesive force when loaded with NPs, maintaining its performance despite reduced viscosity compared with unloaded gel due to the NPs. Ratios like 1:10 displayed significantly reduced adhesion, reflecting insufficient gel cohesion with the added NPs. Furthermore, variations in polymer-to-crosslinker ratios (e.g., 2:10) introduced inconsistencies in adhesion, emphasizing the importance of optimizing crosslinker concentration. These findings a similar to that confirmed in a study by Kośnik *et al*., where significant differences were observed in the adhesive interactions of tested gel formulations with animal tissues.

The results confirm that a polymer-to-crosslinker ratio of 1:4 supports robust mucoadhesion, even with the loaded Cur-FeONPs and IFN-PLGANPs. This formulation offers prolonged skin contact and enhanced therapeutic delivery while preserving flexibility and biocompatibility. It balances mechanical properties essential for stable application under dynamic conditions, making it a superior platform for topical skin cancer treatment.

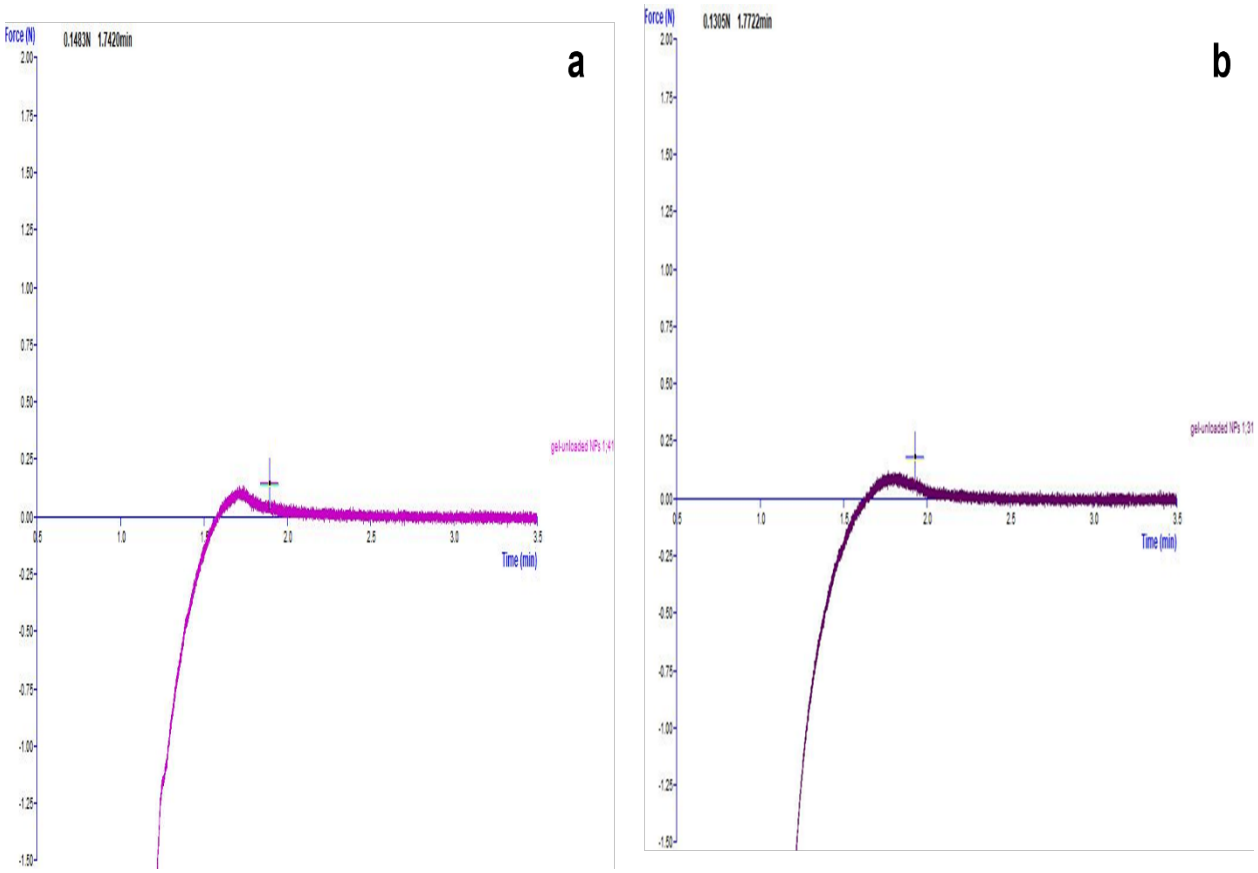


Figure 6.8: Adhesive force of gel determined using hairless porcine skin, for (a) the unloaded gel in a 1:4 ratio and (b) a 1:3 ration of crosslinker to polymer, respectively. This figure demonstrates the adhesive force measurements of two hydrogel formulations using hairless porcine skin, which serves as an ex vivo model to simulate the adhesion properties of the gels on human skin. The data provide important insights into how the gel formulations will adhere to the skin, influencing their performance in topical drug delivery applications. The two formulations tested are based on different crosslinker-to-polymer ratios: 1:4 and 1:3.

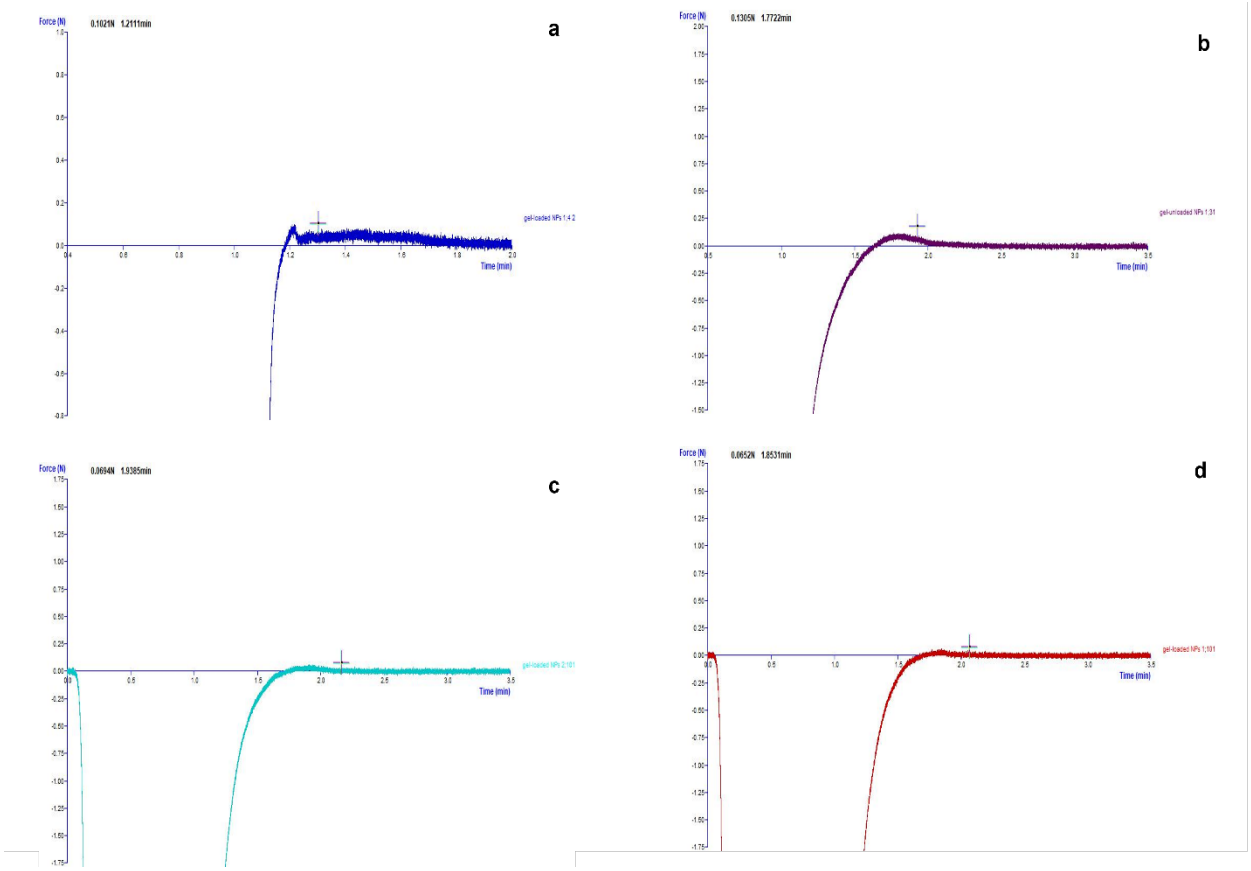


Figure 6.9: Adhesive work of gel determined using hairless porcine skin, for (a) the loaded-NPs in 1:4 ratio, (b) 1:3 ratio, (c) 2:10 ratio and (d) 1:10 ratio crosslinker to polymers, respectively. This figure illustrates the adhesive work of four different NP-loaded hydrogel formulations, each tested on hairless porcine skin. The adhesive work is a critical parameter for assessing the energy required to detach the gel from the skin, which directly influences the performance and retention of topical drug delivery systems. The gel formulations tested are based on varying crosslinker-to-polymer ratios, which alter the gel's structure and adhesive properties. The different ratios are as follows: 1:4, 1:3, 2:10, and 1:10. Each ratio affects the adhesive work, demonstrating how formulation adjustments can impact the bioadhesive behavior of NP-loaded hydrogels.

The 1:4 ratio exhibited optimal performance, with detachment forces exceeding 150 Mn adhesive forces for the unloaded gel and 101 mN for the NP-loaded gel. These findings indicate that while loading NPs reduces hydrogel viscosity, it does not compromise the adhesive strength necessary for prolonged skin application. This demonstrates the suitability of the hydrogel-NP platform for topical use, ensuring strong adhesion even during body movements. Moreover, the *ex vivo* (pig skin) and *in vitro* (cellulose membrane) results confirmed the system's ability to maintain sufficient mechanical integrity for effective application. The adhesive work data for these NP-loaded hydrogel formulations provide valuable insight into their bioadhesive properties and their suitability for topical drug delivery. By adjusting the crosslinker-to-polymer ratio, the adhesive strength of the hydrogel can be fine-tuned to meet specific therapeutic needs, balancing between long-term adhesion and

easy removal. The formulations tested demonstrate how the crosslinking density plays a significant role in controlling the adhesion characteristics, ensuring that the hydrogel formulation can be optimized for various clinical applications, including melanoma treatments and chronic skin conditions.

6.3.4 Degradation Studies

A degradation study was conducted to evaluate the hydrogel-based topical platform system focusing on its dual-release capabilities and the role of polymers (PEG and PLGA) in protecting IFN from rapid degradation. This protective mechanism is crucial as it prevents the loss of IFN's therapeutic efficacy while simultaneously preferring its release from the polymer matrix. The release profile aligns with the multi-component strategy designed to achieve a synergistic therapeutic effect for melanoma treatment. The weight loss percentages of the gel-loaded NPs were recorded as 26.0 ± 3.9%, 65.2 ± 3.2%, and 82.8 ± 1.3% on days 1, 3, and 5, respectively, as depicted in Figure 6.10. These findings highlight the notable impact of compositions of gel-loaded NPs variation on weight loss percentages. Furthermore, variations in drug content showed no significant effect on the weight loss percentages, confirming that the polymer composition and matrix design play a critical role in maintaining the stability and release kinetics of the therapeutic agents.

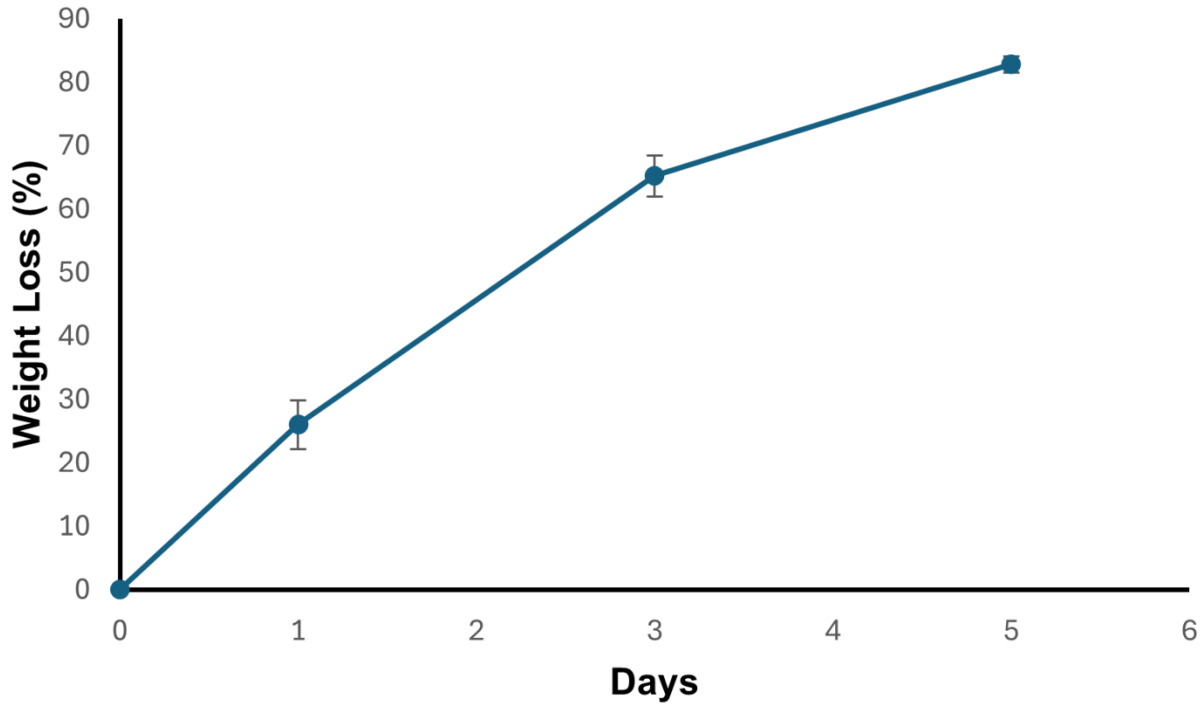


Figure 6.10: Profile representing the weight loss percentage of the NP-loaded gel versus days. This figure presents the degradation profile of the NP-loaded hydrogel system, which was designed to assess its dual-release capabilities and the role of the polymers (PEG and PLGA) in protecting the IFN from rapid degradation. The study aimed to evaluate how the polymer composition and the gel matrix design influence the stability of the encapsulated

IFN while promoting its controlled release over time, which is vital for achieving an optimal therapeutic effect, particularly for melanoma treatment.

This study included extensive physicochemical characterizations that support the stability of the NPs within the hydrogel system. Parameters such as surface charge (zeta potential), particle size, and polydispersity index were evaluated to assess colloidal stability and minimize aggregation risk. Additionally, the hydrogel formulation demonstrated favourable drug loading capacity, sustained release behaviour, and structural integrity, which are indicative of both NP and drug stability. These properties, supported by the literature [246, 247]. collectively contribute to the system's potential stability during short-term storage and therapeutic application.

6.3.5 Cur and IFNα Permeation

The accumulation of Cur and IFNα in skin tissues is critical for achieving pharmacological efficacy, while maintaining a safe therapeutic profile. To evaluate their adequate accumulation, the rate of Cur and IFN released from the combined NP-loaded hydrogel was assessed. Cur exhibited a rapid release within 24 hours, while IFNα showed a sustained release over 5 days after permeation through the Strat-M membrane. The release profile indicated a continuous release of Cur, starting within the first 4 hours and reaching a maximum release of 96.8% after 24 hours. This suggests that Cur achieved therapeutic concentrations within the membrane, ensuring its bioavailability. Conversely, IFNα demonstrated an initial release of up to 40% on Day 1, followed by a controlled release pattern. By Day 3, the release reached 83.5%, progressing to 90.7% by Day 5, as illustrated in Figure 6.11. The flux was calculated to be a maximum of 0.023 for Cur after 12 hours and 3.04 $x10^{-06}$ for IFNα, achieved after 8 hours. These findings highlight the hydrogel's capacity to deliver both active ingredients effectively, combining immediate and sustained release profiles for optimal therapeutic outcomes.

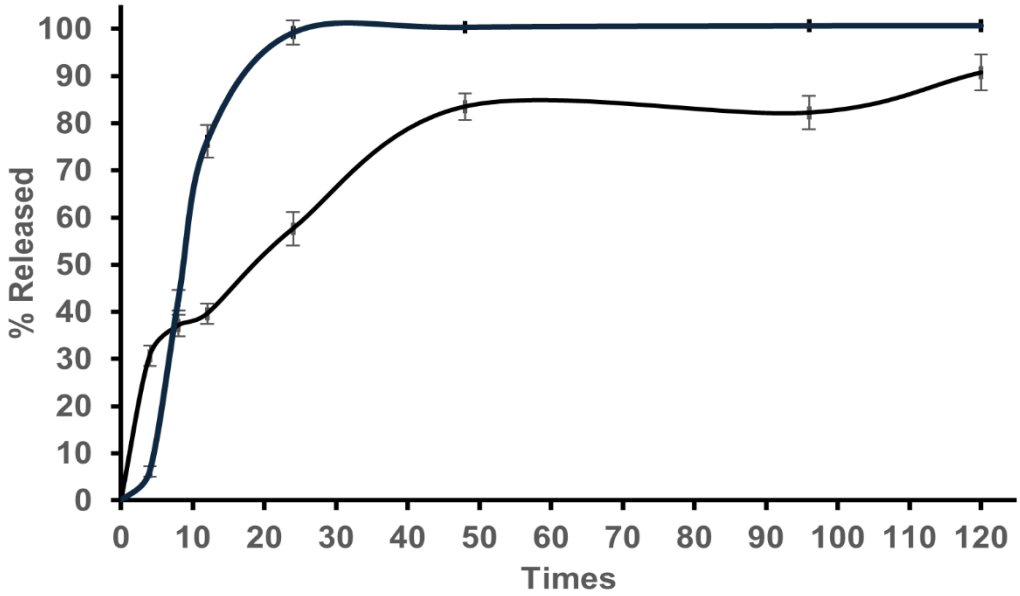


Figure 6.11: Profile representing the permeability percentage of (a) Cur and (b) IFNα from the NP-loaded hydrogel. Data depicted as mean ± SD, n = 3. This figure illustrates the permeation profiles of two active pharmaceutical ingredients, Cur and IFNα, released from the combined NP-loaded hydrogel through a Strat-M membrane. The study evaluates the accumulation and release kinetics of Cur and IFNα in skin tissues, which are crucial for achieving therapeutic efficacy while ensuring safe drug levels for topical applications.

6.3.6 Biocompatibility and Cytotoxicity Assessment of the NP-loaded Hydrogel

6.3.6.1 Cytotoxicity Assessment of the NP-loaded Hydrogel and Unloaded Hydrogel

The MTT assay conducted to assess the % viability of the optimized IFNα-PLGANPs and Cur-FeONPs encapsulated in the hydrogel system on the NIH-3T3 fibroblast cell line, as outlined in Chapter 5. The results revealed that both loaded and unloaded NPs maintained high cell viability, with minimal cytotoxic effects observed at both the lowest and highest treatment concentrations.

The hydrogel (G), composed of alginate cross-linked with Ca^{2+} and lecithin, served as the matrix for delivering NPs. When tested independently, the unloaded hydrogel (G) exhibited no toxicity and demonstrated excellent compatibility with NIH-3T3 cells, confirming its suitability as a reliable and efficient delivery platform. Similarly, gel-loaded NPs at low concentrations were tested on NIH-3T3 fibroblasts over 72 hours, as shown in Figure 6.12. The D value analysis confirmed that these concentrations, as part of the synergistic platform, did not exhibit any toxic effects on normal cells. Furthermore, the unloaded hydrogel (G) also showed a safe and biocompatible effect on cell viability. In contrast, positive and negative controls displayed their expected impact as reported. These results demonstrated no significant reduction in cell viability, confirming that the low-dose concentrations of NPs loaded into the hydrogel are non-toxic to normal cells. These findings underscore the

biocompatibility of the hydrogel-loaded NPs and their safety for therapeutic applications, highlighting their suitability as a platform for advanced drug delivery systems.

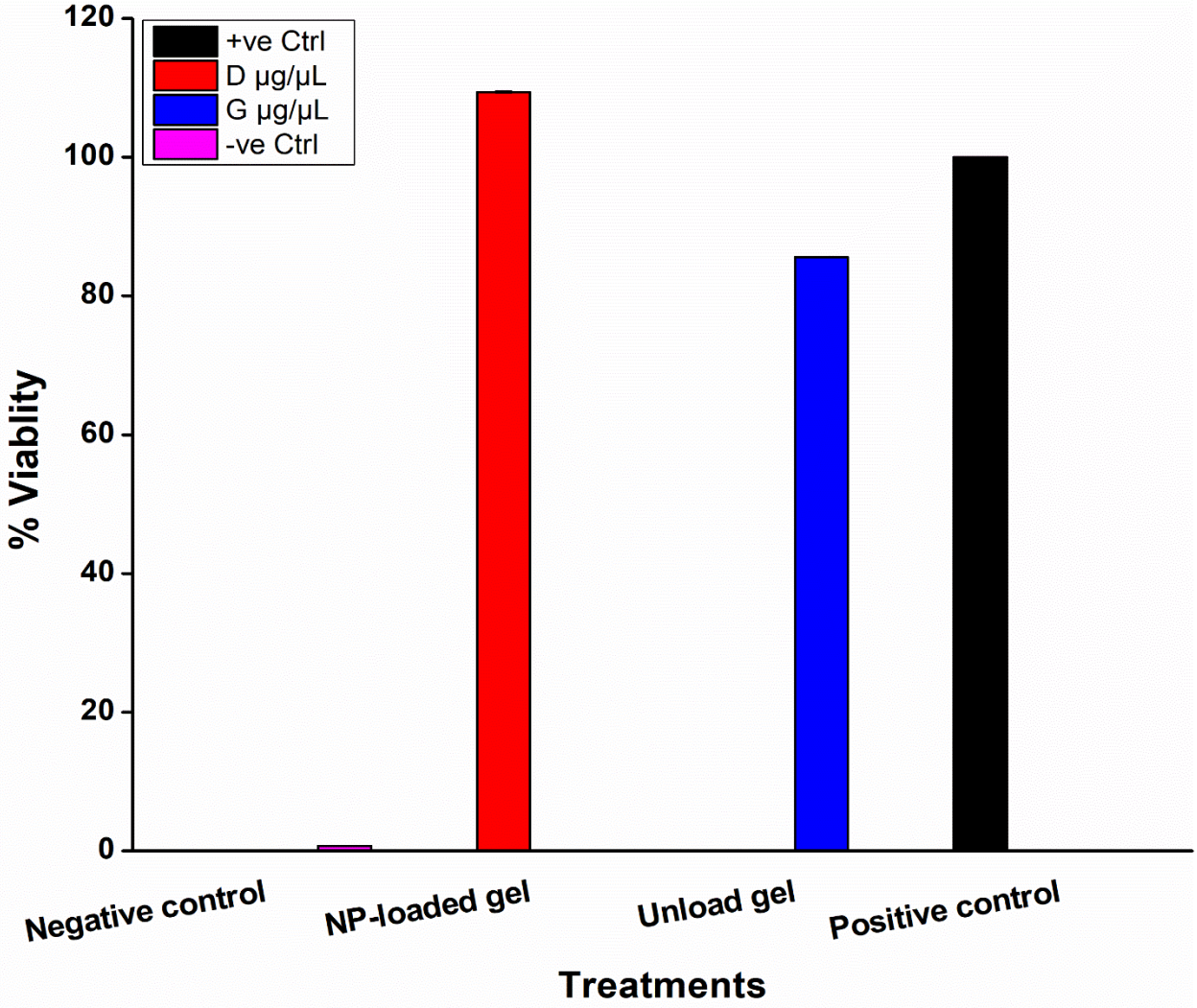


Figure 6.12: NIH-3T3 cell viability of the NP-loaded Gel (D), unloaded-gel (G) and the positive and negative controls. This figure presents the results from an MTT assay conducted to assess the cell viability of the NP-loaded hydrogel system, as well as the unloaded hydrogel, in terms of their cytotoxicity towards the NIH-3T3 fibroblast cell line. The study aimed to evaluate the biocompatibility and safety of the optimized IFNα-PLGANPs and Cur-FeONPs encapsulated within the hydrogel platform, focusing on their potential cytotoxic effects at varying concentrations over a 72-hour period. The findings demonstrate that the hydrogel system, whether loaded with therapeutic NPs or not, is biocompatible and non-toxic to NIH-3T3 cells at the tested concentrations.

6.3.7 Anti-Proliferative Activity of the Hydrogel Topical System

The study evaluated the antiproliferative activity of gel-loaded NPs on the A375 melanoma cell line using the MTT assay, assessing the therapeutic efficacy and safety of the delivery system. Over 72 hours, metabolic changes were monitored to determine the apoptosis-inducing potential of Cur-FeONPs and IFNα-PLGANPs loaded into hydrogel platform.

Evaluation of the results noted that the hydrogel enabled a dual-controlled release of the NPs, maintaining sustained therapeutic doses over time. This feature is crucial in melanoma treatment, where prolonged drug exposure at therapeutic levels can improve outcomes and reduce dosing frequency. Additionally, the combination of Cur-FeONPs and IFNα-PLGANPs within the hydrogel demonstrated enhanced cytotoxicity against A375 cells Figure 6.13. The distinct mechanisms of action of the two NPs complemented each other, increasing apoptosis while minimizing the impact on normal NIH-3T3 fibroblasts. The selective toxicity of the gel-loaded NPs to melanoma cells underscored their specificity, sparing healthy cells and reducing side effects associated with systemic treatments. Moreover, incorporating NPs into the hydrogel provided a stable medium for their delivery, mitigating aggregation and ensuring uniform distribution.

The study revealed that NP-loaded gel significantly inhibited the proliferation of A375 melanoma cells compared to the NPs alone and controls. Cur-FeONPs shown in Chapter 4 did not suppress melanoma cell viability effectively on its own under the concentrations of (50 μg/μl) or less, especially at lower concentrations (50 μg/μl) or less, with a similar trend seen for IFNα-PLGANPs as detailed in Chapter 5.

The dual-release strategy therefore proved highly effective, achieving significant reductions in cell viability and demonstrating the hydrogel's ability to deliver these agents synergistically. This study thus represented synergistic mechanisms and therapeutic potential when combined, Cur-FeONPs and IFNα-PLGANPs exhibited a synergistic reduction in melanoma cell viability, surpassing the effects of either agent alone as showed in Figure 6.13, where the NP-loaded Gel (D) had a significant effect on A375 melanoma compared to the NP-unloaded gel (G) and positive and negative controls. This enhanced efficacy is likely due to their complementary mechanisms. The hydrogel's dual release system additionally ensured sustained and balanced delivery, maintaining therapeutic efficacy while minimizing toxicity to normal cells.

The findings highlight the superiority of the NP-loaded gel system over traditional high-dose monotherapies. The reduced dosing requirements, improved specificity, and safety profile position this system as a promising candidate for advanced melanoma treatment.

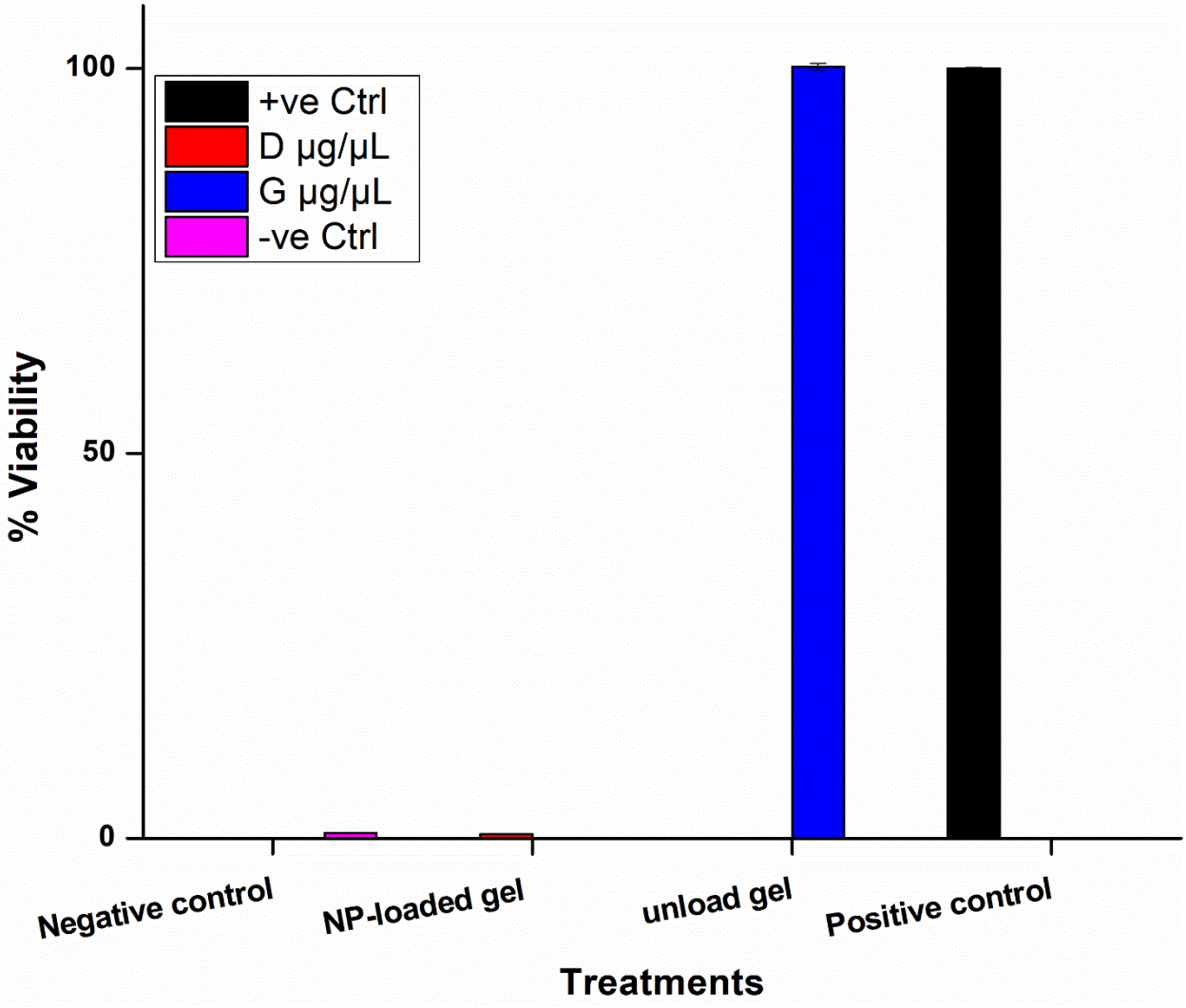


Figure 6.13: % cell viability profiles of MM cells (A375) treated with the NP-loaded Gel (D), the unloaded gel and the negative positive controls after 72 h. Data depicted as mean ± SD, n = 3**.** This figure illustrates the cell viability results obtained from an MTT assay conducted on A375 MM cells after a 72-hour treatment with D, unloaded gel, and the negative and positive controls. The primary objective of this experiment was to assess the cytotoxic effects of the gel formulations and to compare their efficacy in reducing the viability of MM cells.

6.4 Conclusions

Chapter 6 demonstrated the potential of hydrogel-loaded NPs (NPs) as a promising dual-controlled release drug delivery system for skin cancer, specifically targeting melanoma. The systematic evaluation of bioadhesion, rheological, mechanical, and antiproliferative properties of the alginate-soy lecithin hydrogel formulation loaded with Cur-FeONPs and IFNα-PLGANPs has underscored its efficacy and practicality for topical applications.

The rheological studies revealed the hydrogel's temperature-responsive and shear-rate behavior, highlighting its stability during storage and ease of application at physiological temperatures. Compared to cryogels, the hydrogel formulation exhibited superior mechanical

stability, bioadhesion, and retention on the skin, essential for a functional topical therapeutic system. Mechanical and adhesion testing further validated the importance of the optimal polymer-to-crosslinker ratio (1:4) in achieving robust bioadhesion and detachment force, both *in vitro* and *ex vivo*. This formulation demonstrated compatibility with NPs loading without compromising its adhesive properties, ensuring prolonged skin contact and effective therapeutic delivery.

The hydrogel's dual-controlled release system provided significant antiproliferative activity against A375 melanoma cells. By integrating Cur-FeONPs and IFNα-PLGANPs, the system achieved synergistic cytotoxic effects, selectively targeting melanoma cells while sparing normal NIH-3T3 fibroblasts. The combination of these NPs leveraged their complementary mechanisms of action, promoting apoptosis and enhancing immune response while maintaining biocompatibility.

CHAPTER 7

CONCLUSION, LIMITATIONS, AND RECOMMENDATIONS

7.1 Conclusion

A major challenge to the effective treatment of skin cancer is the need for better understanding of how different combination strategies interact with each other. This understanding can help in identifying the patient population that would benefit the most from combination therapy at a practical level. Another critical issue is finding the right balance between effectiveness and safety. Accurate data is required to determine the appropriate dose ratio and timing of synergistic oncology treatments to achieve maximum synergy effect. Numerous ongoing studies are exploring various combinatorial approaches, with a focus on identifying the ideal timing and sequences of combination regimens that can deliver a higher efficacy, durable response, and lower toxicity. Improvements in pharmaceutical technology play an important role in developing advanced treatment regimens, resulting in safer and more effective treatments without significant additional morbidity. Nanotechnology is one such instance where advanced pharmaceutical design can improve combination treatment efficacy by increasing bioavailability and decreasing adverse effects. The treatment of skin cancer is therefore constantly evolving, and there are a number of promising new technologies that are being investigated. These technologies have the potential to revolutionize the way that skin cancer is treated and to improve treatment outcomes for patients.

This thesis has presented a comprehensive exploration of an NP-loaded topical hydrogel as an advanced therapeutic platform for skin cancer treatment, with a focus on melanoma. The research focused on the development and evaluation of a dual-controlled release drug delivery system that leverages the synergistic effects of Cur-FeONPs and IFNα-PLGANPs to enhance therapeutic efficacy while minimizing side effects. Through a series of *in vitro* and *ex vivo* experiments, this study achieved its objectives and demonstrated the potential of this innovative system. This included the synthesis and analysis of the Cur-FeONPs, as well as the development and optimization of IFNα-PLGANP to set criteria to enable for controlled release of IFNα over 5 days. These NPs were thereafter incorporated in a biocompatible hydrogel-based platform composed of an alginate-soy lecithin hydrogel, crosslinked with $CaCl_2$ (1:4 ratio), was this topical system evaluated for its rheological, mechanical, and bioadhesive properties. The results of this analysis determined that the system exhibited temperature-responsive behavior, maintaining stability at room temperature and enhancing

spreadability at physiological temperatures. The shear-thinning property also ensured ease of application and retention on the skin, while the enhanced bioadhesion and mechanical properties of the hydrogel exhibited superior bioadhesive strength and mechanical stability compared to cryogels, ensuring prolonged skin contact and better drug retention under dynamic conditions. It was further determined that the synergistic anticancer efficacy of the formulated NPs exhibited in the incorporation of Cur-FeONPs and IFNα-PLGANPs into the hydrogel enabled dual-controlled release, achieving sustained therapeutic concentrations and enhanced apoptosis in melanoma cells. The synergistic mechanisms of the two NPs significantly improved antiproliferative activity, reduced toxicity to normal cells, and demonstrated specificity in targeting cancer cells. These findings contribute to the advancement of minimally invasive, targeted drug delivery systems for melanoma and potentially other skin cancers. By integrating biocompatible hydrogels with synergistic NPs, this study has laid the groundwork for a novel therapeutic approach that combines efficiency, safety, and practicality.

7.2 Limitations and Recommendations

Despite the promising outcomes, there are some limitations that were identified in this study; one of the challenges of this thesis is the preclinical stage of research. The experiments were conducted primarily *in vitro* and *ex vivo*, which, while valuable, do not fully replicate the complexities of *in vivo* conditions. Animal studies and clinical trials are therefore necessary to validate the efficacy and safety of the system in real-world scenarios.

Additionally, while the dual NPs were successfully synthesized and displayed a highly encapsulation efficiency, the scope of NPs combinations in this study was limited to Cur-FeONPs and IFNα-PLGANPs. While these NPs demonstrated synergistic effects, the potential of other NPs combinations or additional therapeutic agents remains unexplored. On the other hand, although the porcine skin model has similar properties to human skin and was used for the *ex vivo* studies, its variations in skin physiology and responses across species may require the extrapolation of findings to human applications. The formulation and testing processes were furthermore performed on a laboratory scale and scaling up the production of the hydrogel-loaded NPs system for industrial applications may pose technical and economic challenges, which can be explored.

Building on the findings and addressing the limitations, there are some recommendations proposed for future research. Conducting comprehensive animal studies to evaluate the *in vivo* efficacy, safety, and comprehensive pharmacokinetic and pharmacodynamic (PK/PD) evaluations, including drug clearance rates and bioavailability, to establish optimal

therapeutic windows of the hydrogel-loaded NPs will be of significant benefit to ascertain it's *in vivo* efficacy with progression to clinical trials possible to assess the therapeutic outcomes and patient acceptability in a real-trial context. Furthermore, investigating other NPs or drug combinations is possible to enhance the versatility and efficacy of the delivery platform, by exploration of other synergistic combinations of NPs or therapeutic agents (e.g., immunotherapy, checkpoint inhibitors) for improved efficacy, while microneedles can be used to further enhance NP delivery, reach deeper into the tumours and to provide control drug release. Additionally, utilizing advanced human skin models, such as 3D bio-printed skin or organ-on-chip systems, can be of benefit to better replicate physiological conditions and improve the translational value of the findings. Furthermore, evaluating the long-term toxicity, biodegradation profile, and immune compatibility of the hydrogel system under conditions of prolonged application is essential.

Moving forward, integration with clinical pipelines, regulatory frameworks, and GMP-compliant production will be critical. If these translational hurdles are addressed, the system holds promise for future application in personalized, localized cancer therapy, with potential extension to other dermatological and oncological conditions. Additionally, while the lab-scale results of the developed FeONPs-based hydrogel system are promising, successful clinical translation requires addressing several critical challenges related to large-scale production, cost efficiency, regulatory compliance, and formulation stability. It is noted that although the synthesis of FeONPs is relatively cost-effective due to the abundance of iron precursors and the simplicity of the co-precipitation method, the cost-intensive nature of Cur purification and functionalization poses a challenge. To mitigate production expenses at scale, optimization strategies should focus on refining the synthetic route, reducing solvent consumption, and employing continuous manufacturing technologies such as microfluidic systems or spray-drying techniques for hydrogel formulation. From a regulatory standpoint, the pathway for NP -based drug delivery systems remains complex and evolving. Therefore, early engagement with regulatory authorities (e.g., FDA, EMA) is essential. This includes establishing robust quality control protocols, ensuring batch-to-batch reproducibility, and compiling comprehensive preclinical safety, toxicity, and biodistribution data. Demonstrating compliance with Good Manufacturing Practices and validating analytical methods will be critical to support Investigational New Drug applications and subsequent clinical trials. Moreover, formulation stability during scale-up must be rigorously evaluated to ensure the long-term physicochemical integrity of both FeONPs and Cur. This involves addressing challenges such as NP aggregation, hydrogel matrix degradation, and Cur oxidation. Potential strategies to enhance stability include lyophilization, encapsulation within protective polymeric carriers, and the incorporation of antioxidants or stabilizers. Long-term storage

and accelerated stability studies should further be conducted in accordance with the International Council for Harmonisation (ICH) guidelines to ensure product shelf-life and overall integrity.

There are additional consideration to address potential challenges such as environmental stress, NP stability within the gel matrix, and packaging solutions to ensure the integrity and therapeutic efficacy of the formulation during storage and distribution. In this study in terms of storage, preliminary observations suggest that the hydrogel-based topical NPs should ideally be stored in cool, dry conditions preferably between 4°C and 8°C to preserve their structural integrity and prevent premature degradation of both the polymeric matrix and encapsulated NPs. Additional stability studies are recommended for future work to define precise storage conditions and shelf-life. Regarding industrial transport feasibility, the hydrogel films can be adapted into single-use, sterile packaging formats (e.g., topical patch, blister packs or sachets) to maintain their physicochemical stability during transportation.

This study represents a significant step forward in the development of hydrogel-based NP-loaded systems for MM skin cancer treatment. By addressing the identified limitations and following the outlined recommendations, future research can unlock the full potential of this technology, paving the way for innovative, patient-centric, and effective cancer therapies. The findings underscore the importance of interdisciplinary approaches in treating complex medical challenges and provide a strong foundation for ongoing advancements in targeted drug delivery systems.

REFERENCES

1. Diepgen, T.L. and V. Mahler, *The epidemiology of skin cancer.* British Journal of Dermatology, 2002. **146**(s61): p. 1-6.
2. C.S.SANDER, F.H., P.ELSNER AND J.J.THIELEDepartment of Dermatology, Friedrich Schiller University Jena, Erfurter Strasse 35, D-07740 Jena, Germany, *Oxidative stress in malignant melanoma and non-melanomaskin cance.* 2003.
3. Sabir, F., et al., *How to face skin cancer with nanomaterials: A review.* 2021. **11**: p. 11931-11955 %J Biointerface Res. Appl. Chem.
4. Zeng, L., et al., *Advancements in nanoparticle-based treatment approaches for skin cancer therapy.* Molecular Cancer, 2023. **22**(1): p. 10.
5. Siegel, R.L., et al., *Cancer statistics, 2021.* CA: a cancer journal for clinicians, 2021. **71**(1): p. 7-33.
6. Bray, F., et al., *Global cancer statistics 2022: GLOBOCAN estimates of incidence and mortality worldwide for 36 cancers in 185 countries.* CA: A Cancer Journal for Clinicians, 2024. **74**(3): p. 229-263.
7. Ndlovu, B., P. Kellet, and L. Kuonza, *Histological Subtypes, Anatomical Sites, And Incidence Trends Of Non-Melanoma Skin Cancers In South Africa, 1993-2014*.
8. Sung, H., et al., *Global cancer statistics 2020: GLOBOCAN estimates of incidence and mortality worldwide for 36 cancers in 185 countries.* 2021. **71**(3): p. 209-249 %J CA: a cancer journal for clinicians.
9. Tod, B.M., et al., *The incidence of melanoma in South Africa : an exploratory analysis of National Cancer Registry data from 2005 to 2013 with a specific focus on melanoma in black Africans.* South African Medical Journal, 2019. **109**(4): p. 246-253.
10. Kim, J.Y. and H. Dao, *Physiology, Integument*. 2023: StatPearls Publishing, Treasure Island (FL).
11. Akhtar, N. and R.A. Khan, *Liposomal systems as viable drug delivery technology for skin cancer sites with an outlook on lipid-based delivery vehicles and diagnostic imaging inputs for skin conditions'.* Prog Lipid Res, 2016. **64**: p. 192-230.
12. Didona, D., et al., *Non Melanoma Skin Cancer Pathogenesis Overview.* Biomedicines, 2018. **6**(1).
13. Waldman, A. and C. Schmults, *Cutaneous Squamous Cell Carcinoma.* Hematol Oncol Clin North Am, 2019. **33**(1): p. 1-12.
14. Pellegrini, C., et al., *Understanding the Molecular Genetics of Basal Cell Carcinoma.* Int J Mol Sci, 2017. **18**(11).
15. Abbasi, N.R., et al., *Early diagnosis of cutaneous melanoma: revisiting the ABCD*

criteria. Jama, 2004. **292**(22): p. 2771-6.

16. Brash, D.E., *UV signature mutations.* Photochemistry and photobiology, 2015. **91**(1): p. 15-26.
17. Suneet, K., et al., *Magnetic nanofibers based bandage for skin cancer treatment: a non-invasive hyperthermia therapy.* Cancer Reports, 2020. **3**(6): p. e1281.
18. Leffell, D.J. and D.E. Brash, *Sunlight and skin cancer.* Scientific American, 1996. **275**(1): p. 52-59.
19. Pandey, M., et al., *Site-specific vesicular drug delivery system for skin cancer: a novel approach for targeting.* 2021. **7**(4): p. 218 %J Gels.
20. Koynova, R. and B. Tenchov, *Recent patents on nonlamellar liquid crystalline lipid phases in drug delivery.* Recent patents on drug delivery & formulation, 2013. **7**(3): p. 165-173.
21. BOCCI, V., *Evaluation of Routes of Administration of Interferon in Cancer: A Review and a Proposa.* 1984.
22. Gonçalves, L.C., et al., *Superparamagnetic iron oxide nanoparticles dispersed in Pluronic F127 hydrogel: potential uses in topical applications.* RSC advances, 2017. **7**(24): p. 14496-14503.
23. Ivashkiv, L.B. and L.T. Donlin, *Regulation of type I interferon responses.* Nature Reviews Immunology, 2014. **14**(1): p. 36-49.
24. Yen, S.K., et al., *Synthesis of Small-Sized, Porous, and Low-Toxic Magnetite Nanoparticles by Thin POSS Silica Coating.* Chemistry – A European Journal, 2015. **21**(10): p. 3914-3918.
25. Laurent, S., et al., *Magnetic fluid hyperthermia: focus on superparamagnetic iron oxide nanoparticles.* Advances in colloid and interface science, 2011. **166**(1-2): p. 8-23.
26. Hatamie, S., et al., *Curcumin-reduced graphene oxide sheets and their effects on human breast cancer cells.* Materials Science and Engineering: C, 2015. **55**: p. 482-489.
27. Kitture, R., et al., *Fe3O4-citrate-curcumin: promising conjugates for superoxide scavenging, tumor suppression and cancer hyperthermia.* Journal of Applied Physics, 2012. **111**(6).
28. Kundu, S. and U. Nithiyanantham, *In situ formation of curcumin stabilized shape-selective Ag nanostructures in aqueous solution and their pronounced SERS activity.* RSC Advances, 2013. **3**(47): p. 25278-25290.
29. Shahriari, M., et al., *Anticancer potential of curcumin-cyclodextrin complexes and their pharmacokinetic properties.* International Journal of Pharmaceutics, 2023. **631**: p. 122474.

30. Bill, M.A., et al., *Curcumin induces proapoptotic effects against human melanoma cells and modulates the cellular response to immunotherapeutic cytokines.* Mol Cancer Ther, 2009. **8**(9): p. 2726-35.
31. Simões, M.C.F., J.J.S. Sousa, and A.A.C.C. Pais, *Skin cancer and new treatment perspectives: A review.* Cancer Letters, 2015. **357**(1): p. 8-42.
32. Krishnan, V. and S. Mitragotri, *Nanoparticles for topical drug delivery: Potential for skin cancer treatment.* 2020. **153**: p. 87-108 %J Advanced Drug Delivery Reviews.
33. Mao, J.J., et al., *Integrative oncology: Addressing the global challenges of cancer prevention and treatment.* 2022. **72**(2): p. 144–164 %J CA: A Cancer Journal for Clinicians.
34. Zhang, Y., et al., *Physiological model using diffuse reflectance spectroscopy for nonmelanoma skin cancer diagnosis.* 2019. **12**(12): p. e201900154 %J Journal of Biophotonics.
35. Ferlay, J., et al., *Estimating the global cancer incidence and mortality in 2018: GLOBOCAN sources and methods.* 2019. **144**(8): p. 1941–1953 %J International journal of cancer.
36. Ferlay, J., et al., *Cancer incidence and mortality worldwide: sources, methods and major patterns in GLOBOCAN 2012.* 2015. **136**(5): p. E359–E386 %J International journal of cancer.
37. Borgheti-Cardoso, L.N., et al., *Nanotechnology approaches in the current therapy of skin cancer.* Advanced Drug Delivery Reviews, 2020. **153**: p. 109-136.
38. Shimizu, I., et al., *Treatment of squamous cell carcinoma in situ: a review.* Dermatologic surgery, 2011. **37**(10): p. 1394-1411.
39. Matsui, T. and M. Amagai, *Dissecting the formation, structure and barrier function of the stratum corneum.* International immunology, 2015. **27**(6): p. 269-280.
40. Dastgheib, Z.S., et al., *Gold nanostructures in melanoma: Advances in treatment, diagnosis, and theranostic applications.* Heliyon, 2024. **10**(15): p. e35655.
41. Bertrand, N., et al., *Cancer nanotechnology: the impact of passive and active targeting in the era of modern cancer biology.* Advanced drug delivery reviews, 2014. **66**: p. 2-25.
42. Shankaraiah, N., et al., *Diverse targeted approaches to battle multidrug resistance in cancer.* Current Medicinal Chemistry, 2019. **26**(39): p. 7059-7080.
43. Bar-Zeev, M., Y.D. Livney, and Y.G. Assaraf, *Targeted nanomedicine for cancer therapeutics: Towards precision medicine overcoming drug resistance.* Drug Resistance Updates, 2017. **31**: p. 15-30.
44. Rao, J.P. and K.E. Geckeler, *Polymer nanoparticles: Preparation techniques and size-control parameters.* Progress in polymer science, 2011. **36**(7): p. 887-913.

45. Masood, F., *Polymeric nanoparticles for targeted drug delivery system for cancer therapy.* Materials Science and Engineering: C, 2016. **60**: p. 569-578.
46. Zhao, M., et al., *Nanoparticle abraxane possesses impaired proliferation in A549 cells due to the underexpression of glucosamine 6-phosphate N-acetyltransferase 1 (GNPNAT1/GNA1).* International journal of nanomedicine, 2017: p. 1685-1697.
47. Kus, K.J. and E.S. Ruiz, *Non-surgical treatments for keratinocyte carcinomas.* Advances in Therapy, 2021: p. 1-14.
48. Beg, M.S., et al., *Phase I study of MRX34, a liposomal miR-34a mimic, administered twice weekly in patients with advanced solid tumors.* Investigational new drugs, 2017. **35**: p. 180-188.
49. Rosko, A.J., et al., *Contemporary management of early-stage melanoma %J JAMA Facial Plastic Surgery.* 2017.
50. Costa Svedman, F., et al., *Surgical outcomes in patients with cutaneous malignant melanoma in Europe–a systematic literature review.* 2017. **31**(4): p. 603–615 %J Journal of the European Academy of Dermatology and Venereology.
51. Iqbal, J., et al., *Potential phytochemicals in the fight against skin cancer: Current landscape and future Potential phytochemicals in the fight against skin cancer: Current landscape and.* 2019. **109**: p. 1381–1393 %J Biomedicine & Pharmacotherapy.
52. Khan, N.H., et al., *Skin cancer biology and barriers to treatment: Recent applications of polymeric micro/nanostructures.* J Adv Res, 2022. **36**: p. 223-247.
53. Curti, B.D. and M.B. Faries, *Recent advances in the treatment of melanoma.* 2021. **384**(23): p. 2229–2240 %J New England Journal of Medicine.
54. Sim, F.H., et al., *Lymphadenectomy in the management of stage I malignant melanoma: a prospective randomized study.* Mayo Clin Proc, 1986. **61**(9): p. 697-705.
55. Gualdi, G., et al., *Surgical treatment of basal cell carcinoma and squamous cell carcinoma.* 2015. **150**(4): p. 435–47 %J G Ital Dermatol Venereol.
56. Garbe, C., et al., *European consensus-based interdisciplinary guideline for melanoma. Part 2: Treatment-Update 2022 %J European Journal of Cancer.* 2022.
57. Ahmadi, O., et al., *Impact of shave biopsy on diagnosis and management of cutaneous melanoma: a systematic review and meta-analysis.* 2021. **28**(11): p. 6168–6176 %J Annals of Surgical Oncology.
58. Villani, A., et al., *The Treatment of Advanced Melanoma: Therapeutic Update.* 2022. **23**(12): p. 6388 %J International Journal of Molecular Sciences.
59. Melero, I., et al., *Making the most of cancer surgery with neoadjuvant immunotherapy.* 2016. **6**(12): p. 1312–1314 %J Cancer Discovery.

60. Cullen, J.K., et al., *Topical treatments for skin cancer.* 2020. **153**: p. 54-64 %J Advanced drug delivery reviews.
61. Tangboriboon, N., *Chapter 15 - Carbon and Carbon Nanotube Drug Delivery and Its Characterization, Properties, and Applications*, in *Nanocarriers for Drug Delivery*, S.S. Mohapatra, et al., Editors. 2019, Elsevier. p. 451-467.
62. Singh, Y., et al., *Nanoemulsion: Concepts, development and applications in drug delivery.* Journal of controlled release, 2017. **252**: p. 28-49.
63. Lao, C.D., et al., *Current State of Adjuvant Therapy for Melanoma: Less Is More, or More Is Better?* 2022. **42**: p. 1–7 %J American Society of Clinical Oncology Educational Book.
64. Davis, L.E., S.C. Shalin, and A.J. Tackett, *Current state of melanoma diagnosis and treatment.* Cancer Biol Ther, 2019. **20**(11): p. 1366-1379.
65. Gershenwald, J.E., et al., *Melanoma staging: evidence-based changes in the American Joint Committee on Cancer eighth edition cancer staging manual.* 2017. **67**(6): p. 472–492 %J CA: a cancer journal for clinicians.
66. Villani, A., et al., *Merkel Cell Carcinoma: Therapeutic Update and Emerging Therapies.* Dermatology and Therapy, 2019. **9**(2): p. 209-222.
67. Salas-Benito, D., et al., *Paradigms on immunotherapy combinations with chemotherapy.* 2021. **11**(6): p. 1353–1367 %J Cancer discovery.
68. He, Y., et al., *Current state of circulating microRNAs as cancer biomarkers.* Clinical chemistry, 2015. **61**(9): p. 1138-1155.
69. Xu, J., et al., *Chemotherapy plus erlotinib versus chemotherapy alone for treating advanced non-small cell lung cancer: a meta-analysis.* PloS one, 2015. **10**(7): p. e0131278.
70. Amasya, G., et al., *Quality by design case study 1: Design of 5-fluorouracil loaded lipid nanoparticles by the W/O/W double emulsion—Solvent evaporation method.* European Journal of Pharmaceutical Sciences, 2016. **84**: p. 92-102.
71. Haque, T., et al., *Topical therapies for skin cancer and actinic keratosis.* European Journal of Pharmaceutical Sciences, 2015. **77**: p. 279-289.
72. Hafeez, A. and I. Kazmi, *Dacarbazine nanoparticle topical delivery system for the treatment of melanoma.* Scientific reports, 2017. **7**(1): p. 16517.
73. Liu, Q., et al., *Dacarbazine-loaded hollow mesoporous silica nanoparticles grafted with folic acid for enhancing antimetastatic melanoma response.* ACS applied materials & interfaces, 2017. **9**(26): p. 21673-21687.
74. Bragta, P., et al., *Intratumoral administration of carboplatin bearing poly (ε-caprolactone) nanoparticles amalgamated with in situ gel tendered augmented drug delivery, cytotoxicity, and apoptosis in melanoma tumor.* Colloids Surf B

Biointerfaces, 2018. **166**: p. 339-348.

75. Jovanović, S., et al., *Lights and dots toward therapy—carbon-based quantum dots as new agents for photodynamic therapy.* Pharmaceutics, 2023. **15**(4): p. 1170.
76. Xie, J., et al., *Photosensitizer-loaded gold nanocages for immunogenic phototherapy of aggressive melanoma.* 2022. **142**: p. 264–273 %J Acta Biomaterialia.
77. Wen, X., Y. Li, and M.R. Hamblin, *Photodynamic therapy in dermatology beyond non-melanoma cancer: An update.* Photodiagnosis and Photodynamic Therapy, 2017. **19**: p. 140-152.
78. Lucena, S.R., et al., *Combined treatments with photodynamic therapy for non-melanoma skin cancer.* International journal of molecular sciences, 2015. **16**(10): p. 25912-25933.
79. Yang, W., et al., *Surgery combined with photodynamic therapy versus surgery alone for the treatment of non-melanoma skin cancer and actinic keratosis: A retrospective cohort study.* Dermatologic Therapy, 2022. **35**(8): p. e15652.
80. Naidoo, C., C.A. Kruger, and H. Abrahamse, *Photodynamic Therapy for Metastatic Melanoma Treatment: A Review.* Technol Cancer Res Treat, 2018. **17**: p. 1533033818791795.
81. Zhou, F., et al., *Mitochondria-targeting single-walled carbon nanotubes for cancer photothermal therapy.* small, 2011. **7**(19): p. 2727-2735.
82. Bianco, A., K. Kostarelos, and M. Prato, *Applications of carbon nanotubes in drug delivery.* Current opinion in chemical biology, 2005. **9**(6): p. 674-679.
83. da Silva, A.G., et al., *Plasmonic nanorattles as next-generation catalysts for surface plasmon resonance-mediated oxidations promoted by activated oxygen.* Angewandte Chemie International Edition, 2016. **55**(25): p. 7111-7115.
84. Elzoghby, A.O., A.L. Hemasa, and M.S. Freag, *Hybrid protein-inorganic nanoparticles: from tumor-targeted drug delivery to cancer imaging.* Journal of Controlled Release, 2016. **243**: p. 303-322.
85. Grabowska-Jadach, I., et al., *Synthesis, characterization and application of plasmonic hollow gold nanoshells in a photothermal therapy—New particles for theranostics.* Biomedicine & Pharmacotherapy, 2019. **111**: p. 1147-1155.
86. Cheraghi, N., A. Cognetta, and D. Goldberg, *Radiation Therapy in Dermatology: Non-Melanoma Skin Cancer.* 2017. **16**(5): p. 464–469 %J Journal of drugs in dermatology: JDD.
87. Liang, C., et al., *Nanoparticle-mediated internal radioisotope therapy to locally increase the tumor vasculature permeability for synergistically improved cancer therapies.* 2019. **197**: p. 368–379 %J Biomaterials.
88. AUSTRALIA, A.A.I., *ABDOMINAL AORTIC ANEURYSM MORPHOLOGY IN*

ASIANS AND ITS IMPLICATION IN ENDOVASCULAR STENT GRAFTING. ANZ J. Surg, 2005: p. 75.

89. Feng, H., et al., *Clonal integration of a polyomavirus in human Merkel cell carcinoma.* Science, 2008. **319**(5866): p. 1096-1100.
90. Wada-Ohno, M., T. Ito, and M. Furue, *Adjuvant therapy for melanoma.* 2019. **20**(8): p. 1–14 %J Current treatment options in oncology.
91. Zhao, J., et al., *Enhancement of radiosensitization by silver nanoparticles functionalized with polyethylene glycol and aptamer As1411 for glioma irradiation therapy.* International journal of nanomedicine, 2019: p. 9483-9496.
92. Ojha, A., et al., *Nanoparticles and Nanomaterials-Based Recent Approaches in Upgraded Targeting and Management of Cancer: A Review.* Cancers, 2023. **15**(1): p. 162.
93. Sang, W., et al., *Recent advances in nanomaterial-based synergistic combination cancer immunotherapy.* 2019. **48**(14): p. 3771–3810 %J Chemical Society Reviews.
94. Eggermont, A.M., C. Robert, and A. Ribas, *The new era of adjuvant therapies for melanoma.* Nature Reviews Clinical Oncology, 2018. **15**(9): p. 535-536.
95. Eggermont, A.M.M., et al., *Five-Year Analysis of Adjuvant Pembrolizumab or Placebo in Stage III Melanoma.* NEJM Evidence, 2022. **1**(11): p. EVIDoa2200214.
96. Eggermont, A.M.M., et al., *Adjuvant Pembrolizumab versus Placebo in Resected Stage III Melanoma.* New England Journal of Medicine, 2018. **378**(19): p. 1789-1801.
97. Herndon, T.M., et al., *US Food and Drug Administration Approval: peginterferon-alfa-2b for the adjuvant treatment of patients with melanoma.* The oncologist, 2012. **17**(10): p. 1323-1328.
98. Tarhini, A.A., et al., *Phase III study of adjuvant ipilimumab (3 or 10 mg/kg) versus high-dose interferon alfa-2b for resected high-risk melanoma: North American Intergroup E1609.* Journal of Clinical Oncology, 2020. **38**(6): p. 567.
99. Eggermont, A.M.M., et al., *Longer follow-up confirms recurrence-free survival benefit of adjuvant pembrolizumab in high-risk stage III melanoma: updated results from the EORTC 1325-MG/KEYNOTE-054 trial.* Journal of Clinical Oncology, 2020. **38**(33): p. 3925.
100. Rozeman, E.A., et al., *Survival and biomarker analyses from the OpACIN-neo and OpACIN neoadjuvant immunotherapy trials in stage III melanoma.* 2021. **27**(2): p. 256–263 %J Nature Medicine.
101. Tawbi, H.A., et al., *Relatlimab and nivolumab versus nivolumab in untreated advanced melanoma.* New England Journal of Medicine, 2022. **386**(1): p. 24-34.
102. Hu, Z., et al., *Personal neoantigen vaccines induce persistent memory T cell responses and epitope spreading in patients with melanoma.* Nature medicine, 2021.

27(3): p. 515-525.

103. Truong, T.-G., L.B. Kennedy, and S.P. Patel, *25 Years of Adjuvant Therapy in Melanoma: A Perspective on Current Approvals and Insights into Future Directions.* Current Oncology Reports, 2022. **24**(4): p. 533-542.
104. Patel, S.P., et al., *Neoadjuvant–Adjuvant or Adjuvant-Only Pembrolizumab in Advanced Melanoma.* New England Journal of Medicine, 2023. **388**(9): p. 813-823.
105. Song, R., et al., *Acidity-activatable dynamic nanoparticles boosting ferroptotic cell death for immunotherapy of cancer.* Advanced Materials, 2021. **33**(31): p. 2101155.
106. Luo, Z. and X. Liu, *Nanomaterials for cancer immunotherapy, what is the next?* Next Nanotechnology, 2023. **1**: p. 100006.
107. Wang, C., et al., *In situ activation of platelets with checkpoint inhibitors for post-surgical cancer immunotherapy.* Nature Biomedical Engineering, 2017. **1**(2): p. 0011.
108. Luo, M., et al., *A STING-activating nanovaccine for cancer immunotherapy.* Nature nanotechnology, 2017. **12**(7): p. 648-654.
109. Xu, J., et al., *A general strategy towards personalized nanovaccines based on fluoropolymers for post-surgical cancer immunotherapy.* Nature nanotechnology, 2020. **15**(12): p. 1043-1052.
110. Spyratou, E., et al., *Recent advances in cancer therapy based on dual mode gold nanoparticles.* 2017. **9**(12): p. 173 %J Cancers.
111. Hildebrandt, B., et al., *The cellular and molecular basis of hyperthermia.* Critical reviews in oncology/hematology, 2002. **43**(1): p. 33-56.
112. Cabuy, E., *Hyperthermia in cancer treatment.* Reliable Cancer Therapies Energy-based therapies, 2011. **1**(2): p. 1-48.
113. Moyer, H.R. and K.A. Delman, *The role of hyperthermia in optimizing tumor response to regional therapy.* International Journal of Hyperthermia, 2008. **24**(3): p. 251-261.
114. Ganiev, A., S.Y. Abdullaev, and S. Abdurahmonov, *Combined treatment for early-stage skin cancer of the head and neck area.* World Bulletin of Public Health, 2021. **4**: p. 3-6.
115. Nielsen, O.S., M. Horsman, and J. Overgaard, *A future for hyperthermia in cancer treatment?* European Journal of Cancer, 2001. **37**(13): p. 1587-1589.
116. Li, X., et al., *A preliminary study of photoacoustic/ultrasound dual-mode imaging in melanoma using MAGE-targeted gold nanoparticles.* Biochemical and biophysical research communications, 2018. **502**(2): p. 255-261.
117. Sun, M., et al., *Thermally triggered in situ assembly of gold nanoparticles for cancer multimodal imaging and photothermal therapy.* ACS Applied Materials & Interfaces, 2017. **9**(12): p. 10453-10460.
118. Knobler, R., et al., *European dermatology forum - updated guidelines on the use of*

extracorporeal photopheresis 2020 - part 1. J Eur Acad Dermatol Venereol, 2020. **34**(12): p. 2693-2716.

119. Alfred, A., et al., *The role of extracorporeal photopheresis in the management of cutaneous T-cell lymphoma, graft-versus-host disease and organ transplant rejection: a consensus statement update from the UK Photopheresis Society.* Br J Haematol, 2017. **177**(2): p. 287-310.
120. Mercatali, L., et al., *The emerging role of cancer nanotechnology in the panorama of sarcoma.* Front Bioeng Biotechnol, 2022. **10**: p. 953555.
121. Issels, R.D., et al., *Effect of neoadjuvant chemotherapy plus regional hyperthermia on long-term outcomes among patients with localized high-risk soft tissue sarcoma: the EORTC 62961-ESHO 95 randomized clinical trial.* JAMA oncology, 2018. **4**(4): p. 483-492.
122. Mignani, S., et al., *Advances in combination therapies based on nanoparticles for efficacious cancer treatment: an analytical report.* Biomacromolecules, 2015. **16**(1): p. 1-27.
123. Yang, Y. and W. Sun, *Recent advances in redox-responsive nanoparticles for combined cancer therapy.* Nanoscale Advances, 2022. **4**(17): p. 3504-3516.
124. Gunaydin, G., M.E. Gedik, and S. Ayan, *Photodynamic therapy for the treatment and diagnosis of cancer–a review of the current clinical status.* 2021: p. 608 %J Frontiers in Chemistry.
125. Beik, J., et al., *Gold nanoparticles in combinatorial cancer therapy strategies.* Coordination Chemistry Reviews, 2019. **387**: p. 299-324.
126. Ma, N., et al., *Enhanced radiosensitization of gold nanospikes via hyperthermia in combined cancer radiation and photothermal therapy.* 2016. **8**(42): p. 28480–28494 %J ACS applied materials & interfaces.
127. Fahradyan, A., et al. *Updates on the Management of Non-Melanoma Skin Cancer (NMSC)*. Healthcare, 2017. **5**, DOI: 10.3390/healthcare5040082.
128. Weichselbaum, R.R., et al., *Radiotherapy and immunotherapy: a beneficial liaison?* 2017. **14**(6): p. 365–379 %J Nature reviews Clinical oncology.
129. Porceddu, S.V., et al., *Postoperative Concurrent Chemoradiotherapy Versus Postoperative Radiotherapy in High-Risk Cutaneous Squamous Cell Carcinoma of the Head and Neck: The Randomized Phase III TROG 05.01 Trial.* Journal of Clinical Oncology, 2018. **36**(13): p. 1275-1283.
130. Nottage, M.K., et al., *Prospective study of definitive chemoradiation in locally or regionally advanced squamous cell carcinoma of the skin.* Head & neck, 2017. **39**(4): p. 679-683.
131. Maubec, E., et al., *Phase II study of cetuximab as first-line single-drug therapy in*

patients with unresectable squamous cell carcinoma of the skin. J Clin Oncol, 2011. **29**(25): p. 3419-3426.

132. Her, S., D.A. Jaffray, and C. Allen, *Gold nanoparticles for applications in cancer radiotherapy: Mechanisms and recent advancements.* 2017. **109**: p. 84–101 %J Advanced drug delivery reviews.
133. Nagasaka, M., et al., *PD1/PD-L1 inhibition as a potential radiosensitizer in head and neck squamous cell carcinoma: a case report.* 2016. **4**(1): p. 1–4 %J Journal for immunotherapy of cancer.
134. Haymaker, C.L., et al., *Metastatic Melanoma Patient Had a Complete Response with Clonal Expansion after Whole Brain Radiation and PD-1 BlockadeUnique T-cell Clone Expansion after Anti-PD-1.* 2017. **5**(2): p. 100–105 %J Cancer immunology research.
135. Wang, Y., et al., *Combining immunotherapy and radiotherapy for cancer treatment: current challenges and future directions.* 2018. **9**: p. 185 %J Frontiers in pharmacology.
136. Tagliaferri, L., et al., *Immunotherapy and radiotherapy in melanoma: a multidisciplinary comprehensive review.* 2022. **18**(3): p. 1903827 %J Human Vaccines & Immunotherapeutics.
137. Domingues, B., et al., *Melanoma treatment in review.* 2018. **7**: p. 35 %J ImmunoTargets and therapy.
138. Gonzalez, R.J., et al., *Adjuvant Immunotherapy and Radiation in the Management of High-risk Resected Melanoma.* Ochsner J, 2010. **10**(2): p. 108-16.
139. Daneshvar, F., et al., *Combined X-ray radiotherapy and laser photothermal therapy of melanoma cancer cells using dual-sensitization of platinum nanoparticles.* 2020. **203**: p. 111737 %J Journal of Photochemistry and Photobiology B: Biology.
140. Datta, N.R., et al., *Hyperthermia and radiation therapy in locoregional recurrent breast cancers: a systematic review and meta-analysis.* 2016. **94**(5): p. 1073–1087 %J International Journal of Radiation Oncology* Biology* Physics.
141. Gavilán, H., et al., *Magnetic nanoparticles and clusters for magnetic hyperthermia: optimizing their heat performance and developing combinatorial therapies to tackle cancer.* Chemical Society Reviews, 2021.
142. Baronzio, G., et al., *A brief overview of hyperthermia in cancer treatment.* J Integr Oncol, 2014. **3**(115): p. 2.
143. Kim, J.H., E.W. Hahn, and S.A. Ahmed, *Combination hyperthermia and radiation therapy for malignant melanoma.* Cancer, 1982. **50**(3): p. 478-82.
144. Datta, N.R., et al., *Local hyperthermia combined with radiotherapy and-/or chemotherapy: recent advances and promises for the future.* Cancer Treat Rev,

2015. **41**(9): p. 742-53.

145. Vujaskovic, Z., et al., *Temperature-dependent changes in physiologic parameters of spontaneous canine soft tissue sarcomas after combined radiotherapy and hyperthermia treatment.* International Journal of Radiation Oncology*Biology*Physics, 2000. **46**(1): p. 179-185.
146. Cheng, Y., et al., *The Role of Hyperthermia in the Multidisciplinary Treatment of Malignant Tumors.* Integr Cancer Ther, 2019. **18**: p. 1534735419876345.
147. Bienia, A., et al., *Photodynamic therapy and hyperthermia in combination treatment—Neglected forces in the fight against cancer.* 2021. **13**(8): p. 1147 %J Pharmaceutics.
148. Mokhtari, R.B., et al., *Combination therapy in combating cancer.* 2017. **8**(23): p. 38022 %J Oncotarget.
149. Wilson, M.A. and L.M. Schuchter, *Chemotherapy for melanoma.* 2016: p. 209–229 %J Melanoma.
150. Yu, N., et al., *Blue Te Nanoneedles with Strong NIR Photothermal and Laser-Enhanced Anticancer Effects as "All-in-One" Nanoagents for Synergistic Thermo-Chemotherapy of Tumors.* 2018. **7**(21): p. 1800643 %J Advanced Healthcare Materials.
151. Krzykawska-Serda, M., et al., *The role of strong hypoxia in tumors after treatment in the outcome of bacteriochlorin-based photodynamic therapy.* 2014. **73**: p. 239–251 %J Free Radical Biology and Medicine.
152. Song, J., et al., *Rational design of branched nanoporous gold nanoshells with enhanced physico-optical properties for optical imaging and cancer therapy.* 2017. **11**(6): p. 6102–6113 %J ACS nano.
153. Yu, Q., et al., *Copper silicate hollow microspheres-incorporated scaffolds for chemo-photothermal therapy of melanoma and tissue healing.* 2018. **12**(3): p. 2695-2707 %J ACS nano.
154. Meng, Z., et al., *NIR-Laser-Switched In Vivo Smart Nanocapsules for Synergic Photothermal and Chemotherapy of Tumors.* Advanced Materials, 2016. **28**(2): p. 245-253.
155. Wu, J., C. Tang, and C. Yin, Co-delivery of doxorubicin and interleukin-2 via chitosan based nanoparticles for enhanced antitumor efficacy. 2017. 47: p. 81-90 %J Acta biomaterialia.
156. Zou, M.Z., et al., A multifunctional biomimetic nanoplatform for relieving hypoxia to enhance chemotherapy and inhibit the PD-1/PD-L1 axis. 2018. 14(28): p. 1801120 %J Small.
157. van der Most, R.G., B.W. Robinson, and R.A. Lake, Combining immunotherapy with

chemotherapy to treat cancer. Discov Med, 2005. 5(27): p. 265-70.
158. Rosenberg, S.A. and N.P. Restifo, Adoptive cell transfer as personalized immunotherapy for human cancer. 2015. 348(6230): p. 62-68 %J Science.
159. Goff, S.L., et al., Randomized, prospective evaluation comparing intensity of lymphodepletion before adoptive transfer of tumor-infiltrating lymphocytes for patients with metastatic melanoma. 2016. 34(20): p. 2389 %J Journal of Clinical Oncology.
160. Luo, Q., et al., Emerging strategies in cancer therapy combining chemotherapy with immunotherapy. 2019. 454: p. 191-203 %J Cancer Letters.
161. Luke, J.J. and G.K. Schwartz, Chemotherapy in the management of advanced cutaneous malignant melanoma. Clin Dermatol, 2013. 31(3): p. 290-7.
162. Nikolaou, M., et al., Immunotherapy of Cancer: Developments and Reference Points, an Unorthodox Approach. Integr Cancer Ther, 2019. 18: p. 1534735419827090.
163. Chang, D., et al., Biologically targeted magnetic hyperthermia: Potential and limitations. 2018. 9: p. 831 %J Frontiers in pharmacology.
164. Suneet, K., et al., Magnetic nanofibers based bandage for skin cancer treatment: a non-invasive hyperthermia therapy. Cancer Reports, 2020. 3(6): p. e1281.
165. Rajan, A. and N.K. Sahu, Review on magnetic nanoparticle-mediated hyperthermia for cancer therapy. 2020. 22(11): p. 1-25 %J Journal of Nanoparticle Research.
166. Issels, R.D., et al., Neo-adjuvant chemotherapy alone or with regional hyperthermia for localised high-risk soft-tissue sarcoma: a randomised phase 3 multicentre study. Lancet Oncol, 2010. 11(6): p. 561-70.
167. Qi, S., et al., Neutrophil infiltration and whole-cell vaccine elicited by N-dihydrogalactochitosan combined with NIR phototherapy to enhance antitumor immune response and T cell immune memory. Theranostics, 2020. 10(4): p. 1814-1832.
168. Duvic, M., et al., Bexarotene is effective and safe for treatment of refractory advanced-stage cutaneous T-cell lymphoma: multinational phase II-III trial results. J Clin Oncol, 2001. 19(9): p. 2456-71.
169. Ninosu, N., et al., Mogamulizumab Combined with Extracorporeal Photopheresis as a Novel Therapy in Erythrodermic Cutaneous T-cell Lymphoma. Cancers, 2024. 16(1): p. 141.
170. Xi, Y., et al., Bioactive anti-inflammatory, antibacterial, antioxidative silicon-based nanofibrous dressing enables cutaneous tumor photothermo-chemo therapy and infection-induced wound healing. 2020. 14(3): p. 2904-2916 %J ACS nano.
171. Wang, Y., et al., A self-evaluating photothermal therapeutic nanoparticle. 2020. 14(8): p. 9585-9593 %J ACS nano.
172. Yanovsky, R.L., et al., Photodynamic therapy for solid tumors: A review of the

literature. 2019. 35(5): p. 295-303.
173. Zhang, P., et al., Advances in Photodynamic Therapy Based on Nanotechnology and Its Application in Skin Cancer. 2022. 12.
174. Cai, J., et al., 5-aminolevulinic acid mediated photodynamic therapy inhibits survival activity and promotes apoptosis of A375 and A431 cells. 2018. 21: p. 257-262 %J Photodiagnosis and photodynamic therapy.
175. Wang, M., et al., Cancer photo-immunotherapy: from bench to bedside. 2021. 11(5): p. 2218 %J Theranostics.
176. Zhou, F., et al., Local Phototherapy Synergizes with Immunoadjuvant for Treatment of Pancreatic Cancer through Induced Immunogenic Tumor Vaccine. Clin Cancer Res, 2018. 24(21): p. 5335-5346.
177. Relvas, C.M., et al., Nanomaterials for Skin Cancer Photoimmunotherapy. Biomedicines, 2023. 11(5).
178. Nag, S., et al., Nanomaterials-assisted photothermal therapy for breast cancer: State-of-the-art advances and future perspectives. Photodiagnosis and Photodynamic Therapy, 2024. 45: p. 103959.
179. Patil, M., et al., An insight of various vesicular systems, erythrosomes, and exosomes to control metastasis and cancer. Advances in Cancer Biology - Metastasis, 2023. 7: p. 100103.
180. Le, Q.-V., et al., Photosensitizer-Free Phototherapy with Peptide Micelle Nanoadjuvants for Cancer Vaccine against Metastasis of Melanoma. Advanced Therapeutics, 2021. 4(8): p. 2000288.
181. Kato, T., et al., Near Infrared Photoimmunotherapy; A Review of Targets for Cancer Therapy. Cancers (Basel), 2021. 13(11).
182. Gao, D., et al., Multifunctional phototheranostic nanomedicine for cancer imaging and treatment. Materials Today Bio, 2020. 5: p. 100035.
183. Chang, M., et al., Recent advances in hyperthermia therapy-based synergistic immunotherapy. 2021. 33(4): p. 2004788 %J Advanced Materials.
184. Stephen, Z.R. and M. Zhang, Recent Progress in the Synergistic Combination of Nanoparticle-Mediated Hyperthermia and Immunotherapy for Treatment of Cancer. 2021. 10(2): p. 2001415 %J Advanced Healthcare Materials.
185. Riley, R.S. and E.S. Day, Gold nanoparticle-mediated photothermal therapy: applications and opportunities for multimodal cancer treatment. 2017. 9(4): p. e1449 %J Wiley Interdisciplinary Reviews: Nanomedicine and Nanobiotechnology.
186. Moy, A.J. and J.W. Tunnell, Combinatorial immunotherapy and nanoparticle mediated hyperthermia. 2017. 114: p. 175-183 %J Advanced drug delivery reviews.
187. Espinosa, A., et al., Magnetic (hyper) thermia or photothermia? Progressive

comparison of iron oxide and gold nanoparticles heating in water, in cells, and in vivo. 2018. 28(37): p. 1803660 %J Advanced Functional Materials.

188. Ding, B., et al., Large-pore mesoporous-silica-coated upconversion nanoparticles as multifunctional immunoadjuvants with ultrahigh photosensitizer and antigen loading efficiency for improved cancer photodynamic immunotherapy. 2018. 30(52): p. 1802479 %J Advanced Materials.
189. Kleef, R., et al., Low-dose ipilimumab plus nivolumab combined with IL-2 and hyperthermia in cancer patients with advanced disease: exploratory findings of a case series of 131 stage IV cancers - a retrospective study of a single institution. Cancer Immunol Immunother, 2021. 70(5): p. 1393-1403.
190. Qiao, G., et al., Immune correlates of clinical benefit in a phase I study of hyperthermia with adoptive T cell immunotherapy in patients with solid tumors. International Journal of Hyperthermia, 2019. 36(sup1): p. 74-82.
191. Davar, D., et al., High-dose interleukin-2 (HD IL-2) for advanced melanoma: a single center experience from the University of Pittsburgh Cancer Institute. Journal for immunotherapy of cancer, 2017. 5(1): p. 1-10.
192. Knight, A., L. Karapetyan, and J.M. Kirkwood, Immunotherapy in Melanoma: Recent Advances and Future Directions. Cancers (Basel), 2023. 15(4).
193. Hristov, A.C., T. Tejasvi, and A.W. R, Cutaneous T-cell lymphomas: 2021 update on diagnosis, risk-stratification, and management. Am J Hematol, 2021. 96(10): p. 1313-1328.
194. Aires, D. and S. Abhyankar, Early intervention of extracorporeal photopheresis for advancing/progressing cutaneous T-cell lymphoma. Hematological Oncology, 2023. 41(5): p. 809-816.
195. Trautinger, F., et al., EORTC consensus recommendations for the treatment of mycosis fungoides/Sézary syndrome. European Journal of Cancer, 2006. 42(8): p. 1014-1030.
196. Hristov, A.C., T. Tejasvi, and R.A. Wilcox, Cutaneous T-cell lymphomas: 2023 update on diagnosis, risk-stratification, and management. Am J Hematol, 2023. 98(1): p. 193-209.
197. Nana, A.B.A., et al., Multifunctional magnetic nanowires: Design, fabrication, and future prospects as cancer therapeutics. 2019. 11(12): p. 1956 %J Cancers.
198. Imran, M., et al., Overcoming multidrug resistance of antibiotics via nanodelivery systems. Pharmaceutics, 2022. 14(3): p. 586.
199. Hasan, N., et al., Advanced multifunctional nano-lipid carrier loaded gel for targeted delivery of 5-flurouracil and cannabidiol against non-melanoma skin cancer. Environmental Research, 2023. 233: p. 116454.

200. Bhattacharyya, S., et al., Inorganic Nanoparticles in Cancer Therapy. Pharmaceutical Research, 2011. 28(2): p. 237-259.
201. Chandrakala, V., V. Aruna, and G. Angajala, Review on metal nanoparticles as nanocarriers: current challenges and perspectives in drug delivery systems. Emergent Materials, 2022. 5(6): p. 1593-1615.
202. Bhandari, R., et al., Single step synthesis, characterization and applications of curcumin functionalized iron oxide magnetic nanoparticles. Materials Science and Engineering: C, 2016. 67: p. 59-64.
203. Hosseinkazemi, H., et al., Applications of Iron Oxide Nanoparticles against Breast Cancer. Journal of Nanomaterials, 2022. 2022(1): p. 6493458.
204. Yang, Q.-Q., et al., Antimicrobial and anticancer applications and related mechanisms of curcumin-mediated photodynamic treatments. Trends in Food Science & Technology, 2020. 97: p. 341-354.
205. Chircov, C., et al., Dextran-Coated Iron Oxide Nanoparticles Loaded with Curcumin for Antimicrobial Therapies. Pharmaceutics, 2022. 14(5).
206. Ghorbani, M., et al., Curcumin-lipoic acid conjugate as a promising anticancer agent on the surface of gold-iron oxide nanocomposites: A pH-sensitive targeted drug delivery system for brain cancer theranostics. European Journal of Pharmaceutical Sciences, 2018. 114: p. 175-188.
207. Hanini, A., et al., Evaluation of iron oxide nanoparticle biocompatibility. International journal of nanomedicine, 2011: p. 787-794.
208. Darwesh, R. and N.S. Elbialy, Iron oxide nanoparticles conjugated curcumin to promote high therapeutic efficacy of curcumin against hepatocellular carcinoma. Inorganic Chemistry Communications, 2021. 126: p. 108482.
209. Larese Filon, F., et al., Nanoparticles skin absorption: New aspects for a safety profile evaluation. Regulatory Toxicology and Pharmacology, 2015. 72(2): p. 310-322.
210. Slimani, S., et al., Spinel iron oxide by the co-precipitation method: Effect of the reaction atmosphere. Applied Sciences, 2021. 11(12): p. 5433.
211. Elbialy, N.S., S.F. Aboushoushah, and W.W. Alshammari, Long-term biodistribution and toxicity of curcumin capped iron oxide nanoparticles after single-dose administration in mice. Life Sciences, 2019. 230: p. 76-83.
212. Hu, L., et al., Evaluation of High-Performance Curcumin Nanocrystals for Pulmonary Drug Delivery Both In Vitro and In Vivo. Nanoscale Res Lett, 2015. 10(1): p. 381.
213. Chircov, C., et al., Iron oxide–silica core–shell nanoparticles functionalized with essential oils for antimicrobial therapies. Antibiotics, 2021. 10(9): p. 1138.
214. Mohammed, H.B., et al., Eugenol-functionalized magnetite nanoparticles modulate

virulence and persistence in pseudomonas aeruginosa clinical strains. Molecules, 2021. 26(8): p. 2189.
215. Peng, S., et al., Improving curcumin solubility and bioavailability by encapsulation in saponin-coated curcumin nanoparticles prepared using a simple pH-driven loading method. Food & function, 2018. 9(3): p. 1829-1839.
216. Taghavifar, S., F. Afroughi, and M. Saadati Keyvan, Curcumin nanoparticles improved diabetic wounds infected with methicillin-resistant Staphylococcus aureus sensitized with HAMLET. The international journal of lower extremity wounds, 2022. 21(2): p. 141-153.
217. Mi, Y., et al., Viability inhibition of A375 melanoma cellsin vitroby a high-frequency nanosecond-pulsed magnetic field combined with targeted iron oxide nanoparticles via membrane magnetoporation. Nanotechnology, 2021. 32(38).
218. Zhang, Y., et al., Effect of curcumin on the proliferation, apoptosis, migration, and invasion of human melanoma A375 cells. Genet Mol Res, 2015. 14(1): p. 1056-1067.
219. Liao, W., et al., Curcumin inhibited growth of human melanoma A375 cells via inciting oxidative stress. Biomedicine & Pharmacotherapy, 2017. 95: p. 1177-1186.
220. McNab, F., et al., Type I interferons in infectious disease. Nature Reviews Immunology, 2015. 15(2): p. 87-103.
221. Fleitas-Salazar, N., et al., Long-term release of bioactive interferon-alpha from PLGA-chitosan microparticles: in vitro and in vivo studies. Biomaterials Advances, 2022. 143: p. 213167.
222. Vidal, P., Interferon α in cancer immunoediting: From elimination to escape. Scandinavian Journal of Immunology, 2020. 91(5): p. e12863.
223. Ferrantini, M., I. Capone, and F. Belardelli, Interferon-α and cancer: Mechanisms of action and new perspectives of clinical use. Biochimie, 2007. 89(6): p. 884-893.
224. Xiong, F., et al., Direct and indirect effects of IFN-α2b in malignancy treatment: not only an archer but also an arrow. Biomarker Research, 2022. 10(1): p. 69.
225. Weir, S.A., et al., The Immunotherapeutic Role of Type I and III Interferons in Melanoma and Non-Melanoma Skin Cancers. Life (Basel), 2023. 13(6).
226. Barmpalexis, P., et al., Artificial neural networks in the optimization of a nimodipine controlled release tablet formulation. Eur J Pharm Biopharm, 2010. 74(2): p. 316-23.
227. Acharya, G., C.H. Lee, and Y. Lee, Optimization of cardiovascular stent against restenosis: factorial design-based statistical analysis of polymer coating conditions. PLoS One, 2012. 7(8): p. e43100.
228. Ahmed, R.K., et al., Multivariate experimental design: towards more reliable electrochemical detection. Current Opinion in Electrochemistry, 2022. 31: p. 100880.
229. Kumar, G., et al., Central Composite Design Implemented Azilsartan Medoxomil

Loaded Nanoemulsion to Improve Its Aqueous Solubility and Intestinal Permeability: In Vitro and Ex Vivo Evaluation. Pharmaceuticals (Basel), 2022. 15(11).

230. Saez, V., et al. Microencapsulation of recombinant interferon α2 b into poly (D , L-lactide-co-glycolide) microspheres. 2008.
231. Paragkumar N, T., D. Edith, and J.-L. Six, Surface characteristics of PLA and PLGA films. Applied Surface Science, 2006. 253(5): p. 2758-2764.
232. Wan, F., et al., One-Step Production of Protein-Loaded PLGA Microparticles via Spray Drying Using 3-Fluid Nozzle. Pharmaceutical Research, 2014. 31(8): p. 1967-1977.
233. Mukerjee, A. and J.K. Vishwanatha, Formulation, characterization and evaluation of curcumin-loaded PLGA nanospheres for cancer therapy. Anticancer Res, 2009. 29(10): p. 3867-75.
234. Singh, R., et al., Development and characterization of folate anchored Saquinavir entrapped PLGA nanoparticles for anti-tumor activity. Drug development and industrial pharmacy, 2015. 41: p. 1-14.
235. Cleland, J.L., Solvent evaporation processes for the production of controlled release biodegradable microsphere formulations for therapeutics and vaccines. Biotechnol Prog, 1998. 14(1): p. 102-7.
236. Abobaker, M., M. Govender, and Y.E. Choonara, Non-surgical Synergistic Interventions for the Treatment of Skin Cancer. Curr Pharm Des, 2024.
237. Nezhad-Mokhtari, P., et al., A review on the construction of hydrogel scaffolds by various chemically techniques for tissue engineering. European Polymer Journal, 2019. 117: p. 64-76.
238. Czajkowska-Kośnik, A., M. Szekalska, and K. Winnicka, Nanostructured lipid carriers: A potential use for skin drug delivery systems. Pharmacological Reports, 2019. 71(1): p. 156-166.
239. Dattilo, M., et al., Polysaccharide-Based Hydrogels and Their Application as Drug Delivery Systems in Cancer Treatment: A Review. J Funct Biomater, 2023. 14(2).
240. Ibrahim, R., et al. Cell Secretome Strategies for Controlled Drug Delivery and Wound-Healing Applications. Polymers, 2022. 14, DOI: 10.3390/polym14142929.
241. Heger, R., et al., Novel Hydrogel Material with Tailored Internal Architecture Modified by "Bio" Amphiphilic Components-Design and Analysis by a Physico-Chemical Approach. Gels, 2022. 8(2).
242. Norahan, M.H., et al., Structural and biological engineering of 3D hydrogels for wound healing. Bioact Mater, 2023. 24: p. 197-235.
243. Czajkowska-Kośnik, A., E. Szymańska, and K. Winnicka, Nanostructured Lipid Carriers (NLC)-Based Gel Formulations as Etodolac Delivery: From Gel Preparation

to Permeation Study. Molecules, 2022. 28: p. 235.
244. Szekalska, M., et al., Mucoadhesive Alginate/Pectin Films Crosslinked by Calcium Carbonate as Carriers of a Model Antifungal Drug—Posaconazole. Pharmaceutics, 2023. 15(10): p. 2415.
245. Nokoorani, Y.D., et al., Fabrication and characterization of scaffolds containing different amounts of allantoin for skin tissue engineering. Sci Rep, 2021. 11(1): p. 16164.
246. Vinogradov, S.V., E.V. Batrakova, and A.V. Kabanov, Nanogels for oligonucleotide delivery to the brain. Bioconjugate chemistry, 2004. 15(1): p. 50-60.
247. Gonçalves, C., P. Pereira, and M. Gama, Self-assembled hydrogel nanoparticles for drug delivery applications. Materials, 2010. 3(2): p. 1420-1460.

APPENDICES

APPENDIX A

APPENDIX A1

ANIMAL RESEARCH ETHICS COMMITTEE
Registration number: AREC-101210-002

Date: 07/11/2024

Certificate reference: Waiver 07-11-2024-O
Category: O
Applicant: Magdi Abobaker
Department: Department of Pharmacy and Pharmacology.
Email: 2403225@students.wits.ac.za
Contact number: 078 009 6644

Re: Waiver from the Animal Ethics Research Committee of the University of the Witwatersrand

This letter is to confirm that PhD candidate, Magdi Abobaker (student number 2403225)) registered in the Department of Pharmacy and Pharmacology, Faculty of Health Sciences (WITS), does not require full Animal Ethics Research Committee clearance to undertake the work entitled **"A multi-component, dual-release topical platform for skin cancer".**

Reason for waiver
This is an *ex vivo* study in which pig (*Sus scrofa domesticus*) or sheep (*Ovies Aries*) skin samples will be harvested from following termination of the animals in an unrelated studies, housed within the Wits Animal Research Facility (WRAF). No additional animals will be allocated to this study.

Details of the study
Following termination of the animals, skin samples will be excise by the WRAF technical staff. Skin samples will be used to perform *ex vivo* drug permeation studies of a topical hydrogel system incorporating Cur-FeONP and IFN-α. Drug permeability and diffusion studies will be performed using Franz diffusion cell assembly and monitored using a spectrophotometer.

The individuals covered by this waiver include Magdi Abobaker, and supervisors Professor Yahya E. Choonara and Dr Mershen Govender, Department of Pharmacy and Pharmacology (WITS).

Please contact me should you require further information.

Yours sincerely,

Dr Mark Killick
Deputy Chair: Animal Research Ethics Committee
University of the Witwatersrand.
Mail: Mark.Killick@wits.ac.za Office number: 011 717 2362

APPENDIX A2

Send Orders for Reprints to reprints@benthamscience.net

Current Pharmaceutical Design, XXXX, XX, 1-16 1

REVIEW ARTICLE

Non-surgical Synergistic Interventions for the Treatment of Skin Cancer

Magdi Abobaker[1], Mershen Govender[1] and Yahya E. Choonara[1,*]

[1]Wits Advanced Drug Delivery Platform Research Unit, Department of Pharmacy and Pharmacology, School of Therapeutic Sciences, Faculty of Health Sciences, University of the Witwatersrand, 7 York Road, Parktown, Johannesburg 2193, South Africa

ARTICLE HISTORY

Received: December 12, 2023
Accepted: May 02, 2024

DOI:
10.2174/0113816128298629240503065109

Abstract: Skin cancer is broadly classified into two categories *i.e.*, non-melanoma skin cancer (NMSC) and malignant melanoma (MM), with MM having a greater fatality rate than NMSC. A large number of treatment strategies currently exist for these skin cancer types, ranging from monotherapies to complex multifaceted synergistic interventions including dual therapies, trimodality therapy, and multicomponent combinations therapy. These combinatorial cancer treatments have delivered more favorable results when compared with monotherapies, and although combination treatments increase the cost of treatment, these regimens have lower side effect profiles, decreased resistance, high efficacy and an improved long-term response. Synergistic combination treatments for skin cancer are often complex, wide-ranging and encompass diverse platforms with various mechanisms of action. An understanding of the physiological potential, as well the efficacy of such treatments, is therefore vital to ensure patients receive the best possible treatment. This review therefore focuses on the current advancements and existing non-surgical combinative drug delivery methods utilized for treating skin cancer. It encompasses the diverse pharmaceutical delivery systems, clinical outcomes, and oncology strategies employed and aims to highlight the role of non-surgical combination therapies in enhancing patient compliance, reducing treatment durations, and improving overall survival rates while addressing relapses and metastasis. The promising outlook of the research being conducted in this field has also been provided, as well as the barriers to the effective treatment of this complex condition.

Keywords: Skin cancer, non-surgical interventions, melanoma, combination therapies, radiotherapy, chemotherapy.

1. INTRODUCTION

Skin cancers are classified into non-melanoma skin cancer (NMSC) and malignant melanoma (MM), with the former more broadly diagnosed and the cause of a greater number of deaths than the latter. NMSC, which encompasses cancers including basal cell carcinoma (BCC), squamous cell carcinoma (SCC), and actinic keratosis (AK), has a good prognosis if diagnosed early, with treatment often leading to complete a cure. However, in more complicated cases, often due to late diagnosis or incorrect management of the condition, there is a risk of local advancement, particularly with SCC, which may result in metastasis to nearby proximal lymph nodes, leading to the spread of cancer. Additionally, AKs are neoplasms occurring on sun-exposed damaged skin areas which, if left untreated, can progress to SCCs [1]. NMSC is estimated to have caused 65,000 deaths globally, with over 1,000,000 new cases reported, according to the Global Burden of Disease (GBD) and GLOBOCAN 2020 [2-4]. MM, on the contrary, affects the melanocytes found in the lowest layer of the epidermis and is characterized by an aggressive clinical behavior with rapid metastasis of the tumor, spreading to other organs in the human body if not detected and treated early. Other examples of metastatic skin cancers include neuroendocrine tumors, sarcoma, as well as certain lymphomas, which may develop from cancerous white blood cells called B cells and T cells [5-8]. Skin cancer is therefore an aggressive, fatal disease and a global health challenge with incidence rates higher in Caucasians compared to other demographics [9]. One of the main causes of skin cancer and pathogenesis includes exposure to ultraviolet (UV) radiation with UVA1, UVA2 and UVB, of radiation wavelength (340-400 nm), (320-340 nm) and (280-320 nm) respectively, posing a greater risk [10, 11]. It however should be noted that while UV radiation has been determined to be one of the primary causes of skin cancer, it also serves as a valuable treatment modality, particularly as phototherapy (UVA and narrowband UVB) in the treatment of some skin tumors, cutaneous lymphomas, T-cell lymphomas, and Mycosis Fungoides (MF) [12].

According to a study by Iqbal *et al.* a number of factors contribute to skin carcinogenesis, which occurs in three stages: initiation, promotion, and progression (Fig. 1). Anticancer interventions have resultantly been used to treat cancer cells during either of these stages. Skin cancer also has several progression stages, with Stage I involving a genotoxic effect due to tumor initiation, which is a quick process that occurs due to exposure to carcinogens, their delivery into the cells, and their interaction with DNA, while Stage II involves cancer promotion, which is a lengthy phase characterized by the proliferation of cancer cells, with Stage III resulting in tumor progression, accompanied by tumor growth, metastasis, and invasion into the surrounding cells [13].

The common treatment approaches for skin cancer depend on the cancer stage, in addition to genetics, age, location of the carcinoma, genodermatoses, human papillomavirus (HPV) infection, drug, and tobacco use, the presence of severe skin and/or bone infections, as well as other inflammatory diseases [14-17]. Surgery is the most utilized treatment in the early stages, however in advanced stages, a greater number of treatment strategies are applied, including chemotherapy (CT), electrochemotherapy (ECT), photodynamic therapy (PDT), photothermal therapy (PTT), radiotherapy (RT), immunotherapy, thermotherapy, and synergistic multicomponent therapies [18]. ECT, in particular, which has been utilized for the delivering of chemotherapeutic agents for the treatment of skin cancers, such as melanoma and cutaneous B-cell lymphoma, has also been noted to induce an immune response, which may enhance the effectiveness of the treatment [19]. While these therapies have

* Address correspondence to this author at the Wits Advanced Drug Delivery Platform Research Unit, Department of Pharmacy and Pharmacology, School of Therapeutic Sciences, Faculty of Health Sciences, University of the Witwatersrand, 7 York Road, Parktown, Johannesburg 2193, South Africa; Fax: +27-11-642-4355;
E-mail: Yahya.Choonara@wits.ac.za

1381-6128/XX $65.00+.00 © XXXX Bentham Science Publishers

APPENDIX A3

pharmaceutics

MDPI

Article

Co-Formulation of Iron Oxide and PLGA Nanoparticles to Deliver Curcumin and IFNα for Synergistic Anti-Cancer Activity in A375 Melanoma Skin Cancer Cells

Magdi Abobaker [1], Mershen Govender [1] and Yahya E. Choonara [1,*]

[1] Wits Advanced Drug Delivery Platform Research Unit, Department of Pharmacy and Pharmacology, School of Therapeutic Sciences, Faculty of Health Sciences, University of the Witwatersrand, Johannesburg, 7 York Road, Parktown, 2193, South Africa.

* Correspondence: yahya.choonara@wits.ac.za; Tel.: +27-11-717-2052; Fax: +27-11-642-4355.

Abstract: Background/Objectives: Skin cancer remains a significant global health issue, driving the development of new treatment strategies to improve clinical outcomes and prevent recurrence. Traditional monotherapies often face obstacles such as bioactive resistance, prompting interest in combination therapies that enhance efficacy, while minimizing side effects. This study investigated the use of a co-nanoparticle approach of iron oxide nanoparticles (NPs) surface-functionalized with curcumin (Cur-FeONPs) delivered with prolonged-release interferon-alpha (IFNα)-loaded PLGA NPs (IFNα-PLGANPs) for the synergistic treatment of malignant melanoma tested in A375 cells. **Methods**: Extensive *in vitro* characterization studies of the Cur-FeONPs and IFNα-PLGANPs have been performed including zeta-size profiling, morphological studies and structural validation, in addition to cytotoxicity assessments on A375 melanoma and NIH-3T3 fibroblast cells. **Results**: The Cur-FeONP and IFNα-PLGANPs synthesis processes yielded NPs of an average size of 111.0 nm and 97.0 nm, respectively. Morphological and structural validations studies determined the successful synthesis of the nanoparticulate systems with cell viability analyses displaying significant cytotoxicity against A375 melanoma cells for the combination treatment, when compared to the individual platforms, with a minimal effect on NIH-3T3 fibroblast cells. **Conclusions**: The results of this study present a promising synergistic approach for enhanced anti-cancer activity in A375 melanoma skin cancer cells, providing a potential platform for future preclinical and clinical studies.

Keywords: Melanoma; Synergistic treatment; Controlled release; Chemotherapy; Immunotherapy; Curcumin; Interferon alpha; A375 Melanoma Cells.

APPENDIX A4

A Multi-phasic Controlled Release System for Treatment of Skin Cancer

Magdi Abobaker, Mershen Govender, Yahya E. Choonara*

Wits Advanced Drug Delivery Platform Research Unit, Department of Pharmacy and Pharmacology, School of Therapeutic Sciences, Faculty of Health Sciences, University of the Witwatersrand, 7 York Road, Parktown, Johannesburg 2193, South Africa*
*Corresponding Author: Professor Yahya E. Choonara; Email: Yahya.Choonara@wits.ac.za

Introduction

Skin cancers, including non-melanoma skin cancer (NMSC) and malignant melanoma (MM), are primarily caused by excessive exposure to UV light. NMSC is more common globally, especially among Caucasians, with rising incidence rates annually (between 3-8% since the 1960s) [1]. MM, however, leads to more deaths due to metastasis [2], encompassing rare types like Merkel Cell Carcinoma and Kaposi sarcoma [3]. This study investigates an innovative treatment approach for skin cancer, particularly melanoma, using iron oxide nanoparticles (FeO-NPs) functionalized with curcumin and encapsulated interferon-alpha (IFNα) in PLGA nanoparticles (IFNα-PLGANPs). The combined anticancer properties of curcumin and controlled release of IFNα offer a promising, multifaceted therapeutic option, delivered through a biocompatible hydrogel made from natural-based polymeric materials. The precision-guided nanosystem will constitute Curcumin-stabilized Fe_3O_4 nanoparticles (Cur-FeONPs) and the IFNα-PLGANPs delivered in 6 phases as described in (Fig.1).

Experimental method

Cur-FeONPs were synthesized using a one-step coprecipitation method [4]. Additionally, IFNα was encapsulated within PLGA nanoparticles to enable controlled drug release and prevent degradation when combined with Cur-FeONPs. The nanoparticles were produced through a spray-drying formulation technique [5].
TEM&SEM were used for morphological analysis. Zeta Sizer Dynamic Light Scattering and phase-analysis light scattering measurements were conducted on a Zeta Sizer instrument to determine the average hydrodynamic diameter and zeta potential of the synthesized Cur-FeONPs and IFNα-PLGANPs. FTIR analysis was conducted to detect the distinctive functional groups of pure curcumin, Cur-FeONPs, FeONPs and IFNα-PLGANPs using a Spectrum 100 FTIR spectrophotometer. DSC A DSC822E instrument was used to investigate the thermal properties of various formulations synthesized. modifications.

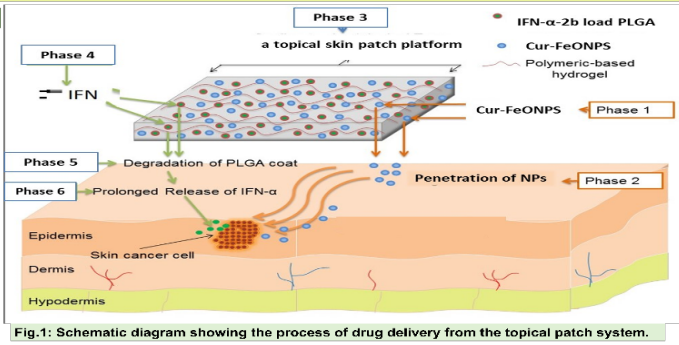


Fig.1: Schematic diagram showing the process of drug delivery from the topical patch system.

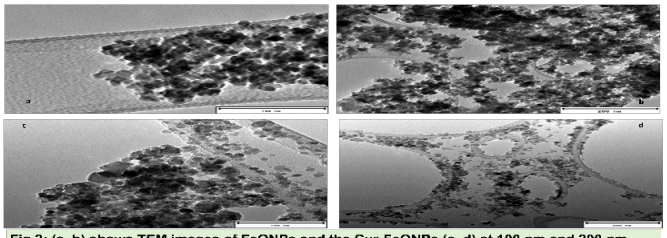


Fig.2: (a, b) shows TEM images of FeONPs and the Cur-FeONPs (c, d) at 100 nm and 200 nm scales.

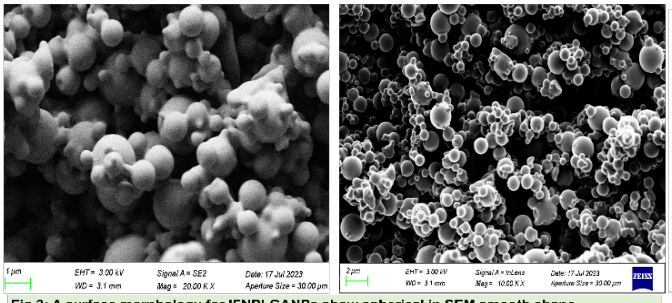


Fig.3: A surface morphology for IFNPLGANPs show spherical in SEM smooth shape.

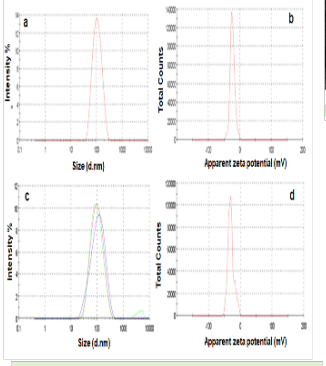


Fig.4: Zeta size and potential of the FeONPs (a & b), and Cur-FeONPs (c and d)

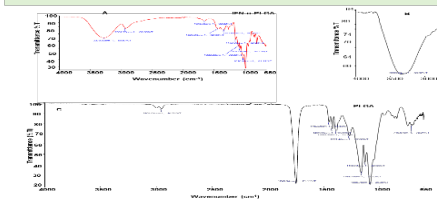
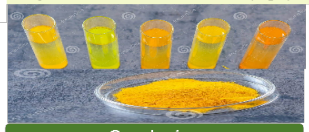


Fig.5: FTIR spectra for (a) IFNα-loaded PLGANPs, (b) IFN-α 2b, and (c) PLGA

Results and discussion

TEM and SEM images confirmed spherical, <100 nm particles and the successful synthesis of samples (Fig.2&3), beneficial for drug delivery. Cur-FeO-NPs showed an average particle size of 86.92 nm , with a high zeta potential indicating stability (Fig.4). IFNα-PLGANPs had an average size of 92.61 nm, with a smooth, spherical morphology confirmed by SEM. FTIR (Fig.5) and DSC (Fig.6) analyses confirmed the functionalization of the nanoparticles and thermal properties. Thermal and FTIR analyses showed stable encapsulation and potential for controlled drug release, with a high encapsulation efficiency of 78.9%. In contrast, the remaining release over the subsequent 5 days was 76.3%, indicating that complete release may take longer than 7 days to reach 100% as showed in (Fig.7).

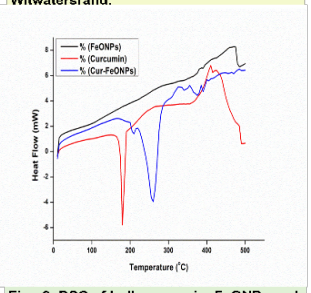


Conclusion

The study developed Cur-FeONPs and IFNα-PLGANPs, showing stable size, zeta potential, and controlled release, indicating potential for enhanced targeted skin cancer therapy through improved cellular uptake and therapeutic efficacy.

Acknowledgements

The research has been supported by the National Research Foundation of South Africa and the Faculty Research Committee of the University of the Witwatersrand.



Figu.6: DSC of bulk curcumin, FeONPs and Cur-FeONPs the shift due to Cur conjugated FeONPs complex formation

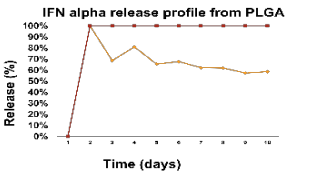


Fig.7: The release of IFN-α2b from PLGA nanoparticles over a 7-day.

References

1. Diepgen, T.L. and V. Mahler, *The epidemiology of skin cancer.* British Journal of Dermatology, 2002. 146(s61): p. 1-6.
2. C.S.SANDER, F.H., P.ELSNER AND J.J.THIELEDepartment of Dermatology, Friedrich Schiller University Jena, Erfurter Strasse 35, D-07740 Jena, Germany, *Oxidative stress in malignant melanoma and non-melanoma skin cancer.* 2003.
3. Sabir, F., et al., *How to face skin cancer with nanomaterials: A review.* 2021. 11: p. 11931-11955 %J Biointerface Res. Appl. Chem.
4. 2. Wan, F., et al., *One-Step Production of Protein-Loaded PLGA Microparticles via Spray Drying Using 3-Fluid Nozzle.* Pharmaceutical Research, 2014. 31(8): p. 1967-1977.
5. Bhandari, R., et al., *Single step synthesis, characterization and applications of curcumin functionalized iron oxide magnetic nanoparticles.* Materials Science and Engineering: C, 2016. 67: p. 59-64.

APPENDIX A5

COIL (collaborative online international learning)

- A COIL is a collaborative activity where students from different Universities work in international teams on a specific project.

COIL: AWARENESS OF PUBLIC HEALTH CHALLENGES IN SOUTH AFRICA AND SPAIN:
University San Pablo CEU –University of the Witwatersrand

- In this COIL students will work on a SPECIFIC **PUBLIC HEALTH ISSUE** **in South Africa and Spain with the aim of raising awareness in CEU and Wits educational communities about the health situation in both countries.**
- All the information gathered by each team will be presented in a final common session.

CEU | Universidad San Pablo





"AWARENESS OF PUBLIC HEALTH CHALLENGES IN SOUTH AFRICA AND SPAIN"

CONFIRMATION OF PARTICIPATION

Magdi Abobaker

presented an oral communication in the topic "Noncommunicable diseases: Obesity and Diabetes" at the **Final Session of the COIL: AWARENESS CAMPAIGNS OF PUBLIC HEALTH CHALLENGES IN SOUTH AFRICA AND SPAIN**

held online on November 13th, 2024

This Collaborative Online International Learning (COIL) project was organized by **Universidad CEU San Pablo** (Spain) and **Wits University** (South Africa)

The Organizing Commitee:

CEU | Universidad San Pablo

WITS UNIVERSITY

APPENDIX A6

A Multi-Component, Dual Release Platform for the Treatment of Skin Cancer

Magdi Abobaker, Mershen Govender, Yahya E. Choonara*.

Wits Advanced Drug Delivery Platform Research Unit, Department of Pharmacy and Pharmacology, School of Therapeutic Sciences, Faculty of Health Sciences, University of the Witwatersrand, 7 York Road, Parktown, Johannesburg 2193, South Africa*

*Corresponding Author:

Professor Yahya E. Choonara. Email: Yahya.Choonara@wits.ac.za

Introduction

This study explores a novel approach to treating skin cancer, focusing on the use of iron oxide nanoparticles (FeO-NPs) functionalized with curcumin (Cur) and encapsulated interferon-alpha (IFNα) in PLGA nanoparticles. Targeting melanoma, this strategy combines the anticancer properties of Cur with the controlled release of IFNα, offering a promising, multifaceted therapeutic option. The topical patch delivery system utilizes a biocompatible hydrogel made from natural-based polymeric materials utilizing the synergistic effects of multi-component interventions in the treatment of skin cancer Figure 1.

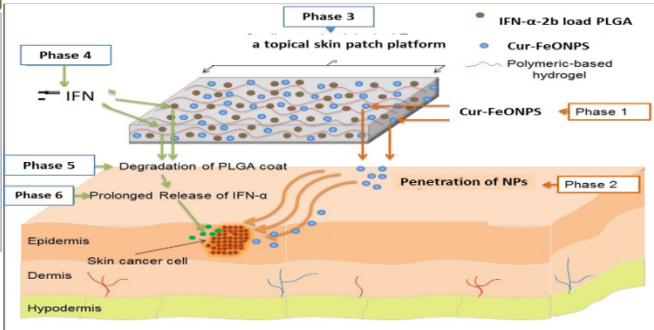


Figure 1: Schematic diagram showing the process of drug delivery from the topical patch system.

Experimental method

Curcumin-stabilized Fe_3O_4 nanoparticles (Cur-FeONPs) were synthesized using a one-step coprecipitation method [1]. Additionally, interferon-alpha (IFNα) was encapsulated within PLGA nanoparticles (IFNα-PLGANPs) to enable controlled drug release and prevent degradation when combined with Cur-FeONPs. The nanoparticles were produced through a spray-drying formulation technique [2].

Characterizations

Zeta Sizer Dynamic Light Scattering and phase-analysis light scattering measurements were conducted on a Zeta Sizer instrument to determine the average hydrodynamic diameter and zeta potential of the synthesized Cur-FeONPs and IFNα-PLGANPs.

SEM & TEM images confirmed the successful synthesis of Cur-FeONPs, Cur, FeONPs and IFNα-PLGANPs
Chemical Structure

FTIR An analysis was conducted to detect the distinctive functional groups of pure curcumin, Cur-FeONPs, FeONPs and IFNα-PLGANPs using a Spectrum 100 FTIR spectrophotometer.

DSC Optimization of IFN-PLGANPs, zeta size and release study as depicted in figure 4.

XRD analysis was conducted using a RIGAKU MiniFlex instrument to evaluate the crystallinity of Cur and IFNα before and after

Table 1: SDS-Page Gel-Electrophoresis Test Gel Components

Chemical	4% sample gel (stacker)	10% sample gel (separator)
	2 gels	2 gels
Acrylamide/ bisacrylamide solution (ml)	0.5	3
Gel buffer (3X) (ml)	1.5	5
Glycerol (ml)		1.5
Add water to final V (ml)	6 (4)	15 (5.5)
Polymerise by adding		
APS (10%) (µl)	45	75
TEMED (µl)	9	7.5

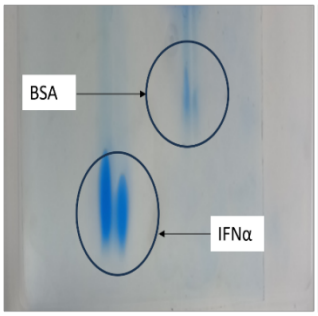


Figure2: Visualization of protein separation and characterization of the molecular weight properties of the IFN-PLGANPs and BSA.

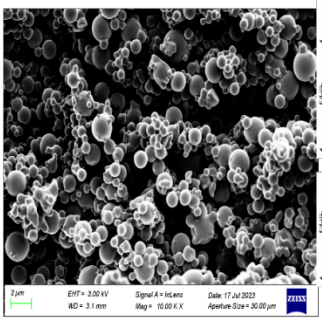


Figure 3: A surface morphology for IFNPLGANPs show spherical in SEM smooth shape.

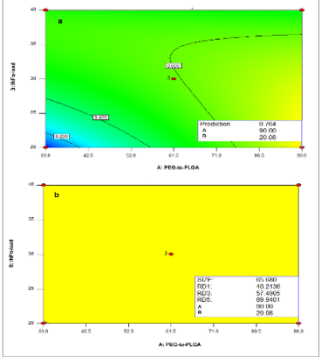


Figure 4: Contour plot of numerical optimization (a) and overlay plot of graphical optimization (b).

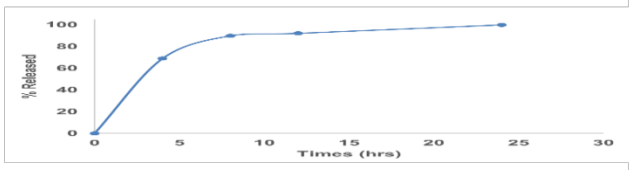


Figure 5. Cur release profile of the synthesized Cure-FeONPs.

Results and discussion

Cur-FeO-NPs showed an average particle size of 86.92 nm, with a high zeta potential indicating stability. SEM and TEM confirmed spherical, <100 nm particles, beneficial for drug delivery. XRD and FTIR analyses confirmed the crystalline structure and functionalization of the nanoparticles. IFNα-PLGANPs had an average size of 92.61 nm, with a smooth, spherical morphology confirmed by SEM. Thermal and FTIR analyses showed stable encapsulation and potential for controlled drug release, with a high encapsulation efficiency of 78.9%.

Conclusion

The study developed curcumin-conjugated iron oxide and interferon-loaded PLGA nanoparticles, showing stable size, negative zeta potential, and controlled release, indicating potential for enhanced targeted skin cancer therapy through improved cellular uptake and therapeutic efficacy. 98 % cell viability on NIH-3T3.

Acknowledgements

The research has been supported by the National Research Foundation of South Africa and the Faculty Research Committee of the University of the Witwatersrand.

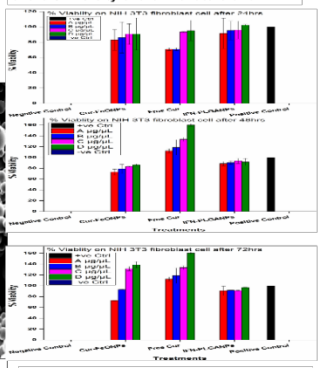


Figure 6:Cytotoxicity assessments to evaluate the cell viability of Cur–FeONPs, free Cur and IFNα-PLGANPs at different concentrations. The experiments will span 24, 48, and 72 hours, involving NIH 3T3 cells with a sample size (n=3).

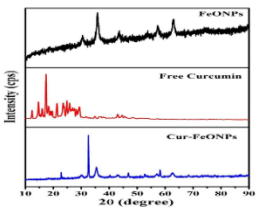


Figure 7: XRD spectra of free Cur, Cur-FeONPs, and free FeONPs.

References

1. Bhandari, R., et al., *Single step synthesis, characterization and applications of curcumin functionalized iron oxide magnetic nanoparticles.* Materials Science and Engineering: C, 2016. 67: p. 59-64.
2. Wan, F., et al., *One-Step Production of Protein-Loaded PLGA Microparticles via Spray Drying Using 3-Fluid Nozzle.* Pharmaceutical Research, 2014. 31(8): p. 1967-1977.